

NASA Contractor Report 3537

NASA  
CR  
3537  
c.1

TECH LIBRARY KAFB, NM



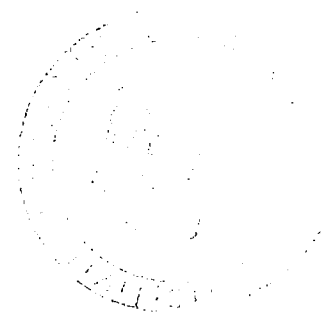
# A Harmonic Analysis Method for Unsteady Transonic Flow and Its Application to the Flutter of Airfoils

F. Edward Ehlers and Warren H. Weatherill

LOAN COPY: RETURN TO  
NASA TECHNICAL LIBRARY  
MAIL STOP 300, B-4

CONTRACT NAS1-15957  
MAY 1982

**NASA**





## NASA Contractor Report 3537

# A Harmonic Analysis Method for Unsteady Transonic Flow and Its Application to the Flutter of Airfoils

F. Edward Ehlers and Warren H. Weatherill

*Boeing Commercial Airplane Company  
Seattle, Washington*

Prepared for  
Langley Research Center  
under Contract NAS1-15957



National Aeronautics  
and Space Administration

Scientific and Technical  
Information Branch

1982



# CONTENTS

	Page
1.0 SUMMARY .....	1
2.0 INTRODUCTION .....	2
3.0 ABBREVIATIONS AND SYMBOLS .....	5
4.0 FORMULATION AND SOLUTION .....	9
5.0 INVESTIGATION OF SHOCK WAVE MOTION ON AN OSCILLATING AIRFOIL .....	12
5.1 Description of Basic Shock Motions and Effects on Flutter .....	12
5.2 Effect of Grid Refinement about the Steady State Shock on the Solution .....	13
5.3 Effect of Shock Point Operator on the Solution .....	14
5.4 Effect of Shock Boundary Conditions on the Solution .....	14
5.5 Incorporating the Effects of the Moving Shock in the Calculation of Lift and Moment .....	16
6.0 CORRELATION OF THEORETICAL CALCULATIONS WITH THE EXPERIMENTS OF NASA AMES RESEARCH CENTER .....	21
6.1 Correlation of Steady State Pressure Distributions .....	21
6.2 Correlation of Unsteady Pressure Distributions .....	22
7.0 FLUTTER ANALYSES OF A NACA 64A010 AIRFOIL .....	25
7.1 Equations of Motion .....	26
7.2 A Nominal Configuration .....	27
7.3 Two Examples for Correlation with Other Analyses .....	30
8.0 IMPROVEMENTS IN NUMERICAL PROCEDURES .....	32
8.1 The Two Step Method .....	32
8.2 The ADI Method of Harmonic Solution Based on Time Integration .....	33
9.0 CONCLUSIONS .....	36
APPENDIX A   Derivation of the Shock Relations for a Moving Shock Referred to the Steady State Shock Locations .....	37
APPENDIX B   Derivation of the Shock Point Operator .....	42
APPENDIX C   Derivation of the Difference Equations for the Two Step Method .....	47
APPENDIX D   Derivation of the ADI Method for the Frequency Domain Solution Based on Time Integration .....	50
REFERENCES .....	62

# LIST OF FIGURES

	Page
A-1 Illustration of u Distribution About a Shock Point .....	41
B-1 Control Volume for Shock Point Operator .....	43
1. Instantaneous Unsteady Pressure Distribution on the Upper Surface of a Pitching NACA 64A010 Airfoil Computed From the Harmonic Solution .....	65
2. Instantaneous Unsteady Pressure Distribution on the Lower Surface of a Pitching NACA 64A010 Airfoil Computed From the Harmonic Solution .....	66
3. Influence of Grid Refinement on the Real Part of the Pressure Pulse, NACA 64A010 Airfoil Oscillating in Pitch About the Quarter-Chord Point, $M=0.8$ , $k=0.3$ .....	67
4. Influence of Grid Refinement on the Imaginary Part of the Pressure Pulse, NACA 64A010 Airfoil Oscillating in Pitch About the Quarter-Chord Point, $M=0.8$ , $k=0.3$ .....	68
5. Influence of Grid Refinement on the Jump in Real Part of Unsteady Potential Across a NACA 64A010 Airfoil Oscillating in Pitch About the Quarter-Chord Point, $M=0.8$ , $k=0.3$ .....	69
6. Influence of Grid Refinement on the Jump in Imaginary Part of Unsteady Potential Across a NACA 64A010 Airfoil Oscillating in Pitch About the Quarter-Chord Point, $M=0.8$ , $k=0.3$ .....	70
7. Three-Dimensional Surface Representation of Real Part of Unsteady Potential, Coarse Grid, $M=0.8$ , $k=0.3$ , $\alpha_m=1^\circ$ .....	71
8. Three-Dimensional Surface Representation of Imaginary Part of Unsteady Potential, Finer Grid, $M = 0.8$ , $k = 0.3$ , $\alpha_m = 1^\circ$ .....	72
9. Three-Dimensional Surface Representation of Imaginary Part of Unsteady Potential, Finest Grid, $M = 0.8$ , $k = 0.3$ , $\alpha_m = 1^\circ$ .....	73
10. Three-Dimensional Surface Representation of Real Part of Unsteady Potential for Solution With Coarse Grid and First Form of the Shock Point Operator, $M = 0.8$ , $k = 0.3$ , $\alpha_m = 1^\circ$ .....	74
11. Three-Dimensional Surface Representation of Imaginary Part of Unsteady Potential for Solution With Coarse Grid and First Form of the Shock Point Operator, $M = 0.8$ , $k = 0.3$ , $\alpha_m = 1^\circ$ .....	75
12. Jump in Unsteady Potential Across Airfoil for Solution With Coarse Grid and First Form of the Shock Point Operator, $M = 0.8$ , $k = 0.3$ , $\alpha_m = 1^\circ$ .....	76
13. Three-Dimensional Surface Representation of Real Part of Unsteady Potential for Solution With Coarse Grid and Third Form of the Shock Point Operator, $M = 0.8$ , $k = 0.3$ , $\alpha_m = 1^\circ$ .....	77
14. Three-Dimensional Surface Representation of Imaginary Part of Unsteady Potential for Solution With Coarse Grid and Third Form of the Shock Point Operator, $M = 0.8$ , $k = 0.3$ , $\alpha_m = 1^\circ$ .....	78
15. Examples of Fitted Shock Obtained From Modifying Captured Shock .....	79

## LIST OF FIGURES (Continued)

	Page
16. Comparison of the Jump in Potential Across the Airfoil for Fitted Shock From Shock Boundary Conditions With Results From the Shock Point Operator, $M = 0.8$ , $k = 0.3$ , $\alpha_m = 1^\circ$ .....	80
17. Effect of Shock Point Operator on Real Part of Unsteady Potential With Weak Steady Shock, $M = 0.8$ , $k = 0.3$ , $\alpha_m = 0^\circ$ , Coarse Grid .....	81
18. Effect of Shock Point Operator on Real Part of Unsteady Potential With Weak Steady Shock, $M = 0.8$ , $k = 0.3$ , $\alpha_m = 0^\circ$ , Fine Grid .....	82
19. Contribution of the Periodically Moving Shock Wave to the Pressure Signal at a Fixed Observation Point. (From Tijdeman, Reference 24) .....	83
20. Comparison of Steady State Pressure Distribution on a NACA 64A010 Airfoil as Computed by EXTRAN2 With NASA-Ames Experiments, $M = 0.75$ , $\alpha_m = 0^\circ$ .....	84
21. Comparison of Steady State Pressure Distribution on a NACA 64A010 Airfoil as Computed by Three Methods With NASA Experiments, $M = 0.8$ , $\alpha_m = 0^\circ$ .....	85
22. Comparison of Steady State Pressure Distribution on a NACA 64A010 Airfoil as Computed by EXTRAN2 With NASA Ames Experiments, $M = 0.842$ , $\alpha_m = 0^\circ$ .....	86
23. Pressure Coefficient Distributions on NACA 64A010 Airfoil Pitching $1^\circ$ About Quarter-Chord Point, $M = 0.75$ , $k = 0.20$ , $\alpha_m = 0^\circ$ .....	87
24. Pressure Coefficient Distributions on NACA 64A010 Airfoil Pitching $1^\circ$ About Quarter-Chord Point, $M = 0.8$ , $k = 0.101$ , $\alpha_m = 0^\circ$ , Real Part .....	88
25. Pressure Coefficient Distributions on NACA 64A010 Airfoil Pitching $1^\circ$ About Quarter-Chord Point, $M = 0.8$ , $k = 0.101$ , $\alpha_m = 0^\circ$ , Imaginary Part ....	89
26. Pressure Coefficient Distributions on NACA 64A010 Airfoil Pitching $1^\circ$ About Quarter-Chord Point, $M = 0.8$ , $k = 0.202$ , $\alpha_m = 0^\circ$ , Real Part .....	90
27. Pressure Coefficient Distributions on NACA 64A010 Airfoil Pitching $1^\circ$ About Quarter-Chord Point, $M = 0.8$ , $k = 0.202$ , $\alpha_m = 0^\circ$ , Imaginary Part ....	91
28. Pressure Coefficient Distributions on NACA 64A010 Airfoil Pitching $1^\circ$ About Quarter-Chord Point, $M = 0.8$ , $k = 0.247$ , $\alpha_m = 0^\circ$ , Real Part .....	92
29. Pressure Coefficient Distributions on NACA 64A010 Airfoil Pitching $1^\circ$ About Quarter-Chord Point, $M = 0.8$ , $k = 0.247$ , $\alpha_m = 0^\circ$ , Imaginary Part ....	93
30. Pressure Coefficient Distributions on NACA 64A010 Airfoil Pitching $1^\circ$ About Quarter-Chord Point, $M = 0.8$ , $k = 0.303$ , $\alpha_m = 0^\circ$ , Real Part .....	94
31. Pressure Coefficient Distributions on NACA 64A010 Airfoil Pitching $1^\circ$ About Quarter-Chord Point, $M = 0.8$ , $k = 0.303$ , $\alpha_m = 0^\circ$ , Imaginary Part ....	95
32. Pressure Coefficient Distributions on NACA 64A010 Airfoil Pitching $1^\circ$ About Quarter-Chord Point, $M = 0.842$ , $k = 0.202$ , $\alpha_m = 0^\circ$ , Real Part .....	96
33. Pressure Coefficient Distributions on NACA 64A010 Airfoil Pitching $1^\circ$ About Quarter-Chord Point, $M = 0.842$ , $k = 0.202$ , $\alpha_m = 0^\circ$ , Imaginary Part ..	97

## LIST OF FIGURES (Continued)

	Page
34. Pressure Coefficient Distributions on NACA 64A010 Airfoil Oscillating 0.05 Semichord in Plunge, $M = 0.8$ , $k = 0.05$ , $\alpha_m = 0^\circ$ , Real Part .....	98
35. Pressure Coefficient Distributions on NACA 64A010 Airfoil Oscillating 0.05 Semichord in Plunge, $M = 0.8$ , $k = 0.05$ , $\alpha_m = 0^\circ$ , Imaginary Part .....	99
36. Pressure Coefficient Distributions on NACA 64A010 Airfoil Oscillating 0.05 Semichord in Plunge, $M = 0.8$ , $k = 0.101$ , $\alpha_m = 0^\circ$ , Real Part .....	100
37. Pressure Coefficient Distributions on NACA 64A010 Airfoil Oscillating 0.05 Semichord in Plunge, $M = 0.8$ , $k = 0.101$ , $\alpha_m = 0^\circ$ , Imaginary Part .....	101
38. Pressure Coefficient Distributions on NACA 64A010 Airfoil Oscillating 0.05 Semichord in Plunge, $M = 0.8$ , $k = 0.151$ , $\alpha_m = 0^\circ$ , Real Part .....	102
39. Pressure Coefficient Distributions on NACA 64A010 Airfoil Oscillating 0.05 Semichord in Plunge, $M = 0.8$ , $k = 0.151$ , $\alpha_m = 0^\circ$ , Imaginary Part .....	103
40. Comparison With Experiment of the Calculated Moment Coefficient About the Leading Edge of a NACA 64A010 Airfoil Oscillating $1^\circ$ in Pitch About the Quarter-Chord Point, $M = 0.8$ , $\alpha_m = 0^\circ$ .....	104
41. Comparison With Experiment of the Calculated Lift Coefficient for a NACA 64A010 Airfoil Oscillating $1^\circ$ in Pitch About the Quarter-Chord Point, $M = 0.8$ , $\alpha_m = 0^\circ$ .....	105
42. Definition of Parameters for an Airfoil Oscillating in Pitch and Plunge .....	106
43. Flutter Velocity and Frequency Versus Mass Ratio for a Flat Plate, $\omega_h/\omega_\alpha = 0.3$ .....	107
44. Flutter Modes (Amplitude Ratio and Phase Difference) Versus Mass Ratio, Flat Plate, $\omega_h/\omega_\alpha = 0.3$ .....	108
45. Flutter Velocity and Frequency Versus Mass Ratio for a NACA 64A010 Airfoil, $\omega_h/\omega_\alpha = 0.3$ .....	109
46. Flutter Modes (Amplitude Ratio and Phase Difference) Versus Mass Ratio, $\omega_h/\omega_\alpha = 0.3$ .....	110
47. Effect of Mach Number on the Steady Pressure Distribution on the Upper Surface of a NACA 64A010 Airfoil .....	111
48. Lift Coefficient Versus Mach Number for a NACA 64A010 Airfoil Oscillating in Plunge .....	112
49. Moment Coefficient Versus Mach Number for a NACA 64A010 Airfoil Oscillating in Plunge .....	113
50. Lift Coefficient Versus Mach Number for a NACA 64A010 Airfoil Oscillating in Pitch .....	114
51. Moment Coefficient Versus Mach Number for a NACA 64A010 Airfoil Oscillating in Pitch About Quarter-Chord .....	115
52. Flutter Velocity and Frequency Ratio Versus Mach Number for a NACA 64A010, $\omega_h/\omega_\alpha = 0.3$ , $\mu = 50$ .....	116
53. Flutter Velocity and Frequency Versus Mach Number for a NACA 64A010 Airfoil, $\omega_h/\omega_\alpha = 0.3$ , $\mu = 100$ .....	117

## LIST OF FIGURES (Continued)

	Page
54. Flutter Velocity and Frequency Versus Mach Number for a NACA 64A010 Airfoil, $\omega_h/\omega_\alpha = 0.3$ , $\mu = 300$ .....	118
55. Flutter Velocity and Frequency Versus Mass Ratio, Subsonic Flow, $\omega_h/\omega_\alpha = 0.6$ .....	120
56. Flutter Modes (Amplitude Ratio and Phase Difference) Versus Mass Ratio, Subsonic Flow .....	121
57. Flutter Velocity and Frequency Versus Mass Ratio for a NACA 64A010 Airfoil .....	122
58. Flutter Modes (Amplitude Ratio and Phase Difference) Versus Mass Ratio for a NACA 64A010 Airfoil .....	123
59. Flutter Velocity and Frequency Versus Mass Ratio for a NACA 64A010 Airfoil .....	124
60. Flutter Modes (Amplitude Ratio and Phase Difference) Versus Mass Ratio for a NACA 64A010 Airfoil .....	125
61. Flutter Velocity and Frequency Versus Mach Number for a NACA 64A010 Airfoil, $\omega_h/\omega_\alpha = 0.6$ , $\mu = 50$ .....	126
62. Flutter Velocity and Frequency Versus Mach Number for a NACA 64A010 Airfoil, $\omega_h/\omega_\alpha = 0.6$ , $\mu = 100$ .....	127
63. Flutter Velocity and Frequency Versus Mach Number for a NACA 64A010 Airfoil, $\omega_h/\omega_\alpha = 0.6$ , $\mu = 300$ .....	128
64. Behavior of U-g Curves with Variation in Mach Number .....	130
65. Flutter Velocity and Frequency Versus Mach Number for a NACA 64A010 Airfoil, "Case A" .....	131
66. Flutter Velocity and Frequency Versus Mach Number for a NACA 64A010 Airfoil, "Case B" .....	133
67. Real Part of Pressure Coefficient Distributions From One- and Two-Step Solution Procedures for a Fine, Full-Size Mesh, $M = 0.8$ , $k = 0.3$ , $\alpha_m = 0^\circ$ .....	135
68. Imaginary Part of Pressure Coefficient Distributions From One- and Two-Step Solution Procedures for a Fine, Full-Size Mesh, $M = 0.8$ , $k = 0.3$ , $\alpha_m = 0^\circ$ .....	136
69. Comparison of Pressure Coefficient Distribution From a Full-Size Mesh With the Distribution From a Reduced Mesh, One-Step Solution, Real Part, $M = 0.8$ , $k = 0.3$ , $\alpha_m = 0^\circ$ .....	137
70. Comparison of Pressure Coefficient Distribution From a Full-Size Mesh With the Distribution From a Reduced Mesh, One-Step Solution, Imaginary Part, $M = 0.8$ , $k = 0.3$ , $\alpha_m = 0^\circ$ .....	138
71. Comparison of Pressure Coefficient Distribution From a Solution With a Full-Size Mesh With the Distribution From a Two-Step Solution, $M = 0.8$ , $k = 0.3$ , $\alpha_m = 0^\circ$ , Real Part .....	139



## LIST OF FIGURES (Concluded)

	Page
72. Comparison of Pressure Coefficient Distribution From a Solution With a Full-Size Mesh With the Distribution From a Two-Step Solution, $M = 0.8$ , $k = 0.3$ , $\alpha_m = 0^\circ$ , Imaginary Part .....	140
73. Comparison of Pressure Coefficient Distribution From an ADI Solution With Linearized Theory for the Flow Over a Flat Plate Oscillating in Pitch About the Leading Edge, $M = 0.9$ , $k = 0.45$ .....	141
74. Comparison of Pressure Coefficient Distribution From an ADI Solution With Linearized Theory for the Flow Over a Flat Plate Oscillating in Pitch About the Leading Edge, $M = 0.9$ , $k = 0.6$ .....	142

## 1.0 SUMMARY

A finite difference method for solving the unsteady transonic flow about harmonically oscillating wings is investigated. The procedure is based on separating the velocity potential into steady and unsteady parts and linearizing the resulting unsteady differential equation for small disturbances. The differential equation for the unsteady velocity potential is linear with spatially varying coefficients and with the time variable eliminated by assuming harmonic motion.

The work of this report is a direct extension of earlier studies and includes correlation with experimental results, typical section flutter calculations for a NACA 64A010 airfoil, and some further theoretical development.

The main results of this study are as follows:

1. A study is made of the representation of the shock motion associated with an oscillating airfoil. The effects of the shock motion and the resulting pressure pulse are shown to be included in the pressure distributions and generalized forces as calculated using the harmonic method.
2. A typical section, two-degree-of-freedom flutter analysis of a NACA 64A010 airfoil for Mach numbers from 0.75 to 0.90 is presented. These studies show a sharp transonic bucket in one case and abrupt changes in instability modes.
3. Analytical and experimental pressure distributions for the NACA 64A010 airfoil are compared at Mach numbers of 0.75, 0.80 and 0.842. The results are presented for plunge and pitch modes and several reduced frequencies.
4. An alternating direction method is derived for the harmonic method. This formulation appears to provide a practical procedure using relaxation solution techniques which do not have solution convergence problems.

## 2.0 INTRODUCTION

Aerodynamic flutter may occur in any flight regime, but its presence at transonic speeds is of special interest to the flutter analyst; first because the critical flutter speed often occurs in this flow regime, and second, because of the difficulty in calculating unsteady transonic air forces. The flutter boundary, when plotted in terms of dynamic pressure versus Mach number, displays a characteristic "bucket" in the transonic regime which may well result in minimum flutter margins. This drop in dynamic pressure is partially due to the increase in magnitude of the pressure coefficients as predicted by linear theory. An additional reduction in this boundary is due to the presence of shocks over the airfoil. The existence of shocks significantly affect the aerodynamic forces in terms of magnitude, distribution, and phase angle with respect to surface motion, all of which are important in the evaluation of flutter. The degrading of the flutter boundary by transonic flow characteristics appears to be particularly important for wings with supercritical airfoil sections. This point is discussed by Ashley in reference 1.

The problem in calculating unsteady transonic flow stems from the presence of moving shocks and the resulting large velocity gradients. This necessitates the consideration of a nonlinear formulation. Also, the flow is "mixed" in the sense that both subsonic and supersonic regions exist and thus in adjacent regions in the flow field the governing differential equations may be of distinctly different character.

The current means for obtaining reliable flutter characteristics in the transonic region is through wind tunnel experiments. This expensive and time consuming process makes it highly desirable to have efficient analytic procedures available for the evaluation of transonic flutter so that the complete flutter characteristics can be studied during all phases of vehicle design and development.

In recent years, the steady-state transonic flow about a lifting surface of finite thickness has been satisfactorily handled using a finite difference formulation of the nonlinear differential equation and relaxation techniques to solve the resulting set of simultaneous equations. The results have correlated well with experimental data. The procedure is time consuming but appears practical and compatible with generally available resources.

The unsteady problem is not, as yet, capable of being handled in as practical a fashion. First of all, it is a problem of considerably more scope, as air forces must be generated for mode shapes and reduced frequencies as well as for the Mach number of the steady problem. Thus, the number of cases to be computed is significantly larger. Secondly, since the additional coordinate of time is included, it has meant a significantly more complicated formulation – either imposing a time integration on top of the spatial relaxation solution, or assuming harmonic motion and working with the resulting complex spatial differential equations.

It is possible to calculate the pressure distributions for unsteady motion using the complete nonviscous, compressible, time dependent differential equations. This has been done, for example, by Magnus and Yoshihara and by Beam and Warming (references 2 and 3). The results are obtained using a finite difference representation of time as well as space derivatives. However, the cost of doing these analyses make this procedure impractical for flutter analyses. This is also a nonlinear analysis which increases the number of cases to be considered, since superposition of solutions is not possible.

A reasonable simplification is achieved by assuming transonic small perturbation from a uniform parallel flow. The resulting time dependent equations have recently been used by Ballhaus and Goorjian (ref. 4) to generate a program called LTRAN2 for analyzing the two-dimensional, low-frequency problem. LTRAN2, which uses an implicit finite difference algorithm to integrate the nonlinear differential equation, is very efficient. This program has been extended by Rizzetta, Yoshihara and Borland to an EXTRAN2 version which includes high frequency terms in the differential equations and boundary conditions (ref. 5), viscous interactions (ref. 6 and 7), and three dimensions (ref. 5).

An alternative to this approach is achieved by separating the velocity potential into steady and harmonically varying unsteady parts. The result is the usual nonlinear differential equation for the steady velocity potential, and a linear equation for the unsteady velocity potential, with spatially varying coefficients which are functions of the steady velocity potential. This is the procedure to which this work is directed. The basic derivation is provided by Ehlers in reference 8, with the results of additional development and exploration described in references 9 through 13. The use of the steady state potential in the unsteady differential equations introduces the steady state flow properties into the propagation of the disturbances from the oscillations of the wing including the shocks. It has been sometimes considered that the solution of the complex differential equation for harmonic motion did not include the effect of shock motion on the unsteady forces. It will be shown that the frequency domain solution does indeed implicitly take into account the lift forces and moments produced by the moving shock wave.

In the following, calculations of the pressure distributions for several Mach numbers and reduced frequencies will be presented and the results compared with the corresponding experimental measurements made on an NACA 64A010 airfoil at the NASA Ames Research Center by Davis and Malcolm (ref. 14). The frequency domain method will also be applied to a two-dimensional flutter analysis which will illustrate the transonic effects of the moving shock on the characteristics of flutter. These flutter results are directly comparable to the results of a linear analysis by Isogai (ref. 15) using air forces which are the first harmonic components from a time integration of the transonic small perturbation equation.

A two step method, which uses the linearized solution for a flat plate to reduce significantly the cost of computing unsteady air loads for a thick airfoil by the

frequency domain technique, will be described. An ADI method of solving the complex differential equation for the potential will be presented which does not have the frequency limitation of the conventional relaxation method. This method may reduce the amount of computer resources for the three-dimensional problem, making three-dimensional transonic analysis practical.

The authors would like to acknowledge the valuable assistance of Dr. Donald Rizzetta for calculating all the EXTRAN2 results.

### 3.0 ABBREVIATIONS AND SYMBOLS

$a$	Streamwise dimension of mesh region; also amplitude of pitching or plunging modes, also elastic axis position (see fig. 42)
$a_n$	Fourier coefficients for $\sin(n\theta_1)$
$A$	Generalized force matrix
$b$	Root semichord of wing or semichord of airfoil; also vertical dimension of mesh region
$b_n$	Fourier coefficients for $\cos(n\theta_1)$
$C_p$	Pressure coefficient, $(p - p_0)/(1/2 \rho_0 U_0^2)$ where $p$ is the local pressure, $p_0$ the freestream static pressure, and $\rho_0$ the freestream air density
$C_L$	Lift coefficient based on chord
$C_{L\alpha}$	Lift coefficient based on chord for pitching motion
$C_{Lh}$	Lift coefficient based on chord for plunging motion
$C_M$	Moment coefficient based on chord
$C_{M\alpha}$	Moment coefficient based on chord for pitching motion
$C_{Mh}$	Moment coefficient based on chord for plunging motion
$f(x,y,t)$	Instantaneous wing shape defined by $z_0 = \delta f(x,y,t)$ ; also shock location
$f$	Frequency in Hertz
$f_0$	Undisturbed wing or airfoil shape
$f_1$	Unsteady contribution to wing or airfoil shape
$g$	Structural damping
$h$	$= \bar{h} e^{i\omega t}$ , airfoil plunging motion, positive down
$i, j$ $I, J$	$x, y$ subscripts and indices for points in the mesh
$i$	$\sqrt{-1}$

$I_\alpha$	Pitching moment of inertia
$k$	Reduced frequency based on semichord, $2\pi fb/U$ . Same as $\omega$ .
$K$	Transonic parameter, $(1-M^2)/(M^2\epsilon)$ ; also generalized stiffness matrix in section 7
$le$	Leading edge
$L$	Total lift; positive upward
$M$	Freestream Mach number; also generalized mass matrix
$M_y$	Total moment about elastic axis
$\bar{n}$	$(n_x, n_y, n_t)$ , unit normal vector to shock
$q$	$\omega^2/\epsilon - i\omega(\gamma - 1)\varphi_{0xx}$
$r_\alpha$	Dimensionless radius of gyration about center of gravity
$S_\alpha$	Static unbalance about elastic axis, positive aft of elastic axis (see fig. 42)
$t$	Time in units of $b/U$
$te$	Trailing edge
$u$	$K - (\gamma + 1)\varphi_{0x}$
$U, V$	Freestream velocity
$x_0, y_0$	Physical coordinates, made dimensionless with the root semichord
$x, y$	Scaled coordinates $(x_0, \mu y_0)$ for the two-dimensional problem
$X_0$	Steady chordwise shock location
$X_1$	Complex amplitude of shock oscillation
$X_m$	Magnitude of $X_1$
$X_\alpha$	Static unbalance about elastic axis, positive for center of gravity aft of elastic axis
$\alpha$	Angle of attack: also $=\bar{a}e^{i\omega t}$ , pitching motion about elastic axis

$\alpha_m$	Mean angle of attack
$\beta_1$	$= [u]$ in section 5 and Appendix A; $e^{-i\omega\Delta t}$ in section 8.2 and Appendix D
$\beta_2$	$= \langle u_x \rangle$
$\gamma$	Ratio of specific heats for air
$\Delta C_p$	Jump in pressure coefficient across airfoil or wake
$\Delta\varphi_1$	Jump in $\varphi_1$ at plane of wing or vortex wake
$\Delta\varphi_{1te}$	Jump in $\varphi_1$ at wing trailing edge
$\delta$	Thickness ratio, also finite difference operator
$\epsilon$	$(\delta/M)^{2/3}$
$\lambda_1$	$\omega M/(1 - M^2)$
$\mu$	Scale factor on $y_0$ , $\mu = \delta^{1/3} M^{2/3}$ ; also airfoil to air mass ratio, $m/(\pi\rho b^2)$ , where $m$ is the sectional mass per unit span and $\rho$ is the freestream density
$\nu$	Phase of shock amplitude $X_1$
$\theta_1$	$= \omega t + \nu$
$\rho$	Free stream density
$\varphi$	Complete, scaled perturbation velocity potential; also used for the unsteady potential in finite difference equations with subscripts
$\varphi_0$	Steady scaled perturbation velocity potential
$\varphi_1$	Unsteady scaled perturbation velocity potential
$\varphi_2$	$= \varphi_1 - \psi_1$
$\psi_1$	Flat plate complex potential; also linear time dependent potential
$\psi$	Time dependent potential
$\omega$	Reduced frequency in radians; same as $k$



$\omega_\alpha$	Pitch mode resonant frequency, radians per second
$\omega_h$	Plunge mode resonant frequency, radians per second

#### Notation

[ ]	Denotes jump in quantity across shock
< >	Denotes mean value of quantity at shock
$\Delta$	Denotes jump in quantity across airfoil; also increment of lift and moment coefficient from shock motion in section 5.5

#### Matrix Notation

[ ]	Rectangular matrix
{ }	Column matrix
[1]	Unit matrix

#### Subscripts

F	Flutter condition
---	-------------------

## 4.0 FORMULATION AND SOLUTION

Since the mathematical derivation of the method for the solution of the unsteady velocity potential for the flow about a harmonically oscillating wing is presented in reference 8, the discussion here will be limited to a brief outline of the procedure for two dimensions. The complete nonlinear differential equation was simplified by assuming the flow to be a small perturbation from a uniform stream near the speed of sound. The resulting equation for unsteady flow is

$$\left[ K - (\gamma - 1)\varphi_t - (\gamma + 1)\varphi_x \right] \varphi_{xx} + \varphi_{yy} - (2\varphi_{xt} + \varphi_{tt}) / \epsilon = 0 \quad (4.1)$$

where  $K = (1 - M^2) / (M^2 \epsilon)$ ,  $M$  is the freestream Mach number of velocity  $U_0$  in the  $x$ -direction,  $x$  and  $y$  are made dimensionless to the semichord  $b$  of the airfoil and the time  $t$  to the ratio  $b/U_0$ . With the airfoil shape as a function of time defined by the relation

$$y_0 = \delta f(x, t)$$

the linearized boundary condition becomes

$$\varphi_y = f_x(x, t) + f_t(x, t) \quad (4.2)$$

The quantity  $\delta$  is associated with properties of the airfoil (such as maximum thickness ratio, camber, or maximum angle of attack) and is assumed to be small. The coordinate  $y$  is scaled to the dimensionless physical coordinate  $y_0$  according to

$$y = \delta^{1/3} M^{2/3} y_0$$

and  $\epsilon$  is given in terms of  $\delta$  by

$$\epsilon = (\delta/M)^{2/3}$$

The pressure coefficient is found from the relation

$$C_p = -2\epsilon(\varphi_x + \varphi_t)$$

The preceding differential equation is simplified by assuming harmonic motion and by assuming the velocity potential to be separable into a steady-state potential and a potential representing the unsteady effects. We write for a perturbation velocity potential

$$\varphi = \varphi_0(x, y) + \varphi_1(x, y)e^{i\omega t} \quad (4.3)$$

and for the body shape

$$y_0 = \delta f(x, t) = \delta \left[ f_0(x) + f_1(x)e^{i\omega t} \right]$$

Since the steady-state terms must satisfy the boundary conditions and the differential equation in the absence of oscillations, we obtain

$$\left[ K - (\gamma + 1)\varphi_{0x} \right] \varphi_{0xx} + \varphi_{0yy} = 0 \quad (4.4)$$

with

$$\varphi_{0,y} = f_0(x), \quad y = 0, \quad -1 \leq x \leq 1 \quad (4.5)$$

On the assumption that the oscillations are small and products of  $\varphi_1$  may be neglected, equations (4.1) and (4.2) with the aid of equations (4.4) and (4.5) yield

$$\left\{ \left[ K - (\gamma + 1)\varphi_{0,x} \right] \varphi_{1,x} \right\}_x + \varphi_{1,yy} - (2i\omega/\epsilon)\varphi_{1,x} + q\varphi_1 = 0 \quad (4.6)$$

where

$$q = \omega^2/\epsilon - i\omega(\gamma - 1)\varphi_{0,xx}$$

subject to the wing boundary conditions

$$\varphi_{1,y} = f_1(x) + i\omega f_1(x), \quad y = 0, \quad -1 \leq x \leq 1 \quad (4.7)$$

A computer program for solving the steady state transonic flow about lifting airfoils based on equations (4.4) and (4.5) was developed by Cole, Murman, and Krupp (refs. 16 and 17). For some calculations of unsteady flow, the latest version called TSFOIL (ref. 18) was used to compute the coefficients for the difference equations. Steady-state solutions from the time dependent method of Rizzetta and Chin (ref. 19), called EXTRAN2, to solve equation (4.1), were also used. An additional improvement on locating the shock is also available both in TSFOIL and EXTRAN2. For airfoils at high Mach numbers and angles of attack, TSFOIL and EXTRAN2 predict shock positions considerably aft of experimental measurements. To overcome this difficulty, Jou and Murman (ref. 20) developed a phenomenological model for the displacement thickness effects of shock wave boundary layer interactions. A wedge (or ramp) is introduced behind the shock to simulate the thickening of the boundary layer. Unsteady flow examples are presented with the steady state potential computed both with and without the viscous ramp.

The similarity of the unsteady differential equation to the steady-state equation suggests that the method of Cole, Murman, and Krupp should be an effective way to solve equation (4.6) for the unsteady potential  $\varphi_1$ . Note that equation (4.6) is of mixed type, being elliptic or hyperbolic whenever equation (4.4) is elliptic or hyperbolic. Central differencing was used at all points for the y derivative and all subsonic or elliptic points for the x derivatives. Backward (or upstream) differences were used for the x derivatives at all hyperbolic points.

The boundary condition that the pressure be continuous across the wake from the trailing edge was found in terms of the jump in potential  $\Delta\varphi_1$  to be

$$\Delta\varphi_1 = \Delta\varphi_{1,te} e^{-i\omega(x-x_{te})} \quad (4.8)$$

where  $\Delta\varphi_{1,te}$  is the jump in the potential at  $x = x_{te}$  just downstream of the trailing edge and is determined to satisfy the Kutta condition that the jump in pressure vanish at the

trailing edge. The quantity  $\Delta\phi_1$  is also used in the difference formulation for the derivative  $\phi_{1yy}$  to satisfy continuity of normal flow across the trailing edge wake.

For the set of difference equations to be determinate, the boundary conditions on the outer edges of the mesh must be specified. In the original unsteady formulation, these boundary conditions were derived from asymptotic integral relations in a manner parallel to that used by Klunker (ref. 21) for steady flow. A later formulation (ref. 10) applies an outgoing plane wave boundary condition to the outer edges of the mesh. This boundary condition is numerically simpler to apply and is equivalent to the 1st order nonreflecting boundary conditions derived by Engquist and Majda (ref. 22).

The preferred numerical approach to solving the resulting large-order set of difference equations is a relaxation procedure, which permits the calculation to be made as a sequence of relatively small problems. However, as discussed in preceding NASA reports by the authors (refs. 9 and 10), a significant problem of convergence with the relaxation procedure was encountered that severely limits the range of Mach number and reduced frequency for which solutions may be obtained. Accordingly, an out-of-core solver (ref. 23) was developed to solve the complete set of difference equations simultaneously, which for two-dimensional flow is fairly efficient. Recently, an ADI method based on the time dependent method to obtain frequency domain solutions was derived and preliminary results indicate no frequency limitation on convergence. This method is derived in Appendix D and the results discussed in section 8.2.

## 5.0 INVESTIGATION OF SHOCK WAVE MOTION ON AN OSCILLATING AIRFOIL

### 5.1 DESCRIPTION OF BASIC SHOCK MOTIONS AND EFFECTS ON FLUTTER

Tijdeman (ref. 24) has experimentally observed and measured the motion of shocks on an airfoil with an oscillating flap. He has found three types of shock motions. Type A is sinusoidal shock-wave motion. This is characterized by a shock whose position varies sinusoidally along the chord as the flap is oscillated sinusoidally. Even for small frequencies, there is a significant phase shift between shock positions and flap motion. A change in shock strength is also observed with the shock strength attaining its maximum at its farthest upstream position. Type B is interrupted shock wave motion and is characterized by the disappearance of the shock wave during its backward motion. Type C is the upstream propagated shock wave. When the flow is just supercritical, a shock wave forms on the upper surface as the flap just passes the maximum downward deflection. The shock wave moves upstream at first gaining in strength, continues to move upstream while decreasing in strength, then leaves the airfoil at the leading edge. This phenomenon is repeated periodically.

Ashley (ref. 1) and McGrew et al (ref. 25) indicate that the predominant factor in the failure of linearized theory to predict accurately the forces in transonic flow is the presence of shock waves on the upper surface and sometimes the lower surface of the wing. The motion of these shocks along the chord can introduce large unsteady moments. Ashley (ref. 1) in a simple approximate analysis has shown that this shock motion usually destabilizes single degree pitching motion and can have a profound effect on flexure-torsion motion.

It has been frequently stated that the existing frequency domain methods (i.e. the methods of Ehlers, in reference 8, and Traci et al., in references 26 and 27) assume a fixed shock location, and hence do not yield forces which include the effect of shock motions. It was thought that special treatment was required to incorporate these efforts. However, even the earliest computations in reference 8, show the complex pressure pulse at the steady state shock location which was observed by Tijdeman in his experiments (ref. 24). We can find out whether a frequency domain solution represents a moving shock by combining the complex pressure  $C_{p1}$  from the frequency domain solution with the steady state pressure coefficient  $C_{p0}$  in the form

$$C_p = C_{p0} + \text{real}(C_{p1}e^{i\omega t})$$

By varying the time  $t$  we obtain the pressure coefficients shown in figures 1 and 2 (these results do not contain the shock point operators discussed in section 5) for the upper and lower airfoil surfaces. The amplitude of the pitching NACA 64A010 airfoil is +2 degrees about a mean angle of attack of -0.21 degrees. The Mach number is 0.8 with a reduced frequency of 0.247. From these graphs we see that the shock position does indeed move although the amplitude of motion may be much smaller than the

amplitude experimentally observed. Since the frequency domain method is linear, only type A shock motion is possible from the theory. In sections 5.2, 5.3, and 5.4, we shall show that the effect of shock motion is indeed incorporated in the frequency domain method used here. It should also be noted the shock motion effects are included in the procedure used by Traci et al., in references 26 and 27.

## 5.2 EFFECT OF GRID REFINEMENT ABOUT THE STEADY STATE SHOCK ON THE SOLUTION

For strong shocks, the complex pressure pulse did not appear to be accurately described by the initial grid which was relatively coarse in the neighborhood of the shock. Accordingly, the grid was refined in the vicinity of the the shock in an attempt to improve the definition of the pressure pulse. Figures 3 and 4 show the jump in pressure coefficient across the airfoil for three successively refined grids for  $M = 0.8$ , a mean angle of attack of one degree, and a reduced frequency of 0.3. This example was chosen for study because of the presence of a strong shock which occurs on only one side of the airfoil. Since grid refinement does not define the pulse more accurately it appears that the pressure is singular at the steady state shock location. Since this singularity is of lower order for the perturbation potential than for the pressure coefficient which involves the first derivative with respect to  $x$ , we examined the jump in  $\varphi_1$  across the airfoil for the same three potential distributions. These results are plotted in figures 5 and 6. It is seen that, as the grid is refined about the steady state shock location, a jump in the unsteady potential appears across the shock.

In Appendix A, the jump conditions across the shock are derived. The analysis follows the work of Murman, Hafez, and Ritzk (ref. 28), who expanded the shock conditions about the steady state location. The condition that the velocity potential be continuous across the moving shock is applied at the fixed location of the steady state shock, leading to the continuity of  $\varphi_0$ , the steady state potential. Also, for the unsteady potential, the complex amplitude of shock motion is defined by the jump in the unsteady potential and the pressure jump across the steady shock. This is given by the relation

$$[\varphi_1] + X_1 [\varphi_{0_x}] = 0 \quad (5.2.1)$$

where  $X_1$  is the complex amplitude of the shock motion and denotes the jump in the quantity across the steady shock. Hence it appears that the solution with the refined grid does indeed have the essential information for calculating the effects of the moving shock, since once we find the jump in  $\varphi_1$  the amplitude of shock motion is found from the foregoing formula.

The effect of refining the grid on the perturbation potential was further investigated by examining three dimensional representations of the potential distributions, portions of which are shown in figures 7 to 9. The developing of the jump in  $\varphi_1$  at the steady state shock location is apparent. Figure 9 exhibits a sharp spike away from the airfoil at the shock. On a physical basis, the spike would be

expected to occur at the airfoil surface. This is undoubtedly due to some of the points along the column of the shock being treated inconsistently as elliptic, while others are hyperbolic because of errors introduced from interpolation of the steady state potential in refining the grid about the shock. As we shall see, this problem is remedied by the introduction of a shock point operator which is described in the next section.

### 5.3 EFFECT OF SHOCK POINT OPERATOR ON THE SOLUTION

To capture steady state shocks accurately, Krupp and Murman (ref. 17) introduced a shock point operator to the difference formulation of the transonic small perturbation differential equation. A similar shock point operator was derived in reference 10 for unsteady harmonic transonic flow and applied to the three dimensional problem. The differential equation is written in conservation form and the divergence theorem is applied to the derivative terms for an infinitesimal rectangle enclosing points on opposite sides of the shock. The derivation is repeated in Appendix B with some improvements. Three forms of the difference equation for  $\varphi_{1x}$  are presented. The original form yields a weighted average of upwind and central differences for  $\varphi_{1x}$  at the point  $i,j$ . The second uses a weighted average of central differences for  $\varphi_{1x}$  at the points  $i$  and  $i-1$ . The third is essentially  $\varphi_{1x}$  defined by the difference between values of  $\varphi_1$  at the right and left sides of the control volume for the shock point operator (see figure B-1 and the discussion in appendix B). Forms 2 and 3 are identical for equally spaced points.

When the shock point operator is introduced, the solution exhibits a jump in  $\varphi_1$  at the shock for the coarse grid as well as for the fine grid. Figures 10 and 11 are three-dimensional graphs of the real and imaginary parts of  $\varphi_1$  on the  $xy$  grid plane for  $M = 0.8$ , a mean angle of attack of  $1^\circ$ , and the NASA 64A010 airfoil pitching about the quarter-chord point at a reduced frequency of  $k = 0.3$ . The jump in unsteady potential,  $\varphi_1$ , across the airfoil is given in figure 12 for the same solution using the first form of the shock point operator. The jump in  $\varphi_1$  across the shock is most easily seen in the imaginary component of  $\varphi_1$  in figures 11 and 12. Williams (ref. 29) has shown that the perturbation potential at the shock location has a singularity on the downstream side of the shock of the form  $x \log x$  at  $x = 0$ . The finite difference solution in figures 11 and 12 would seem to indicate such a singularity. When the third form of the shock point operator is used, however, the jump in  $\varphi_1$  is more pronounced in the real part but there appears to be no evidence of the  $x \log x$  singularity in the real part although the imaginary part is essentially the same (see figs. 13 and 14).

### 5.4 EFFECT OF SHOCK POINT BOUNDARY CONDITIONS ON THE SOLUTION

We have seen that for the shock point operator in the presence of strong shocks that a jump in  $\varphi_1$  occurs at the steady state shock location. It is also possible to replace the shock point operator with the shock boundary conditions in equation (A-23). These conditions were coded and applied to the rows near the airfoil where the shock is strongest. The shock point operator was applied to the remaining rows. For the

boundary conditions to work successfully it was found necessary to use a fitted shock instead of the captured shock where the shock effects are smeared over 3 or 4 grid spaces. Since we had no steady state program with a shock fitting routine (see, e.g. Seebass et al, ref. 30), we manually constructed fitted shocks for the first 5 rows away from the airfoil. Figure 15 shows some examples by the plot of  $-u$  where  $u = K - (\gamma + 1) \varphi_{0,x}$  along the rows. To obtain a reference result for comparison, we also used the same  $u$  distribution containing the fitted shock in a conventional solution using the shock point operator. The extrapolated jump in  $\varphi_1$  across the airfoil is compared in figure 16 for the two solutions. The Mach number is 0.8 and the NACA 64A010 airfoil was pitched about the quarter chord point at a mean angle of attack of  $1^\circ$  with a reduced frequency of 0.3. The amplitude of shock motion for the two solutions is about the same but the phase differs considerably. The value of  $X_1$  computed by equation (5.2.1) is  $0.769-3.493i$  for the shock boundary conditions and  $1.735-2.090i$  for the shock point operator. For a pitch amplitude of  $1/2^\circ$ , using the shock boundary conditions gives a somewhat larger shock motion of 3.1% of the chord compared with 2.4% of the chord for the shock point operator. The shock point operator with the captured shock gives  $X_1 = 1.62-2.31i$  with a motion of 2.4% of the chord. For the shock point operator, a fitted shock has little effect on the result.

Since the shock point operator and shock boundary conditions give somewhat different results, it seems appropriate to see what the difference is between the jump conditions at the shock resulting from the two relations. From equation (A-21) the boundary condition that was applied is

$$\langle 2i\omega/\epsilon + u_x \rangle [\varphi_1] - [u] \langle \varphi_{1,x} \rangle = 0 \quad (5.4.1)$$

where  $[ ]$  denotes the jump in the quantity across the steady state shock, while  $\langle \rangle$  denotes the average value at the shock. Applying the divergence theorem about a section of the shock to the differential equation for  $\varphi_1$  yields

$$[u\varphi_{1,x} - 2i\omega/\epsilon] n_x + [\varphi_y] n_y = 0$$

Since  $n_y = 0$  and  $[u] = 0$  for a normal shock, using the identity

$$[u\varphi_{1,x}] = \langle u \rangle [\varphi_{1,x}] + \langle \varphi_{1,x} \rangle [u]$$

yields

$$[u] \langle \varphi_{1,x} \rangle - \langle 2i\omega/\epsilon \rangle [\varphi_1] = 0$$

for the jump across the shock. The term  $u_x$  is seen to be lacking. This is the contribution from expanding  $u$  on the moving shock about the steady state shock position. It appears that at the shock point we can satisfy the difference equation at the shock but the shock condition in equation (5.4.1) is not satisfied. If we satisfy the correct shock relations of equation (5.4.1) then we cannot satisfy the difference equation.



The shock point operator is easier to apply since it does not require special fitting of the shock and is the form used for all subsequent calculations discussed in this document.

When the shock is weak, there is no distinct jump in  $\varphi_1$  at the steady state shock. Figure 17 shows the real part of the jump in  $\varphi_1$  across the airfoil for the NACA 64A010 airfoil at  $M = 0.8$  and zero angle of attack, using the shock point operator and a uniform grid about the shock. Even refinement of the grid as in Figure 18 does not produce a definite jump in  $\varphi_1$  at the shock. Note that in the vicinity of the shock the slope changes rapidly. This change in the slope produces the large pressure pulse shown in the examples in section 6.0.

### 5.5 INCORPORATING THE EFFECT OF THE MOVING SHOCK WAVE IN THE CALCULATION OF LIFT AND MOMENT

Once the solution  $\varphi_1$  is found then the amplitude of shock motion is found from equation (A-15); that is

$$X_1 = (\gamma + 1)[\varphi_1]/\beta_1$$

where  $\beta_1 = [u] = [K - (\gamma + 1)\varphi_{0x}]$ . Since the jump in  $\varphi_1$  is complex then we write

$$X_1 = X_m e^{i\nu}$$

where  $X_m$  is the magnitude of  $X_1$  and  $\nu$  is the phase angle. The shock motion about the steady state position is given by

$$aX_1 e^{i\omega t} = aX_m e^{i(\omega t + \nu)} = aX_m e^{i(\theta + \nu)}$$

where  $a$  is the amplitude of oscillation of the airfoil motion, here assumed small. Let  $\theta_1 = \theta + \nu$  then the shock motion is described by

$$aX_m e^{i\theta_1}$$

Figure 19 illustrates the pressure pulse produced on the airfoil by the moving shock wave from Tijdeman (ref. 24). The unsteady pressure pulse is seen to be

$$-2\epsilon [\varphi_{0x}] H(x - x_0 - aX_m \sin \theta_1)$$

where  $[\varphi_{0x}] = \varphi_{0x}^+ - \varphi_{0x}^-$  and  $H(t)$  is the unit step function which equals 0 for  $t < 0$  and equals unity for  $t > 0$ . Here + and - denote downstream and upstream values. We now compute the Fourier coefficients for the pressure pulse. Expressing the Fourier series in the form

$$\sum_{n=1}^{\infty} a_n \sin n\theta_1 + \sum_{n=0}^{\infty} b_n \cos n\theta_1$$

we find the values of  $a_n$  and  $b_n$  are given by

$$a_n = \frac{1}{\pi} \int_{-\pi}^{\pi} (-2\epsilon [\varphi_{0x}]) H(x - x_0 - aX_m \sin \theta_1) \sin n\theta_1 d\theta_1$$

$$b_n = \frac{1}{\pi} \int_{-\pi}^{\pi} (-2\epsilon [\varphi_{0x}]) H(x - x_0 - aX_m \sin \theta_1) \cos n\theta_1 d\theta_1$$

We assume  $x > x_0$  but  $x - x_0 < aX_m$ . Then

$$a_n = -\frac{2\epsilon [\varphi_{0x}]}{\pi} \left\{ \int_{-\pi}^{\sin^{-1}\left(\frac{x-x_0}{aX_m}\right)} \sin n\theta_1 d\theta_1 + \int_{\pi - \sin^{-1}\left(\frac{x-x_0}{aX_m}\right)}^{\pi} \sin n\theta_1 d\theta_1 \right\}$$

$$a_n = \frac{2\epsilon [\varphi_{0x}]}{\pi n} \left\{ \cos n \left( \sin^{-1} \left[ \frac{x - x_0}{aX_m} \right] \right) [1 - (-1)^n] \right\}$$

Similarly,

$$b_n = -\frac{2\epsilon [\varphi_{0x}]}{\pi} \left\{ \int_{-\pi}^{\sin^{-1}\left(\frac{x-x_0}{aX_m}\right)} \cos n\theta_1 d\theta_1 + \int_{\pi - \sin^{-1}\left(\frac{x-x_0}{aX_m}\right)}^{\pi} \cos n\theta_1 d\theta_1 \right\}$$

$$b_n = -\frac{2\epsilon [\varphi_{0x}]}{\pi n} \left\{ \sin n \left( \sin^{-1} \left[ \frac{x - x_0}{aX_m} \right] \right) [1 + (-1)^n] \right\}$$

The terms of the Fourier expansion of the pressure pulse for the first harmonic become

$$\begin{aligned} a_1 \sin \theta_1 &= \frac{4\epsilon [\varphi_{0x}]}{\pi} \sqrt{1 - \left( \frac{x - x_0}{aX_m} \right)^2} \sin(\nu + \omega t) \\ &= \text{Imag} \left\{ \frac{4\epsilon [\varphi_{0x}]}{\pi} \sqrt{1 - \left( \frac{x - x_0}{aX_m} \right)^2} e^{i\nu} e^{i\omega t} \right\} \end{aligned}$$

Choosing the pressure pulse as defined by

$$\text{Imag}[(c + id)e^{i\omega t}]$$

we see that the complex pressure pulse is given by

$$c + id = \frac{4\epsilon [\varphi_{0x}] X_1}{\pi X_m} \sqrt{1 - \left(\frac{x - x_0}{aX_m}\right)^2}$$

The contribution to the lift and moment from this pressure pulse can be integrated in closed form. Thus for the lift we have

$$\begin{aligned} 2\Delta C_L &= \frac{4\epsilon [\varphi_{0x}] X_1}{\pi X_m} \int_{x_0 - aX_m}^{x_0 + aX_m} \sqrt{1 - \left(\frac{x - x_0}{aX_m}\right)^2} dx \\ &= \frac{4\epsilon [\varphi_{0x}] X_1 a}{\pi} \int_{-1}^1 \sqrt{1 - t^2} dt \\ &= 2\epsilon [\varphi_{0x}] aX_1 = -2\epsilon a [\varphi_1] \end{aligned}$$

where we have used equation (A-15). The 2 factor is needed to make the lift coefficient based on chord rather than semichord. Note that the contribution to the lift is equivalent to a pressure distribution

$$-2\epsilon [\varphi_1] a\delta(x - x_0)$$

where  $\delta(t)$  is the Dirac delta function.

For the moment we have

$$4\Delta C_m = \frac{4\epsilon [\varphi_{0x}] X_1}{\pi X_m} \int_{x_0 - aX_m}^{x_0 + aX_m} (x - x_a) \sqrt{1 - \left(\frac{x - x_0}{aX_m}\right)^2} dx$$

Let  $t = (x - x_0)/aX_m$ , then

$$\begin{aligned} 4\Delta C_m &= \frac{4\epsilon [\varphi_{0x}] aX_1}{\pi} \int_{-1}^1 [x_0 - x_a + aX_m t] \sqrt{1 - t^2} dt \\ 4\Delta C_m &= (x_0 - x_a) \Delta C_L \end{aligned}$$

To find an estimate of higher harmonics on the lift and moment, we consider the second harmonic terms, these are

$$a = 0$$

$$\begin{aligned} b_2 \cos 2\theta_1 &= -\frac{2\epsilon [\varphi_{0x}]}{\pi} \sin 2 \left( \sin^{-1} \left[ \frac{x - x_0}{aX_m} \right] \right) \cos 2(\nu + \omega t) \\ &= \text{Real} \left\{ -\frac{2\epsilon [\varphi_{0x}] X_1^2}{\pi X_m^2} \left( \frac{x - x_0}{aX_m} \right) \sqrt{1 - \left( \frac{x - x_0}{aX_m} \right)^2} e^{2i\omega t} \right\} \end{aligned}$$

The complex lift from this term is

$$\begin{aligned} 2 \Delta C_L &= -\frac{2\epsilon [\varphi_{0x}] X_1^2}{\pi X_m^2} \int_{x_0 - aX_m}^{x_0 + aX_m} \left( \frac{x - x_0}{aX_m} \right) \sqrt{1 - \left( \frac{x - x_0}{aX_m} \right)^2} dx \\ &= -\frac{2\epsilon [\varphi_{0x}] a X_1^2}{X_m} \int_{-1}^1 t \sqrt{1 - t^2} dt = 0 \end{aligned}$$

The moment is seen to be

$$\begin{aligned} 4 \Delta C_m &= -\frac{2\epsilon [\varphi_{0x}] a X_1^2}{\pi X_m} \int_{-1}^1 [x_0 - x_a + aX_m t] t \sqrt{1 - t^2} dt \\ &= -\epsilon [\varphi_{0x}] X_1^2 a^2 / 4 = \epsilon [\varphi_1] a^2 X_1 / 4 \end{aligned}$$

The lift from the second harmonic is seen to be zero and the moment is second order in the amplitude of the airfoil motion compared to first order for the first harmonic. Thus the higher harmonics in the shock motion can be neglected.

We have seen that in the solution a jump in  $\varphi_1$  occurs across fairly strong shocks. To compute the total lift coefficient we must integrate

$$2C_L = -2\epsilon a \int_{-1}^1 \left\{ \Delta \varphi_{1x} + i\omega \Delta \varphi_1 + [\Delta \varphi_1] \delta(x - x_0) \right\} dx$$

where we have added the contribution from the moving shock wave in the form of a delta function distribution. The quantity  $\Delta \varphi_1$  can be integrated numerically in spite of the jump in  $\Delta \varphi_1$ .

Consider the combination

$$\int_{-1}^1 \left\{ \Delta\varphi_{1x} + [\Delta\varphi_1] \delta(x - x_0) \right\} dx$$

For  $x$  greater than  $x_0$ , we account for the discontinuity in  $\varphi_1$  in integrating  $\varphi_{1x}$ . Thus

$$\begin{aligned} \int_{-1}^1 \Delta\varphi_{1x} dx &= -\Delta\varphi_1(-1) + \Delta\varphi_1^- - \Delta\varphi_1^+ + \Delta\varphi_1(1) + [\Delta\varphi_1] \\ &= \Delta\varphi_{1te} \end{aligned}$$

Thus the integration of  $\Delta\varphi_{1x}$  plus the contribution from the shock motion gives the value of  $\Delta\varphi_1$  at the trailing edge found from the integration. The lift is then given by

$$2C_L = -2\epsilon a \left[ \Delta\varphi_{1te} + \int_{-1}^1 i\omega \Delta\varphi_1 dx \right]$$

This is the same form obtained for continuous  $\Delta\varphi_1$ . A similar analysis for the moment coefficient yields

$$4C_m = -2\epsilon a \left[ \Delta\varphi_{1te} + \int_{-1}^1 (i\omega x - 1) \Delta\varphi_1 dx \right] - x_a C_L$$

These two formulas were also obtained by Williams (ref. 29).

When the trapezoidal rule of integration is applied, no special consideration of the shock is necessary. When a Simpson's rule type of integration is employed, the immediate step in  $\varphi_1$  at the shock is treated by the trapezoidal rule with the remainder of the wing integrated by the Simpson's rule formula. For the grid distribution currently employed, integration by the trapezoidal rule agrees to four places with the Simpson's rule result. This is the method used in all the calculations presented.

## 6.0 CORRELATION OF THEORETICAL CALCULATIONS WITH THE EXPERIMENTS OF NASA AMES RESEARCH CENTER

Calculations by the frequency domain method were made at Mach numbers and reduced frequencies which can be compared with the experimental measurements of Davis and Malcolm (ref. 14) on a NACA 64A010 airfoil at the NASA Ames Research Center. Only the zero mean angle of attack cases were studied since the  $4^\circ$  results appear to contain an excessive amount of separation which the theory is not able to take into account.

### 6.1 CORRELATION OF STEADY STATE PRESSURE DISTRIBUTIONS

It is essential that the theoretical steady state pressure distributions also agree with the measurements, since the steady state potential is used in the coefficients of the equations for the calculation of the unsteady pressures. The steady state potential distributions were computed by the program EXTRAN2 described by Rizzetta and Chin (ref. 19), although some calculations were made using TSFOIL (ref. 18). For identical boundary conditions the two programs yield almost identical results. For a few cases unsteady pressures were also computed by EXTRAN2. The first harmonic of the Fourier expansion was calculated from the time dependent solution to compare with the complex pressures of the frequency domain method and with the corresponding NASA experimental data.

Figure 20 compares the EXTRAN2 steady state pressure distributions on the airfoil with the NASA-Ames measurements at a Mach number of 0.75 and a zero angle of attack. Agreement is seen to be quite good. In this example the flow is completely subsonic. The NACA 64A010 airfoil used by NASA is not quite symmetric. For the calculations included here, the measured airfoil coordinates listed in Davis and Malcolm (ref. 14) were used for the boundary conditions, with the leading edge slopes modified by Riegel's rule in which the slopes  $s$  are replaced by  $s\sqrt{1+s^2}$  and with some further changes to reduce the excessive pressure rise at the leading edge which occurred when all the slopes were determined by the coordinates. Riegel's rule eliminates the singularity in the slope at the leading edge of a blunt airfoil.

Figure 21 compares the steady state pressures computed by three methods for a Mach number of 0.8 and zero angle of attack. The dotted curve is the EXTRAN2 results with the Riegel's rule modification. The other two curves are obtained by using TSFOIL with the NASA Ames coordinates and two different scalings but without the application of Riegel's rule. The classical Spreiter scaling is that presented in section 4 and follows naturally from the procedure of mathematically simplifying the differential equation. The Krupp scaling is empirical and leads to the following definitions of  $K$  and  $\epsilon$ :

$$K = (1 - M^2) / (M\delta^{2/3}), \quad \epsilon = \delta^{2/3} / M^{3/4}$$

Although all the unsteady calculations were made with the Spreiter scaling, the program is capable of using either parameterization.

The shock is farthest aft and is stronger for the empirical Krupp scaling than for the conventional Spreiter scaling which EXTRAN2 also uses. All subsequent unsteady calculations were made with Spreiter scaling. The application of Riegel's rule improves the pressure distribution in the leading edge region of the airfoil but the shock wave is weaker than the measured shock.

Figure 22 shows a graph of the upper and lower pressure distributions for  $M = 0.842$  and zero angle of attack. Here the agreement between experiment and theory is better, with the shock strength more accurately defined by the calculations than for the 0.8 Mach number case.

## 6.2 CORRELATION OF UNSTEADY PRESSURE DISTRIBUTIONS

Using the steady state potential distribution for  $M = 0.75$  represented by the pressure distribution in figure 20 to evaluate the coefficients of the unsteady difference equations, the complex unsteady pressure distribution was calculated for the NACA 64A010 airfoil oscillating in pitch about the quarter chord point at a reduced frequency of  $k = 0.20$ . Figure 23 shows plots of the real and imaginary parts of the jump in pressure coefficients across the airfoil for both theory and experiment. Also shown is the flat plate, solution for  $M = 0.75$  and  $k = 0.2$ . Since the flow is completely subsonic, the linearized and the frequency domain solutions are both smoothly varying without a large pressure pulse. Both the experimental results and the airfoil calculations show a greater pressure amplitude near the leading edge than the linearized or flat plate solution. Even for strictly a subsonic case, the influence of the steady flow potential in the coefficients of the differential equation has a significant effect on the pressure distribution.

Figures 24 through 31 show the jump in pressure coefficients across the airfoil oscillating in pitch about the quarter chord point for  $M = 0.8$ , using the steady state potential from EXTRAN2 represented by the dotted line pressure in figure 21. In figures 24 and 25, the first harmonic from an EXTRAN2 time dependent solution is also included with the frequency domain solution for  $k = 0.101$ . In the nonlinear EXTRAN2 solution, the shock pressure pulse is aft of that of the frequency domain solution and is closer to the experimental location. In the frequency domain solution, the shock wave pressure pulse is located at the steady state shock position. The mean shock location of the time dependent solution is generally downstream of the steady state shock position.

An examination of figures 24 through 31 indicates that the current linear theory locates the shock pressure pulse a distance between 5 and 10% of the chord upstream of the measured position. In figures 24 and 25 for  $k = 0.101$ , the amplitude of the shock pulse from the frequency domain solution is closer to the experiment than the EXTRAN2 calculations. For  $k = 0.202$ , figures 26 and 27, the magnitude of the pressure coefficients from the frequency domain solution compares favorably with experiment, particularly in the region between the leading edge and the shock. For  $k = 0.247$ , figures 28 and 29 compare the pressure jump from both the time dependent method and

frequency domain method with experiment. In the leading edge region in figure 28, EXTRAN2, which is dependent on amplitude and uses the 1° amplitude of the experiment, overpredicts the real component of the pressure, while the frequency domain method, which is independent of amplitude, is in better agreement with experiment. Aft of the shock, the two theories are fairly close but the real part has a sign opposite from the experiment, although the magnitude is small.

Figures 30 and 31 compare the two theoretical calculations with experiment for  $k = 0.303$ . Except for the sharp pulse, the two theories compare well for the real component of the pressure jump. The frequency domain solution gives a higher peak in better agreement with the measurements. The experimental results exhibit greater oscillation with position along the chord. The large peak in the real part just upstream of the shock pressure pulse at about one-third chord is not predicted by either theory. It may be entirely eliminated by removing a single point from the measured data and hence may possibly be attributed to scatter in the experimental data.

The frequency domain solutions for the NACA 64A010 airfoil oscillating in pitch about the quarter chord point at a Mach number of 0.842, using the steady state potential from figure 22, is given in figures 32 and 33 for a reduced frequency of 0.202. For this example, the jump in pressure in the region from the leading edge to the shock is fairly accurately predicted by theory. However, the theory yields a large pressure pulse at the shock which is not found in the experimental data. From the strong steady state shock indicated by the pressure distribution in figure 22, one should expect from past experience a fairly large pressure pulse in the unsteady solution.

Figures 34 to 39 present for  $M = 0.8$  the jump in unsteady pressure across a NACA 64A010 airfoil oscillating in plunge at an amplitude of 0.05 chord for reduced frequencies of  $k = 0.05, 0.101, \text{ and } 0.151$ . In these examples, the nonlinear time dependent solution of EXTRAN2 predicts the shock pulse position more accurately than the frequency domain solution. The program EXTRAN2 produces a larger jump in pressure in the region between the leading edge and the shock than either the frequency domain method or the experiment. This discrepancy is not understood. The frequency domain method is in closer agreement with experiment although the magnitude for the leading edge is still overpredicted.

For the NACA 64A010 airfoil oscillating in pitch at  $M = 0.8$  and zero mean angle of attack, the theoretical lift and moment coefficients are compared with the experimental data of Davis and Malcolm (ref. 14) in figure 40. The real component of the lift is in good agreement with experiment, but the imaginary component of the theory shows a trend opposite to the experiment in the frequency range 0.05 to 0.2. In both theory and experiment, the imaginary component of the lift goes to zero as the frequency goes to zero although the theory drops more sharply than the experiment. Figure 40 also includes data of Isogai (ref. 15) which generally follows the trends of the present theory.



Figure 41 compares the real and imaginary parts of the moment coefficient about the leading edge for the same airfoil oscillating in pitch at  $M = 0.8$  for several values of reduced frequency. The real component of the moment from the theory is greater than the experimental values but appears to have nearly the same trend. As in the lift case, the imaginary component goes to zero more rapidly than the experimental data. The results of Isogai (ref. 15) are generally in accord with the present theory.

## 7.0 FLUTTER ANALYSES OF A NACA 64A010 AIRFOIL

Typical section, two-degree-of-freedom flutter analyses of a NACA 64A010 airfoil are presented and discussed in this section. The flutter results were calculated using the harmonic aerodynamic procedures discussed in sections 4 and 5. Results from two of the three configurations studied are compared with results obtained by Isogai in reference 15, using time-integration procedures. Generally, the flutter characteristics determined from the two aerodynamic procedures compare favorably. Flutter analyses using the time-integration methods predict a deeper flutter bucket than the analyses using harmonic procedures. There are no experimental results available for correlation with the analytical results of this section.

The reader is referred to papers by Ashley (ref. 1), Isogai (ref. 15) and Yang et al (refs. 31 and 32) for comprehensive reviews of papers and reports concerned with flutter analyses of airfoils in transonic flow and only a few comments will be offered here to put the current investigations in perspective. First, there have been questions raised concerning the flutter results published by Traci et al (ref. 26) and whether or not these results include the effects of shock motion. Section 5 of this report discusses this point in detail, and it is now hoped that flutter results obtained with harmonic procedures will be recognized as true transonic flutter analyses, which include the effects of shock motion and the resulting pressure pulse.

While everyone agrees that transonic flow is a nonlinear phenomenon, there remains controversy as to the extent flutter analyses have to be performed in nonlinear fashion to obtain useful results. In this respect, the results of Isogai (ref. 15) are of special interest for comparison with calculations of this investigation. Isogai uses a nonlinear aerodynamic procedure to calculate time-dependent pressure distributions, but extracts only the first harmonic of these pressure distributions for use in a linear V-g type flutter solution. Generally, Isogai's results exhibit the flutter boundary variations in the transonic regime that were obtained during the present investigation. Isogai also has an interesting discussion of the validity of using linear unsteady airforces for transonic flutter analyses.

The other flutter results, which are relatively comparable to the investigation discussed here, are presented by Yang et al in ref. 31. First, it should be noted that the NACA 64A010 airfoil studied in reference 31 was scaled down to 8.9% maximum thickness-to-chord ratio. Second, both aerodynamic theories used, i.e. LTRAN2 based on the time-integration method (ref. 4) and STRANS2/UTRANS2 based on the harmonic method (ref. 26), were limited to small reduced frequencies, lower Mach numbers and small values of  $\lambda_1 = \omega M / (1 - M^2)$ . Although the results presented by Yang, et al., do show a degradation in flutter velocity in the transonic regime, these results do not manifest the change in flutter modes that will be discussed below.

## 7.1 EQUATIONS OF MOTION

The flutter problem is formulated in conventional V-g fashion (see, e.g., Chapter 9 of Bisplinghoff, Ashley and Halfman, ref. 33). Starting with the sketch showing the parameters and sign conventions for a binary system (fig. 42), the equations of motion are written as

$$\begin{aligned} m\ddot{h} + S_\alpha \ddot{\alpha} + K_h h &= -L \\ S_\alpha \ddot{h} + I_\alpha \ddot{\alpha} + K_\alpha \alpha &= M_y \end{aligned} \quad (7.1)$$

where  $L$  and  $M_y$  are the total lift (positive up) and pitching moment (about the elastic axis, positive nose up) per unit span. The inertial quantities  $M$ ,  $S_\alpha$  and  $I_\alpha$ , are the mass, static unbalance, and moment of inertia per unit span about the elastic axis. Equation (7.1) may be rewritten as

$$\begin{aligned} \ddot{h}/b + x_\alpha \ddot{\alpha} + \omega_h^2 h/b &= -\frac{L}{mb} \\ x_\alpha \ddot{h}/b + r_\alpha^2 \ddot{\alpha} + \omega_\alpha^2 r_\alpha^2 \alpha &= \frac{M_y}{mb^2} \end{aligned} \quad (7.2)$$

where  $x_\alpha = S_\alpha/(mb)$ ,  $r_\alpha = \sqrt{I_\alpha/(mb^2)}$ ,  $\omega_h = \sqrt{K_h/m}$  and  $\omega_\alpha = \sqrt{K_\alpha I_\alpha}$ . Assuming simple harmonic motion,  $h = \bar{h}e^{i\omega t}$  and  $\alpha = \bar{\alpha}e^{i\omega t}$ , and writing the lift and moment in coefficient form, reduces equation (7.2) to

$$\begin{aligned} -\bar{h} - x_\alpha \bar{\alpha} + (\omega_h / \omega)^2 \bar{h} &= -\frac{\rho U^2 c}{2mb\omega^2} C_L \\ -x_\alpha \bar{h} - r_\alpha^2 \bar{\alpha} + r_\alpha^2 (\omega_\alpha / \omega)^2 \bar{\alpha} &= \frac{\rho U^2 c^2}{2mb^2\omega^2} C_M \end{aligned} \quad (7.3)$$

when  $\rho$  is the free stream density and  $U$  is free stream velocity. The lift and moment coefficients may be written as

$$\begin{aligned} C_L &= \frac{C_{Lh}}{2} \cdot \bar{h}/b + C_{L\alpha} \cdot \bar{\alpha} \\ C_M &= \frac{C_{Mh}}{2} \cdot \bar{h}/b + C_{M\alpha} \cdot \bar{\alpha} \end{aligned}$$

leading to the eigenvalue equation written in matrix form as

$$\left[ [M] + \frac{1}{\pi \mu k^2} [A] - \chi [K] \right] \begin{Bmatrix} \bar{h}/b \\ \bar{\alpha} \end{Bmatrix} = \begin{Bmatrix} 0 \\ 0 \end{Bmatrix} \quad (7.4)$$

where

$$[M] = \begin{bmatrix} 1 & x_\alpha \\ x_\alpha & r_\alpha^2 \end{bmatrix}$$

$$[K] = \begin{bmatrix} (\omega_h/\omega_\alpha)^2 & 0 \\ 0 & r_\alpha^2 \end{bmatrix}$$

$$[A] = \begin{bmatrix} -\frac{C_{Lh}}{2} & -C_{L\alpha} \\ C_{Mh} & 2C_{M\alpha} \end{bmatrix}$$

and the unknown eigenvalue  $\chi$  is equal to  $(\omega_\alpha/\omega)^2 (1 + ig)$  where  $g$  is the structural damping. The parameters  $\mu$  and  $k$  are the mass ratio and reduced frequency, respectively.

The aerodynamic coefficients  $C_{Lh}$ ,  $C_{L\alpha}$ ,  $C_{Mh}$  and  $C_{M\alpha}$  for an arbitrary elastic axis position may be obtained from those calculated for an alternate axis  $a'$  using the following transformations:

$$\begin{Bmatrix} C_{Lh} \\ C_{L\alpha} \\ C_{Mh} \\ C_{M\alpha} \end{Bmatrix} = \begin{bmatrix} 1 & 0 & 0 & 0 \\ (a' - a)/2 & 1 & 0 & 0 \\ -(a' - a)/2 & 0 & 1 & 0 \\ -(a' - a)^2/4 & -(a' - a)/2 & (a' - a)/2 & 1 \end{bmatrix} \begin{Bmatrix} C'_{Lh} \\ C'_{L\alpha} \\ C'_{Mh} \\ C'_{M\alpha} \end{Bmatrix}$$

The airforces for this report are calculated with an elastic axis at the quarter-chord.

It should be noted that the airforces are calculated for the measured and modified NACA 64010 airfoil described in section 6.1 which is slightly nonsymmetric and 10.6% thick.

## 7.2 A NOMINAL CONFIGURATION

Flutter results were first obtained for a NACA 64A010 airfoil with the following values for the stiffness and mass parameters:

$$\begin{aligned} x_\alpha &= 0.25 \\ r_\alpha &= 0.5 \\ \omega_h/\omega_\alpha &= 0.3, 0.6 \\ \mu &= 25 \text{ to } 300 \end{aligned}$$

Results for a frequency ratio,  $\omega_h/\omega_\alpha$ , of 0.3 are presented in figures 43 through 54. Figure 43 shows the flutter velocity coefficient and frequency versus mass ratio for purely subsonic conditions: an airfoil of vanishing thickness (i.e. a "flat plate") at

$M = 0.85$  and the airfoil configuration at  $M = 0.75$  and  $0.80$ . These curves are considered typical for the subsonic condition. The curves are smooth with both the flutter velocity coefficient and frequency decreasing with increasing  $\mu$  (i.e. decreasing air density). Figure 44 shows the amplitude ratio and phase difference of the plunging and pitching motions at the elastic axis versus mass ratio for the same subsonic conditions. Here, the amplitude ratio increases (becomes more predominantly plunge) and the phase angle decreases with increasing  $\mu$ . Thus, as the aerodynamic damping diminishes, the mode of instability tends towards the first natural frequency at the system.

Figure 45 shows the flutter velocity coefficient and frequency versus mass ratio for Mach numbers where the flow is transonic (i.e. mixed subsonic and supersonic flow over the airfoil) and significant shocks exist on the airfoil. The flutter velocity coefficient has the same general behavior as for the subsonic condition, but with much sharper gradients at the lower values of  $\mu$ . Also, the flutter frequency plot indicates a change in flutter mode between  $M = 0.83$  and  $0.842$ . At higher values of  $\mu$ , the mode of instability tends to the first natural mode for values of Mach numbers of  $0.83$  and below, and to the second natural mode at  $M = 0.842$  and above. This is reflected in the plots of frequency ratio (fig. 45) and of amplitude and phase angle (fig. 46). Note that there is another change in flutter mode in the neighborhood of the Mach number at which the shock leaves the trailing edge, a phenomenon that will be discussed with later examples.

Mixed subsonic-supersonic flow appears about  $M = 0.78$ . The shock first appears just ahead of midchord, and moves aft as the Mach number is increased until it finally moves off the trailing edge between  $M = 0.885$  and  $0.90$ . The location of the shock on the upper surfaces for  $M = 0.75$  to  $M = 0.90$  may be determined from the static pressure distributions shown in figure 47. For even higher Mach numbers, a detached shock wave appears in front of the leading edge, and this shock again moves aft as Mach number is increased until it becomes nearly attached to the leading edge. The shock, and its subsequent motion in conjunction with the motion of the airfoil, results in the now well recognized pressure pulse in unsteady pressure distributions. The corresponding change in the generalized air forces from the flat plate to the airfoil solution may be profound as shown in figures 48 to 51. For this case, the imaginary part of the  $C_{m\alpha}$  term changes sign (becomes positive) between  $M = 0.82$  and  $M = 0.88$ . This phenomenon helps to explain the switch to a predominantly torsion mode instability described in the preceeding paragraph. The gradients in the generalized forces in this Mach number range are severe, and more evaluations are required to properly define the behavior in the  $M = 0.85$  to  $M = 0.9$  range. Note that the points are connected assuming relatively little change in the air forces above  $M = 0.90$ .

Plots of flutter velocity coefficient and frequency versus Mach number for  $\mu = 50$  are shown in figure 52. The flutter boundary for an airfoil of vanishing thickness is shown by the dot-dash line. The corresponding boundary for the NACA 64A010 airfoil is shown by the solid line. The change in mode shape between  $M = 0.83$  and  $M = 0.842$

results, at this mass ratio, in a narrow "chimney" in the boundary, and a high flutter speed over a very small range of Mach numbers. The flutter velocity coefficient for the airfoil immediately below  $M = 0.83$  is very slightly less than for the flat plate. The flutter boundary for the airfoil at Mach numbers above  $M = 0.842$  is well above the flat plate boundary. Thus, the airfoil for  $\mu = 50$  exhibits a slight "transonic bucket" in Mach number range  $M = 0.75$  to  $M = 0.83$ , and undergoes a change in flutter mode between  $M = 0.83$  and  $0.842$  with a resulting rise in the flutter boundary. Flutter solutions were also run for  $M = 0.885$  and  $M = 0.9$ ; however, for the  $k$  values studied, there were no flutter crossings.

As discussed in section 6, the harmonic air forces used in the flutter analyses were calculated using two different steady velocity potential distributions; the first assumed nonviscous flow, the second used a "viscous-wedge" – a moving wedge-nosed ramp to approximate the effect of viscosity on the flow (see ref. 20). The flutter boundary calculated, including the viscous ramp effects in the steady state potential, are shown as a dashed line in figure 52 to provide an indication of the sensitivity of the flutter results to the inclusion of viscosity effects. The effect of the viscous ramp is to move the shock slightly forward which results in moving the abrupt rise in flutter velocity to a slightly higher Mach number. In this particular case, the results at  $M = 0.83$  are very sensitive to the viscous effects, and somewhat sensitive at  $M = 0.87$ . The calculations at  $M = 0.885$  and  $M = 0.9$  were made only without the viscous ramp.

Similar results are presented in figures 53 and 54 for  $\mu$  values of 100 and 300. As  $\mu$  is increased, the transonic bucket at Mach numbers below 0.83 increases slightly, and the boundary for  $M = 0.842$  and above drops significantly until it falls below the flat plate results. Thus, at  $\mu = 300$ , the flutter boundary for the airfoil is below that for flat plate except in the immediate vicinity of  $M = 0.83$  to  $M = 0.842$ . For this mass ratio, a flutter crossing was obtained at  $M = 0.885$ . No crossings were obtained at  $M = 0.9$  for the range of  $k$  values studied.

The next set of figures (figs. 55 to 63) examines the same configuration for a frequency ratio of 0.6. Generally, the flutter boundary patterns are the same as for  $\omega_h/\omega_\alpha = 0.3$ . Thus, figures 55 and 56 show the results for purely subsonic cases, and both the flutter velocity and frequency behave as discussed for figures 43 and 44. Figures 57 and 58 compare an essentially subsonic case ( $M = 0.83$ , with viscous ramp) with a transonic case ( $M = 0.842$ , with viscous ramp). The results at  $M = 0.842$ , show two flutter modes. The first, which is critical at all but very low mass ratios, is the predominantly plunge mode associated with the first natural mode of the system. The second, which is critical only at very low mass ratios is the predominantly torsion mode associated with the second natural mode of the system. This phenomenon is demonstrated for a second flight condition in figures 59 and 60. Here the results for the airfoil without viscous effects are compared with results for the flat plate.

Plots of flutter velocity coefficient and frequency versus Mach number for  $\omega_h/\omega_\alpha = 0.6$  are presented in figures 61 through 63. The flutter boundary

characteristics are similar to those for a frequency ratio of 0.3. However, the flutter boundary for this case is triple-valued for some Mach numbers. The behavior of the V-g curves as the flutter boundary starts to rise is sketched in figure 64. As the Mach number is increased, the V-g curve bends over, resulting in two crossings of the  $g = 0$  axis. As the Mach number is increased further, the excursion of V-g curve into the positive  $g$  half of the V-g plane is reduced until the curve no longer crosses.

The result is that the portion of boundary in the neighborhood of  $M_C$  to  $M_D$  represents lightly damped instabilities. As  $\mu$  increases, the sudden rise in the flutter boundary of the basic mode moves to higher Mach numbers, and the depth of the associated transonic bucket increases slightly. Also, as  $\mu$  increases the flutter boundary associated with the systems second natural mode moves to lower values. Again, solutions were run at  $M = 0.885$  and  $M = 0.9$ . For  $M = 0.885$ , a crossing was obtained only at  $\mu = 300$  for the  $k$  values studied. Crossings were obtained for all  $\mu$  values at  $M = 0.9$ . The instability mode at  $M = 0.9$  appears to be tending towards the first natural mode of the system again and thus represents a change in flutter mode from the Mach number range 0.842 to 0.87. Interpretation of the results at  $M = 0.885$  and  $\mu = 300$  is not clear, and in connecting the points in figure 63 we have tried to match modal amplitudes and phase angle differences.

### 7.3 TWO EXAMPLES FOR CORRELATION WITH OTHER ANALYSES

Isogai, in reference 15, computed two flutter examples using air forces from a time-integration scheme. These examples were analyzed with a linear flutter analysis using the first harmonic components from air forces calculated with a nonlinear transonic small perturbation procedure. Results of reanalyzing these two examples using the transonic aerodynamic procedures described in sections 4 and 5 are discussed in this section.

The first example, called "Case A" by Isogai, was developed to simulate "the vibrational characteristics of a typical chordwise section of a swept wing." The following values are used for the mass and stiffness parameters of a binary system:

$$a = -2.0, \quad x_\alpha = 1.8, \quad r_\alpha = 1.865, \quad \omega_h/\omega_\alpha = 1.0, \quad \mu = 60$$

Plots of flutter velocity coefficient and frequency versus Mach number for "Case A" are shown in figure 65. Four results are presented: (1) flat plate, (2) the results of reference 15 as estimated from the plots therein, and results using the harmonic procedures of this report both (3) without viscous effects and (4) with viscous effects.

The flutter boundary for this example exhibits the same characteristics as that of the preceding example with the abrupt change in flutter mode in the neighborhood of  $M = 0.85$ . This example has a significantly larger transonic bucket than the previous example, with  $U_F/(b\omega_\alpha \sqrt{\mu})$  for the airfoil at  $M = 0.84$  being half the flat plate value. The pattern for boundary based on the harmonic procedure looks quite similar to that from the time-integration study. However, the dip for the harmonic solution is not quite

as great as that from the time-integration solution. The rise in the flutter speed at the initial change in flutter mode appears to occur at the same Mach number for the two calculations without viscous effects. The inclusion of viscous effects (which results in moving the shock forward on the airfoil) moves the velocity rise to a slightly higher Mach number. The change in flutter mode as measured in terms of  $\omega_F/\omega_\alpha$  is significantly greater for the harmonic solution than for the time-integration solution. Also, the harmonic solution again shows three distinct parts to the flutter boundary. The first, at Mach numbers for which the flow is purely subsonic, is the classical flutter mode which in this case is mostly plunge. The second, at Mach numbers for which there are shocks over the chord of the wing, is a predominantly pitch mode. The third, taking over at Mach numbers for which the shock approaches the trailing edge, is again related to the predominantly plunge mode.

The level of the flutter velocity coefficient after the change in mode shape is significantly higher for the time-integration air forces than for the harmonic air forces. It would be expected that the flutter characteristics at  $M = 0.9$  and  $M = 1.01$  would be similar since the airforces for these two Mach numbers are nearly the same (see figs. 12g, 12h and 14 of ref. 15).

The second example examined by Isogai, "Case B," uses the following structural parameters:

$$a = -0.30, \quad x_\alpha = 0.5, \quad r_\alpha = 0.7, \quad \omega_h/\omega_\alpha = 0.2, \quad \mu = 60$$

which represents a nominal unswept wing. Plots of flutter velocity coefficient and frequency versus Mach number are presented in figure 66. Again, results are presented for the flat plate and the harmonic procedures, with and without viscous effects, and are compared with the results of reference 15. Again, there is an abrupt change in flutter mode shape in the neighborhood of  $M = 0.83$ . The transonic bucket in the flutter boundary just below  $M = 0.83$  is significantly less from the harmonic analyses than from the time-integration analysis. Note that for Case A, the two buckets were very similar. The flutter velocity coefficient at  $M = 0.85$ , which is just above the Mach number at which the flutter mode has changed, matches very well between the harmonic and time-integration analyses.



## 8.0 IMPROVEMENTS IN NUMERICAL PROCEDURES

Two new numerical procedures were investigated. One method, called the two step method, has the possibility of considerable improvement in computing time. The difference in potential between the airfoil and a flat plate can be computed with good accuracy using a solution region which is smaller than that required for calculating a full transonic potential. Even though two calculations are required, considerable computer time is saved because the more complicated mixed flow problem is computed using a much reduced mesh.

The second numerical procedure is an alternating direction implicit (ADI) technique similar to the relaxation method but does not have the limitation to frequencies below the critical value related to Mach number and mesh size. This was tested for two-dimensional flow but has more practical application to three-dimensional flow where the direct solution has memory requirements beyond the capacity of current computing machines.

### 8.1 THE TWO STEP METHOD

On comparing the potential distributions for a harmonic flat plate solution with that for the full transonic flow over an airfoil at the same Mach number and reduced frequency, it was discovered that the difference in potentials was significant only for the region close to the airfoil. Hence, if one could obtain a linearized solution for the flat plate potential at a greatly reduced computing cost, then the transonic harmonic solution for the difference between the flat plate potential and the potential for the transonic flow over the airfoil could be computed for a much reduced mesh region near the airfoil.

The complex potential for mixed flow  $\varphi_1$  is assumed to be the sum of the flat plate potential  $\psi_1$  and a potential  $\varphi_2$  ;i.e.,

$$\varphi_1 = \psi_1 + \varphi_2 \quad (8.1.1)$$

Here  $\psi_1$  satisfies the linearized differential equation for unsteady subsonic flow or

$$K\psi_{1xx} + \psi_{1yy} - 2i\omega\psi_{1x}/\epsilon + (\omega^2/\epsilon)\psi_1 = 0 \quad (8.1.2)$$

Substituting equation (8.1.1) in the transonic differential equation for  $\varphi_1$  and using equation (8.1.2.) lead to the same differential equation for  $\varphi_2$  as that for  $\varphi_1$  but with source terms which depend upon  $\varphi_0$  and  $\psi_1$ . The solution of  $\varphi_2$  is carried out in the same way as for  $\varphi_1$  since the source terms merely introduce additional non-zero right hand sides into the system of difference equations. The complete derivation of the equations is presented in appendix C.

Figures 67 to 68 compare the jump in pressure coefficients for the full perturbation potential  $\varphi_1$ , for the flat plate solution  $\psi_1$  and for the difference potential  $\varphi_2$ . Computations were made on the full mesh. Adding the results of the potentials  $\psi_1$  and  $\varphi_2$  can be seen to yield the values for  $\varphi_1$ .

To obtain a measure of the improvement in using the solution of the flat plate over the full mesh to obtain the complete  $\varphi_1$  for the reduced mesh, the transonic solution was found for the full mesh and for the reduced mesh in a single step. Figures 69 and 70 indicate that the accuracy of the solution is not adequate with the reduced mesh.

The solution for  $\varphi_2$  with the source terms calculated from the flat plate solution for the complete 68 by 50 mesh was obtained using a reduced mesh of 51 by 22 extracted from the complete 68 by 50 mesh. The combined pressure distribution for  $\psi_1$  and  $\varphi_2$  is compared with that for  $\varphi_1$  over the complete mesh in figures 71 and 72. The accuracy is seen to be satisfactory.

Even though the flat plate solution was obtained from the direct solution of the finite difference equation instead of the kernel function method, considerable reduction was found in the cost of obtaining the complete transonic solution. The computing times are roughly proportional to the square of the number of grid points. Since the flat plate solution is antisymmetric, only one-half of the grid points need be used. Thus the flat plate solution requires only about 1/4 of the time for the complete  $\varphi_1$  solution. The reduced grid of 51 by 22 has only 1/3 the number of points and hence requires only about 1/9 of the time for the full solution. This is a combined time of only 36% of the original full solution. The time for obtaining the flat plate solution could be possibly reduced by an order of magnitude by taking advantage of its pure elliptic form. Thus the solution cost could be substantially reduced by using the two step method.

## 8.2 THE ADI METHOD OF HARMONIC SOLUTION BASED ON TIME INTEGRATION

Because of the size of the matrix for three-dimensional flow, a preferred method of solution is some form of relaxation in which the direct solution of the large system of difference equations is obtained by a sequence of smaller steps. Conventional relaxation methods for both two dimensions and three dimensions have been found to be limited in the range of frequencies for which the method converges (see references 9 and 10). However, when the equation with the time variable,  $t$ , is retained, solutions of harmonic motion may be calculated for any frequency range using relaxation type procedures. Under the assumption of small perturbations near the speed of sound, the differential equation for the perturbation potential is of the form

$$\left[ K - (\gamma + 1)\psi_x \right] \psi_{xx} + \psi_{yy} - (2\psi_{xt} + \psi_{tt}) / \epsilon = 0 \quad (8.2.1)$$

Rizzetta and Chin (ref. 19) developed an ADI method for solving this equation which is an extension of the method of Ballhaus and Goorjian for small frequencies.

Equation (8.2.1) is linearized by separating the potential into steady state and unsteady potentials under the assumption of small oscillations. The steady state potential  $\varphi_0$  satisfies the classic nonlinear transonic small perturbation differential equation with the time derivative term in equation (8.2.1) deleted. The linear differential equation for the unsteady perturbation potential  $\psi_1$  then becomes

$$\left( u\psi_{1x} \right)_x + \psi_{1yy} - \left( 2\psi_{1xt} + \psi_{1tt} \right) / \epsilon = 0 \quad (8.2.2)$$

where  $u = K - (\gamma + 1)\varphi_{0x}$ . Applying the operator factorization procedure similar to that of Rizzetta and Chin (ref. 19) we can solve equation (8.2.2) for each time step by an x sweep given by the difference equation

$$2\delta_x(\tilde{\psi} - \psi^n) / (\epsilon\Delta t) = \left[ \delta_x(u\delta_x\tilde{\psi}) + \delta_x(u\delta_x\psi^n) \right] / 2 + \delta_{yy}\psi^n \quad (8.2.3)$$

followed by a y sweep of the form

$$\left( \psi^{n+1} - 2\psi^n + \psi^{n-1} \right) / (\epsilon\Delta t^2) + 2\delta_x(\psi^{n+1} - \tilde{\psi}) / (\epsilon\Delta t) = \delta_{yy}(\psi^{n+1} - \psi^n) / 2 \quad (8.2.3)$$

where  $\psi^n = \psi(n\Delta t)$  and the tilda denotes an intermediate value of  $\psi$  between  $n$  and  $n+1$ . Here  $\delta_x$  on the left-hand side is the backward difference. The differences on the right-hand side are central differences at all elliptic points. However,  $\delta_x(u\delta_x)$  for hyperbolic points is the backward difference.

The linearized boundary conditions that the flow velocity on the wing equal the velocity of motion on the surface is

$$\psi_y = f_x + f_t$$

We introduce harmonic motion of the airfoil and let

$$\psi^n = \varphi^n e^{i\omega n \Delta t}$$

then

$$\varphi_y^n = f_x + i\omega f$$

and the quantity  $\varphi^n$  approaches constant values at each point as  $t \rightarrow \infty$ .

The complete derivation of this method is included in appendix D. The boundary conditions used on the wake are those applied in the direct solution and in the relaxation procedure.

For the first calculations, the same boundary conditions used in the direct harmonic solution were applied to the mesh boundaries, but this introduced reflections which caused oscillations in the complex potential  $\varphi$ . When the mesh boundary conditions used by Kwak (ref. 34) were applied to the difference equations (8.2.3) and (8.2.4), the oscillations were eliminated allowing  $\varphi$  to converge to complex constants at every point of the grid. The simpler first order mesh boundary conditions of Engquist

and Majda (ref. 22) were also tried. These boundary conditions for pure harmonic motion reduce to those used in the direct harmonic solution and are simpler than the boundary conditions of Kwak. They also eliminated the boundary reflections.

A stability analysis of the difference equation has not been made because of the complexity of the three time levels introduced by the second time derivative. A Von Neumann analysis of the small frequency form ( $\phi_{tt}$  deleted) is simple and is presented in appendix D. This form of the equation is equivalent to the method of Traci, Albano, and Farr (refs. 26 and 27) which has the same frequency limitation as our method. The difference equation resulting from dropping the first term in parentheses of equation (8.2.4) was found to be unconditionally stable. Since the method of Rizzetta and Chin (ref. 19) was found to be stable for all frequencies tried, it appears that equations (8.2.3) and (8.2.4) are also convergent for all frequencies.

Solutions were found for  $M = 0.9$  and reduced frequencies of 0.45 and 0.6, which are well above the critical frequency of the mesh. The results for the flat plate are compared with the method of Rowe et al. (refs. 35 and 36) in figures 73 and 74. The comparison with linearized theory is not quite as good as that for the direct solution.

These results are preliminary. Choosing the size of the time step to speed up convergence and studies to improve the accuracy are needed. A solution for mixed flow has not been tried but this should cause no difficulty, as solution convergence is independent of whether the flow is subsonic or truly transonic.

## 9.0 CONCLUSIONS

This investigation has centered on further development and evaluation of a harmonic procedure for analyzing unsteady transonic air forces. It has shown that the moving shock associated with an oscillating airfoil is represented in the pressure distributions and generalized air forces as calculated with harmonic procedures. Pressure distributions of an NACA 64A010 airfoil have been correlated with distributions calculated with both harmonic and time-integration procedures. The results appear satisfactory as might be expected for an inviscid solution.

Two-degree-of-freedom flutter analysis of the NACA 64A010 airfoil have been performed. It is found that the flutter boundary through the Mach number region for which a shock is attached to the airfoil surface may include a flutter "bucket" (the boundary may be well below that for a flat plate) and a change in mode shape resulting in a region of low damping and/or a significant rise in flutter velocity. It would be helpful to have experimental transonic flutter results to compare with the analytical results.

Theoretical developments from this investigation include development of an ADI method which appears to provide a practical relaxation solution approach for the three-dimensional problem. Also, preliminary results are presented from a two step procedure in which the full velocity potential is found as the sum of the potential for a flat plate and an increment in potential due to the thickness distribution. Both of these procedures are promising but require further development and assessment.

# APPENDIX A

## DERIVATION OF THE SHOCK RELATIONS FOR A MOVING SHOCK REFERRED TO THE STEADY STATE SHOCK LOCATION

The partial differential equation for transonic small disturbance unsteady flow is given in reference 8 as

$$\left[ K - (\gamma + 1)\varphi_x \right] \varphi_{xx} + \varphi_{yy} - \varphi_{xt} / \epsilon - (\varphi_x + \varphi_t)_t / \epsilon = 0 \quad (\text{A-1})$$

Here we have dropped the term  $\varphi_t \varphi_{xx}$  to be consistent with Hafez, Risz, and Murman (ref. 28), whose approach we shall follow in the subsequent analysis. (See also Williams (ref. 29) and Seebass, et al. (ref. 30) for similar analyses.) The term  $\varphi_t \varphi_{xx}$  has been found to have only a small effect on the solution. To develop the shock conditions we express this equation in conservation form. Equation (A-1) becomes

$$\left\{ -\varphi_t / \epsilon + \left[ K\varphi_x - (\gamma + 1)\varphi_x^2 / 2 \right] \right\}_x + \left\{ \varphi_y \right\}_y - \left\{ \varphi_t + \varphi_x \right\}_t / \epsilon = 0 \quad (\text{A-2})$$

Applying the divergence theorem about a thin region containing the shock yields

$$-\left[ \varphi_t \right] n_x / \epsilon + \left[ K\varphi_x - (\gamma + 1)\varphi_x^2 / 2 \right] n_x + \left[ \varphi_y \right] n_y - \left[ \varphi_t + \varphi_x \right] n_t / \epsilon = 0 \quad (\text{A-3})$$

where  $(n_t, n_x, n_y)$  is the normal to the shock and  $[ ]$  denotes the jump in the quantity across the shock.

The continuity of tangential velocity is given by

$$[\nabla \varphi] \times \bar{n} = 0 \quad (\text{A-4})$$

$$[\varphi] = 0 \quad (\text{A-5})$$

Equation (A-4) when expanded gives

$$\begin{vmatrix} [\varphi_x] & [\varphi_y] & [\varphi_t] \\ n_x & n_y & n_t \end{vmatrix} = 0 \quad (\text{A-6})$$

or

$$[\varphi_x] n_y - [\varphi_y] n_x = 0 \quad (\text{A-7})$$

$$[\varphi_x] n_t - [\varphi_t] n_x = 0 \quad (\text{A-8})$$

Let  $f(x,y,t) = 0$  be the shock surface, then since  $\nabla f \sim n$ , we have

$$n_y/n_x = f_y/f_t = - (dx/dy)_f \quad (\text{A-9})$$

$$n_t/n_x = f_t/f_x = - (dx/dt)_f \quad (\text{A-10})$$

To simplify equation (A-3) we divide by  $[\varphi_x]n_x$ . After substituting

$$\begin{aligned} [\varphi_x^2] / 2 &= 1/2 (\varphi_x^+ + \varphi_x^-) (\varphi_x^+ - \varphi_x^-) \\ &= \langle \varphi_x \rangle [\varphi_x] \end{aligned}$$

where  $\langle \varphi_x \rangle = (\varphi_x^+ + \varphi_x^-)/2$ , we obtain for equation (A-3)

$$-\frac{[\varphi_t]}{\epsilon[\varphi_x]} + \langle K - (\gamma + 1)\varphi_x \rangle + \frac{[\varphi_y]n_y}{[\varphi_x]n_x} - \frac{[\varphi_t]n_t}{\epsilon[\varphi_x]n_x} - \frac{n_t}{\epsilon n_x} = 0$$

We now eliminate  $[\varphi]$  by means of equations (A-7) and (A-8). Thus

$$\frac{-2n_t}{\epsilon n_x} + \langle K - (\gamma + 1)\varphi_x \rangle + \left( \frac{n_y}{n_x} \right)^2 - \left( \frac{n_t}{n_x} \right)^2 / \epsilon = 0.$$

Substituting equations (A-9) and (A-10) leads to

$$\frac{2}{\epsilon} \frac{dx}{dt} + \langle K - (\gamma + 1)\varphi_x \rangle + \left( \frac{dx}{dy} \right)^2 - \frac{1}{\epsilon} \left( \frac{dx}{dt} \right)^2 = 0 \quad (\text{A-11})$$

Let

$$\varphi = \varphi_0 + a \text{ Real } \left\{ \varphi_1 e^{i\omega t} \right\} \quad (\text{A-12})$$

$$X = X_0 + a \text{ Real } \left\{ X_1 e^{i\omega t} \right\} \quad (\text{A-13})$$

where  $\varphi_0$  is the steady state potential,  $X_0$  is the steady shock location and  $a$  is the amplitude of motion. Expanding about the steady state shock location yields for equation (A-5)

$$\begin{aligned} [\varphi] &= [\varphi] + aX_1[\varphi_x]e^{i\omega t} + \dots \\ &= [\varphi_0 + a\varphi_1 e^{i\omega t}] + aX_1 e^{i\omega t} [\varphi_{0x} + a\varphi_{1x} e^{i\omega t}] + \dots \end{aligned}$$

Setting the coefficient of each power of  $a$  equal to zero yields for the first two terms in the expansion

$$[\varphi_0] = 0 \quad (\text{A-14})$$

$$[\varphi_1] + X_1 [\varphi_{0_x}] = 0 \quad (\text{A-15})$$

Similarly, expanding equation (A-11) yields

$$\begin{aligned} & 2ai\omega X_1 e^{i\omega t} / \epsilon + \langle K - (\gamma + 1)\varphi_{0_x} - (\gamma + 1)a\varphi_{1_x} e^{i\omega t} + \dots \rangle \\ & + \langle -(\gamma + 1)\varphi_{0_{xx}} - a(\gamma + 1)\varphi_{1_{xx}} e^{i\omega t} \rangle aX_1 e^{i\omega t} + \left(\frac{dx_0}{dy}\right)^2 \\ & + 2a \left(\frac{dx_0}{dy}\right) \left(\frac{dx_1}{dy}\right) e^{i\omega t} + O(a^2) = 0 \end{aligned}$$

Equating the coefficient of each power of  $a$  equal to zero leads to the following shock relations

$$\begin{aligned} & \langle K - (\gamma + 1)\varphi_{0_x} \rangle + \left(dx_0/dy\right)^2 = 0 \\ & 2i\omega X_1 / \epsilon - (\gamma + 1) \langle \varphi_{1_x} + X_1 \varphi_{0_{xx}} \rangle + 2 \left(\frac{dx_0}{dy}\right) \left(\frac{dx_1}{dy}\right) = 0 \end{aligned} \quad (\text{A-16})$$

In two-dimensional flow the shock is nearly normal and we obtain

$$\langle K - (\gamma + 1)\varphi_{0_x} \rangle = \langle u \rangle = 0 \quad (\text{A-17})$$

$$2i\omega X_1 / \epsilon - (\gamma + 1) \langle \varphi_{1_x} + X_1 \varphi_{0_{xx}} \rangle = 0 \quad (\text{A-18})$$

$$\langle 2i\omega / \epsilon - (\gamma + 1)\varphi_{0_{xx}} \rangle X_1 - (\gamma + 1) \langle \varphi_{1_x} \rangle = 0 \quad (\text{A-19})$$

To apply the shock conditions of equation (A-19) we need to express equation (A-19) in terms of  $\varphi_0$  and  $\varphi_1$ . Thus eliminating  $X_1$  by equation (A-15) we obtain

$$\langle 2i\omega / \epsilon - (\gamma + 1)\varphi_{0_{xx}} \rangle [\varphi_1] + (\gamma + 1) \langle \varphi_{1_x} \rangle [\varphi_{0_x}] = 0 \quad (\text{A-20})$$

Now

$$(\gamma + 1)\varphi_{0_x} = K - u$$



and

$$(\gamma + 1)\varphi_{0_{xx}} = -u_x$$

Equation (A-20) then takes the form

$$\langle 2i\omega / \epsilon + u_x \rangle [\varphi_1] - [u] \langle \varphi_{1_x} \rangle = 0 \quad (\text{A-21})$$

From figure A-1 on the following page we define

$$\beta_1 = [u] = (u_{i_s+1,j} - u_{i_s j}) \quad (\text{A-22})$$

and

$$\beta_2 = \langle u_x \rangle = 1/2 \left\{ \frac{u_{i_s j} - u_{i_s-1 j}}{x_{i_s-1/2} - x_{i_s-3/2}} + \frac{u_{i_s+2 j} - u_{i_s+1 j}}{x_{i_s+3/2} - x_{i_s+1/2}} \right\}$$

$$\beta_2 = \frac{u_{i_s j} - u_{i_s-1 j}}{x_{i_s} - x_{i_s-2}} + \frac{u_{i_s+2 j} - u_{i_s+1 j}}{x_{i_s+2} - x_{i_s}}$$

The shock boundary condition in equation (A-21) then becomes

$$\left( \beta_2 + 2i\omega / \epsilon \right) \left( \varphi_{i_s j} - \varphi_{i_s-1 j} \right) - \frac{\beta_1}{2} \left\{ \frac{\varphi_{i_s+1 j} - \varphi_{i_s j}}{x_{i_s+1} - x_{i_s}} + \frac{\varphi_{i_s-1 j} - \varphi_{i_s-2 j}}{x_{i_s-1} - x_{i_s-2}} \right\} = 0 \quad (\text{A-23})$$

This equation replaces the finite difference representation of the differential equation when shock boundary conditions are employed.

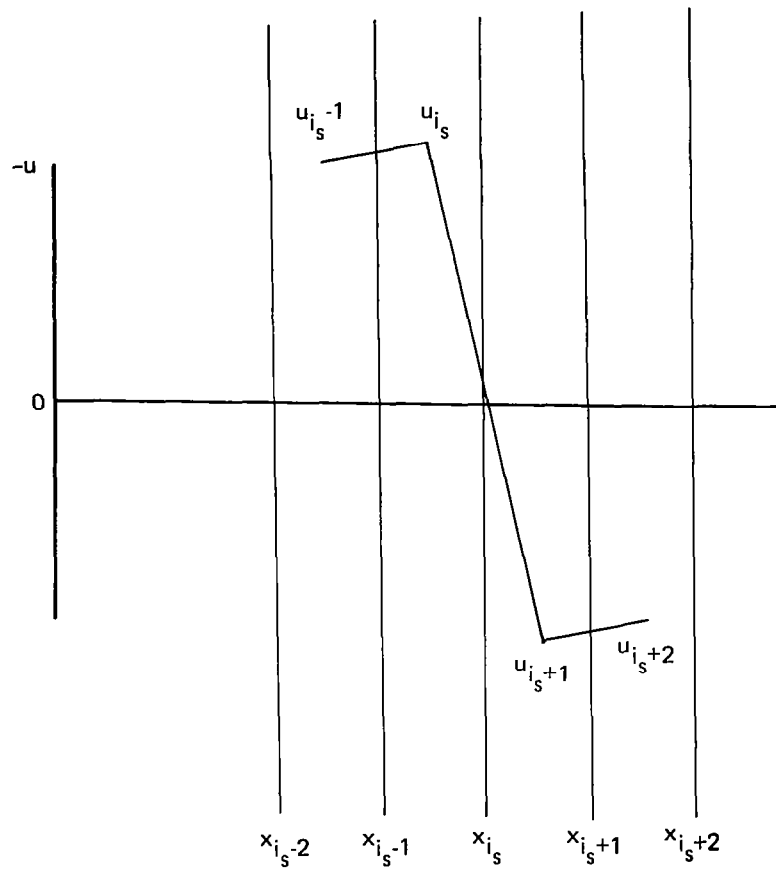


*Figure A-1.—Illustration of  $u$  Distribution About a Shock Point.*

## APPENDIX B DERIVATION OF THE SHOCK POINT OPERATOR

When a rapidly decelerating flow is supersonic upstream of the point  $i,j$  ( $u_{i-1/2,j} < 0$ ) and the flow becomes subsonic downstream of the point  $i,j$  ( $u_{i+1/2,j} > 0$ ), a shock wave then lies between the points  $i$  and  $i + 1$ . To satisfy the appropriate jump conditions across the shock, the difference operator for the point  $i,j$  must be conservative. To obtain such an operator we apply the divergence theorem

$$\int_V \nabla \cdot \bar{F} \, dv = \int_S \bar{F} \cdot \bar{n} \, d_s$$

to the differential operator expressed in conservation form for the control volume consisting of lines drawn midway between consecutive columns and rows of mesh points as shown in figure B-1 on the following page. Here  $\bar{n}$  is the outward normal to the closed surface. We shall consider only two-dimensional flow, but the generalization to three-dimensional flow requires only the addition of the central difference operator for  $\varphi_{1zz}$  at the point  $i,j,k$ .

The basic partial differential equation, equation (17) of Ehlers (ref. 8), has the form

$$\left( u\varphi_{1x} - 2i\omega\varphi_1 / \epsilon \right)_x + \varphi_{1yy} + q\varphi_1 = 0 \quad (B-1)$$

where  $u = K - (\gamma + 1)\varphi_{0x}$ . Hence the vector  $F$  is

$$\bar{F} = u\varphi_{1x} - 2i\omega\varphi_1 / \epsilon, \quad \varphi_{1y}$$

and the approximate evaluation of the surface integral in equation (B-1) yields

$$\begin{aligned} & \ell_y \left[ u_{i+1/2,j} \varphi_{x_{i+1/2,j}} - u_{i-3/2,j} \varphi_{x_{i-3/2,j}} - 2i\omega \left( \varphi_{i+1/2,j} - \varphi_{i-3/2,j} \right) / \epsilon \right] \\ & + \ell_x \varphi_{y_{ij+1/2}} - \ell_x \varphi_{y_{ij-1/2}} + q_{ij} \ell_x \ell_y \varphi_{ij} = 0 \end{aligned}$$

where  $i+1/2$  denotes the value of the quantity at the point midway between  $x_i$  and  $x_{i+1}$ ; and similarly, for the other half integer subscripts. Dividing the equation by  $\ell_x \ell_y$  puts the equation in difference form:

$$\begin{aligned} & \left[ u_{i+1/2,j} \varphi_{x_{i+1/2,j}} - u_{i-3/2,j} \varphi_{x_{i-3/2,j}} \right] / \ell_x - 2(i\omega/\epsilon) \left[ \varphi_{i+1/2,j} - \varphi_{i-3/2,j} \right] / \ell_x \\ & + \left[ \varphi_{y_{ij+1/2}} - \varphi_{y_{ij-1/2}} \right] / \ell_y + q_{ij} \varphi_{ij} = 0 \end{aligned} \quad (B-2)$$

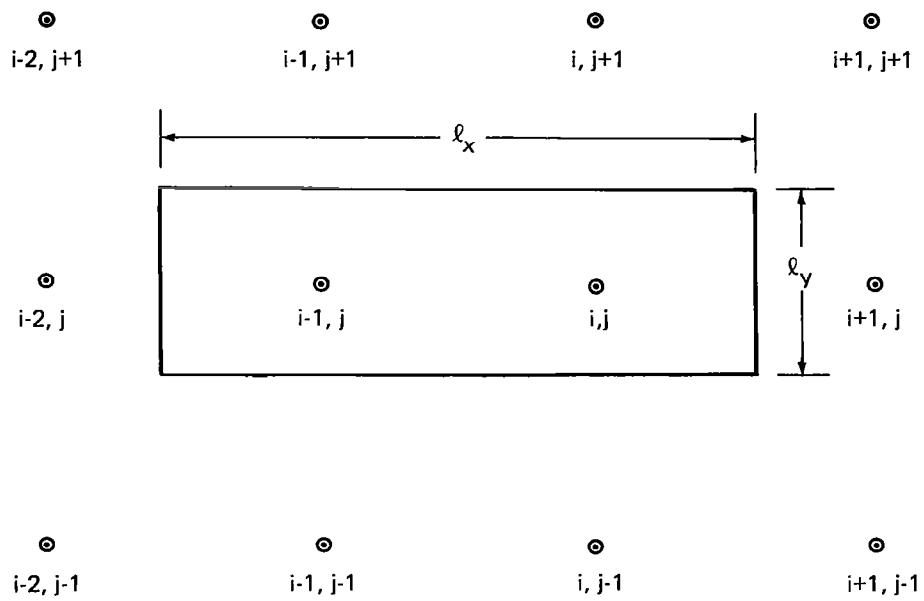


*Figure B-1.—Control Volume for Shock Point Operator*

Now

$$\begin{aligned}
\left[ \varphi_{i+1/2j} - \varphi_{i-3/2j} \right] / \ell_x &= \left[ \varphi_{i+1/2j} - \varphi_{i-1/2j} + \varphi_{i-1/2j} - \varphi_{i-3/2j} \right] / \ell_x \\
&= \left[ (x_{i+1/2} - x_{i-1/2}) \varphi_{x_{ij}} + (x_{i-1/2} - x_{i-3/2}) \varphi_{x_{i-1j}} \right] / (x_{i+1/2} - x_{i-3/2}) \\
&= \left[ (x_{i+1} - x_{i-1}) \varphi_{x_{ij}} + (x_i - x_{i-2}) \varphi_{x_{i-1j}} \right] / [x_{i+1} + x_i - x_{i-1} - x_{i-2}]
\end{aligned}$$

In reference 8 we substituted the central difference operator for  $\varphi_{x_{ij}}$  the upwind difference operator for  $\varphi_{x_{i-1j}}$  and obtained

$$\begin{aligned}
\left[ \varphi_{i+1/2j} - \varphi_{i-3/2j} \right] / \ell_x &= DX_1 \left[ c_{2j}(\varphi_{ij} - \varphi_{i-1j}) - d_{1i-1}(\varphi_{i-1j} - \varphi_{i-2j}) \right] / (DX_1 + DX_2) \\
&+ DX_2 \left[ c_{1i}(\varphi_{i+1j} - \varphi_{ij}) + d_{1i}(\varphi_{ij} - \varphi_{i-1j}) \right] / (DX_1 + DX_2) \quad (B-3)
\end{aligned}$$

where  $DX_1 = x_i - x_{i-2}$ ,  $DX_2 = x_{i+1} - x_{i-1}$ , and  $c_{1i}$ ,  $d_{1i}$ , and  $c_{2i}$  are given in equations (19), (20), and (26) of reference 8. This form was chosen to make equation (B-3) equal to a weighted average of upwind and central difference for  $\varphi_{1x}$ . An alternate form, with perhaps better justification, is obtained by replacing  $\varphi_{x_{ij}}$  and  $\varphi_{x_{i-1j}}$  with their central difference forms. In place of equation (B-3) we get

$$\begin{aligned}
\left[ \varphi_{i+1/2j} - \varphi_{i-3/2j} \right] / \ell_x &= DX_1 \left[ c_{1i-1}(\varphi_{ij} - \varphi_{i-1j}) + d_{1i-1}(\varphi_{i-1j} - \varphi_{i-2j}) \right] / (DX_1 + DX_2) \\
&+ DX_2 \left[ c_{1i}(\varphi_{i+1j} - \varphi_{ij}) + d_{1i}(\varphi_{ij} - \varphi_{i-1j}) \right] / (DX_1 + DX_2) \quad (B-4)
\end{aligned}$$

A second modified form is found by substituting

$$\begin{aligned}
\varphi_{i+1/2j} &= (\varphi_{ij} + \varphi_{i+1j}) / 2 \\
\varphi_{i-3/2j} &= (\varphi_{i-1j} + \varphi_{i-2j}) / 2
\end{aligned}$$

We then obtain

$$\left( \varphi_{i+1/2j} - \varphi_{i-3/2j} \right) / \ell_x = (\varphi_{i+1j} + \varphi_{ij} - \varphi_{i-1j} - \varphi_{i-2j}) / (DX_1 + DX_2) \quad (B-5)$$

From the standpoint of simplicity and logic, the second modified form is to be preferred. The first modified form is identical to the second when the  $x$  grid in the vicinity of the shock is uniform.

The first bracketed term in equation (B-2) yields for the second x derivative term

$$\begin{aligned}
& \left[ u_{i+1/2 \ j} \varphi_{x_{i+1/2 \ j}} - u_{i-3/2 \ j} \varphi_{x_{i-3/2 \ j}} \right] / \ell_x \\
& = D_1 \left[ 2c_{i-1} u_{i-1/2 \ j} (\varphi_{ij} - \varphi_{i-1j}) - 2d_{i-1} u_{i-3/2 \ j} (\varphi_{i-1j} - \varphi_{i-2j}) \right] \\
& \quad + D_2 \left[ 2c_i u_{i+1/2 \ j} (\varphi_{i+1j} - \varphi_{ij}) - 2d_i u_{i-1/2 \ j} (\varphi_{ij} - \varphi_{i-1j}) \right] \tag{B-6}
\end{aligned}$$

with  $D_1 = DX_1/(DX_1 + DX_2)$  and  $D_2 = DX_2/(DX_1 + DX_2)$ . The y derivative becomes

$$\varphi_{yy_{ij}} = (\varphi_{y_{ij+1/2}} - \varphi_{y_{ij-1/2}}) / \ell_y = 2a_j \varphi_{ij-1} - 2(a_j + b_j) \varphi_{ij} + 2b_j \varphi_{ij+1} \tag{B-7}$$

where  $a_j$  and  $b_j$  are given in equation (23) of reference 8.

Finally the difference equation at the shock point  $ij$  is obtained by substituting either equation (B-3), (B-4), or (B-5) into equation (B-2). After some simplification, we obtain, for equation (B-2),

$$\begin{aligned}
& a_j \varphi_{ij-1} - (a_j + b_j + D_2 E_1 + D_2 E_2 - D_1 E_3 - q_{ij} / 2) \varphi_{ij} + b_j \varphi_{ij+1} \\
& = (D_1 E_3 + D_1 E_4 - D_2 E_2) \varphi_{i-1j} - D_1 E_4 \varphi_{i-2j} - D_2 E_1 \varphi_{i+1j} \tag{B-8}
\end{aligned}$$

where

$$\begin{aligned}
E_1 &= c_i u_{i+1/2 \ j} - i\omega c_{1i} / \epsilon \\
E_2 &= d_i u_{i-1/2 \ j} - i\omega d_{1i} / \epsilon \\
E_3 &= c_{i-1} u_{i-1/2 \ j} + i\omega d_{1i-1} / \epsilon \\
E_4 &= d_{i-1} u_{i-3/2 \ j} + i\omega d_{1i-1} / \epsilon \tag{B-9}
\end{aligned}$$

For the first modified shock point operator, equation (B-8) remains unchanged but  $E_3$  and  $E_4$  are changed to

$$\begin{aligned}
E_3 &= c_{i-1} u_{i-1/2 \ j} - i\omega c_{1i-1} / \epsilon \\
E_4 &= d_{i-1} u_{i-3/2 \ j} - i\omega d_{1i-1} / \epsilon \tag{B-10}
\end{aligned}$$

For the second modified shock point operator, the difference equation replacing (B-8) and (B-9) is

$$\begin{aligned}
& a_j \varphi_{ij-1} - (a_j + b_j - q_{ij} / 2 + E_1 + E_2 - E_3) \varphi_{ij} + b_j \varphi_{ij+1} \\
& = (E_4 + E_3 - E_2) \varphi_{i-1j} - E_1 \varphi_{i+1j} + E_4 \varphi_{i-2j} \tag{B-11}
\end{aligned}$$

where

$$\begin{aligned}
 E_1 &= D_2 c_i u_{i+1/2\ j} - i\omega \sqrt{\epsilon} (DX_1 + DX_2) \\
 E_2 &= D_2 d_i u_{i-1/2\ j} + i\omega \sqrt{\epsilon} (DX_1 + DX_2) \\
 E_3 &= D_1 c_{i-1} u_{i-1/2\ j} - i\omega \sqrt{\epsilon} (DX_1 + DX_2) \\
 E_4 &= D_1 d_{i-1} u_{i-3/2\ j} + i\omega \sqrt{\epsilon} (DX_1 + DX_2)
 \end{aligned} \tag{B-12}$$

## APPENDIX C

### DERIVATION OF THE DIFFERENCE EQUATIONS FOR THE TWO STEP METHOD

The two step method utilizes the simpler solution of the flat plate to reduce the grid size necessary to obtain a transonic harmonic unsteady solution for the flow over an airfoil. The differential equation for transonic harmonic unsteady flow is given in reference 8 by

$$\left\{ \left[ K - (\gamma + 1)\varphi_{0x} \right] \varphi_{1x} \right\}_x + \varphi_{1yy} - (2i\omega / \epsilon)\varphi_{1x} + \left[ \omega^2 / \epsilon - i\omega(\gamma - 1)\varphi_{0xx} \right] \varphi_1 = 0 \quad (C-1)$$

We assume that  $\varphi_1$  is a sum of solutions,  $\psi_1$  and  $\varphi_2$ , or

$$\varphi_1 = \psi_1 + \varphi_2 \quad (C-2)$$

where  $\psi_1$  is the flat plate solution which satisfies the partial differential equation

$$K\psi_{1xx} + \psi_{1yy} - (2i\omega / \epsilon)\psi_{1x} + (\omega^2 / \epsilon)\psi_1 = 0 \quad (C-3)$$

and  $\varphi_2$  is the difference between the transonic and the flat plate solutions. Substituting equation (C-2) into (C-1) and simplifying the resulting equation by means of equation (C-3) yields

$$\begin{aligned} & \left( u\varphi_{2x} \right)_x - (2i\omega / \epsilon)\varphi_{2x} + \varphi_{2yy} - \left[ \omega^2 / \epsilon - i\omega(\gamma - 1)\varphi_{0xx} \right] \varphi_2 \\ &= \left[ (\gamma + 1)\varphi_{0x}\psi_{1x} \right]_x + i\omega(\gamma - 1)\varphi_{0xx}\psi_1 \\ &= \left[ (K - u)\psi_{1x} \right]_x - i\omega(\gamma - 1)u_x\psi_1 / (\gamma + 1) \end{aligned}$$

At  $x = x_i$ , we note that

$$u_x = \frac{u_{i+1/2} - u_{i-1/2}}{x_{i+1/2} - x_{i-1/2}} = 2 \frac{u_{i+1/2} - u_{i-1/2}}{x_{i+1} - x_{i-1}}$$

For practical notation in coding, we used

$$u_{i+1/2} \rightarrow u_{i+1j}$$

$$u_{i-1/2} \rightarrow u_{ij}$$

then

$$\begin{aligned} & \left[ (K - u)\psi_{1x} \right]_x - \frac{i\omega(\gamma - 1)}{\gamma + 1} u_x \psi_1 \\ &= 2(K - u_{i+1j})c_i(\psi_{1i+1j} - \psi_{1ij}) - 2(K - u_{ij})d_i(\psi_{1ij} - \psi_{1i-1j}) \\ & \quad - 2i\omega(\gamma - 1)(u_{i+1j} - u_{ij})\psi_{1ij} / [(\gamma + 1)(x_{i+1} - x_{i-1})] \end{aligned}$$



The difference operator of the left hand side is derived in reference 8, and the variables  $c_i$  and  $d_i$  are also defined there. Since we divided by 2 in constructing the difference operator of the left hand side, the right hand side becomes

$$\begin{aligned} \text{RHS}(I,J) = & (K - u_{i+1j})c_i(\psi_{1i+1j} - \psi_{1ij}) - (K - u_{ij})d_i(\psi_{1ij} - \psi_{1i-1j}) \\ & - ic_{3i}\psi_{1ij}(u_{i+1j} - u_{ij}) \end{aligned}$$

where  $c_{3i} = \omega(\gamma - 1)/[(\gamma + 1)(X_{i+1} - X_{i-1})]$ .

Since the boundary conditions on the wing are satisfied by the flat plate solution, we have

$$\partial\varphi_2/\partial y = 0, \quad -1 \leq x \leq 1, \quad y = 0.$$

The jump condition in  $\varphi_2$  at the trailing edge is treated the same way as the full solution and the wake boundary conditions are identical.

The boundary conditions on the upstream  $x$  boundaries of the mesh for  $\varphi_2$  are obtained from matching the differential operator  $\partial/\partial x + i\omega M/(1-M)$  of the wing with that of the flat plate, i.e.,

$$\varphi_{1x} - i\omega M\varphi_1/(1-M) = \psi_{1x} - i\omega M\psi_1/(1-M)$$

Since  $\varphi_1 = \varphi_2 + \psi_1$ , we have

$$\varphi_{2x} - i\omega M\varphi_2/(1-M) = 0$$

This is the standard outgoing wave boundary condition which we used for the complete solution of  $\varphi_1$ . Thus the mesh boundary conditions for  $\varphi_2$  are the same as for the full perturbation potential.

At hyperbolic points, the flat plate solutions satisfy the elliptic difference equation while the complete potential satisfies

$$\begin{aligned} & c_{i-1}u_{ij}(\varphi_{ij} - \varphi_{i-1j}) - d_{i-1}u_{i-1j}(\varphi_{i-1j} - \varphi_{i-2j}) \\ & - (i\omega/\epsilon) \left[ c_{2i}(\varphi_{ij} - \varphi_{i-1j}) - d_{1i-1}(\varphi_{i-1j} - \varphi_{i-2j}) \right] \\ & + \delta_{yy}\varphi_{ij}/2 + \left[ \omega^2/2\epsilon + c_{3i}(u_{i+1j} - u_{ij}) \right] \varphi_{ij} = 0 \end{aligned}$$

Then substituting  $\varphi = \psi_1 + \varphi_2$  yields

$$\begin{aligned}
& c_{i-1} u_{ij} (\varphi_{2ij} - \varphi_{2i-1j}) - d_{i-1} u_{i-1j} (\varphi_{2i-1j} - \varphi_{2i-2j}) + \delta_{yy} \psi_{1ij} / 2 \\
& - (i\omega/\epsilon) \left[ c_{2i} (\varphi_{2ij} - \varphi_{2i-1j}) - d_{1i-1} (\varphi_{2i-1j} - \psi_{2i-2j}) \right] \\
& + \left[ \omega^2 / 2\epsilon + c_{3i} (u_{i+1j} - u_{ij}) \right] \varphi_{2j} = \\
& - \left\{ c_{i-1} u_{ij} (\psi_{1ij} - \psi_{1i-1j}) - d_{i-1} u_{i-1j} (\psi_{1i-1j} - \psi_{1i-2j}) \right. \\
& - (i\omega/\epsilon) \left[ c_{2i} (\psi_{1ij} - \psi_{1i-1j}) - d_{1i-1} (\psi_{1i-1j} - \psi_{1i-2j}) \right] \\
& \left. + \delta_{yy} \psi_{1ij} / 2 + \left[ \omega^2 / 2\epsilon + c_{3i} (u_{i+1j} - u_{ij}) \right] \psi_{1ij} \right\}
\end{aligned}$$

Since  $\psi_1$  satisfies the flat plate equation, then

$$\begin{aligned}
& \delta_{yy} \psi_{1ij} / 2 + \left( \omega^2 / 2\epsilon \right) \psi_{1ij} = -Kc_i (\psi_{1i+1j} - \psi_{1ij}) - Kd_i (\psi_{1ij} - \psi_{1i-1j}) \\
& + (i\omega/\epsilon) \left[ c_{1i} (\psi_{1i+1j} - \psi_{1ij}) + d_{1i} (\psi_{1ij} - \psi_{1i-1j}) \right]
\end{aligned}$$

and the right hand side becomes

$$\begin{aligned}
\text{RHS(I,J)} &= (Kc_i - i\omega c_{1i} / \epsilon) (\psi_{1i+1j} - \psi_{1ij}) \\
&+ \left[ Kd_i - c_{i-1} u_{ij} - i(\omega/\epsilon) (d_{1i} - c_{2i}) \right] (\psi_{1ij} - \psi_{1i-1j}) \\
&+ (d_{i-1} u_{i-1j} - i\omega d_{1i-1} / \epsilon) (\psi_{1i-1j} - \psi_{1i-2j}) \\
&- c_{3i} (u_{i+1j} - u_{ij}) \psi_{1ij}
\end{aligned}$$

## APPENDIX D

### DERIVATION OF THE ADI METHOD FOR FREQUENCY DOMAIN BASED ON TIME INTEGRATION

To treat the unsteady flow at transonic speeds we separate the potential  $\varphi$  into steady and unsteady potentials

$$\varphi(x,y,t) = \varphi_0(x,y) + \psi(x,y,t) \quad (D-1)$$

The differential equation for  $\varphi$  is given in reference 8 by equation (12) as

$$\left[ K - (\gamma + 1)\varphi_x \right] \varphi_{xx} + \varphi_{yy} - (2\varphi_{xt} + \varphi_{tt}) / \epsilon = 0 \quad (D-2)$$

where we have dropped the terms  $\varphi_t \varphi_{xx}$  and  $\varphi_x \varphi_{xt}$  which have been found to have little effect on the solution. The steady state potential  $\varphi_0$  satisfies equation (D-2) without the last two time derivative terms. Then assuming small unsteady perturbations, we find the linear equation for  $\psi$  on substituting equation (D-1) becomes

$$\left[ K - (\gamma + 1)\varphi_{0x} \right] \psi_{xx} - (\gamma + 1)\psi_x \varphi_{0xx} + \psi_{yy} - (2\psi_{xt} + \psi_{tt}) / \epsilon = 0 \quad (D-3)$$

or

$$\left( u \psi_x \right)_x + \psi_{yy} - (2\psi_{xt} + \psi_{tt}) / \epsilon = 0 \quad (D-4)$$

where

$$u = K - (\gamma + 1)\varphi_{0x} \quad (D-5)$$

The ADI method of Rizzetta and Chin (ref. 19) for solving equation (D-4) is given by two sweeps for each time step. Modifying the difference equations for our particular linear partial differential equation yields

For the x sweep:

$$2\delta_x (\tilde{\psi} - \psi^n) / (\epsilon \Delta t) = \left[ \delta_x (u \delta_x \tilde{\psi}) + \delta_x (u \delta_x \psi^n) \right] / 2 + \delta_{yy} \psi^n \quad (D-6)$$

For the y sweep:

$$\begin{aligned} (\psi^{n+1} - 2\psi^n + \psi^{n-1}) / (\epsilon \Delta t^2) + 2\delta_x (\psi^{n+1} - \tilde{\psi}) / (\epsilon \Delta t) \\ = \delta_{yy} (\psi^{n+1} - \psi^n) / 2 \end{aligned} \quad (D-7)$$

For the boundary conditions on the wing, we use

$$\psi_y = f_x + f_t \quad (D-8)$$

We assume harmonic motion for the airfoil. Then equation (D-8) becomes

$$\psi_y = (f_x + i\omega f)e^{i\omega t} \quad (D-9)$$

We now introduce  $\psi^n = \varphi^n e^{i\omega n \Delta t}$  and the boundary conditions become

$$\varphi_y^n = f_x + i\omega f \quad (D-10)$$

Substituting  $\varphi^n$  into equation (D6) and factoring  $e^{i\omega(n+1)\Delta t}$  lead to the following difference equation for the x sweep:

$$\begin{aligned} & 2\delta_x \tilde{\varphi} / (\epsilon \Delta t) - \delta_x (u \delta_x \tilde{\varphi}) / 2 \\ & = \beta_1 \left[ \delta_x (u \delta_x \varphi^n) / 2 + \delta_{yy} \varphi^n + 2\delta_x \varphi^n / (\epsilon \Delta t) \right] \end{aligned} \quad (D-11)$$

For the y sweep we obtain

$$\begin{aligned} & (\varphi^{n+1} - 2\beta_1 \varphi^n + \beta_1^2 \varphi^{n-1}) / (\epsilon \Delta t^2) + 2\delta_x (\varphi^{n+1} - \tilde{\varphi}) / (\epsilon \Delta t) \\ & = \delta_{yy} (\varphi^{n+1} - \beta_1 \varphi^n) / 2 \end{aligned} \quad (D-12)$$

where

$$\beta_1 = e^{-i\omega \Delta t}$$

### FINITE DIFFERENCE FORMULAS FOR THE X SWEEP

We shall solve equation (D-11) for  $\tilde{\varphi}$ . Hence we write

$$2\delta_x \tilde{\varphi} / (\epsilon \Delta t) - \delta_x (u \delta_x \tilde{\varphi}) / 2 = \beta_1 \left[ 2\delta_x \varphi^n / (\epsilon \Delta t) + \delta_{yy} \varphi^n + \delta_x (u \delta_x \varphi^n) / 2 \right] \quad (D-13)$$

Following Rizzetta and Chin (ref. 19), we shall use a backward or upwind difference for the first derivative with respect to x, and for the remaining space derivatives we shall use the form programmed in A344 and described in reference 8. Thus we have for elliptic points, with

$$c_{4i} = 2 / [\epsilon \Delta t (x_i - x_{i-1})]$$

the difference equation

$$\begin{aligned} & c_{4i} (\tilde{\varphi}_{ij} - \tilde{\varphi}_{i-1j}) - c_i u_{i+1j} (\tilde{\varphi}_{i+1j} - \tilde{\varphi}_{ij}) + d_i u_{ij} (\tilde{\varphi}_{ij} - \tilde{\varphi}_{i-1j}) \\ & = \beta_1 \left[ c_{4i} (\varphi_{ij}^n - \varphi_{i-1j}^n) + 2a_j (\varphi_{ij-1}^n - \varphi_{ij}^n) - 2b_j (\varphi_{ij}^n - \varphi_{ij+1}^n) \right. \\ & \quad \left. + c_i u_{i+1j} (\varphi_{i+1j}^n - \varphi_{ij}^n) - d_i u_{ij} (\varphi_{ij}^n - \varphi_{i-1j}^n) \right] \end{aligned} \quad (D-14)$$

For coding the coefficients we write the equations in the form

$$\text{SUB1(I)} * \tilde{\varphi}_{i-2j} + \text{SUB(I)} * \tilde{\varphi}_{i-1j} + \text{DIAG(I)} * \tilde{\varphi}_{ij} + \text{SUPER(I)} * \tilde{\varphi}_{i+1j} = \text{RHS(I)} \quad (\text{D-15})$$

At elliptic points this becomes

$$\begin{aligned} \text{SUB1(I)} &= 0.0 \\ \text{SUB(I)} &= -c_{4i} - d_i u_{ij} \\ \text{DIAG(I)} &= c_{4i} + c_i u_{i+1j} + d_i u_{ij} \\ \text{SUPER(I)} &= -c_i u_{i+1j} \\ \text{RHS(I)} &= \beta_1 \left[ c_{4i} (\varphi_{ij}^n - \varphi_{i-1j}^n) + 2a_j (\varphi_{ij-1}^n - \varphi_{ij}^n) - 2b_j (\varphi_{ij}^n - \varphi_{ij+1}^n) \right. \\ &\quad \left. + c_i u_{i+1j} (\varphi_{i+1j}^n - \varphi_{ij}^n) - d_i u_{ij} (\varphi_{ij}^n - \varphi_{i-1j}^n) \right] \end{aligned} \quad (\text{D-16})$$

At hyperbolic points we use backward differences for the second derivative terms in  $x$  and the difference equations becomes

$$\begin{aligned} &c_{4i} (\tilde{\varphi}_{ij} - \tilde{\varphi}_{i-1j}) - c_{i-1} u_{ij} (\tilde{\varphi}_{ij} - \tilde{\varphi}_{i-1j}) + d_{i-1} u_{i-1j} (\tilde{\varphi}_{i-1j} - \tilde{\varphi}_{i-2j}) \\ &= \beta_1 \left[ c_{4i} (\varphi_{ij}^n - \varphi_{i-1j}^n) + 2a_j (\varphi_{ij-1}^n - \varphi_{ij}^n) - 2b_j (\varphi_{ij}^n - \varphi_{ij+1}^n) \right. \\ &\quad \left. + c_{i-1} u_{ij} (\varphi_{ij}^n - \varphi_{i-1j}^n) - d_{i-1} u_{i-1j} (\varphi_{i-1j}^n - \varphi_{i-2j}^n) \right] \end{aligned} \quad (\text{D-17})$$

The resulting coefficients in equation (D-15) are

$$\begin{aligned} \text{SUB1(I)} &= -d_{i-1} u_{i-1j} \\ \text{SUB(I)} &= -c_{4i} + c_{i-1} u_{ij} + d_{i-1} u_{i-1j} \\ \text{DIAG(I)} &= c_{4i} - c_{i-1} u_{ij} \\ \text{SUPER(I)} &= 0.0 \\ \text{RHS(I)} &= \beta_1 \left[ c_{4i} (\varphi_{ij}^n - \varphi_{i-1j}^n) + 2a_j (\varphi_{ij-1}^n - \varphi_{ij}^n) - 2b_j (\varphi_{ij}^n - \varphi_{ij+1}^n) \right. \\ &\quad \left. + c_{i-1} u_{ij} (\varphi_{ij}^n - \varphi_{i-1j}^n) - d_{i-1} u_{i-1j} (\varphi_{i-1j}^n - \varphi_{i-2j}^n) \right] \end{aligned} \quad (\text{D-18})$$

## DERIVATION OF MESH BOUNDARY CONDITIONS

For the boundary conditions on the mesh we use the simple nonreflecting boundary conditions derived by Engquist and Majda (ref. 22). For the upstream  $x$  boundary and our particular form of the equation we have

$$\psi_x - M \psi_t / (1 - M) = 0 \quad (D-19)$$

which becomes

$$\left( \psi_{2j}^{n+1/2} - \psi_{1j}^{n+1/2} \right) / (x_2 - x_1) - M \left( \psi_{1+1/2j}^{n+1} - \psi_{1+1/2j}^n \right) / [(1 - M)\Delta t] = 0 \quad (D-20)$$

in which we apply the boundary conditions at  $x = (x_1 + x_2)/2$ . Since

$$\psi^{n+1/2} = (\psi^{n+1} + \psi^n) / 2, \quad \psi_{1+1/2} = (\psi_1 + \psi_2) / 2$$

we have

$$\varphi_{1j}^{n+1} = \bar{c}_{k1} \varphi_{2j}^{n+1} + \chi_j \quad (D-21)$$

where

$$\chi_j = \beta_1 (\varphi_{2j}^n - \bar{c}_{k1} \varphi_{1j}^n)$$

$$\bar{c}_{k1} = (1 - c_{k1}) / (1 + c_{k1})$$

$$c_{k1} = M(x_2 - x_1) / [(1 - M)\Delta t] \quad (D-22)$$

Similarly the lower outgoing wave type boundary condition is

$$\psi_y - M \sqrt{K} \psi_t / (1 - M^2) = 0$$

and we get

$$\left( \psi_{i2}^{n+1/2} - \psi_{i1}^{n+1/2} \right) / (y_2 - y_1) - M \sqrt{K} \left( \psi_{i3/2}^{n+1} - \psi_{i3/2}^n \right) / [(1 - M^2)\Delta t] = 0$$

At  $y = (y_1 + y_2)/2$  this becomes

$$\varphi_{i1}^{n+1} = \bar{c}_{k2} \varphi_{i2}^{n+1} + \chi_1 \quad (D-23)$$

where

$$\begin{aligned}\bar{c}_{k2} &= (1 - c_{k2}) / (1 + c_{k2}) \\ c_{k2} &= M \sqrt{K} (y_2 - y_1) / [(1 - M^2) \Delta t] \\ x_1 &= \beta_1 (\varphi_{i2}^n - \bar{c}_{k2} \varphi_{i1}^n)\end{aligned}\tag{D-24}$$

For the downstream  $x$  boundary, the boundary conditions at  $x = (x_{i\max} + x_{i\max-1})/2$  are

$$\psi_x + M \psi_t / (1 + M) = 0\tag{D-25}$$

which becomes

$$\varphi_{i\max j}^{n+1} = \varphi_{i\max-1 j}^{n+1} \bar{c}_{k3} + x_{4j}\tag{D-26}$$

where

$$\bar{c}_{k3} = (1 - c_{k3}) / (1 + c_{k3})\tag{D-27}$$

$$c_{k3} = M (x_{i\max} - x_{i\max-1}) / [(1 + M) \Delta t]$$

$$x_{4j} = \beta_1 (\varphi_{i\max-1 j}^n - \bar{c}_{k3} \varphi_{i\max j}^n)\tag{D-28}$$

The upper  $y$  mesh outgoing plane wave boundary conditions are

$$\psi_y + M \sqrt{K} \psi_t / (1 - M^2) = 0\tag{D-29}$$

In the same manner the difference form of the boundary conditions is seen to be

$$\varphi_{ij\max}^{n+1} = \bar{c}_{k4} \varphi_{ij\max-1}^{n+1} + x_2\tag{D-30}$$

where

$$c_{k4} = M \sqrt{K} (y_{j\max} - y_{j\max-1}) / [(1 - M^2) \Delta t]$$

$$\bar{c}_{k4} = (1 - c_{k4}) / (1 + c_{k4})\tag{D-31}$$

and

$$x_2 = \beta_1 (\varphi_{ij\max-1}^n - c_{k4} \varphi_{ij\max}^n)\tag{D-32}$$

## APPLICATION OF THE MESH BOUNDARY CONDITIONS TO THE DIFFERENCE EQUATIONS FOR THE X SWEEP

For  $i = 2$ , we apply the upstream  $x$  boundary condition, namely, equation (D-21), which becomes

$$\tilde{\varphi}_{1j} = \bar{c}_{k1} \tilde{\varphi}_{2j} + \chi_0 \quad (D-33)$$

Substitution into equation (D-15) yields, with the aid of equation (D-16)

$$\text{DIAG}(2) = \text{DIAG}(2) + \bar{c}_{k1} \text{SUB}(2) \quad (D-34)$$

$$\text{RHS}(2) = \text{RHS}(2) - \chi_0 \text{SUB}(2)$$

$$\text{SUB}(2) = 0.0 \quad (D-35)$$

where

$$\chi_0 = \beta_1 \left( \varphi_{2j}^n - \bar{c}_{k1} \varphi_{1j}^n \right)$$

Boundary conditions on the upper and lower boundaries have no effect on the  $x$  sweep.

For  $i = i_{\max} - 1$ , we apply the downstream boundary conditions

$$\tilde{\varphi}_{i_{\max}j} = \bar{c}_{k3} \varphi_{i_{\max}-1j} + \chi_3 \quad (D-36)$$

Then we modify DIAG, SUPER, and RHS by

$$\text{DIAG}(I) = \text{DIAG}(I) + \bar{c}_{k3} \text{SUPER}(I)$$

$$\text{RHS}(I) = \text{RHS}(I) - \chi_3 \text{SUPER}(I)$$

$$\text{SUPER}(I) = 0.0 \quad (D-37)$$

for  $I = \text{IMAX} - 1$ . Here,

$$\chi_3 = \beta_1 \left( \varphi_{i_{\max}-1j}^n - \bar{c}_{k3} \varphi_{i_{\max}j} \right)$$

## BOUNDARY CONDITIONS ON THE WING

We apply the boundary conditions on the airfoil at  $y = 0$  which lies halfway between the  $j = j_m$  and the  $j = j_m + 1$   $y$  grid points. We apply the boundary conditions

$$\varphi_y = F_i^L \quad (D-38)$$



where  $F_i^L$  is given by equation (D-10) for the lower surface. In difference form this becomes

$$\left( \varphi_{ij_m+1} - \varphi_{ij_m} \right) / \left( y_{j_m+1} - y_{j_m} \right) = \left( \varphi_{ij_m+1} - \varphi_{ij_m} \right) / h = F_i^L$$

Hence

$$-b_{j_m} \left( \varphi_{ij_m}^n - \varphi_{ij_m+1}^n \right) = b_{j_m} h F_i^L \quad (D-39)$$

where

$$b_j = 1 / \left( y_{j+1} - y_{j-1} \right) \left( y_{j+1} - y_j \right)$$

and

$$h = y_{j_m+1} - y_{j_m}$$

Then the right hand side term is modified by

$$\text{RHS(I)} = \text{RHS(I)} + 2\beta_1 \left( h F_i^L + \varphi_{ij_m}^n - \varphi_{ij_m+1}^n \right) b_{j_m} \quad (D-40)$$

Similarly for  $j = j_m + 1$  we have

$$a_{j_m+1} \left( \varphi_{ij_m}^n - \varphi_{ij_m+1}^n \right) = -a_{j_m+1} h F_i^U \quad (D-41)$$

and the right hand side is modified by

$$\text{RHS(I)} = \text{RHS(I)} - 2\beta_1 a_{j_m+1} \left( h F_i^U + \varphi_{ij_m}^n - \varphi_{ij_m+1}^n \right) \quad (D-42)$$

We apply the same harmonic boundary conditions in the wake as in the A344 program. Thus, the jump in potential across the wake is given by

$$\Delta\varphi(x) = \Delta\varphi_{te} e^{i\omega(x-x_{te})}$$

We add  $\Delta\varphi$  to the  $\varphi_{yy}$  difference to make  $\varphi_y$  continuous across the wake. From equation (D-16) we have for  $j = j_m$

$$\begin{aligned} \text{RHS(I)} = & \beta_1 \left[ c_{4i} \left( \varphi_{ij_m}^n - \varphi_{i-1j_m}^n \right) + 2a_{j_m} \left( \varphi_{ij_m-1}^n - \varphi_{ij_m}^n \right) \right. \\ & - 2b_{j_m} \left( \varphi_{ij_m}^n - \varphi_L^n - \varphi_{ij_m+1}^n + \varphi_U^n \right) + c_i u_{i+1j_m} \left( \varphi_{i+1j_m}^n - \varphi_{ij_m}^n \right) \\ & \left. - d_i u_{ij_m} \left( \varphi_{ij_m}^n - \varphi_{i-1j_m}^n \right) \right] \quad (D-43) \end{aligned}$$

Defining  $\Delta\varphi_i^n = \varphi_U^n - \varphi_L^n$ , we obtain

$$\text{RHS(I)} = \text{RHS(I)} - 2\beta_1 b_{j_m} \Delta\varphi_i^n$$

Similarly, for  $j = j_m + 1$ .

$$\text{RHS}(I) = \text{RHS}(I) + 2\beta_1 a_{j_m+1} \Delta \varphi_i^n \quad (\text{D-44})$$

The boundary conditions on the wing for hyperbolic points are the same as for elliptic points, and all mesh boundary conditions are subsonic.

### DIFFERENCE EQUATIONS FOR THE Y SWEEP

We solve the difference equation (D-12) for the  $n+1$  time step. Thus we rewrite equation (D-12) in the form

$$\begin{aligned} & \delta_{yy} \varphi^{n+1} / 2 - \varphi^{n+1} / (\epsilon \Delta t^2) - 2\delta_x \varphi^{n+1} / (\epsilon \Delta t) \\ & = \beta_1 \left[ \delta_{yy} \varphi^n / 2 + (\beta_1 \varphi^{n-1} - 2\varphi^n) / (\epsilon \Delta t^2) \right] - 2\delta_x \tilde{\varphi} / (\epsilon \Delta t) \end{aligned}$$

Writing out the differences, we get

$$\begin{aligned} & a_j (\varphi_{ij-1}^{n+1} - \varphi_{ij}^{n+1}) - b_j (\varphi_{ij}^{n+1} - \varphi_{ij+1}^{n+1}) - E_1 \varphi_{ij}^{n+1} - c_{4i} (\varphi_{ij}^{n+1} - \varphi_{i-1j}^{n+1}) \\ & = -c_{4i} (\tilde{\varphi}_{ij} - \tilde{\varphi}_{i-1j}) + \beta_1 \left[ a_j (\varphi_{ij-1}^n - \varphi_{ij}^n) - b_j (\varphi_{ij}^n - \varphi_{ij+1}^n) \right. \\ & \quad \left. - 2E_1 \varphi_{ij}^n + \beta_1 E_1 \varphi_{ij}^{n-1} \right] \end{aligned} \quad (\text{D-45})$$

where  $c_{4i} = 2/[\epsilon \Delta t(x_i - x_{i-1})]$ ,  $E_1 = 1/(\epsilon \Delta t^2)$  and  $\beta_1 = e^{-i\omega \Delta t}$

In the same manner as in the x sweep we define the coefficients

$$\text{SUB}(J) * \varphi_{ij-1}^{n+1} + \text{DIAG}(J) * \varphi_{ij}^{n+1} + \text{SUPER}(J) * \varphi_{ij+1}^{n+1} = \text{RHS}(J) \quad (\text{D-46})$$

Then

$$\begin{aligned} \text{SUB}(J) &= a_j \\ \text{DIAG}(J) &= -a_j - b_j - E_1 - c_{4i} \\ \text{SUPER}(J) &= b_j \\ \text{RHS}(J) &= -c_{4i} (\tilde{\varphi}_{ij} - \tilde{\varphi}_{i-1j}) + \beta_1 \left[ a_j (\varphi_{ij-1}^n - \varphi_{ij}^n) \right. \\ & \quad \left. - b_j (\varphi_{ij}^n - \varphi_{ij+1}^n) - 2E_1 \varphi_{ij}^n + \beta_1 E_1 \varphi_{ij}^{n-1} \right] - c_{4i} \varphi_{i-1j}^{n+1} \end{aligned} \quad (\text{D-47})$$

Note that the right-hand side contains a term of the  $n+1$  step. Since we are sweeping in the direction of increasing  $i$ , this term is known from the previous column solution. This sweep replaces the values of  $\tilde{\varphi}$  by the values of  $\varphi^{n+1}$ . Hence the old values of  $\tilde{\varphi}_{i-1j}$  must be saved before written over by the  $n+1$  value of  $\varphi_{i-1j}$  prior to going to the  $i$ th column calculations.

#### APPLICATION OF THE MESH BOUNDARY CONDITIONS FOR THE Y SWEEP

For boundary conditions on upstream boundary,  $i + 2$ , we have from equation (D-23)

$$\varphi_{1j}^{n+1} = \varphi_{2j}^{n+1} \bar{c}_{k1} + \chi_j \quad (D-48)$$

where

$$\chi_j = \beta_1 \left( \varphi_{2j}^n - \bar{c}_{k1} \varphi_{1j}^n \right)$$

Substituting into equations (D-46) and (D-47) modifies the coefficients according to

$$\text{DIAG}(J) = \text{DIAG}(J) + \bar{c}_{k1} c_{42}$$

$$\text{RHS}(J) = \text{RHS}(J) - c_{42} \chi_j + c_{42} \varphi_{1j}^{n+1}$$

The last term is to correct for the last term in  $\text{RHS}(J)$  in equation (D47).

For the revised coefficients on the lower mesh boundary,  $j = 2$ , we substitute the boundary conditions

$$\varphi_{i1}^{n+1} = \varphi_{i2}^{n+1} \bar{c}_{k2} + \chi_1$$

into equation (D-45) and modify the coefficients in equation (D-46) according to

$$\text{DIAG}(2) = \text{DIAG}(2) + \bar{c}_{k2} \text{SUB}(2)$$

$$\text{RHS}(2) = \text{RHS}(2) - \text{SUB}(2) \chi_1 \quad D-49)$$

where

$$\text{SUB}(2) = 0.0$$

For the revised coefficients on the upper mesh boundary,  $j = j_{\max} - 1$ , we substitute the boundary conditions

$$\varphi_{ij_{\max}}^{n+1} = \varphi_{ij_{\max}-1}^{n+1} \bar{c}_{k4} + \chi_2$$

into equation (D-45) and then modify the coefficients in equation (D-47) according to

$$\begin{aligned} \text{DIAG}(\text{JMAX} - 1) &= \text{DIAG}(\text{JMAX} - 1) + \text{SUPER}(\text{JMAX} - 1) \bar{c}_{k4} \\ \text{RHS}(\text{JMAX} - 1) &= \text{RHS}(\text{JMAX} - 1) - \text{SUPER}(\text{JMAX} - 1) \chi_2 \\ \text{SUPER}(\text{JMAX} - 1) &= 0.0 \end{aligned} \quad (\text{D-50})$$

where

$$\chi_2 = \beta_1 \left( \varphi_{ij_{\max}-1}^n - \bar{c}_{k4} \varphi_{ij_{\max}}^n \right)$$

The difference equation is not affected by the downstream boundary conditions. However, since all mesh boundary values of  $\varphi$  must be computed after each sweep we need to use equations (D-25) and (D-27) to find  $\varphi_{i_{\max}j}$ .

For the revised coefficients for the airfoil boundary conditions, we apply the boundary conditions of equations (D-39) to equation (D-43). This yields for the second term of equations (D-45) at  $j = j_m$

$$-b_{j_m} \left( \varphi_{ij_m}^{n+1} - \varphi_{ij_m+1}^{n+1} \right) = b_{j_m} h F_i^L \quad (\text{D-51})$$

This term then contributes to the RHS term with a change of sign and eliminates terms from DIAG and SUPER. A term similar to equation (D51) is obtained from the right-hand side of equation (D-45). Thus the coefficients in equation (D-47) are modified by

$$\begin{aligned} \text{DIAG}(\text{JM}) &= \text{DIAG}(\text{JM}) + b_{j_m} \\ \text{SUPER}(\text{JM}) &= 0.0 \\ \text{RHS}(\text{JM}) &= \text{RHS}(\text{JM}) + b_{j_m} \left[ \beta_1 \left( h F_i^L + \varphi_{ij_m}^n - \varphi_{ij_m+1}^n \right) - h F_i^L \right] \end{aligned} \quad (\text{D-52})$$

We now consider the terms for the upper airfoil boundary,  $j = j_m + 1$ . From equation (D-41), we have

$$a_{j_m+1} \left( \varphi_{ij_m}^{n+1} - \varphi_{ij_m+1}^{n+1} \right) = -a_{j_m+1} h F_i^u \quad (\text{D-53})$$

This again contributes an additional term to the right-hand side. Applying equation (D-53) the right hand side of equation (D-47) yields

$$\text{DIAG}(\text{JM} + 1) = \text{DIAG}(\text{JM} + 1) + a_{j_m+1}$$

$$\text{SUB}(\text{JM} + 1) = 0.0$$

$$\text{RHS}(\text{JM} + 1) = \text{RHS}(\text{JM} + 1) - a_{j_m+1} \left[ \beta_1 \left( h F_i^u + \varphi_{ij_m}^n - \varphi_{ij_m+1}^n \right) - h F_i^u \right] \quad (\text{D-54})$$

For  $j = j_m$  and  $j = j_m + 1$ , we must also revise the coefficients for the wake boundary condition. For  $j = j_m$ , we obtain for the second term of equation (D-45)

$$- b_{j_m} \left( \varphi_{ij_m}^{n+1} - \varphi_L^{n+1} + \varphi_u^{n+1} - \varphi_{ij_m+1}^{n+1} \right) = - b_{j_m} \left( \varphi_{ij_m}^{n+1} - \varphi_{ij_m+1}^{n+1} \right) - b_{j_m} \Delta \varphi_i^{n+1} \quad (\text{D-55})$$

This adds  $b_{j_m} \Delta \varphi_i^{n+1}$  to the RHS term. Also applying equation (D55) to the similar terms of the RHS in equation (D-47), we obtain for the modified right-hand side

$$\text{RHS}(\text{JM}) = \text{RHS}(\text{JM}) + b_{j_m} \left( \Delta \varphi_i^{n+1} - \beta_1 \Delta \varphi_i^n \right) \quad (\text{D-56})$$

Similarly for  $j = j_m + 1$ , we get

$$\text{RHS}(\text{JM} + 1) = \text{RHS}(\text{JM} + 1) - a_{j_m+1} \left( \Delta \varphi_i^{n+1} - \beta_1 \Delta \varphi_i^n \right) \quad (\text{D-57})$$

## STABILITY ANALYSIS OF THE METHOD FOR SMALL FREQUENCY

Because of the three steps in time required by the  $\varphi_{tt}$  term, a von Neumann stability analysis of the difference equations (D-11) and (D-12) is difficult and has not been made. Dropping the  $\varphi_{tt}$  term is equivalent to assuming small frequency. The corresponding frequency domain method was derived by Traci, Albano, and Farr (refs. 26, 27) and was solved using the relaxation technique. Their difference equations have the same frequency limitation as our equations. Since a stability analysis of the equation neglecting the term  $\varphi_{tt}$  is simple we shall analyze the difference equations (D-11) and (D-12) with the first term of equation (D-12) deleted, or

$$2\delta_x \tilde{\varphi} / (\epsilon \Delta t) - \delta_x (u \delta_x \tilde{\varphi}) / 2 = \beta_1 \left[ 2\delta_x \varphi^n / (\epsilon \Delta t) + \delta_x (u \delta_x \varphi^n) / 2 + \delta_{yy} \varphi^n \right] \quad (\text{D-58})$$

$$2\delta_x \varphi^{n+1} / (\epsilon \Delta t) - \delta_{yy} \varphi^{n+1} / 2 = 2\delta_x \tilde{\varphi} / (\epsilon \Delta t) - \beta_1 \delta_{yy} \varphi^n / 2 \quad (\text{D-59})$$

The error in  $\varphi^n$  for equally spaced points in the grid may be represented by an expression of the form

$$E_{kj}^n = \sum_{\ell, m} a_{\ell m}^n \exp[i(k\ell\pi\Delta x/a + jm\Delta/b)]$$

and the stability of each component will be examined separately. Now, we have for the flat plate,

$$2\delta_x \varphi^n / \epsilon \Delta t \sim \alpha_1 \left[ 1 - \exp(-i\pi \ell \Delta x / a) \right] \quad (D-60)$$

$$\delta_x (u \delta_x \varphi^n) = K \left( \varphi_{i+1j}^n - 2\varphi_{ij}^n + \varphi_{i-1j}^n \right) / \Delta x^2 \sim -2\alpha_2 \varphi^n \quad (D-61)$$

where

$$\alpha_1 = 2/(\epsilon \Delta t \Delta x), \quad \alpha_2 = K \left( 1 - \cos \frac{\ell \pi \Delta x}{a} \right) / \Delta x^2$$

and an exponential factor common to all terms is not written. Similarly

$$\delta_{yy} \varphi^n \simeq -2\alpha_3 \varphi^n \quad (D-62)$$

where  $\alpha_3 = (1 - \cos m\pi\Delta y/b)/\Delta y^2$ . With equations (D-60), (D-61), and (D-62) substituted into equations (D-58) and (D-59), we obtain, with

$$\begin{aligned} \tilde{\varphi} \left[ \alpha_1 \left( 1 - e^{-i\theta_1} \right) + \alpha_2 \right] &= \beta_1 \varphi^n \left[ \alpha_1 \left( 1 - e^{-i\theta_1} \right) - \alpha_2 - 2\alpha_3 \right] \\ \varphi^{n+1} \left[ \alpha_1 \left( 1 - e^{-i\theta_1} \right) + \alpha_2 \right] &= \alpha_1 \left( 1 - e^{i\theta_1} \right) \tilde{\varphi} + \beta_1 \alpha_3 \varphi^n \end{aligned}$$

where  $\theta_1 = \pi \Delta x/a$ .

Eliminating  $\tilde{\varphi}$  from the second equation by means of the first yields the following relation for the amplification factor, after some algebraic manipulations,

$$\varphi^{n+1} / \varphi^n = \beta_1 \left\{ \frac{\alpha_1 (1 - e^{-i\theta_1}) - \alpha_2}{\alpha_1 (1 - e^{-i\theta_1}) + \alpha_2} \right\} \left\{ \frac{\alpha_1 (1 - e^{-i\theta}) - \alpha_3}{\alpha_1 (1 - e^{-i\theta}) + \alpha_3} \right\}$$

The magnitude of  $\beta_1$  is unity and the magnitude of the two factors in curly brackets is seen to be less than unity since they are of the form

$$[(a-b) - ic] / [(a+b) - ic]$$

for  $a, b, c$  positive and real. Thus the time dependent method equivalent to the relaxation method of Traci, Albano, and Farr (ref. 26) converges for all frequencies. Since the time dependent method of Rizzetta and Chin has been found to be stable for a wide range of frequencies it appears that the ADI method for harmonic motion described by equation (D-11) and (D-12) is also convergent for all frequencies.

## REFERENCES

1. Ashley, H.: "On the Role of Shocks in the 'Sub-Transonic' Flutter Phenomenon." AIAA Journal, Vol. 17, No. 3, March 1980, pp. 187-197.
2. Magnus, R.; and Yoshihara, M.: "Calculations of Transonic Flow Over an Oscillating Airfoil." AIAA Paper No. 75-98, January 1975.
3. Beam, R.M.; and Warming, R.E.: "Numerical Calculations of Two-Dimensional Unsteady Transonic Flows with Circulation." NASA TN D-7605, February 1974.
4. Ballhaus, W.F.; and Goorjian, P.M.: "Implicit Finite-difference Computations of Unsteady Transonic Flows About Airfoils." AIAA Journal, Vol. 15, No. 12, December 1977, pp. 1728-1735.
5. Borland, C.; Rizzetta, D.; Yoshihara, H.: "Numerical Solution of Three-Dimensional Unsteady Transonic Flow Over Swept Wings." AIAA Paper No. 80-1369, July 1980.
6. Rizzetta, D.; and Yoshihara, H.: "Computations of the Pitching Oscillation of a NACA 64A010 Airfoil in the Small Disturbance Limit." AIAA Paper No. 80-0128, January 1980.
7. Rizzetta, D.; and Yoshihara, H.: "Oscillation Supercritical Airfoils in the Transonic Regime with Viscous Interactions." AGARD Conference, Aix-de-Provence, September 1980.
8. Ehlers, F.E.: "A Finite Difference Method for the Solution of the Transonic Flow Around Harmonically Oscillating Wings." NASA CR-2257, January 1974.
9. Weatherill, W.H.; Ehlers, F.E.; and Sebastian, J.D.: "Computation of the Transonic Perturbation Flow Fields Around Two- and Three-Dimensional Oscillating Wings." NASA CR-2599, December 1975.
10. Weatherill, W.H.; Sebastian, J.D.; and Ehlers, F.E.: "The Practical Application of a Finite Difference Method for Analyzing Transonic Flow Over Oscillating Airfoils and Wings." NASA CR-2933, 1978.
11. Ehlers, F.E.; Sebastian, J.D.; and Weatherill, W.H.: "An Investigation of Several Factors Involved in a Finite Difference Procedure for Analyzing the Transonic Flow About Oscillating Airfoils and Wings." NASA CR-159143, 1979.
12. Weatherill, W.H.; and Ehlers, F.E.: "A User's Guide for A344 - A Program Using a Finite Difference Method to Analyze Transonic Flow Over Oscillating Airfoils." NASA CR-159141, 1979.
13. Weatherill, W.H.; Ehlers, F.E.; Yip, E.; and Sebastian, J.D.: "Further Investigation of a Finite Difference Procedure for Analyzing the Transonic Flow About Harmonically Oscillating Airfoils and Wings." NASA CR-3195, 1980.

14. Davis, S.S.; and Malcolm, G.N.: "Experimental Unsteady Aerodynamics of Conventional and Supercritical Airfoils." NASA TM 81221, August 1980.
15. Isogai, K.: "Numerical Study of Transonic Flutter of a Two Dimensional Airfoil." NAL TR-617T, National Aerospace Inst., Tokyo, Japan, July 1980. See also "Transonic Dip Mechanism of flutter of a Sweptback Wing: Part II," AIAA Journal, Vol. 19, No. 9, September 1981, pp. 1240, 1241
16. Murman, E.M.; and Cole, J.D.: "Calculation of Plane Steady Transonic Flow." AIAA Journal, Vol. 9, January 1971, pp. 114-121.
17. Krupp, J.A.; and Murman, E.M.: "Computation of Transonic Flows Past Lifting Airfoils and Slender Bodies." AIAA Journal, Vol. 10, July 1972, pp. 880-887.
18. Stahara, S.S.: "Operational Manual for Two-Dimensional Transonic Code TSFOIL." NASA CR-3064, December 1973.
19. Rizzetta, D.P.; Chin, W.C.: "Effect of Frequency in Unsteady Transonic Flow." AIAA Journal, Vol. 117, July 1979, p. 779-781.
20. Jou, W-H.; and Murman, E.M.: "A Phenomenological Model for Displacement Thickness Effects of Transonic Shock Wave-Boundary Layer Interactions," AGARD Conference, Colorado Springs, Colorado, September 29, 1980.
21. Klunker, E.B.: "Contribution to Methods for Calculating the Flow About Thin Lifting Wings at Transonic Speeds - Analytic Expressions for the Far Field." NASA TN D-6530, 1971.
22. Engquist, B.; and Majda, A.: "Radiation Boundary Conditions for Acoustic and Elastic Wave Calculations." Communications on Pure and Applied Mathematics, Vol. 32, May 1979, pp. 313-357.
23. Yip, E.L.: "FORTRAN Subroutines for Out-of-Core Solutions of Large Complex Linear Systems." NASA CR-159142, December 1979.
24. Tijdeman, H.: "Investigations of the Transonic Flow Around Oscillating Airfoils." NLR TR 77090 Nat. Aerosp. Lab. (Amsterdam), 1977. (Available from DTIC as AD B027 633.)
25. McGrew, J.A.; Giesing, J.P.; Pearson, R.M.; Zuhuruddin, K.; Schmidt, M.; and Kalman, T.P.: "Supercritical Wing Flutter." AFFDL-TR-78-37, March 1978.
26. Traci, R.M.; Albano, E.D.; and Farr, J.L., Jr.: "Small Disturbance Transonic Flows About Oscillating Airfoils and Planar Wings." AFFDL-TR-75-100, August 1975.
27. Traci, R.M.; Albano, E.D.; and Farr, J.L. Jr.: "Perturbation Method for Transonic Flows About Oscillating Airfoils." AIAA Journal, Vol. 14, No. 9, September 1975, pp. 1258-1265.
28. Hafez, M.M.; Rizk, M.H.; and Murman, E.M.: "Numerical Solution of the Unsteady Transonic Small-Disturbance Equations." Paper presented at the 44th Meeting of the Structures and Materials Panel of AGARD, Lisbon, Portugal, 17-22 April 1977.



29. Williams, M.H.: "Linearization of Unsteady Transonic Flows Containing Shocks." AIAA Journal, Vol. 17, April 1979, p. 394.
30. Seebass, A.R.; Yu, N.J.; and Fung, K-Y.: "Unsteady Transonic Flow Computations." Unsteady Aerodynamics, AGARD Conference Proceedings No. 227, September 1977.
31. Yang, T.Y.; Striz, A.G.; and Guruswamy, P.: "Flutter Analysis of a Two-Degree-of-Freedom MBB A-3 Supercritical Airfoil in Two-Dimensional Transonic Flow." AIAA Paper No. 80-0736, May 1980.
32. Yang, T.Y.; Guruswamy, P.; Striz, A.G.; and Olsen, J.J.: "Flutter Analysis of a NACA 64A006 Airfoil in Small Disturbance Transonic Flow." AIAA Journal of Aircraft, Vol. 17, No. 4, April 1980 pp. 225-232.
33. Bisplinghoff, R.L.; Ashley, H.; and Halfman, R.L.: "Aeroelasticity." Addison Wesley Publishing Co., Cambridge, Mass., 1955.
34. Kwak, D.: "Non-Reflecting Far-Field Boundary Conditions for Unsteady Transonic Flow Computation." AIAA Paper No. 80-1393, July 1980.
35. Rowe, W.S.; Winther, B.A.; and Redman, M.C.: "Prediction of Unsteady Aerodynamic Loadings Caused by Trailing Edge Control Surface Motions in Subsonic Compressible Flow - Analysis and Results." NASA CR-2003, March 1972.
36. Redman, M.C.; Rowe, W.S.; and Winther, B.A.: "Prediction of Unsteady Aerodynamic Loadings Caused by Trailing Edge Control Surface Motions in Subsonic Compressible Flow - Computer Program Description." NASA CR-112015, March 1972.

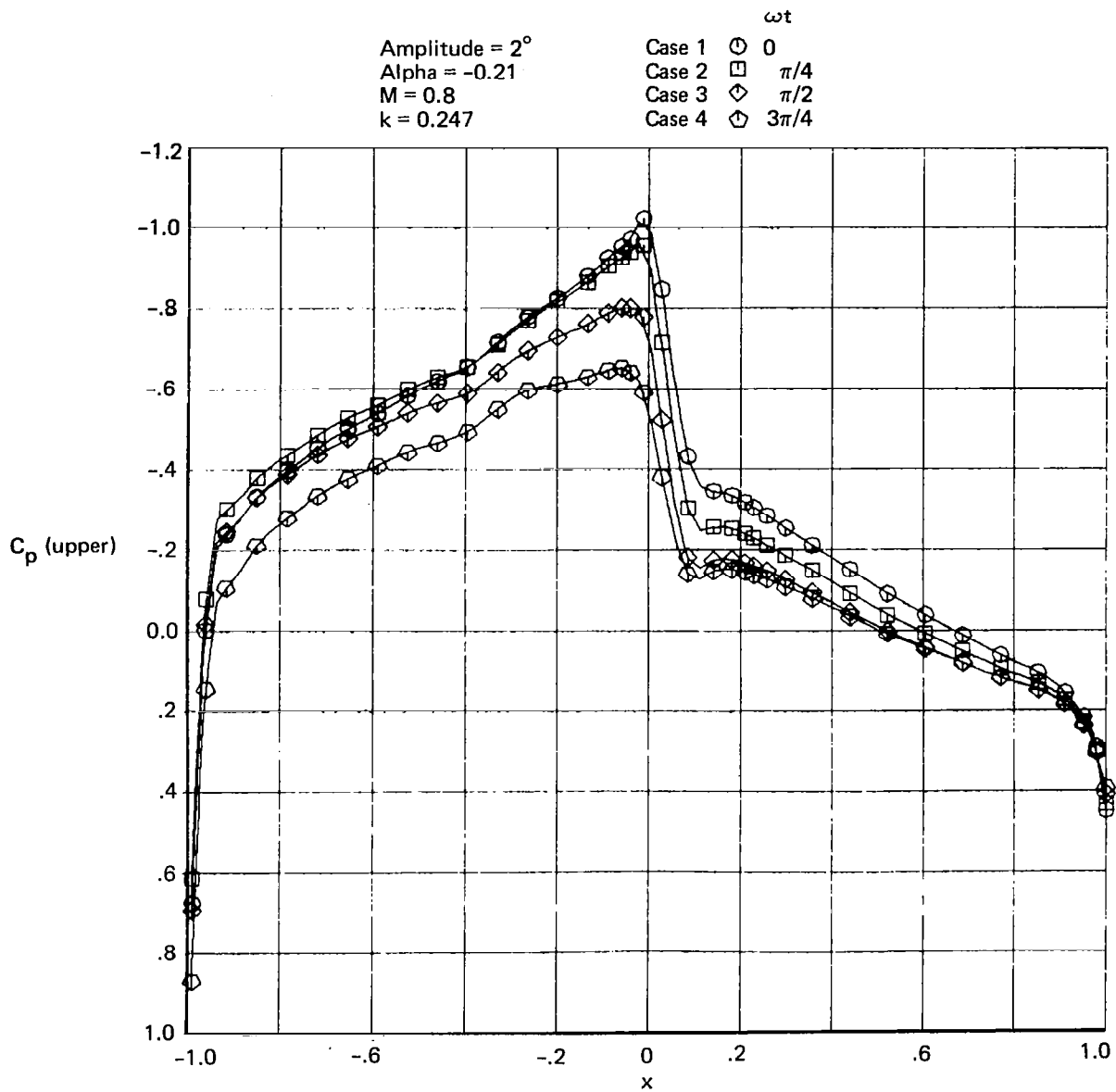


Figure 1.—Instantaneous Unsteady Pressure Distribution on the Upper Surface of a Pitching NACA 64A010 Airfoil Computed From the Harmonic Solution

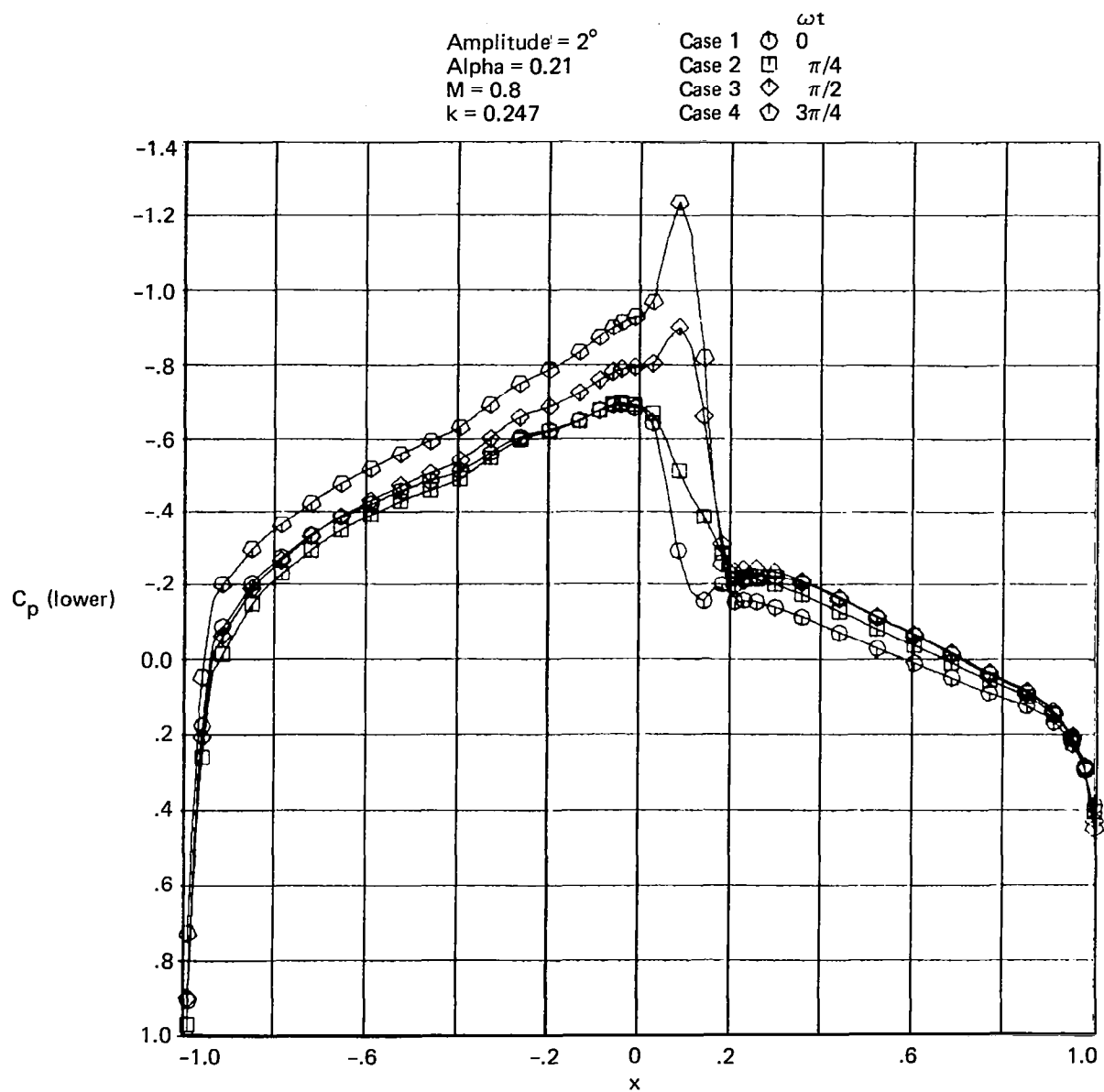


Figure 2.—Instantaneous Unsteady Pressure Distribution on the Lower Surface of a Pitching NACA 64A010 Airfoil Computed From the Harmonic Solution

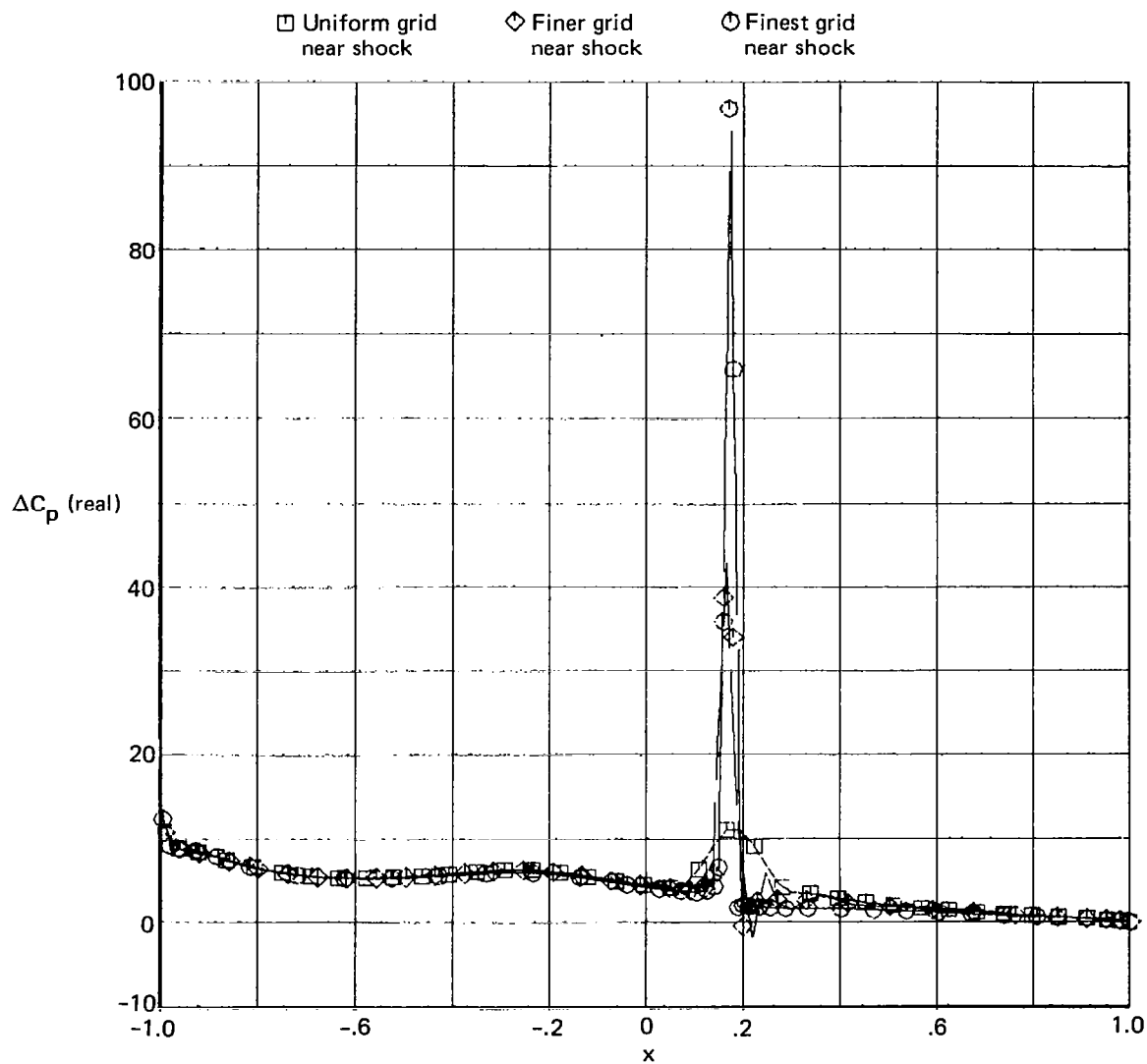


Figure 3.—Influence of Grid Refinement on the Real Part of the Pressure Pulse, NACA 64A010 Airfoil Oscillating in Pitch About the Quarter-Chord Point,  $M=0.8$ ,  $k=0.3$

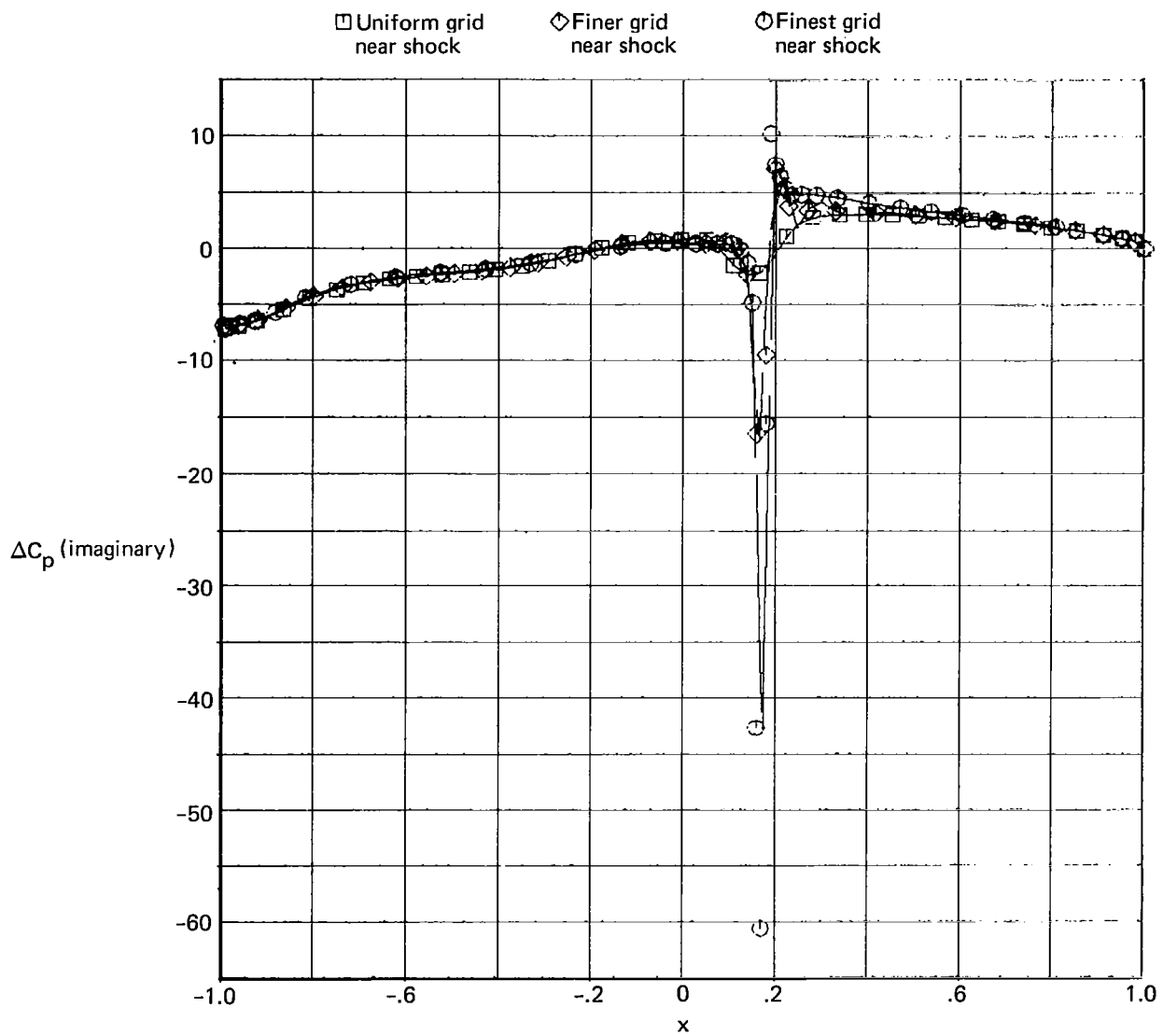


Figure 4.—Influence of Grid Refinement on the Imaginary Part of the Pressure Pulse, NACA 64A010 Airfoil Oscillating in Pitch About the Quarter-Chord Point,  $M=0.8$ ,  $k=0.3$

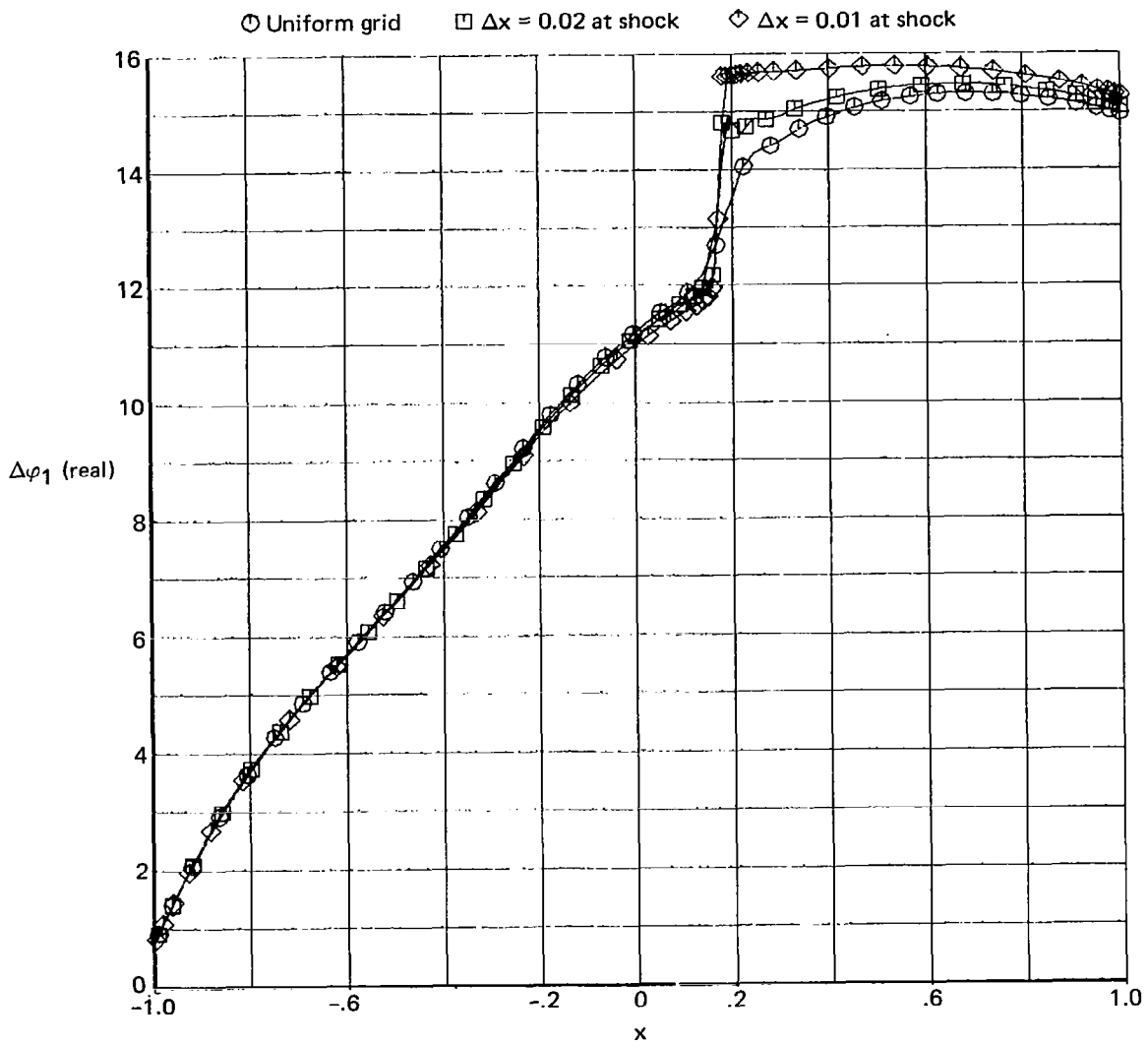


Figure 5.—Influence of Grid Refinement on the Jump in Real Part of Unsteady Potential Across a NACA 64A010 Airfoil Oscillating in Pitch About the Quarter-Chord Point,  $M=0.8$ ,  $k=0.3$

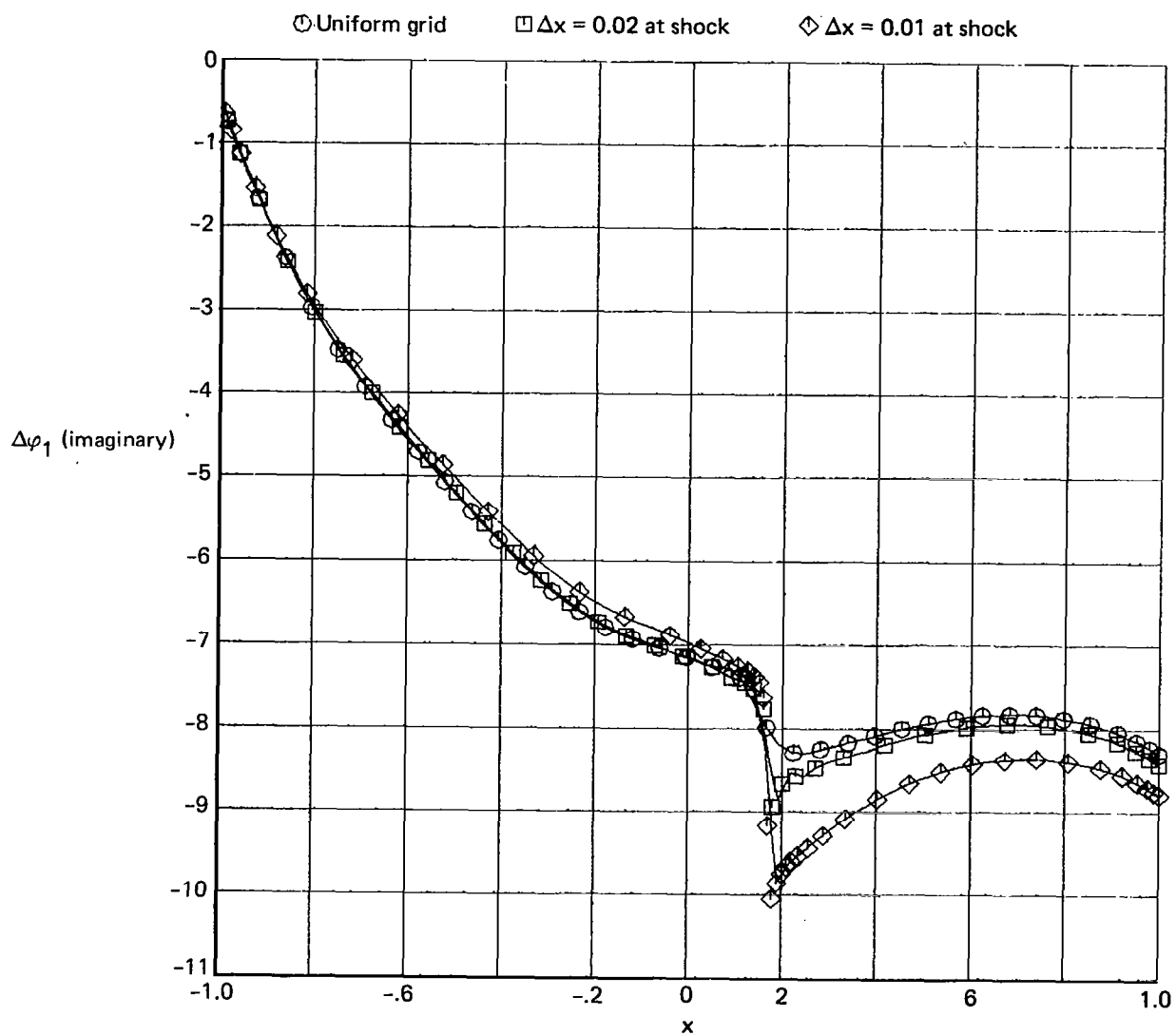


Figure 6.—Influence of Grid Refinement on the Jump in Imaginary Part of Unsteady Potential Across a NACA 64A010 Airfoil Oscillating in Pitch About the Quarter-Chord Point,  $M=0.8, k=0.3$

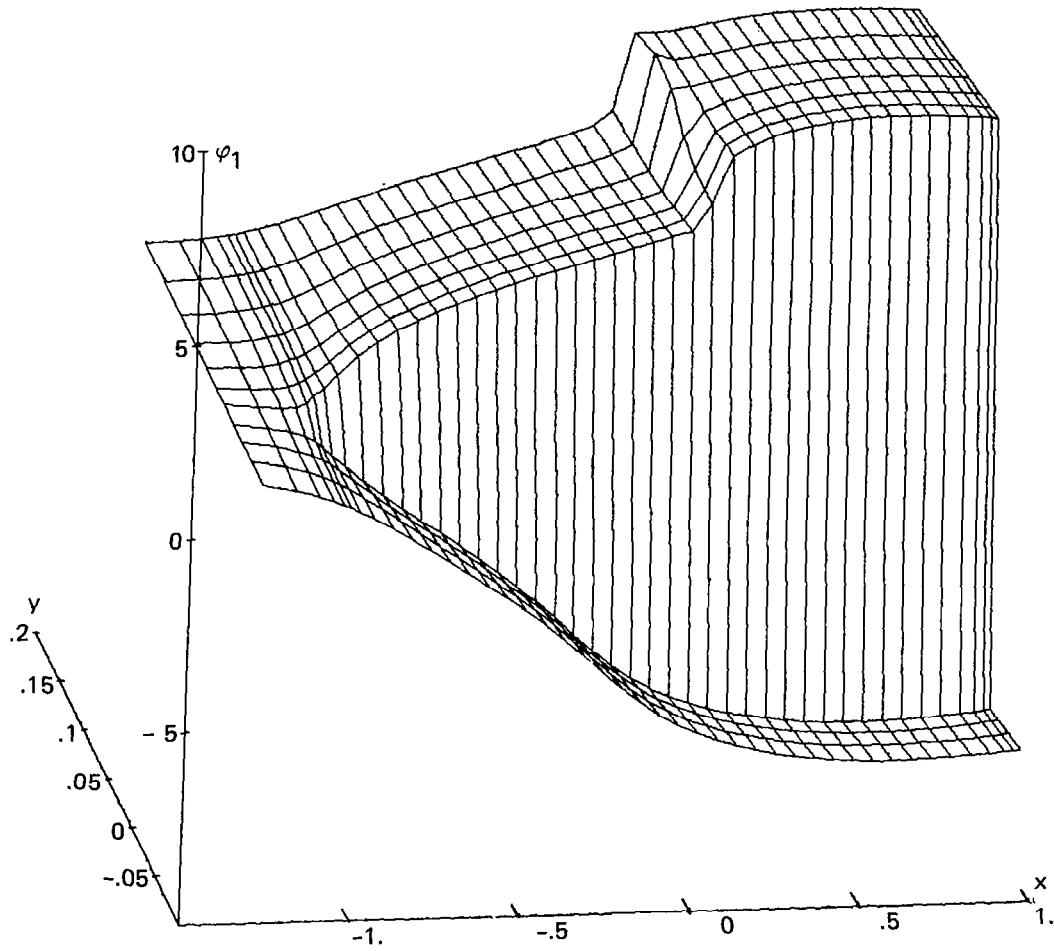
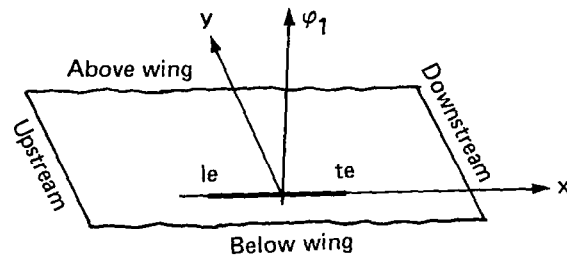


Figure 7.—Three-Dimensional Surface Representation of Real Part of Unsteady Potential, Coarse Grid,  $M=0.8, k=0.3, \alpha_m=1^\circ$



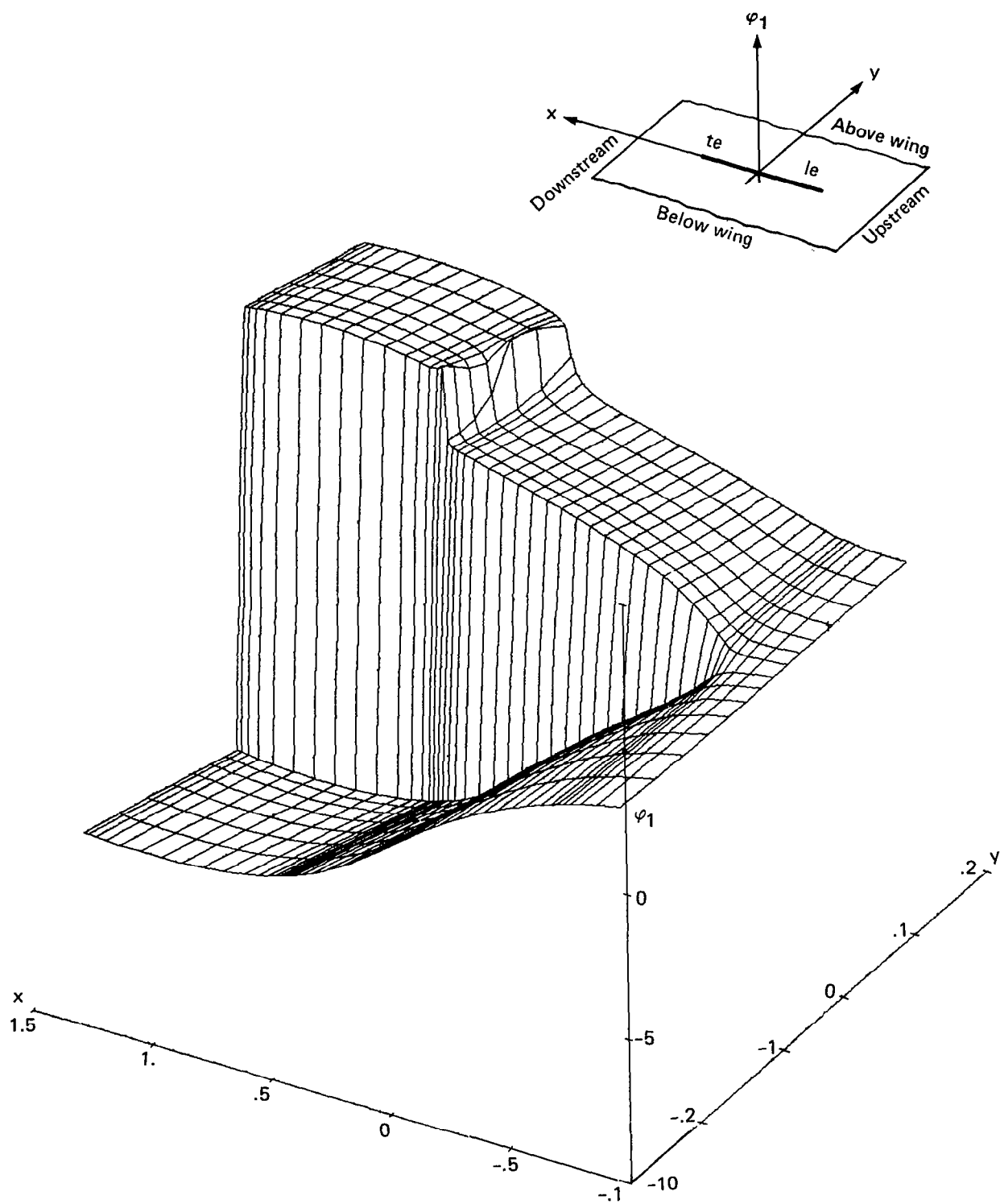


Figure 8.—Three-Dimensional Surface Representation of Imaginary Part of Unsteady Potential, Finer Grid,  $M=0.8$ ,  $k=0.3$ ,  $\alpha_m=1^\circ$

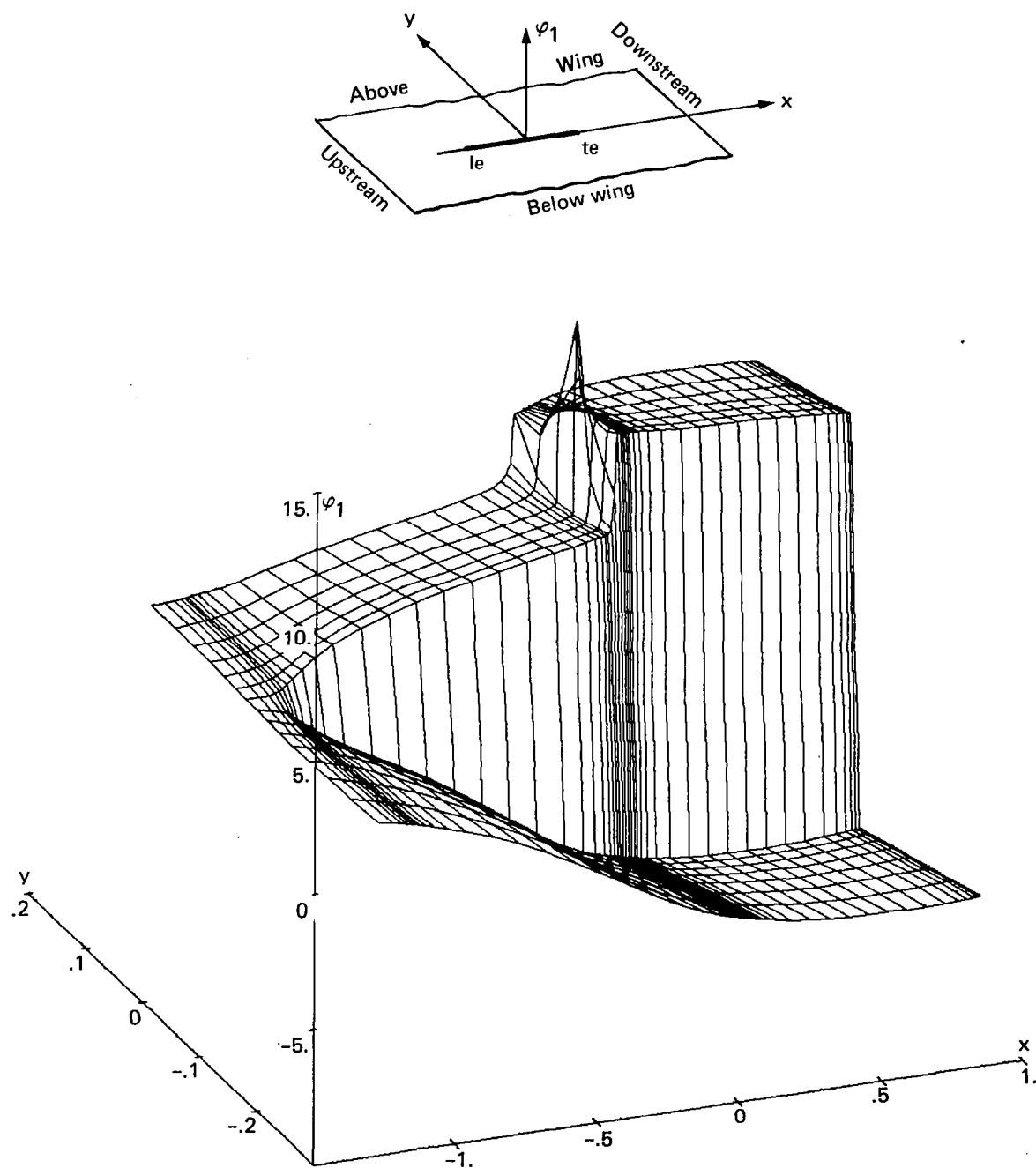


Figure 9.—Three-Dimensional Surface Representation of Imaginary Part of Unsteady Potential, Finest Grid,  $M=0.8$ ,  $k=0.3$ ,  $\alpha_m=1^\circ$

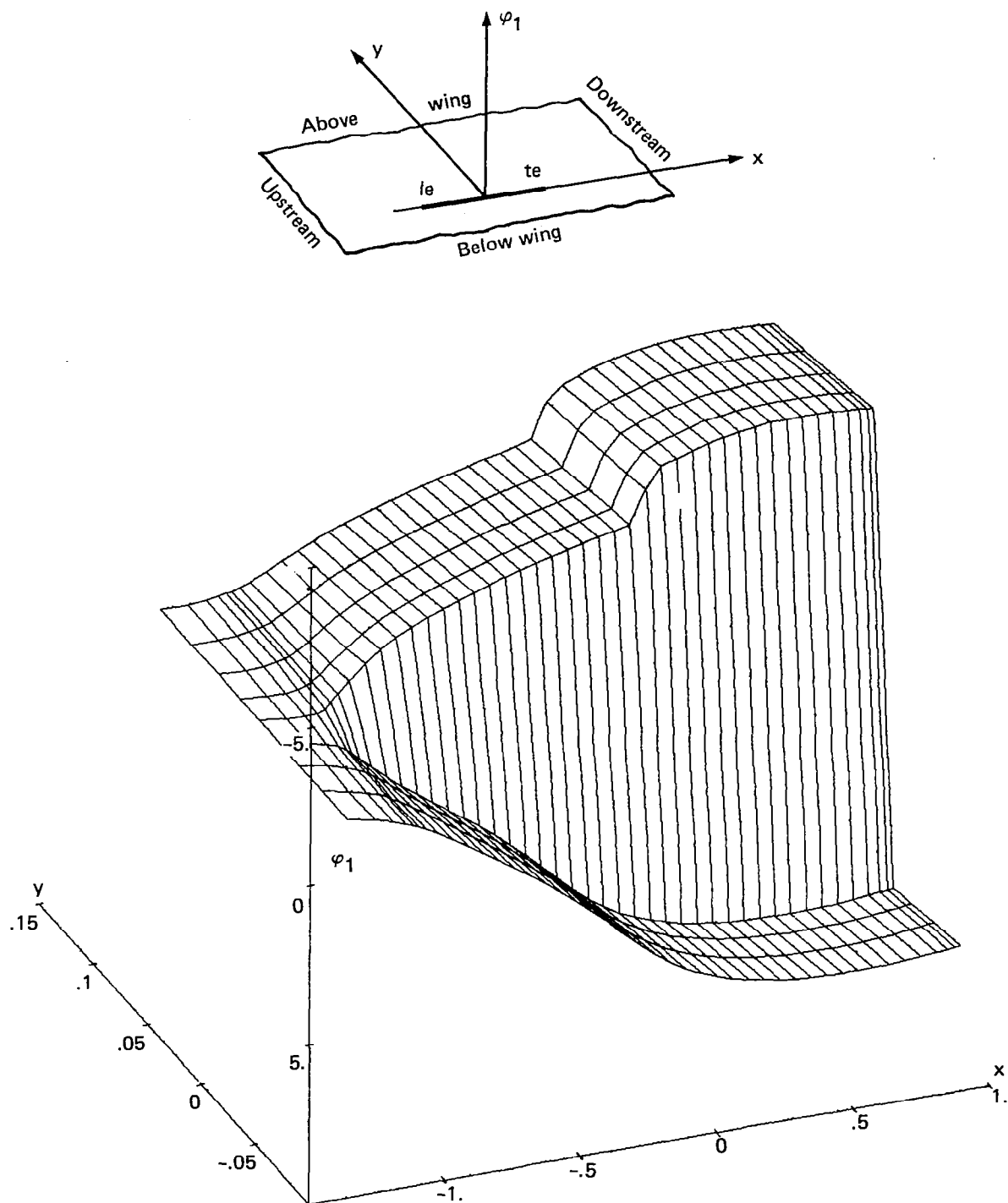


Figure 10.—Three-Dimensional Surface Representation of Real Part of Unsteady Potential for Solution With Coarse Grid and First Form of the Shock Point Operator,  $M=0.8, k=0.3, \alpha_m=1^\circ$

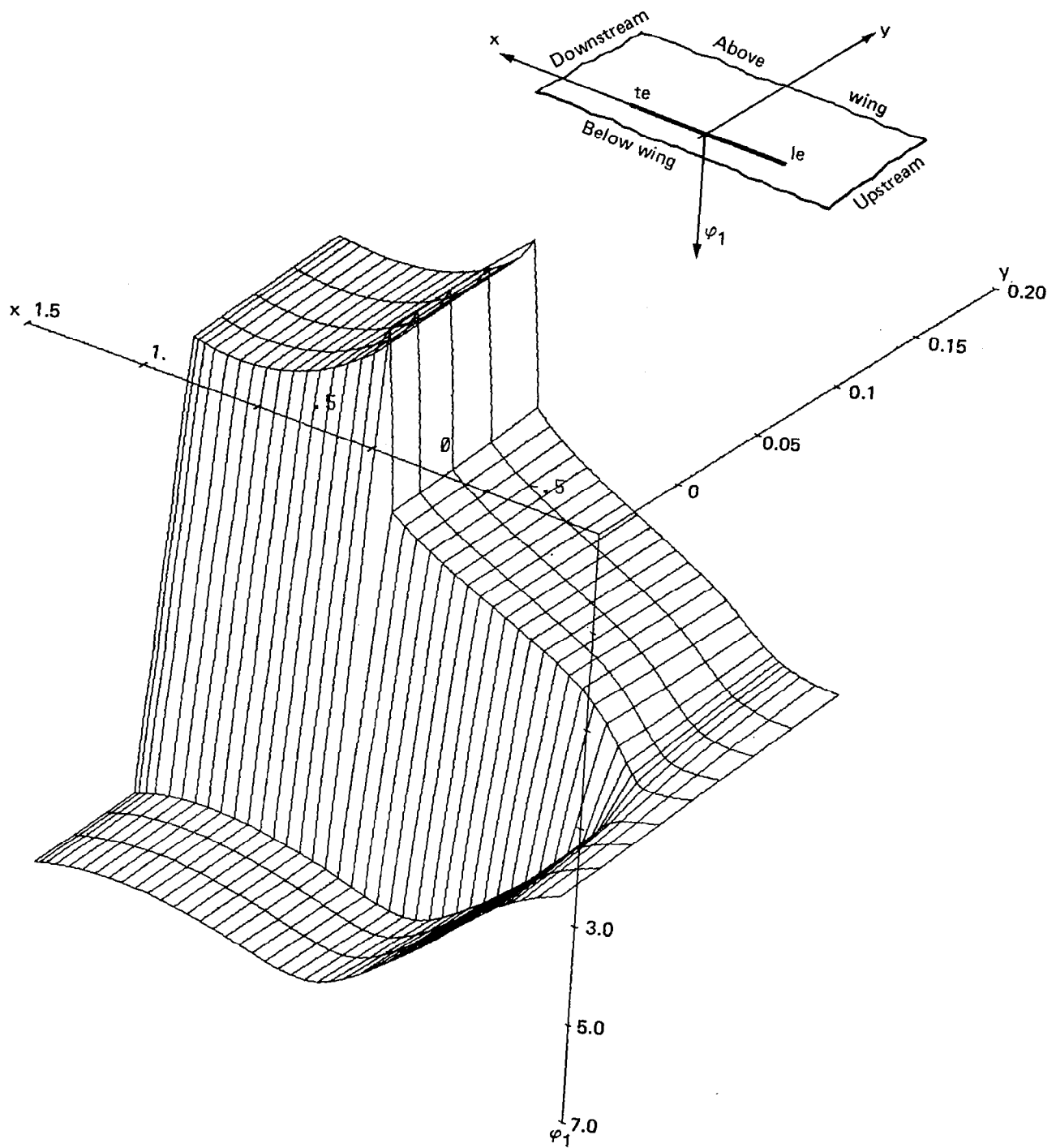


Figure 11.—Three-Dimensional Surface Representation of Imaginary Part of Unsteady Potential for Solution With Coarse Grid and First Form of the Shock Point Operator,  $M=8, k=0.3, \alpha_m=1^\circ$

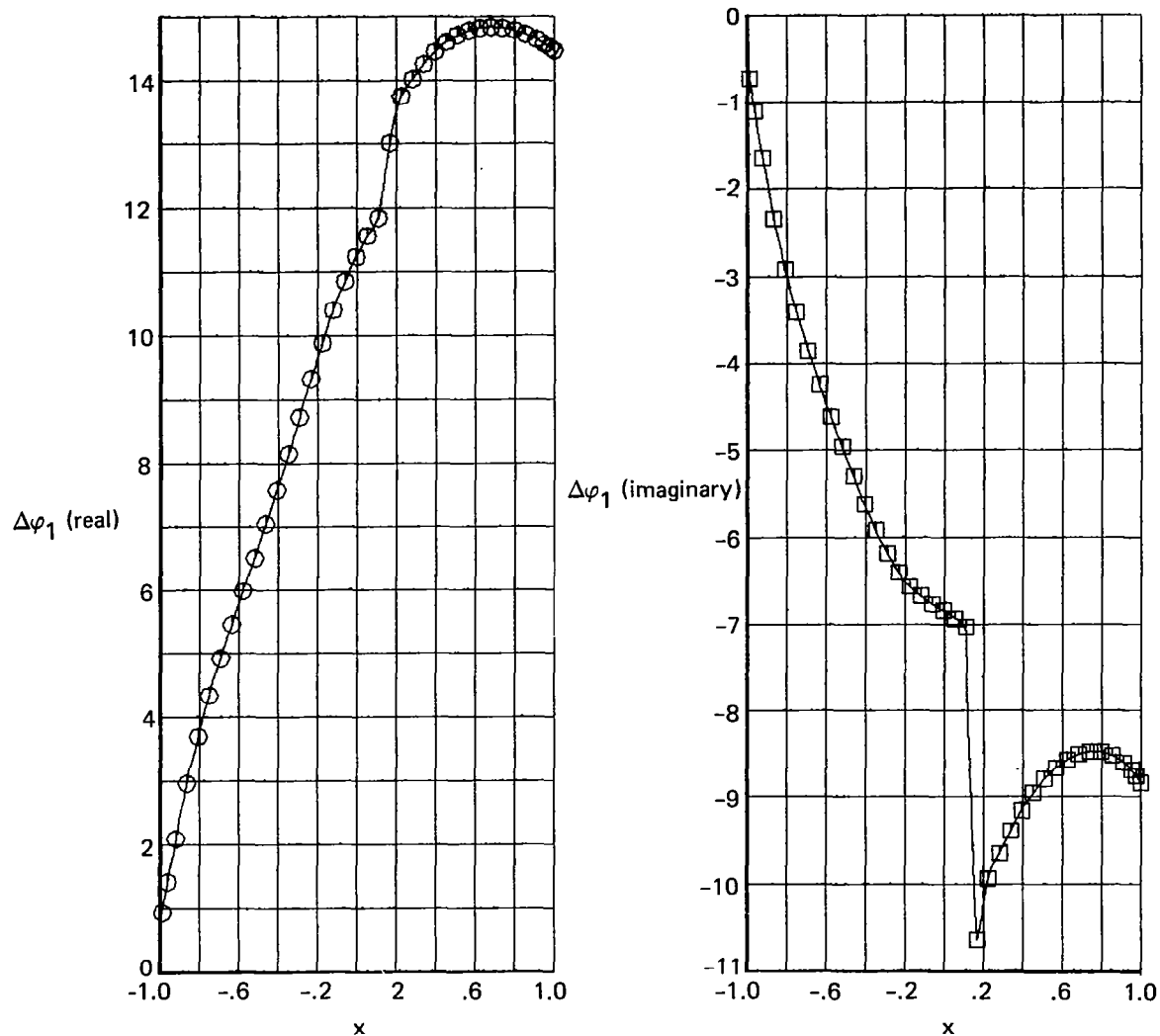


Figure 12.—Jump in Unsteady Potential Across Airfoil for Solution With Coarse Grid and First Form of the Shock Point Operator,  $M=0.8$ ,  $k=0.3$ ,  $\alpha_m=1^\circ$

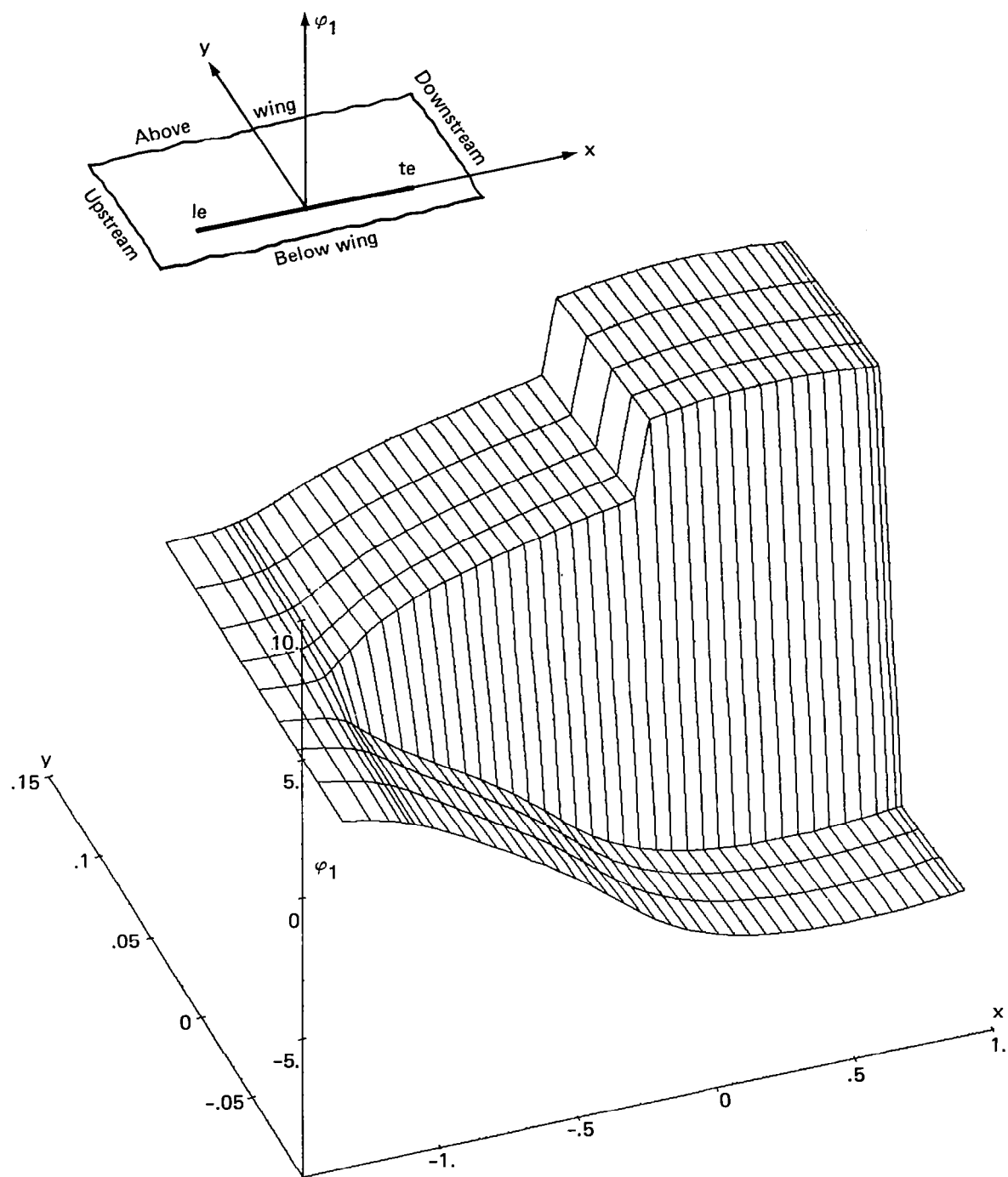


Figure 13.—Three-Dimensional Surface Representation of Real Part of Unsteady Potential for Solution With Coarse Grid and Third Form of the Shock Point Operator,  $M=0.8$ ,  $k=0.3$ ,  $\alpha_m=1^\circ$

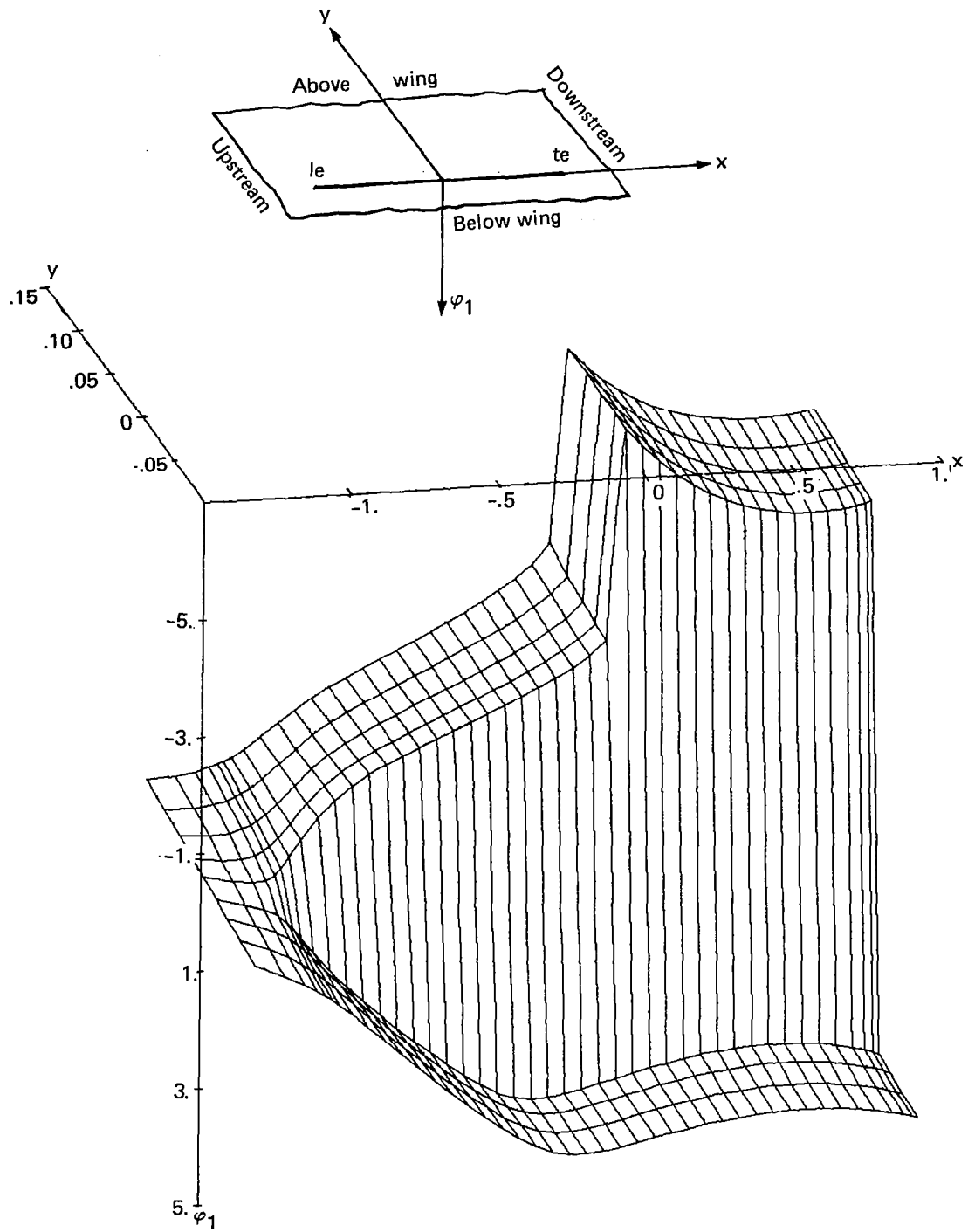


Figure 14.—Three-Dimensional Surface Representation of Imaginary Part of Unsteady Potential for Solution With Coarse Grid and Third Form of the Shock Point Operator,  $M=0.8$ ,  $k=0.3$ ,  $\alpha_m=1^\circ$

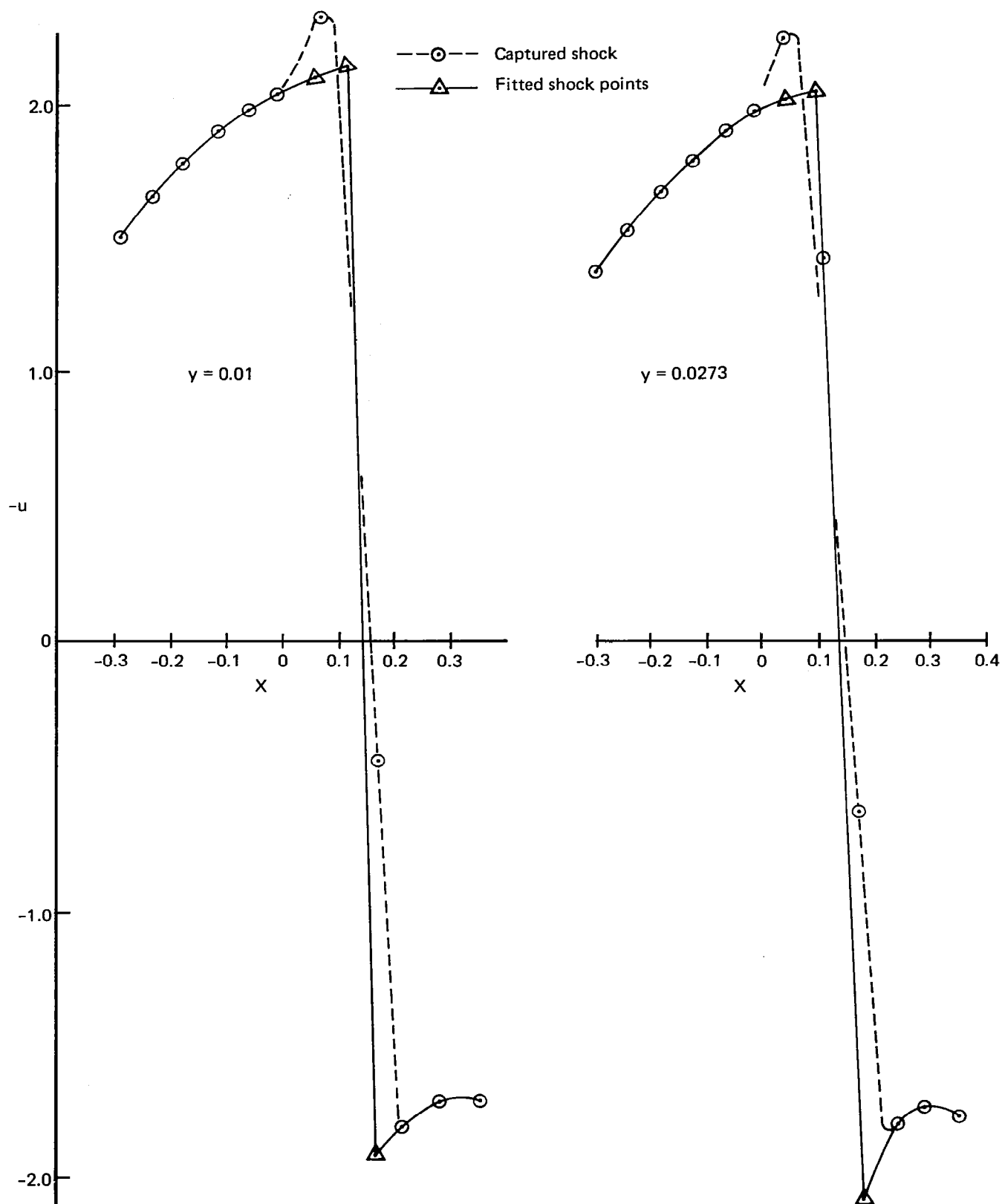


Figure 15.—Examples of Fitted Shock Obtained From Modifying Captured Shock



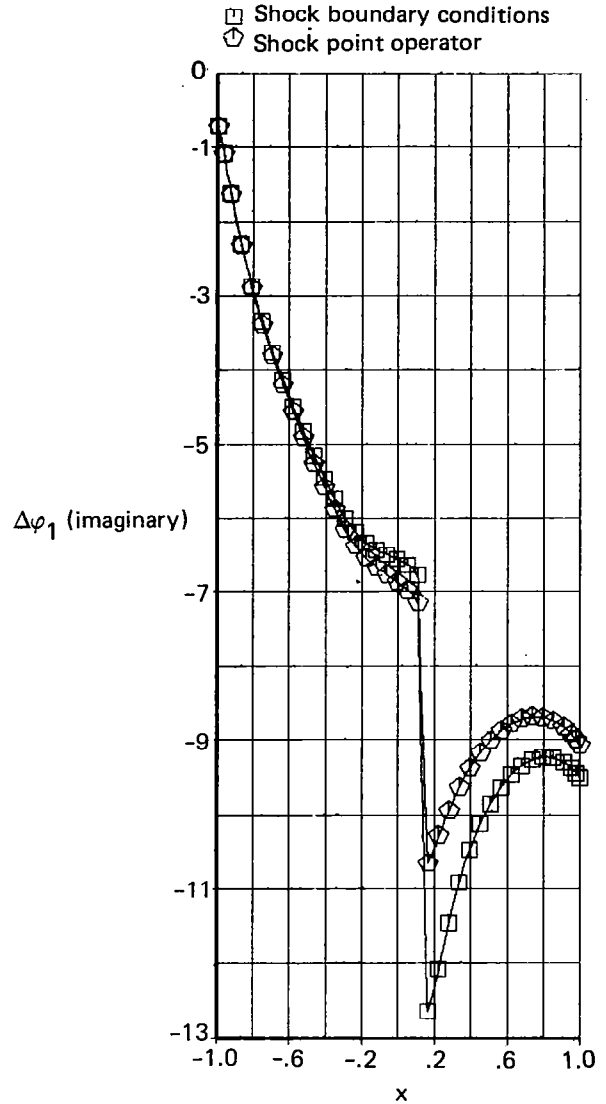
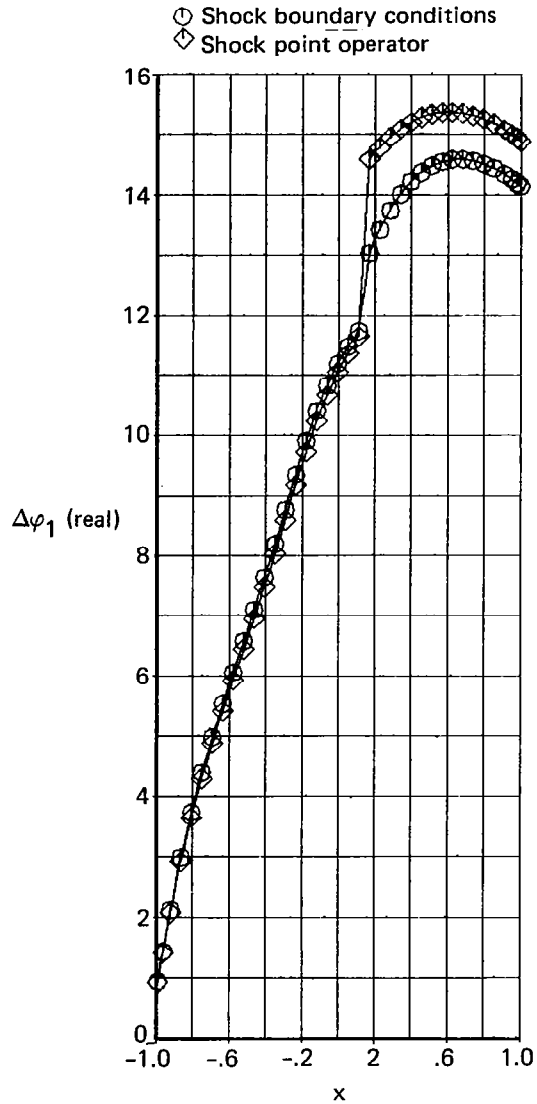


Figure 16.—Comparison of the Jump in Potential Across the Airfoil for Fitted Shock From Shock Boundary Conditions With Results From the Shock Point Operator,  $M=0.8$ ,  $k=0.3$ ,  $\alpha_m=1^\circ$

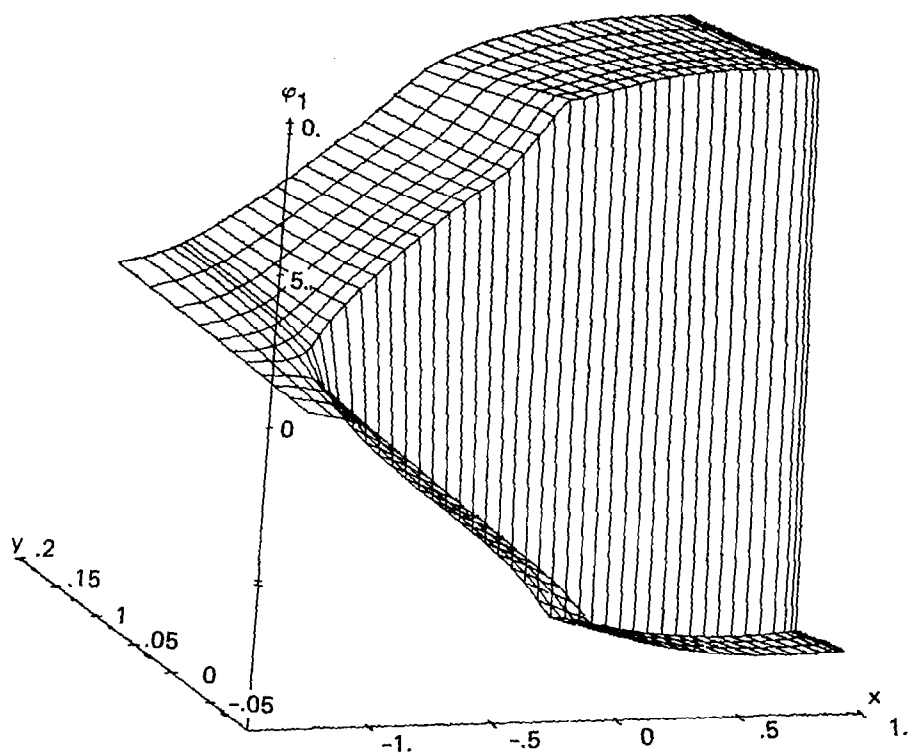
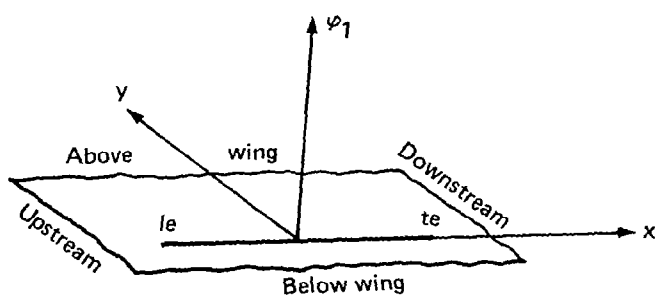


Figure 17.—Effect of Shock Point Operator on Real Part of Unsteady Potential  
With Weak Steady Shock,  $M=0.8$ ,  $k=0.3$ ,  $\alpha_m=0^\circ$ , Coarse Grid

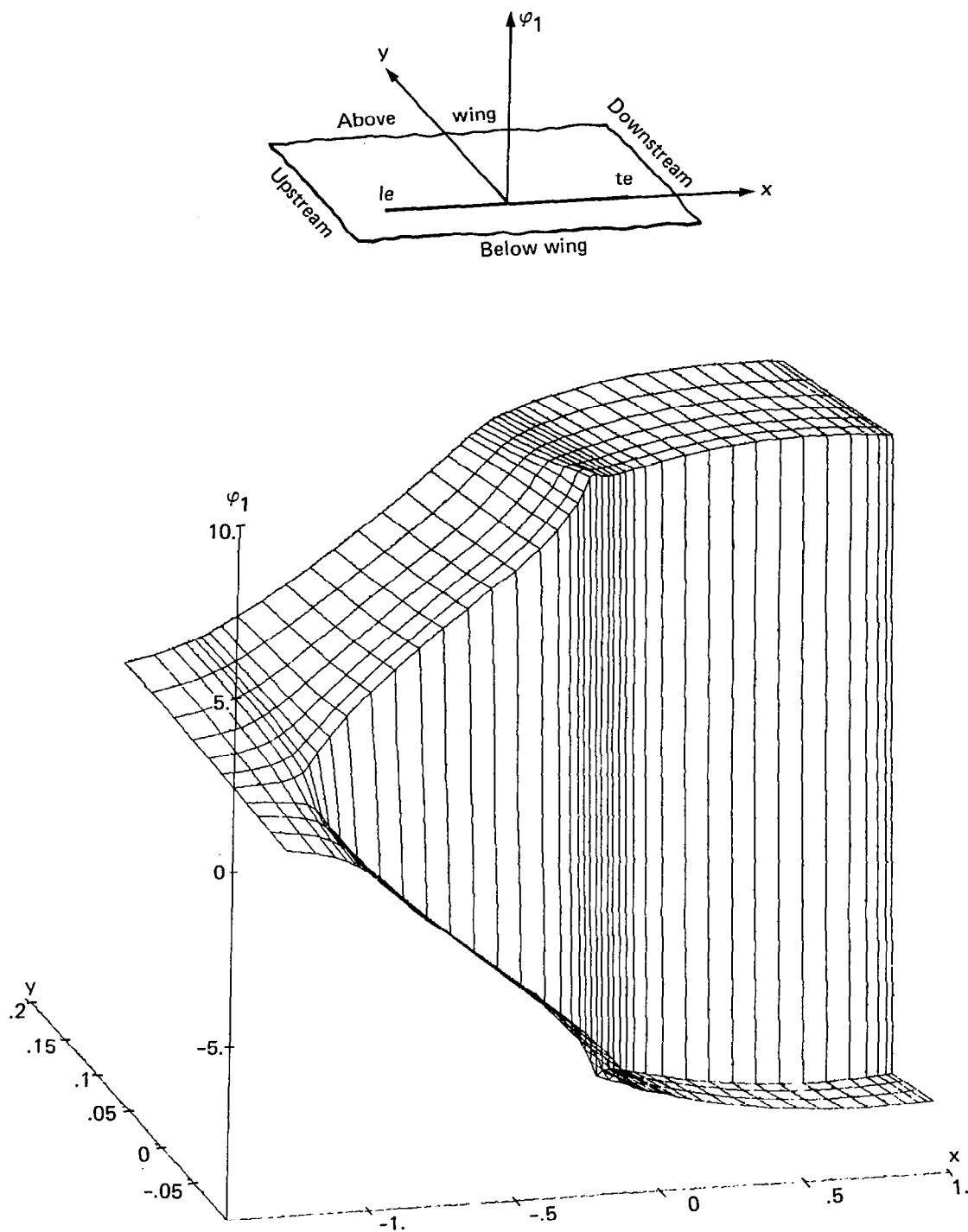


Figure 18.—Effect of Shock Point Operator on Real Part of Unsteady Potential With Weak Steady Shock,  $M=0.8$ ,  $k=0.3$ ,  $\alpha_m=0^\circ$ , Fine Grid

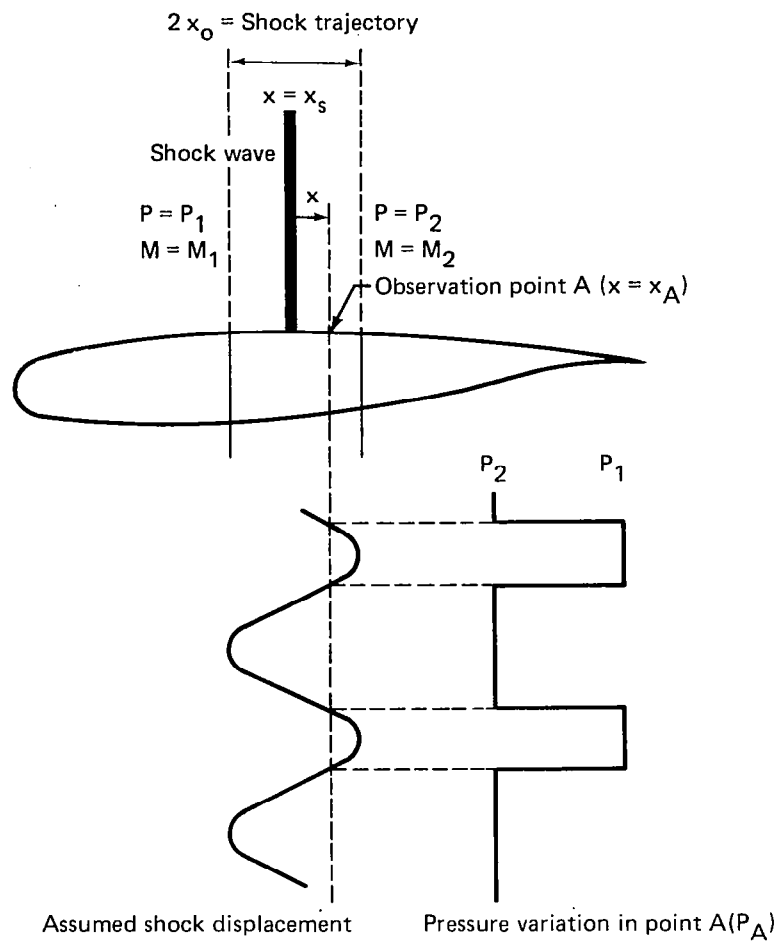


Figure 19.—Contribution of the Periodically Moving Shock Wave to the Pressure Signal at a Fixed Observation Point. (From Tijdeman, Reference 24)

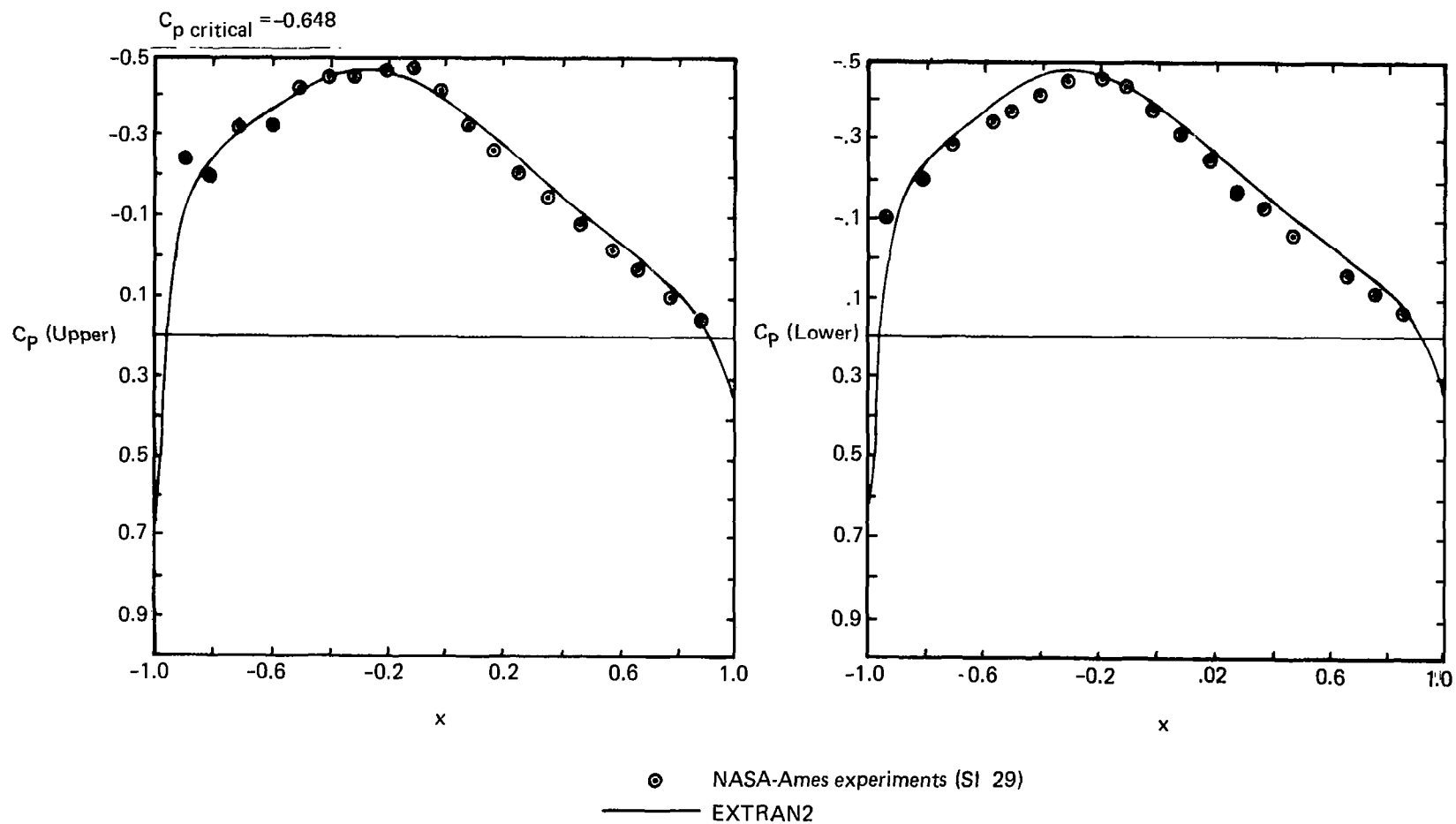


Figure 20.—Comparison of Steady State Pressure Distribution on a NACA 64A010 Airfoil as Computed by EXTRAN2 With NASA-Ames Experiments,  $M=0.75$ ,  $\alpha_m=0^\circ$

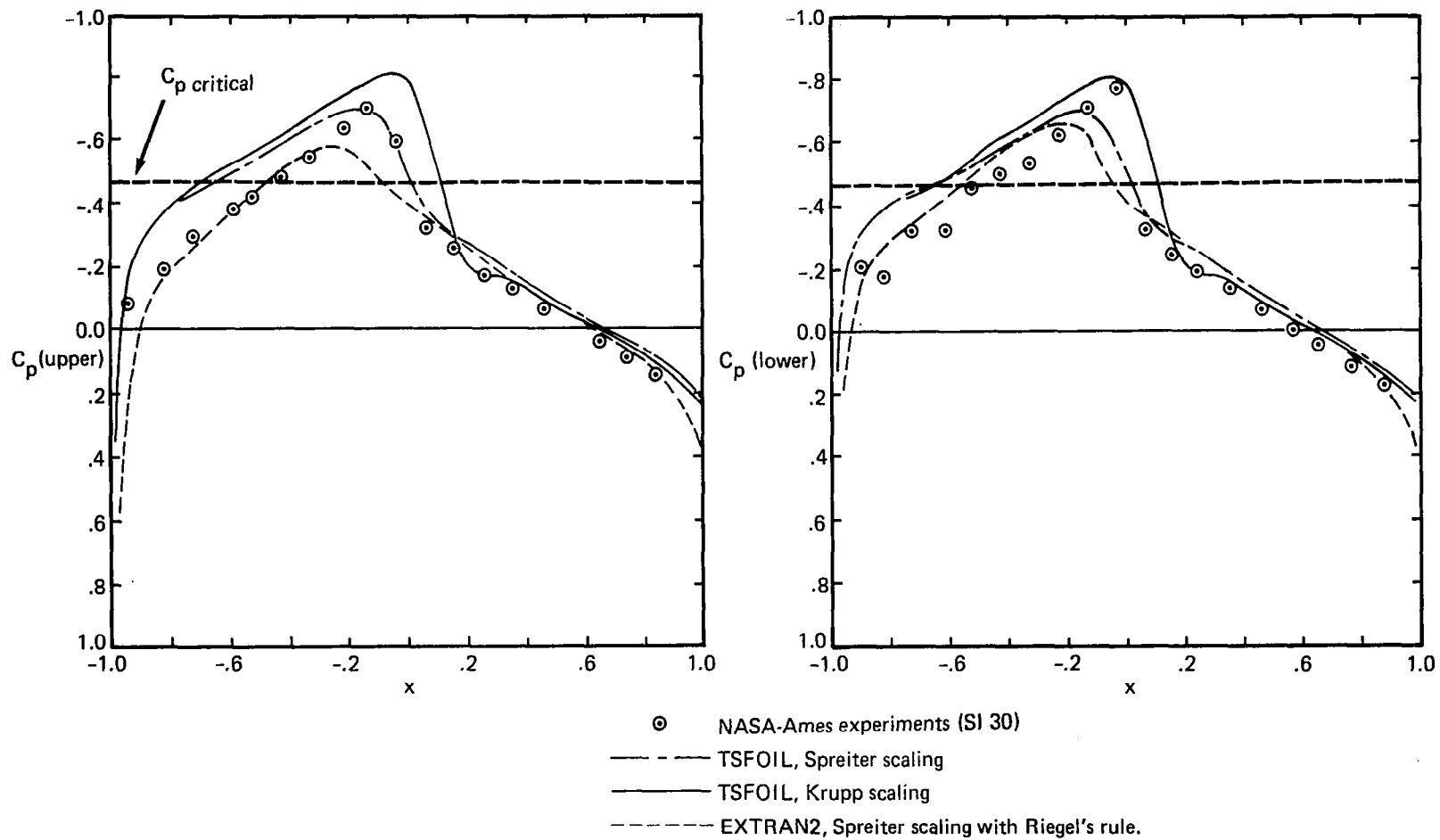


Figure 21.—Comparison of Steady State Pressure Distribution on a NACA 64A010 Airfoil as Computed by Three Methods With NASA Experiments,  $M=0.8$ ,  $\alpha_m=0^\circ$

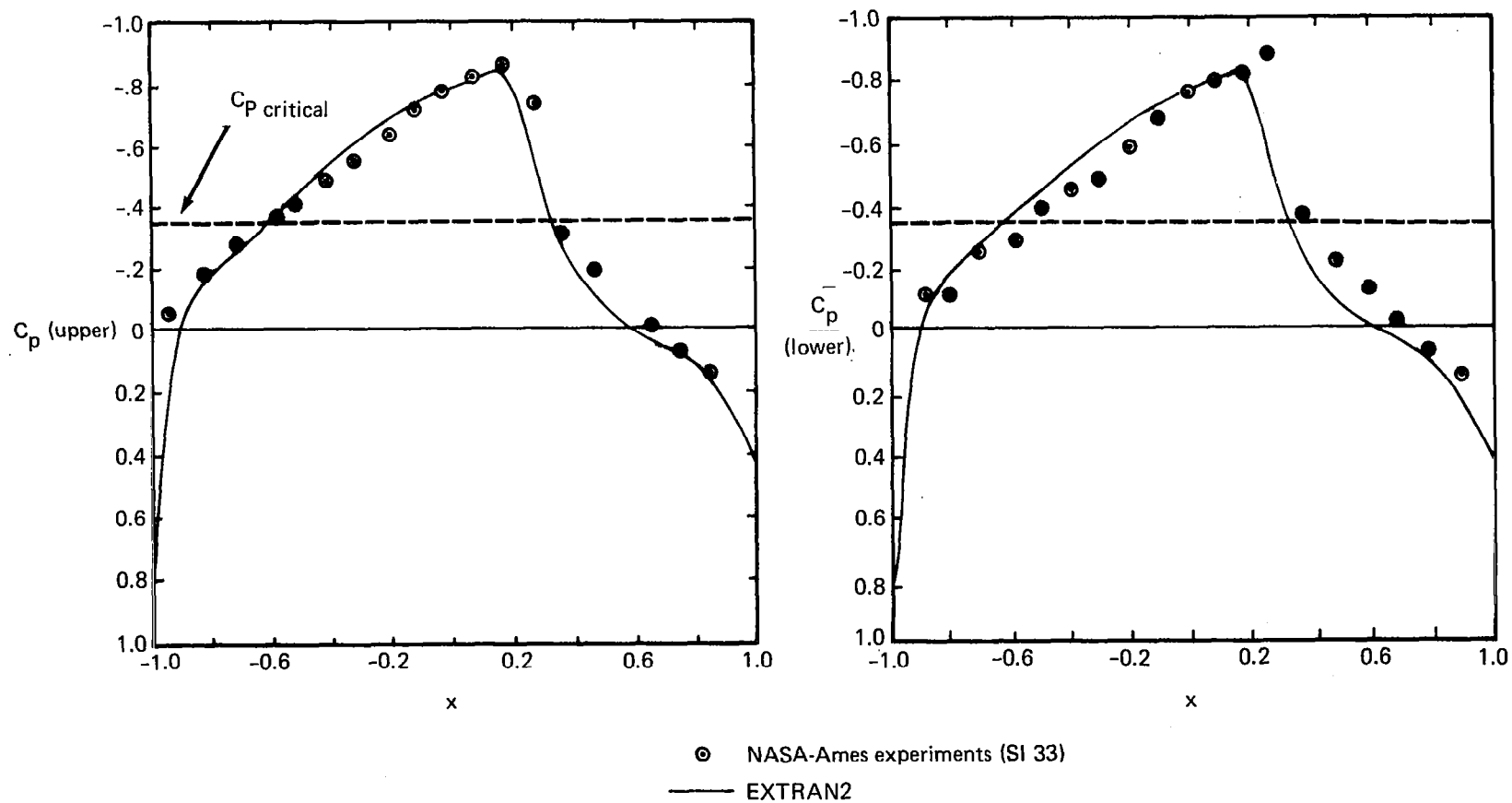
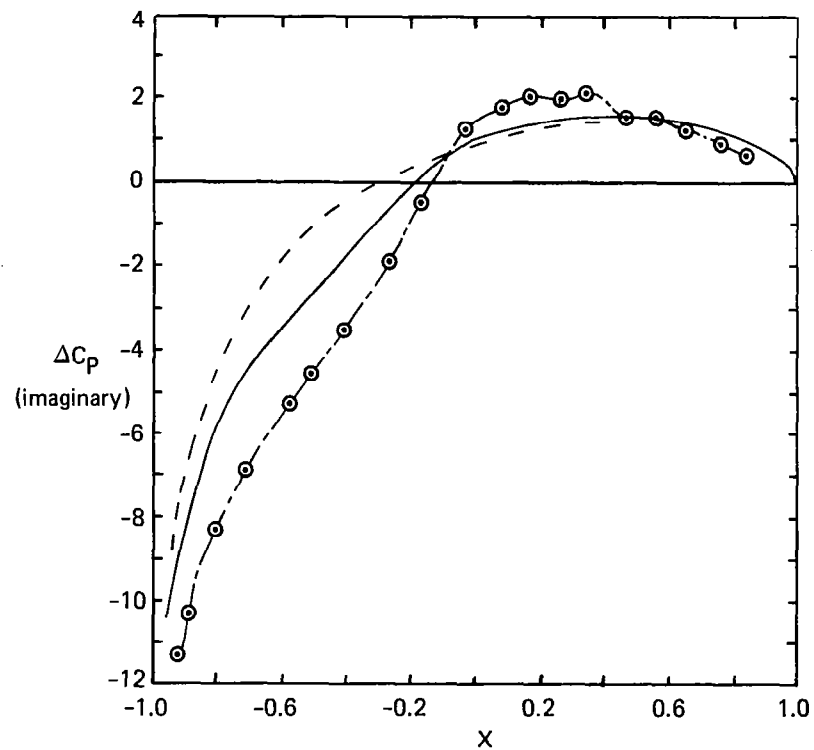
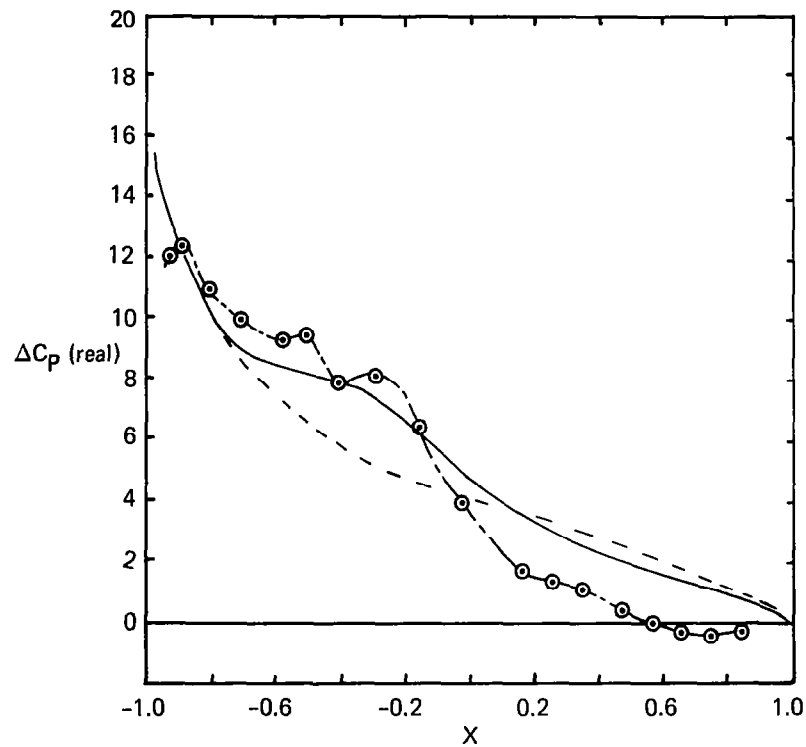


Figure 22.—Comparison of Steady State Pressure Distribution on a NACA 64A010 Airfoil as Computer by EXTRAN2 With NASA Ames Experiments,  $M=0.842$ ,  $\alpha_m = 0^\circ$



Airfoil pitching about quarter chord point

- NASA-Ames experiments (DI 46)
- Present theory
- - - Flat plate

Figure 23.—Pressure Coefficient Distributions on NACA 64A010 Airfoil Pitching  $1^\circ$  About Quarter-Chord Point,  $M=0.75$ ,  $k=0.20$ ,  $\alpha_m=0^\circ$



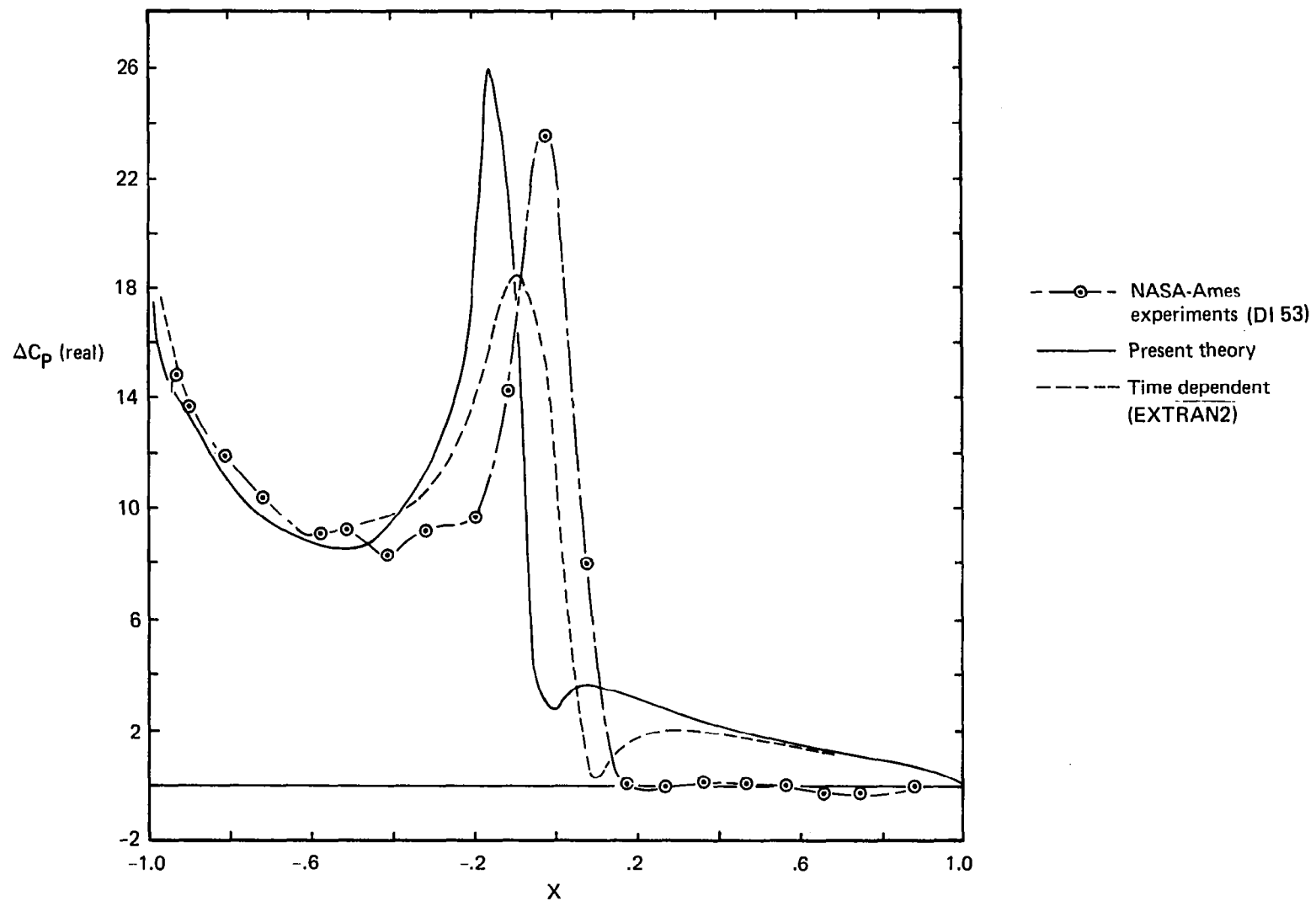


Figure 24.—Pressure Coefficient Distributions on NACA 64A010 Airfoil Pitching  $1^\circ$  About Quarter-Chord Point,  $M=0.8$ ,  $k=0.101$ ,  $\alpha_m=0^\circ$ , Real Part

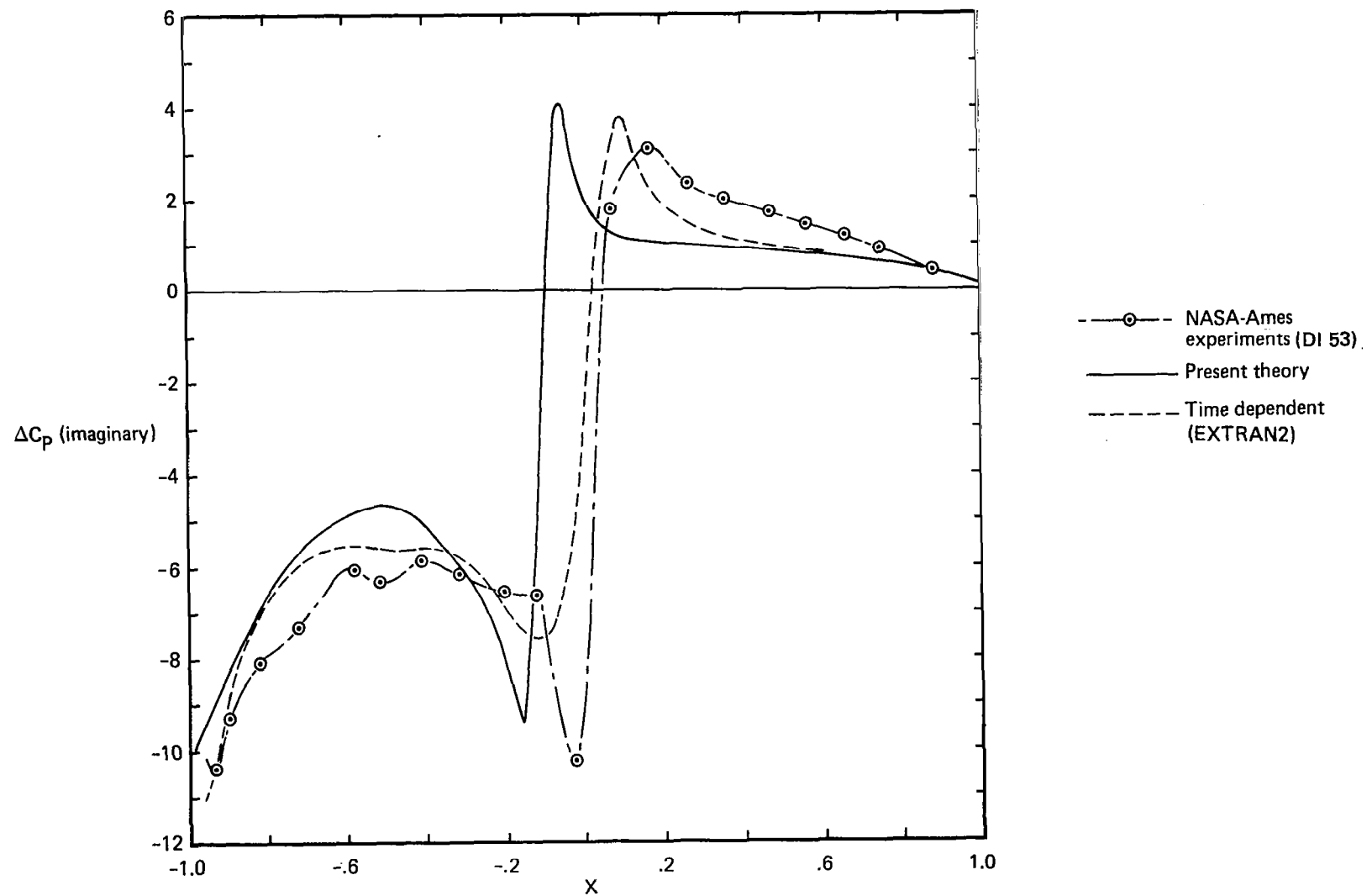


Figure 25.—Pressure Coefficient Distributions on NACA 64A010 Airfoil Pitching  $1^\circ$  About Quarter-Chord Point,  $M=0.8$ ,  $k=0.101$ ,  $\alpha_m=0^\circ$ , Imaginary Part

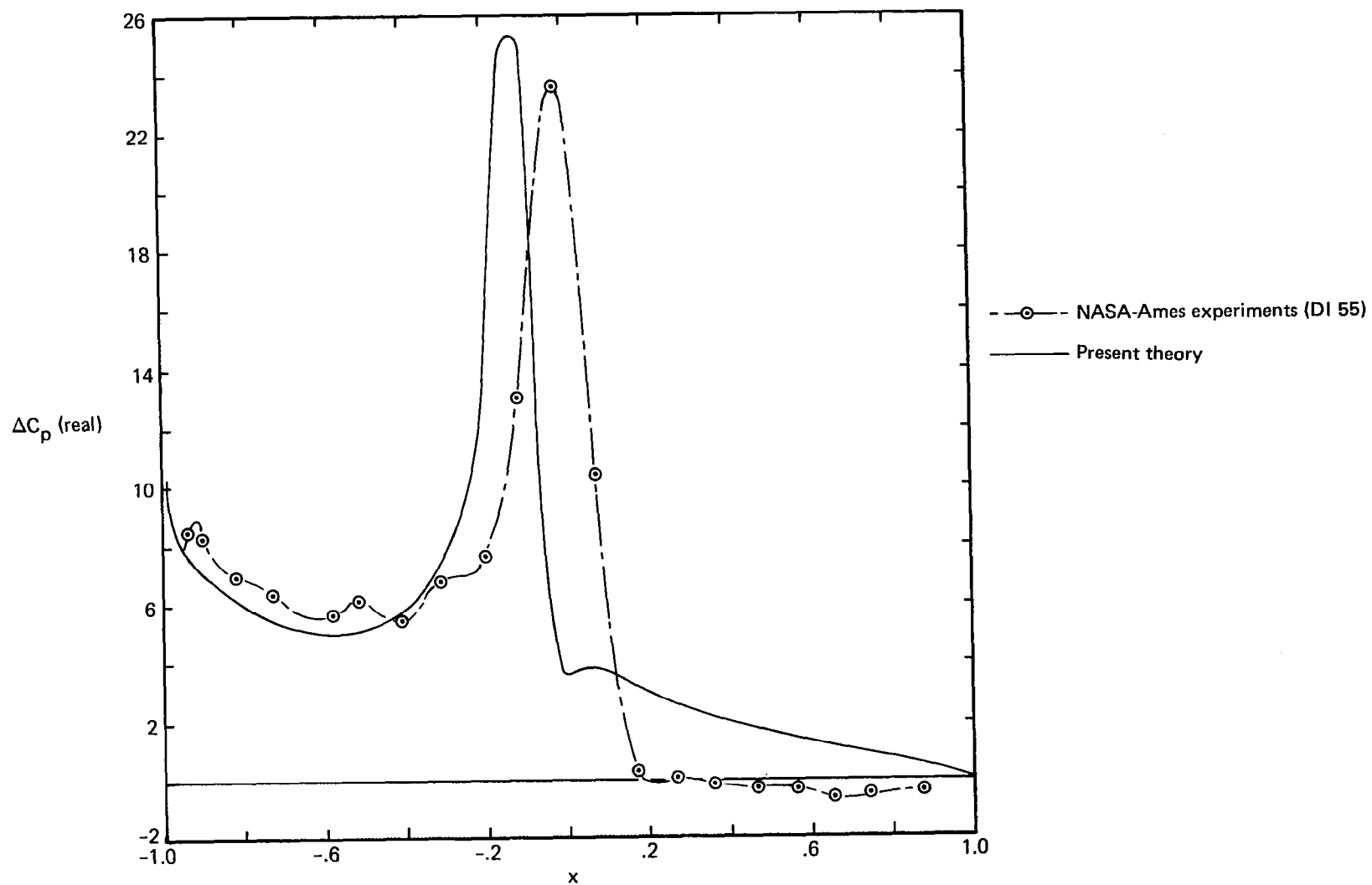


Figure 26.—Pressure Coefficient Distributions on NACA 64A010 Airfoil Pitching  $1^\circ$  About Quarter-Chord Point,  $M=0.8$ ,  $k=0.202$ ,  $\alpha_m=0^\circ$ , Real Part

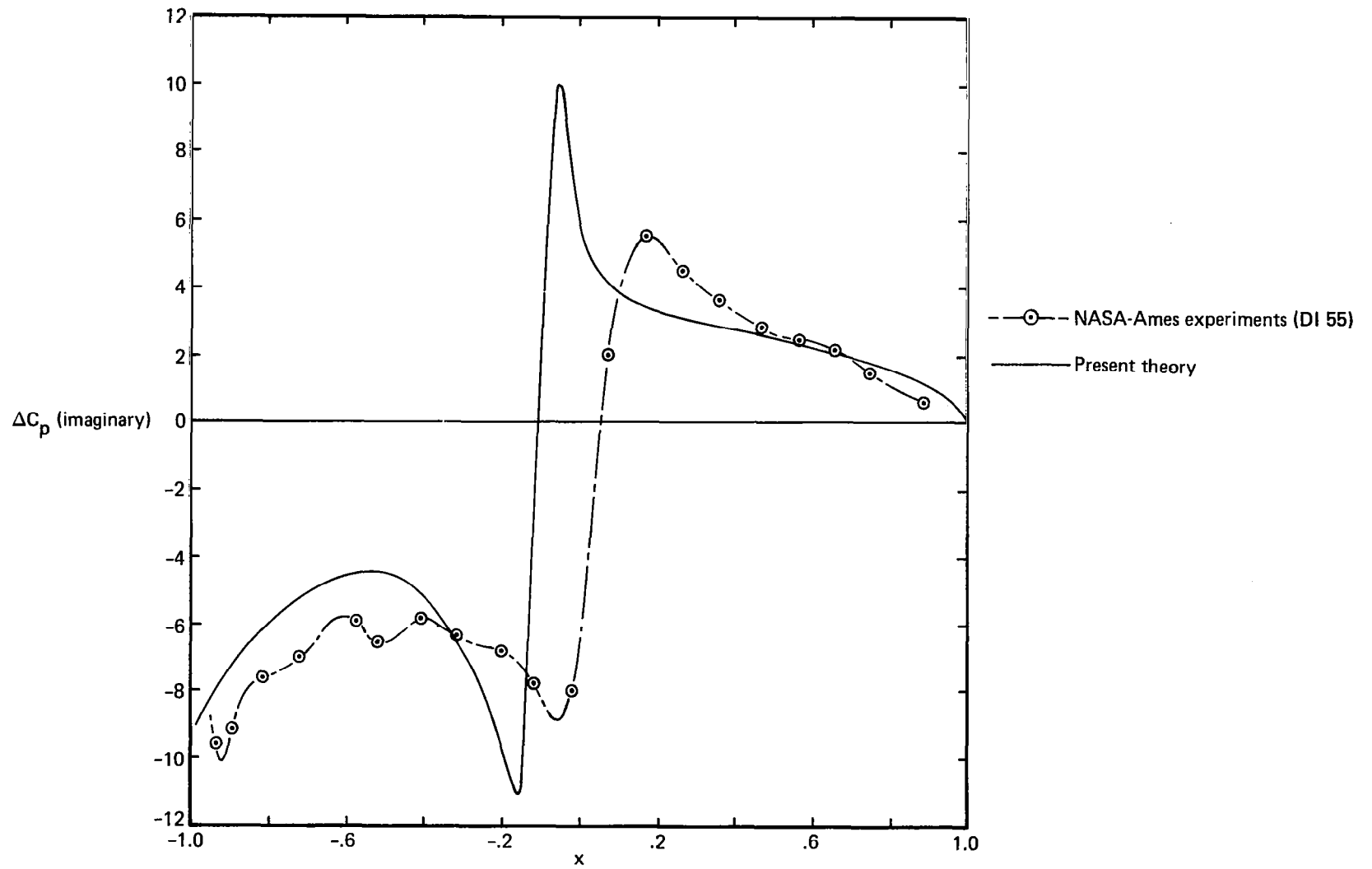


Figure 27.—Pressure Coefficient Distributions on NACA 64A010 Airfoil Pitching  $1^\circ$  About Quarter-Chord Point,  $M=0.8$ ,  $k=0.202$ ,  $\alpha_m=0^\circ$ , Imaginary Part

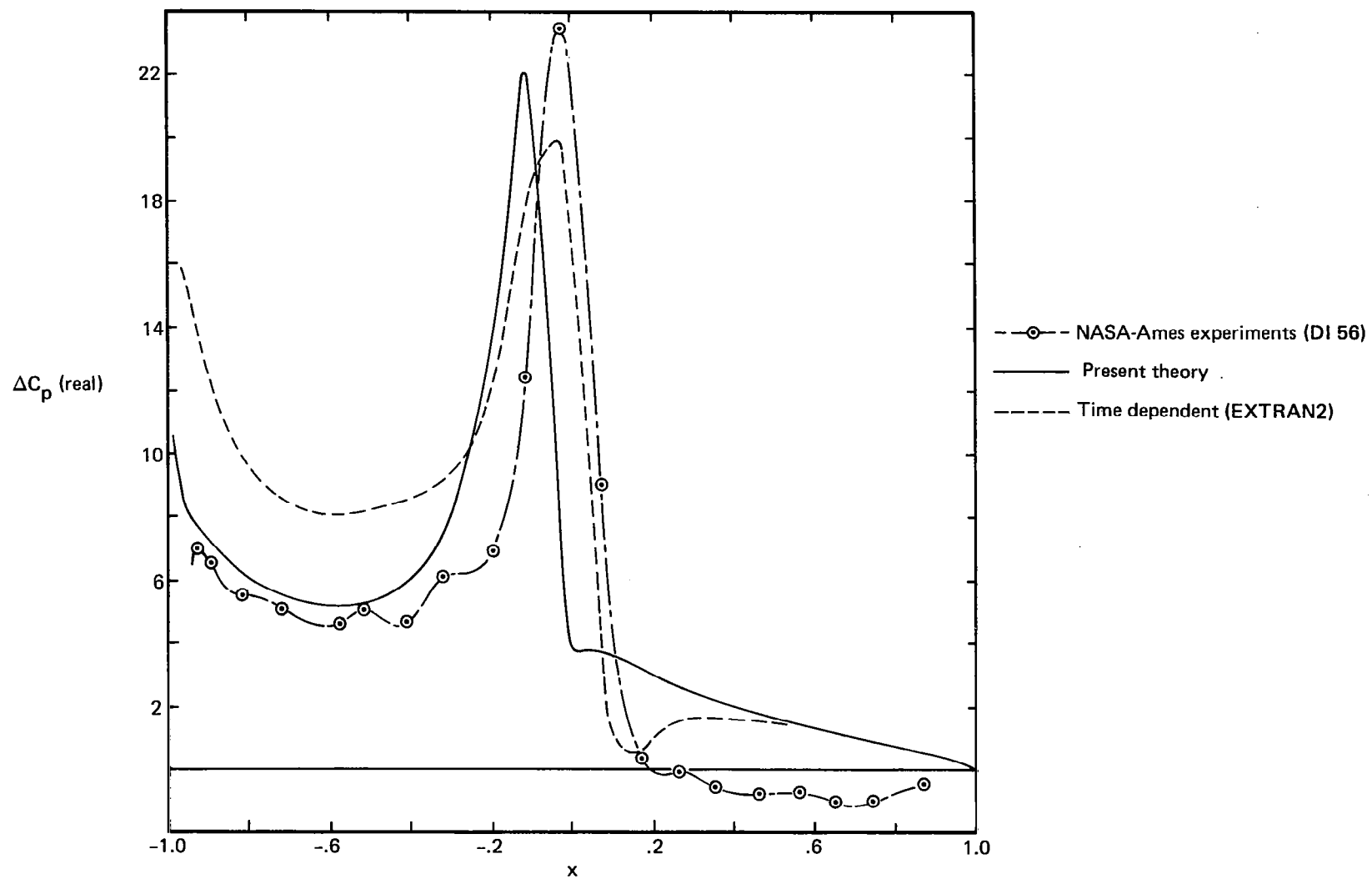


Figure 28.—Pressure Coefficient Distributions on NACA 64A010 Airfoil Pitching  $1^\circ$  About Quarter-Chord Point,  $M=0.8$ ,  $k=0.247$ ,  $\alpha_m=0^\circ$ , Real Part

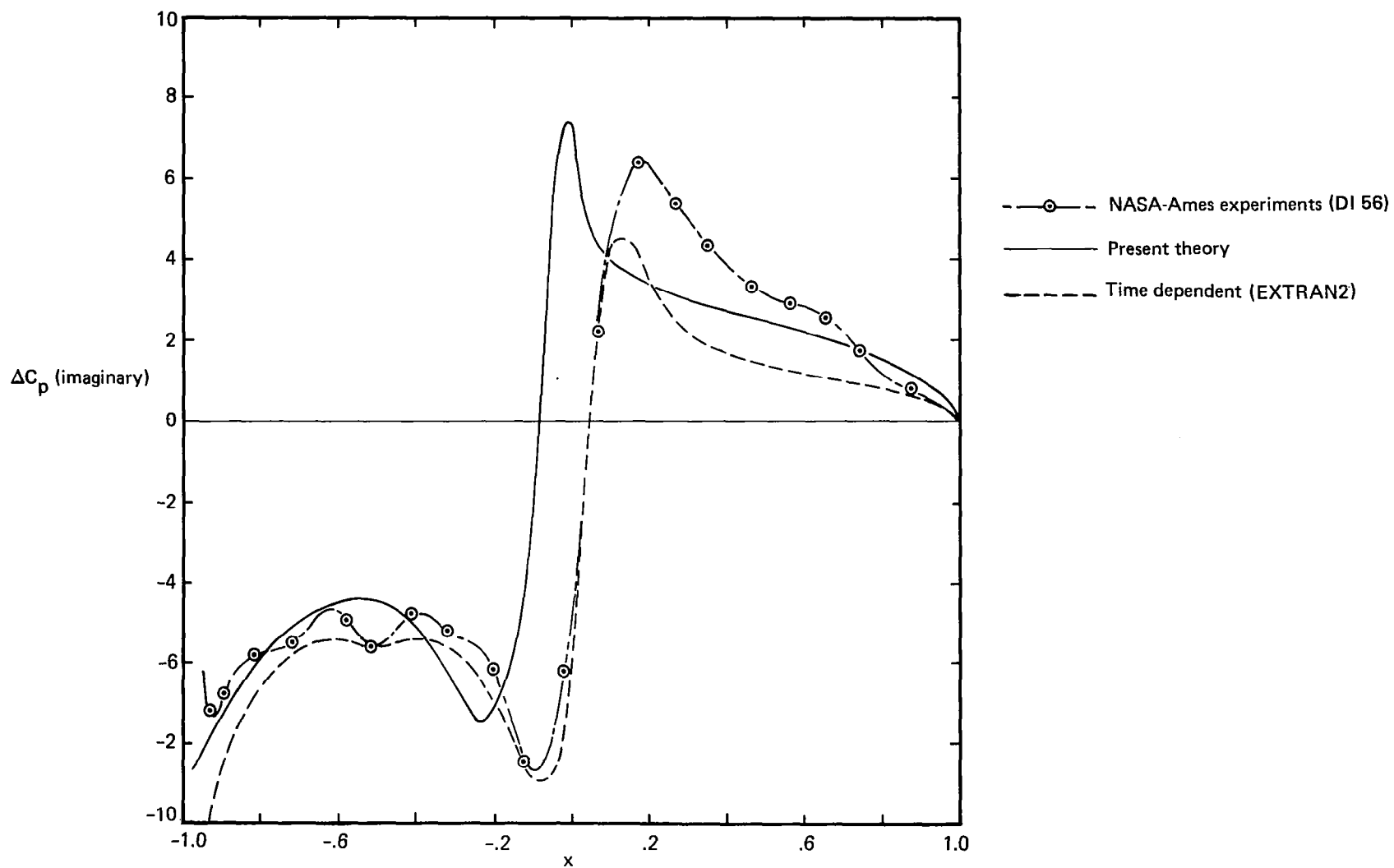


Figure 29.—Pressure Coefficient Distributions on NASA 64A010 Airfoil Pitching  $1^\circ$  About Quarter-Chord Point,  $M=0.8$ ,  $k=0.247$ ,  $\alpha_m = 0^\circ$ , Imaginary Part

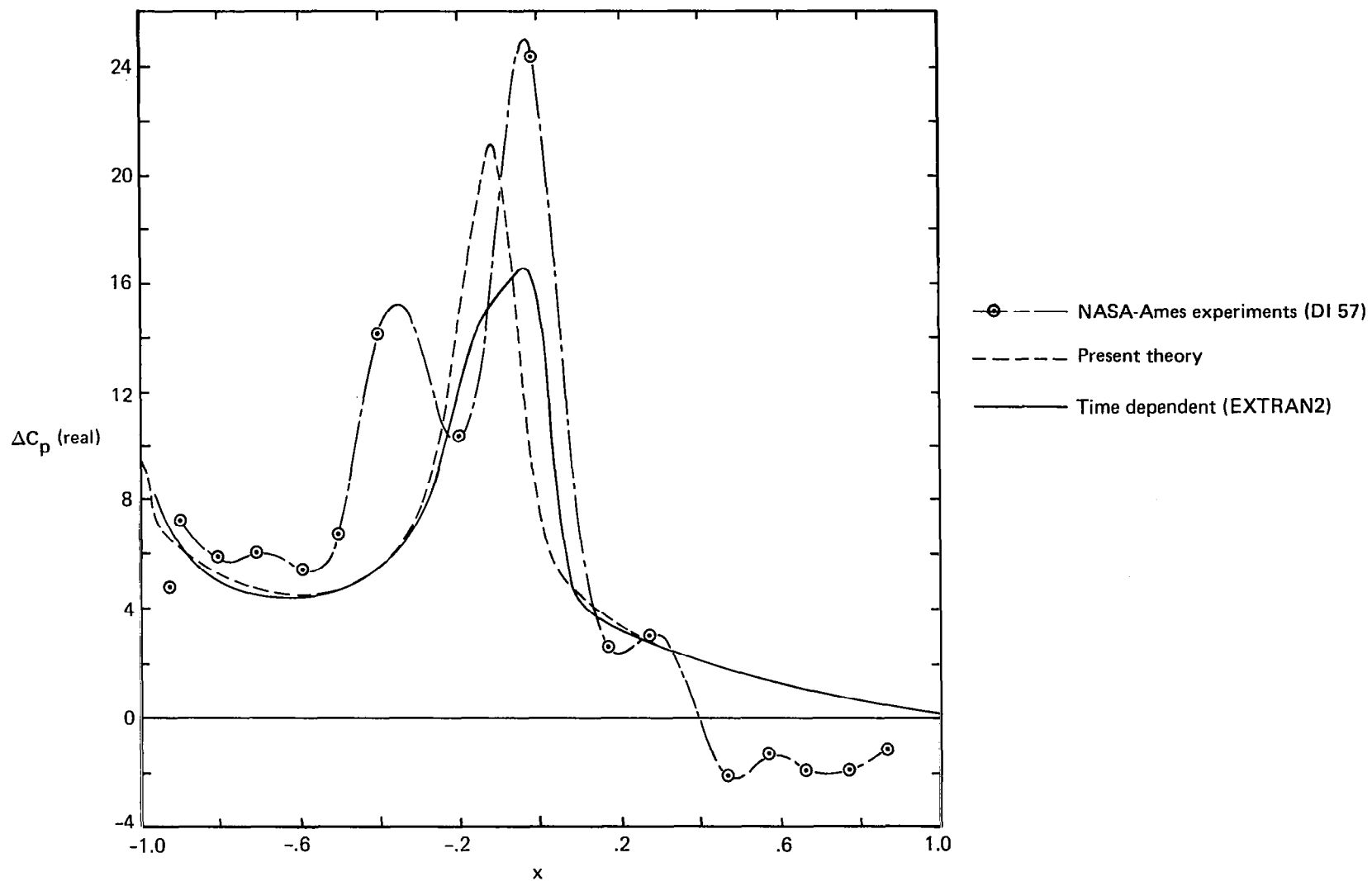


Figure 30.—Pressure Coefficient Distributions on NACA 64A010 Airfoil Pitching  $1^\circ$  About Quarter-Chord Point,  $M=0.8$ ,  $k=0.303$ ,  $\alpha_m=0^\circ$ , Real Part

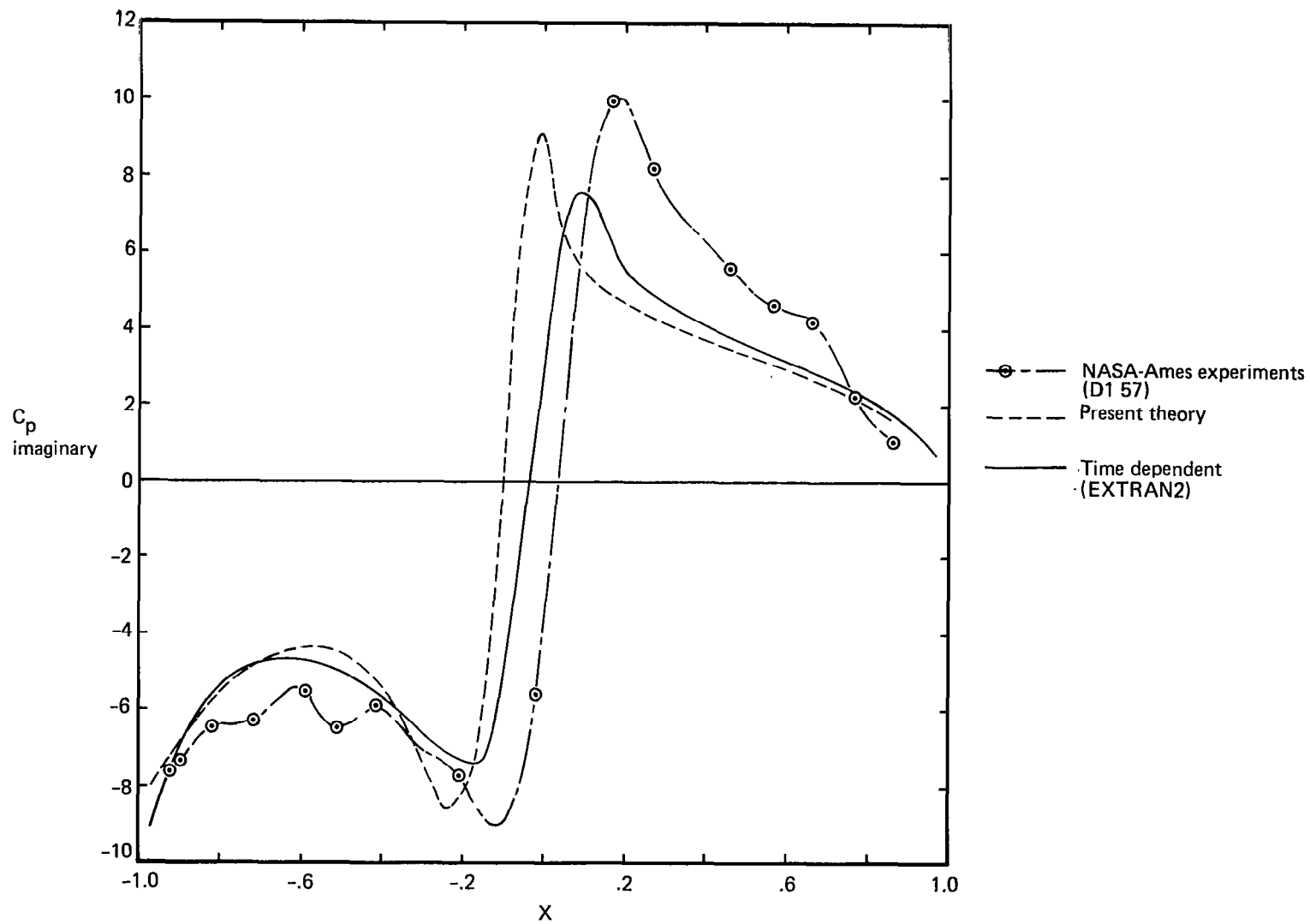


Figure 31.—Pressure Coefficient Distributions on NACA 64A010 Airfoil Pitching  $1^\circ$  About Quarter-Chord Point,  $M=0.8$ ,  $k=0.303$ ,  $\alpha_m=0^\circ$ , Imaginary Part



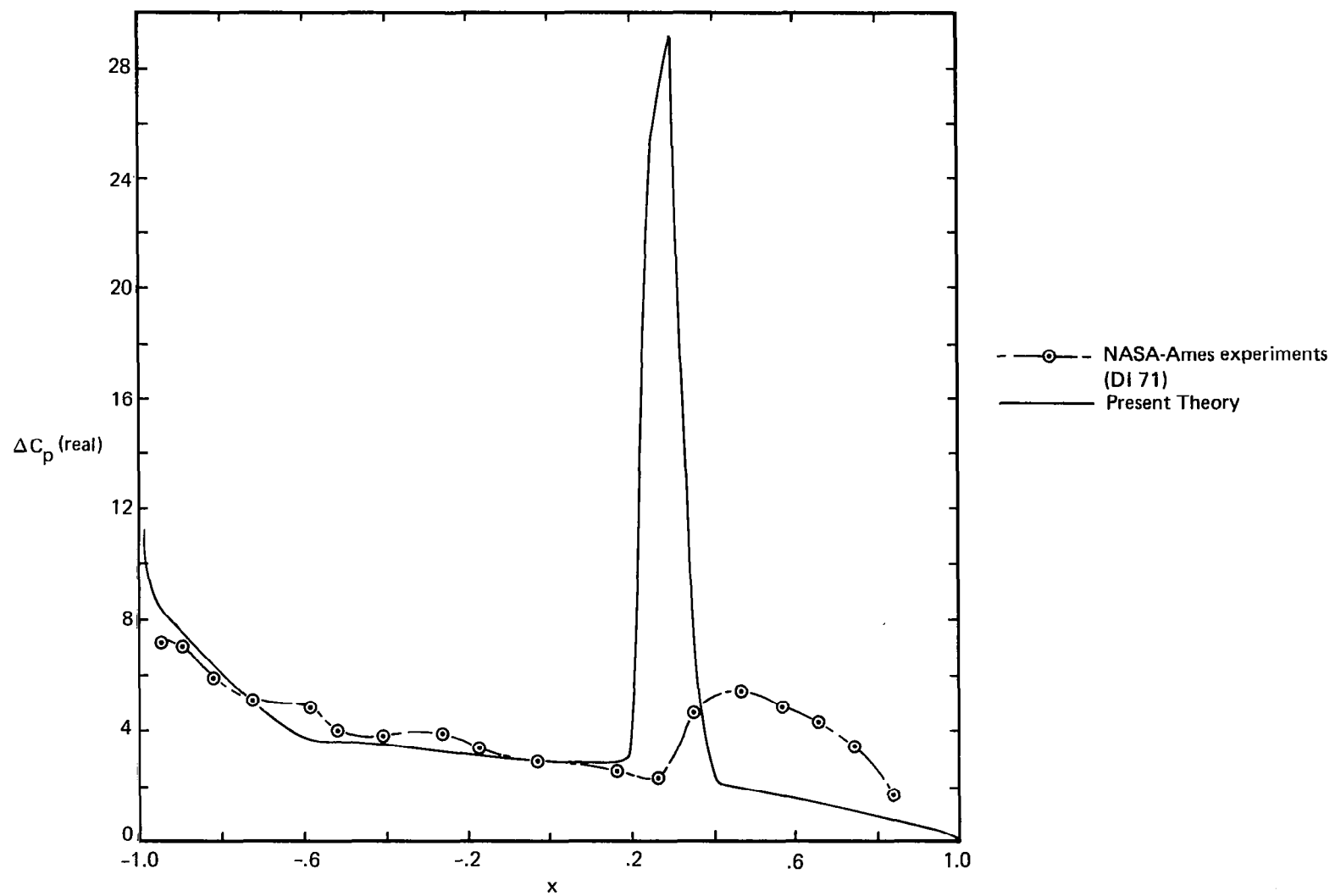


Figure 32.—Pressure Coefficient Distributions on NACA 64A010 Airfoil Pitching  $1^\circ$   
About Quarter-Chord Point,  $M=0.842$ ,  $k=0.202$ ,  $\alpha_m=0^\circ$ , Real Part

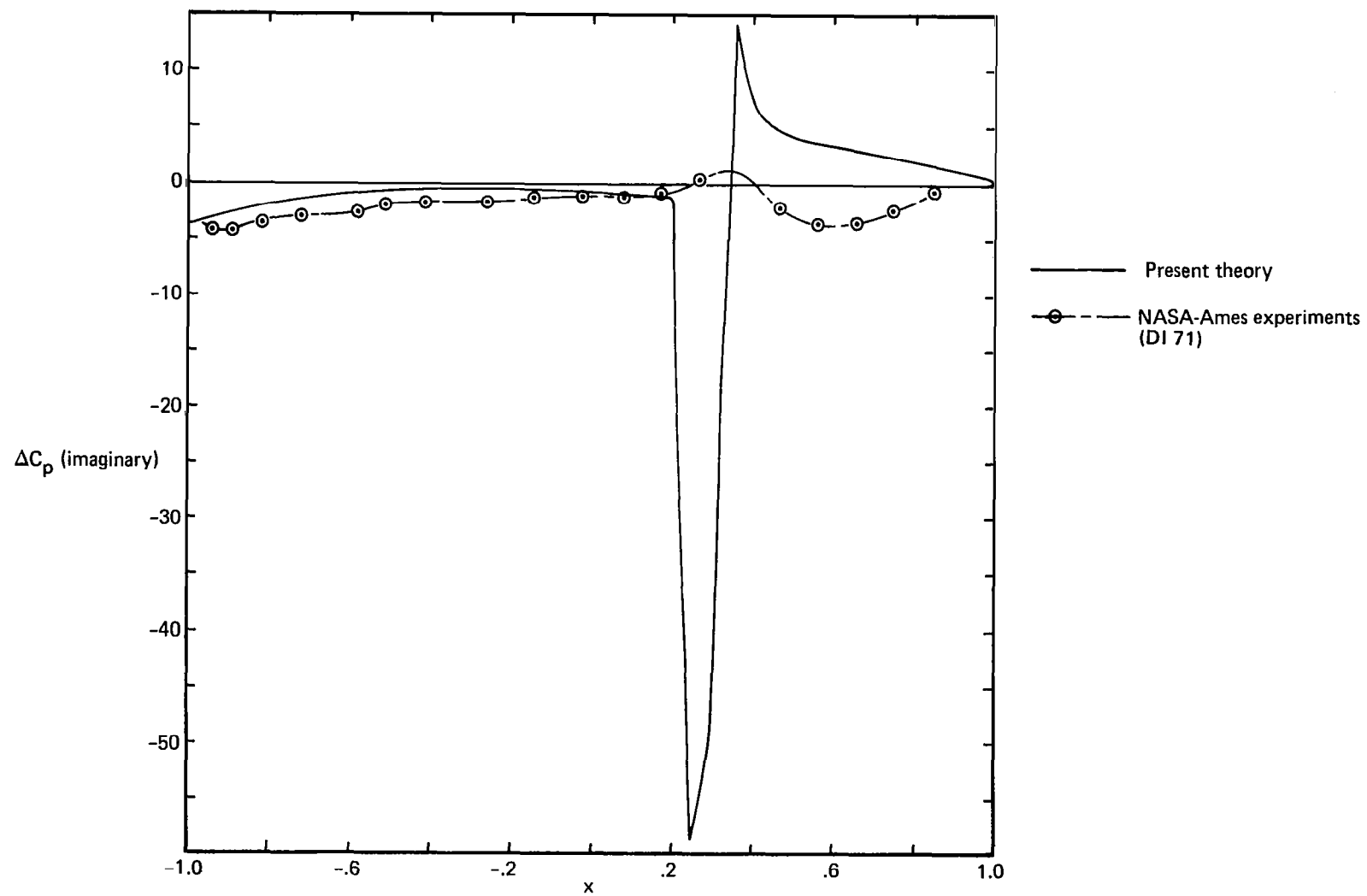


Figure 33.—Pressure Coefficient Distributions on NACA 64A010 Airfoil Pitching  $1^\circ$  About Quarter-Chord Point,  $M=0.842$ ,  $k=0.202$ ,  $\alpha_m=0^\circ$ , Imaginary Part

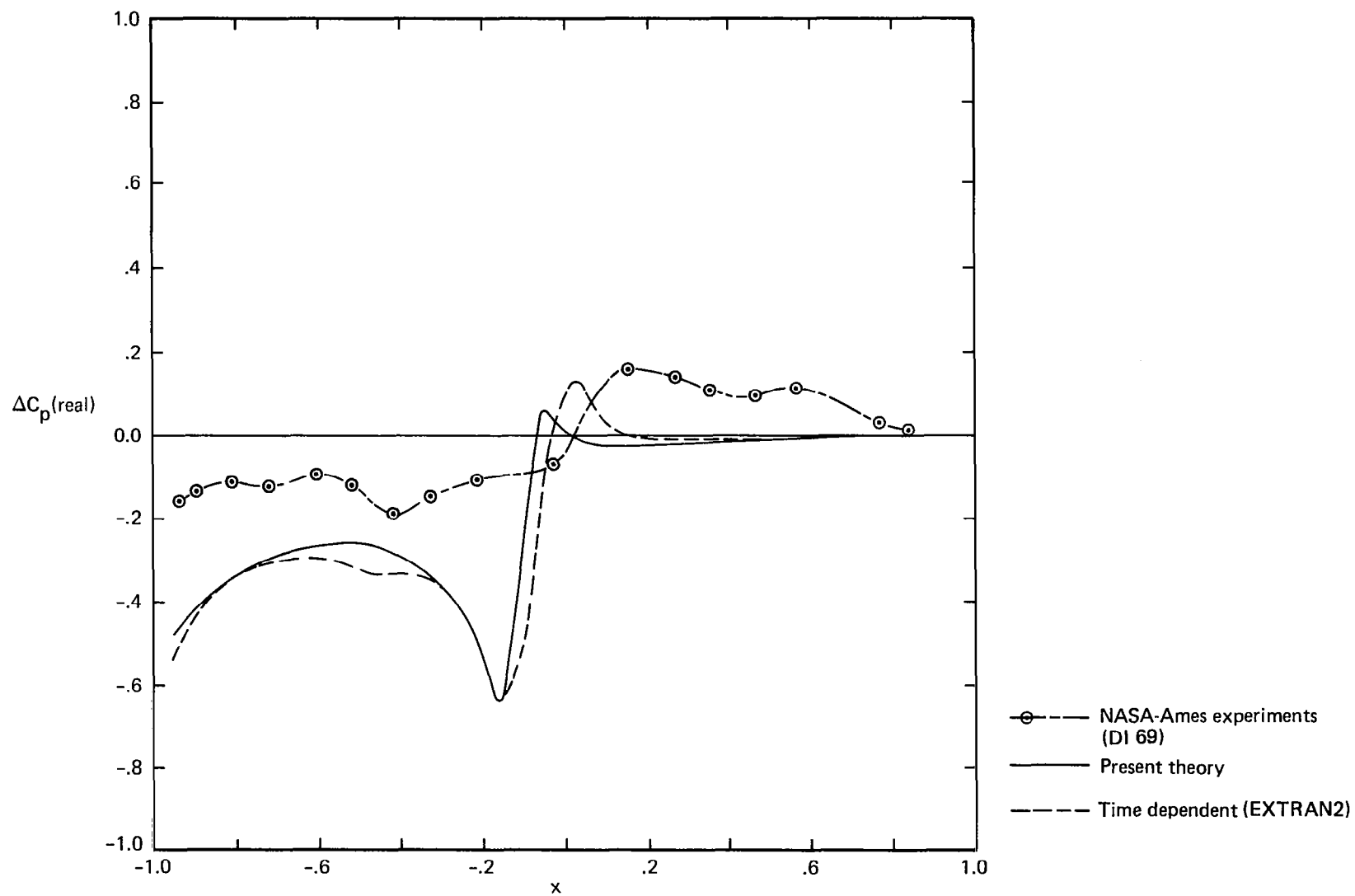


Figure 34.—Pressure Coefficient Distributions on NACA 64A010 Airfoil Oscillating 0.05 Semichord in Plunge,  $M=0.8$ ,  $k=0.05$ ,  $\alpha_m = 0^\circ$ , Real Part

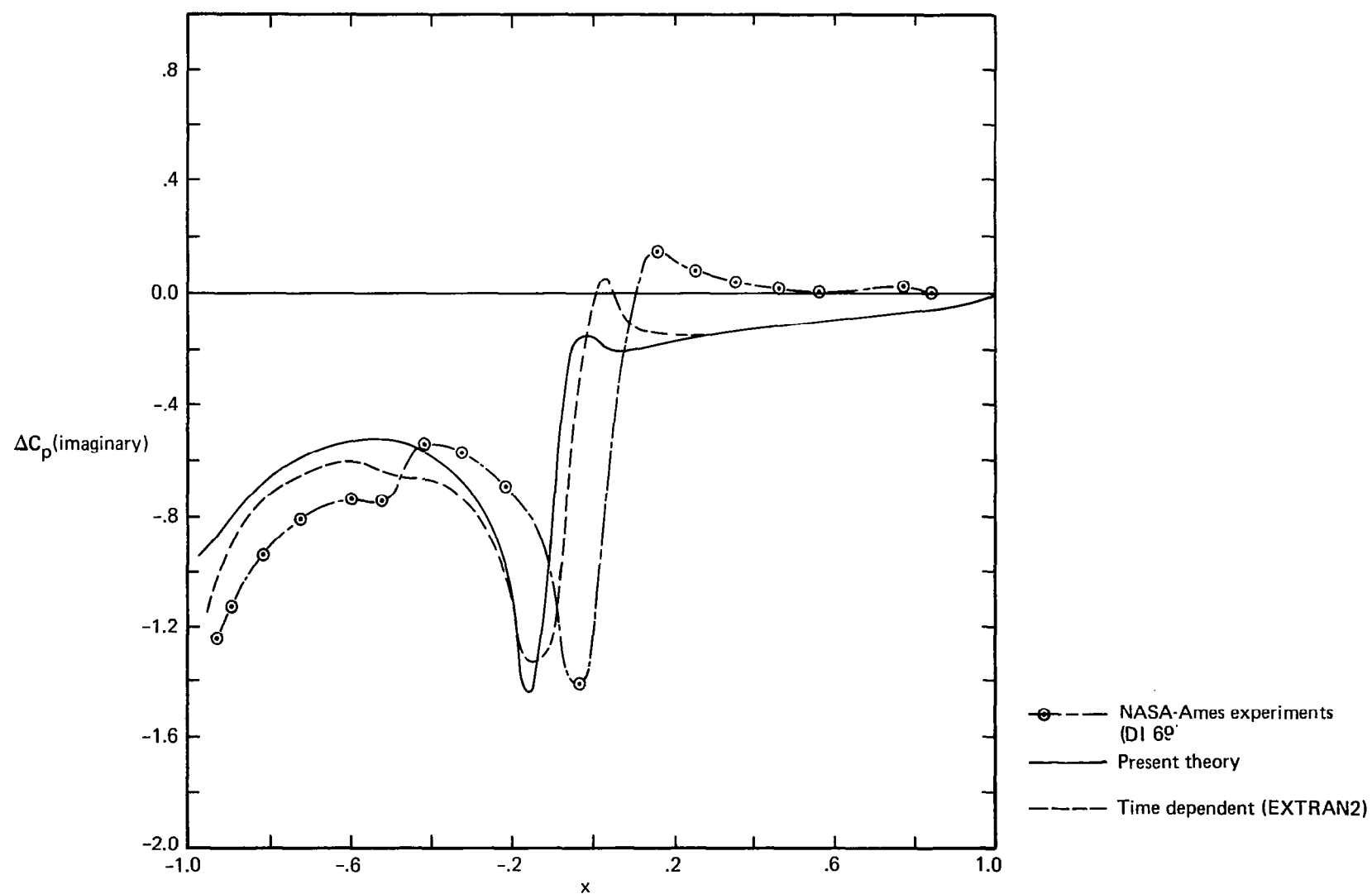


Figure 35.—Pressure Coefficient Distributions on NACA 64A010 Airfoil Oscillating 0.05 Semichord in Plunge,  $M=0.8$ ,  $k=0.05$ ,  $\alpha_m = 0^\circ$ , Imaginary Part

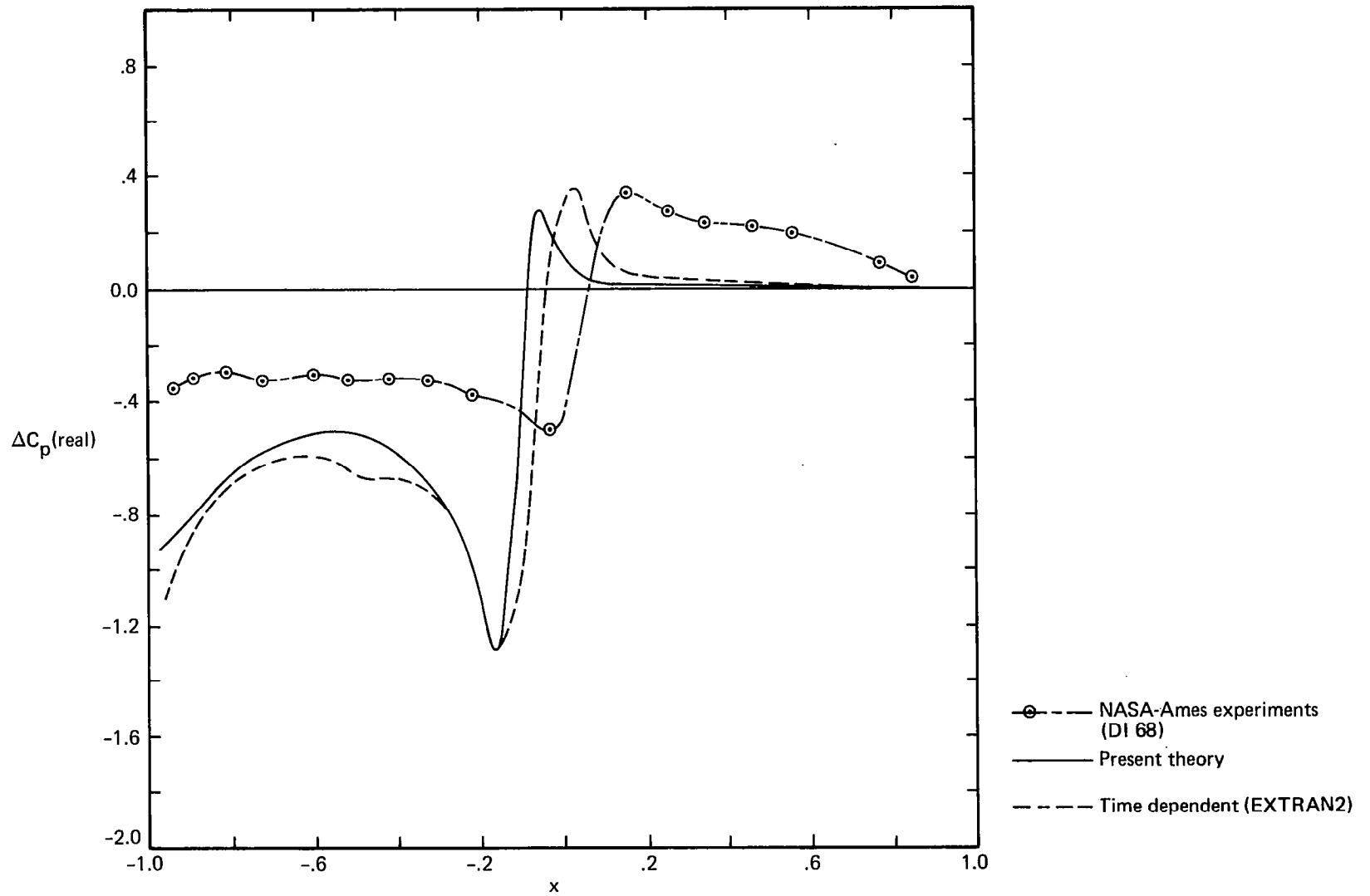


Figure 36.—Pressure Coefficient Distributions on NACA 64A010 Airfoil Oscillating 0.05 Semichord in Plunge,  $M=0.8$ ,  $k=0.101$ ,  $\alpha_m = 0^\circ$ , Real Part

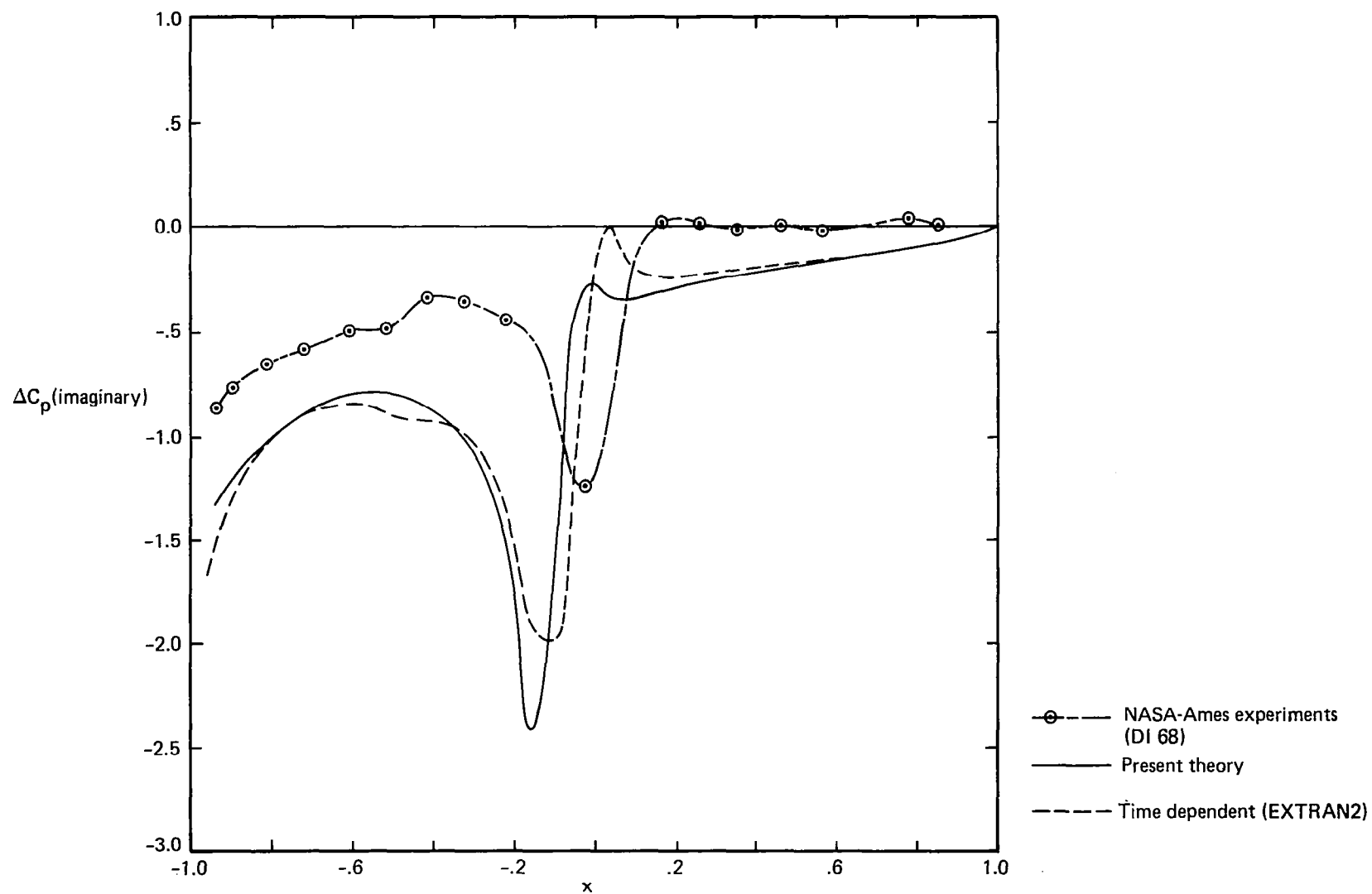


Figure 37.—Pressure Coefficient Distribution on NACA 64A010 Airfoil Oscillating 0.05 Semichord in Plunge,  $M=0.8$ ,  $k=0.101$ ,  $\alpha_m = 0^\circ$ , Imaginary Part

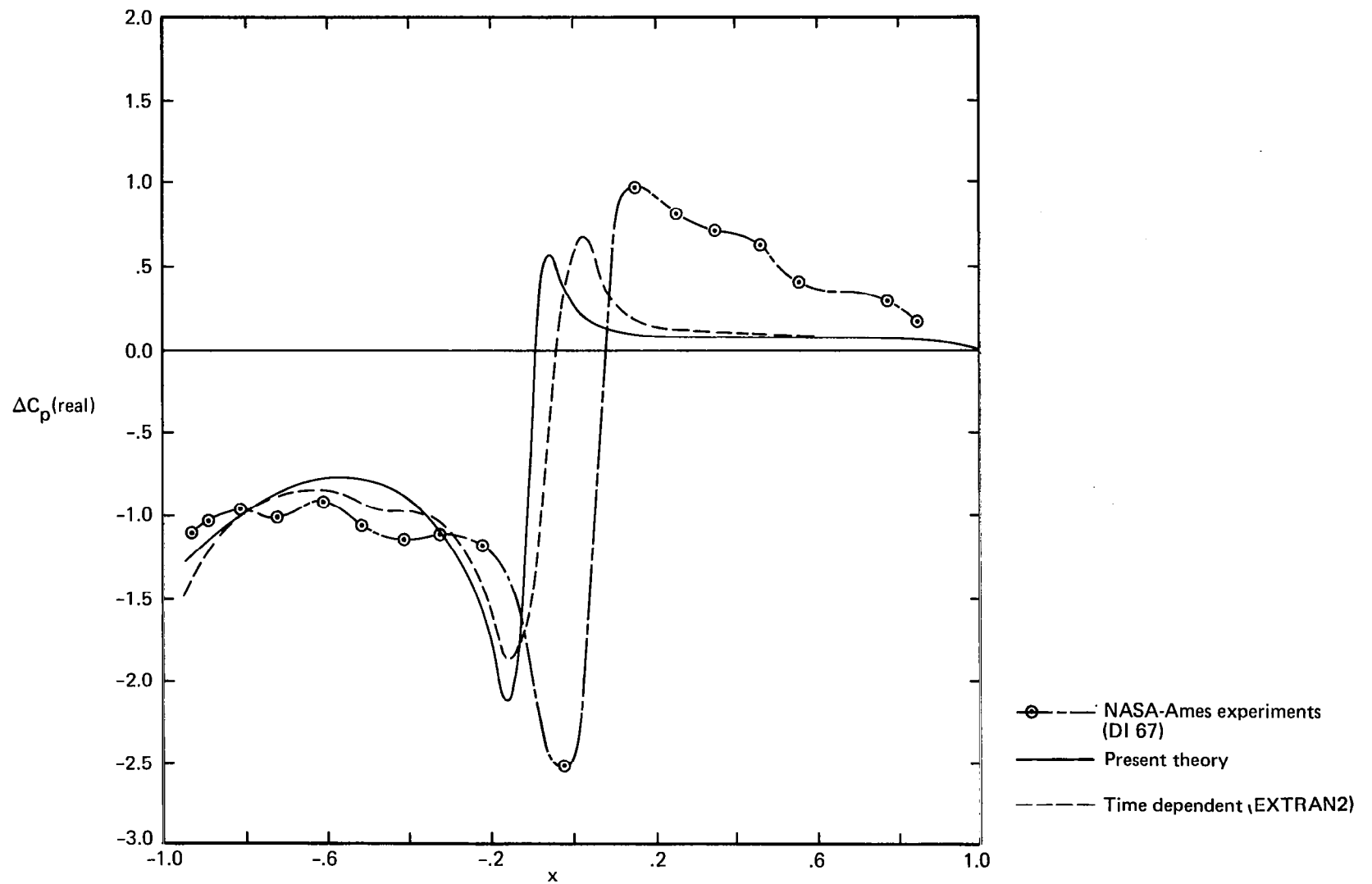


Figure 38.—Pressure Coefficient Distributions on NACA 64A010 Airfoil Oscillating 0.05 Semichord in Plunge,  $M=0.8$ ,  $k=0.151$ ,  $\alpha_m = 0^\circ$ , Real Part

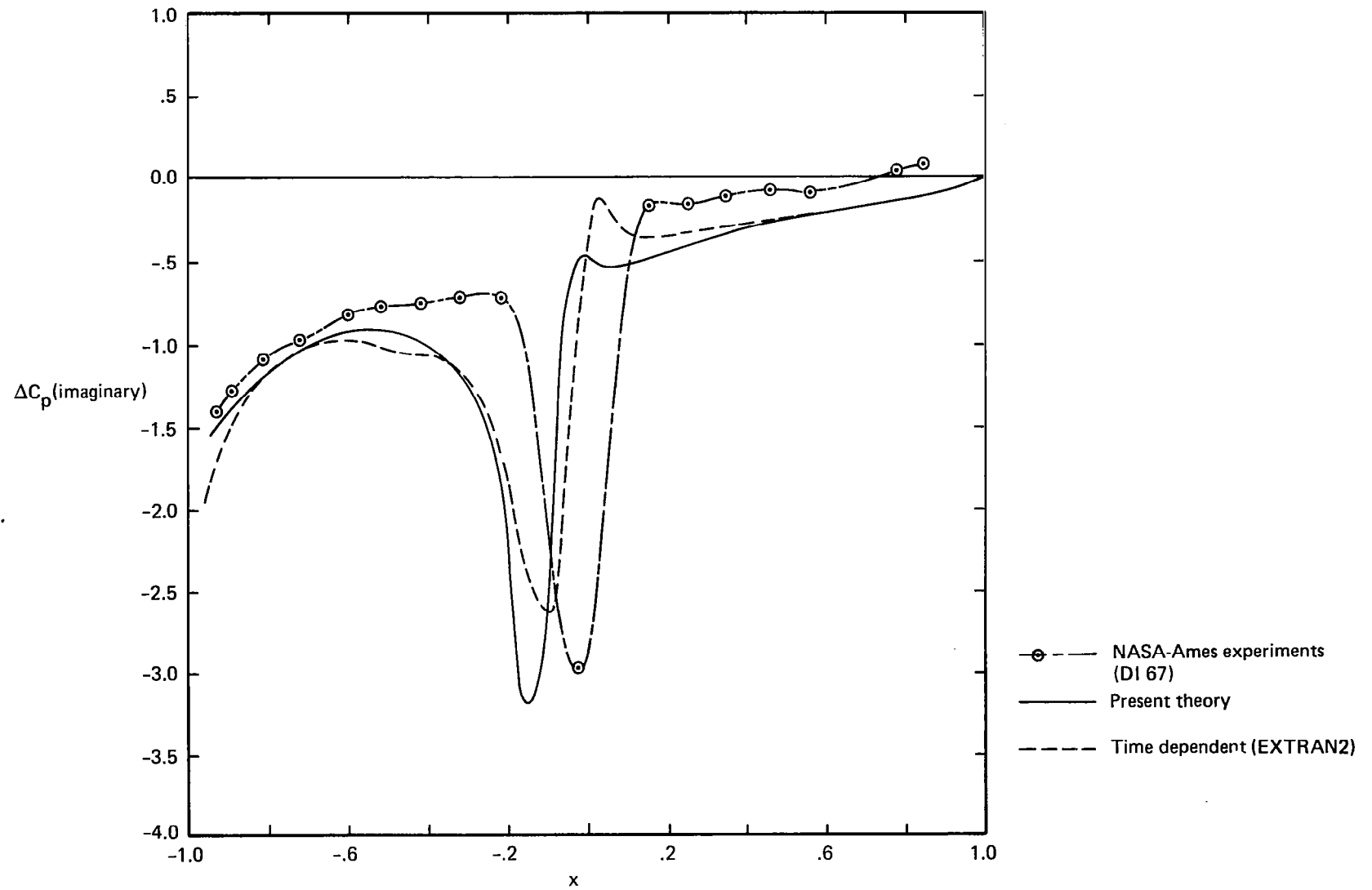


Figure 39.—Pressure Coefficient Distributions on NACA 64A010 Airfoil Oscillating 0.05 Semichord in Plunge,  $M=0.8$ ,  $k=0.151$ ,  $\alpha_m = 0^\circ$ , Imaginary Part



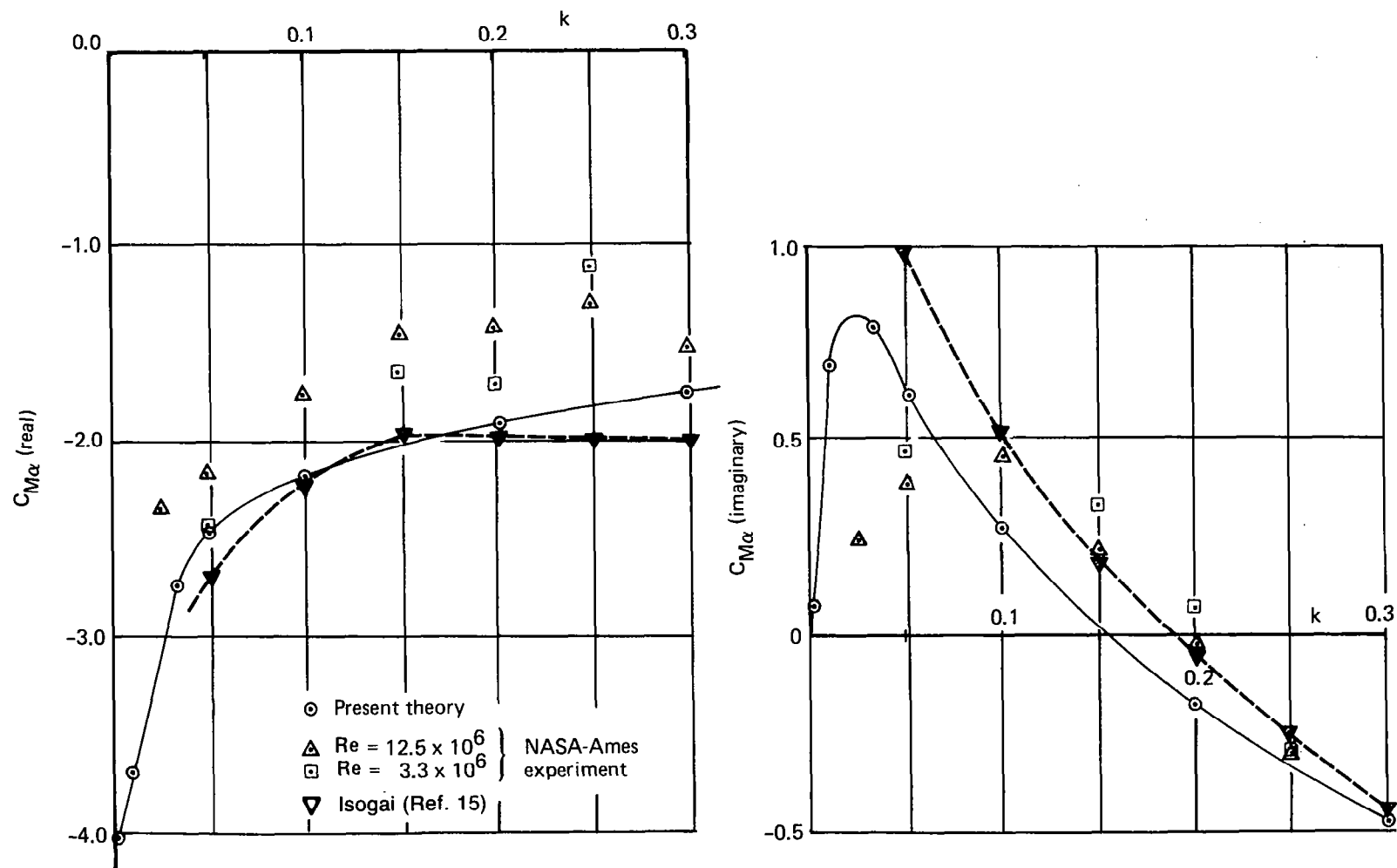


Figure 40.—Comparison With Experiment of the Calculated Moment Coefficient About the Leading Edge of a NACA 64A010 Airfoil Oscillating  $1^\circ$  in Pitch About the Quarter-Chord Point,  $M=0.8$ ,  $\alpha_m=0^\circ$

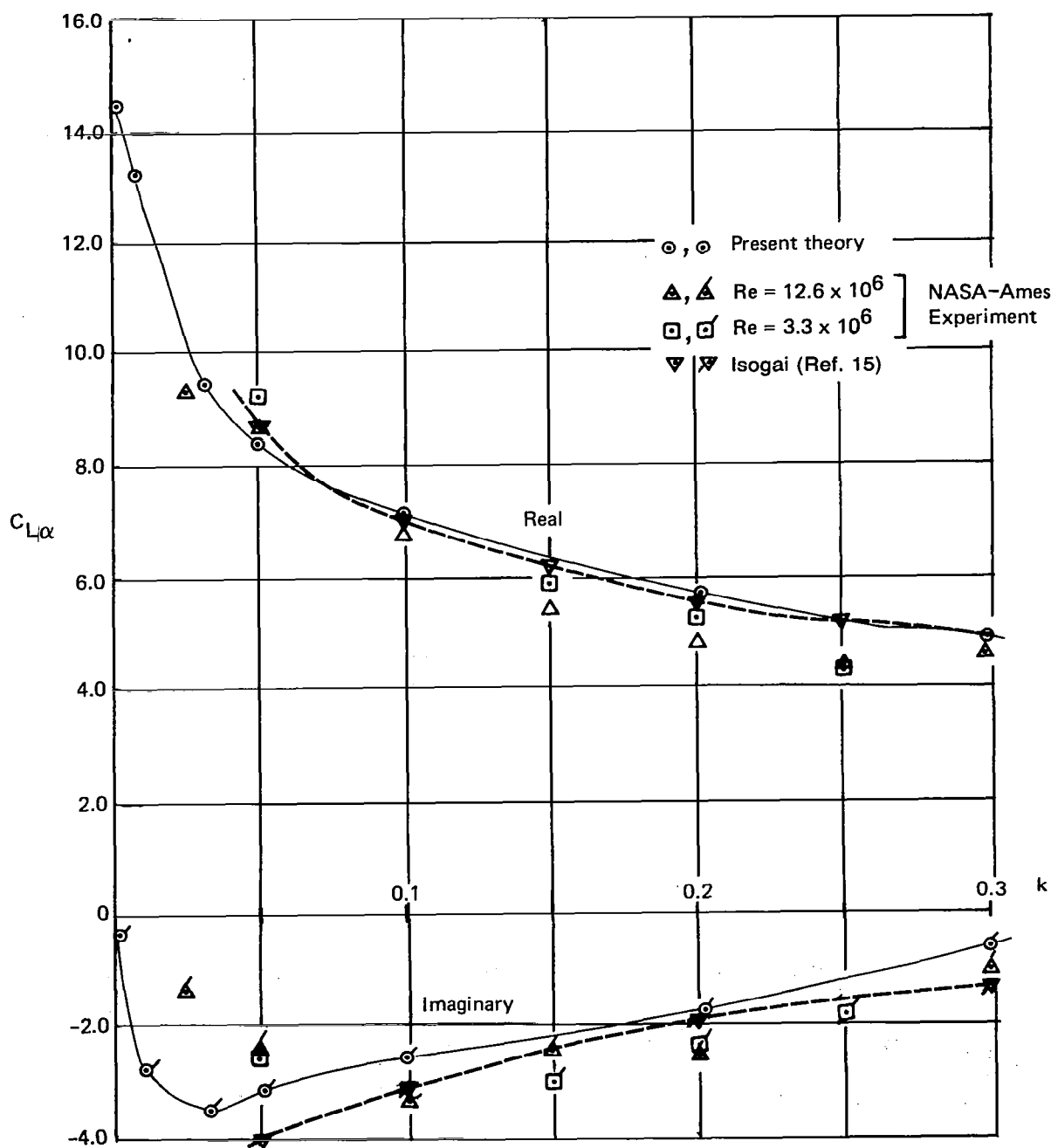


Figure 41.—Comparison With Experiment of the Calculated Lift Coefficient for a NACA 64A010 Airfoil Oscillating  $1^\circ$  in Pitch About the Quarter-Chord Point,  $M=0.8$ ,  $\alpha_m=0^\circ$

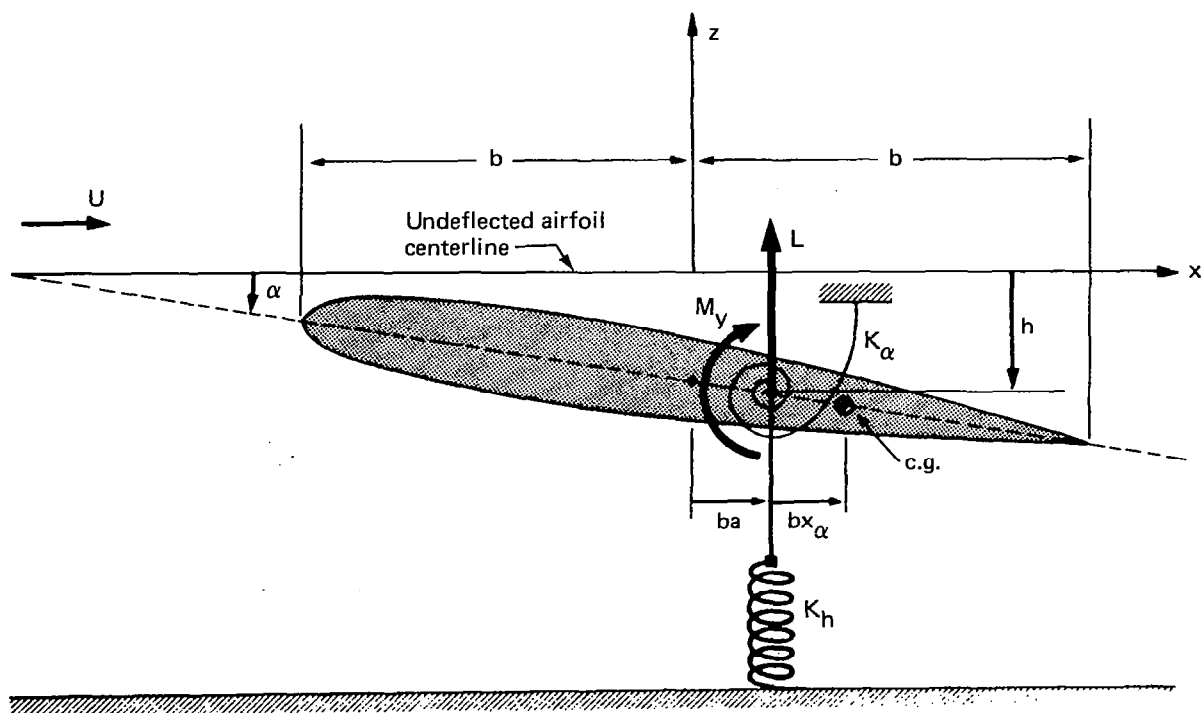


Figure 42.—Definition of Parameters for an Airfoil Oscillating in Pitch and Plunge

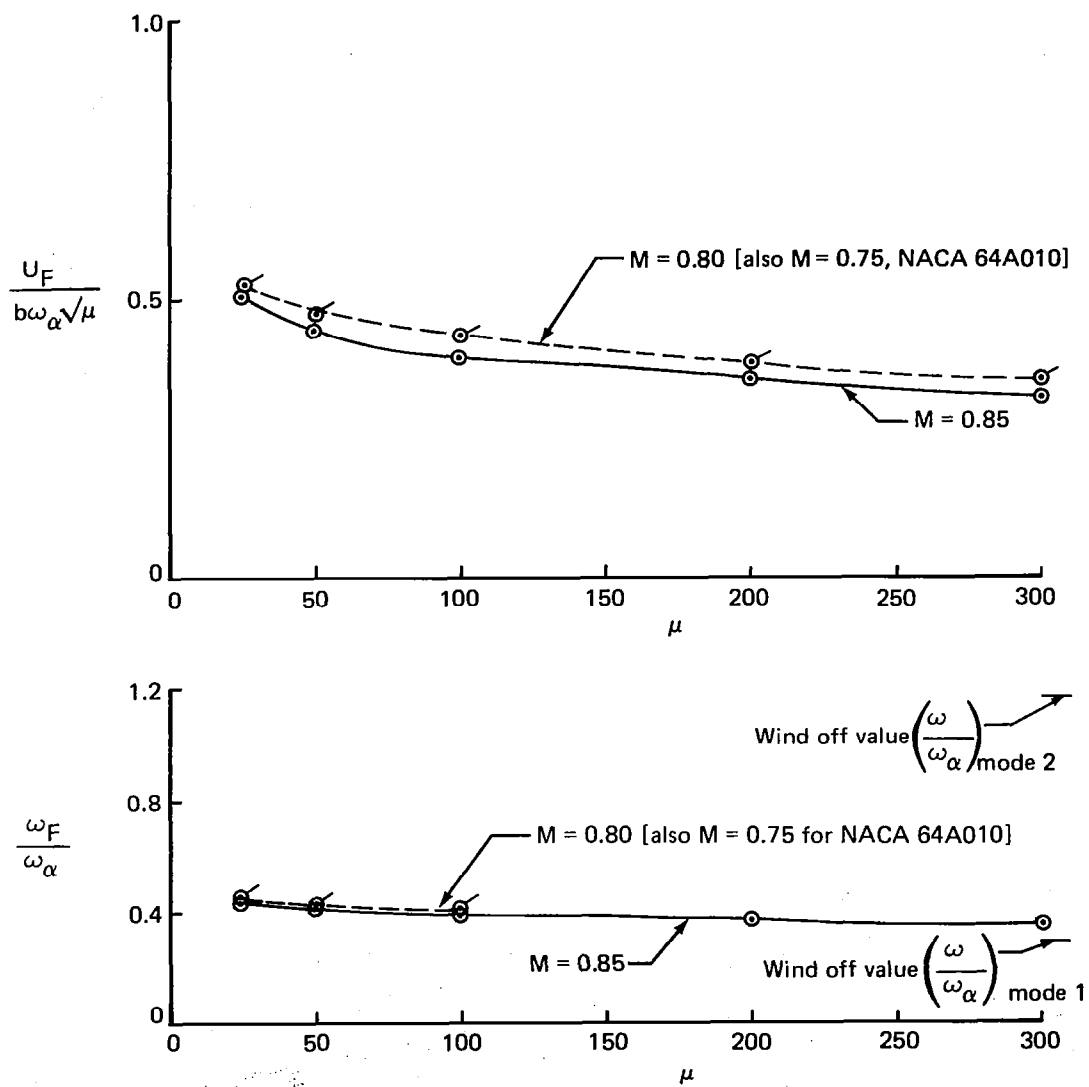


Figure 43.—Flutter Velocity and Frequency Versus Mass Ratio for a Flat Plate,  $\omega_h/\omega_\alpha = 0.3$

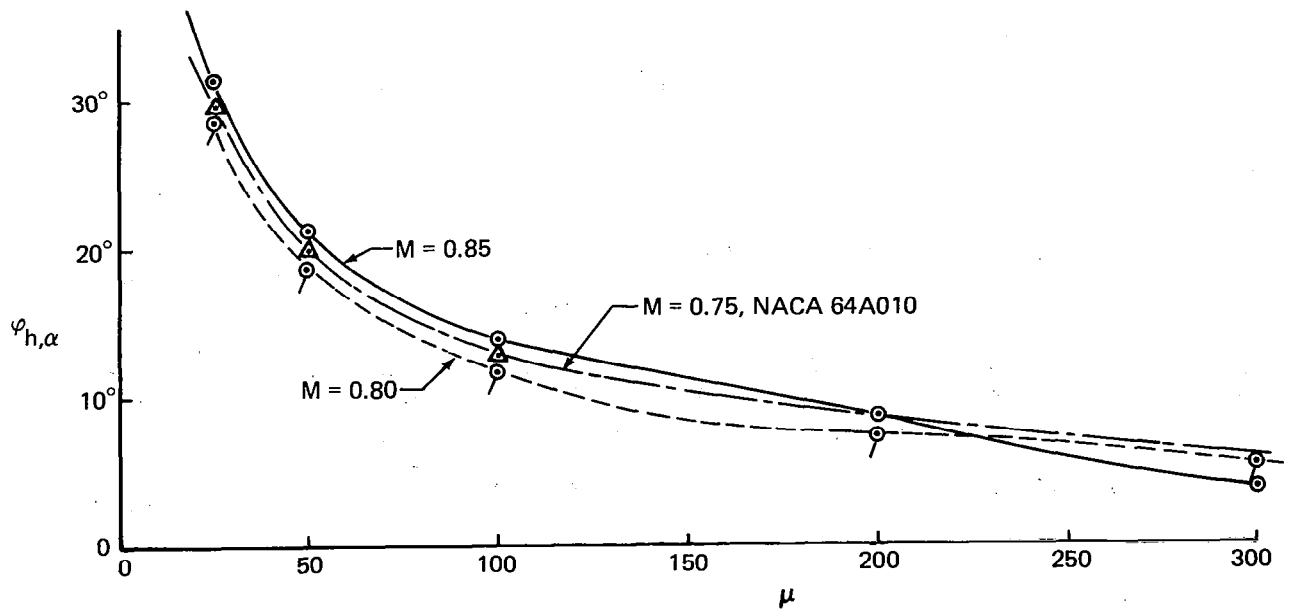
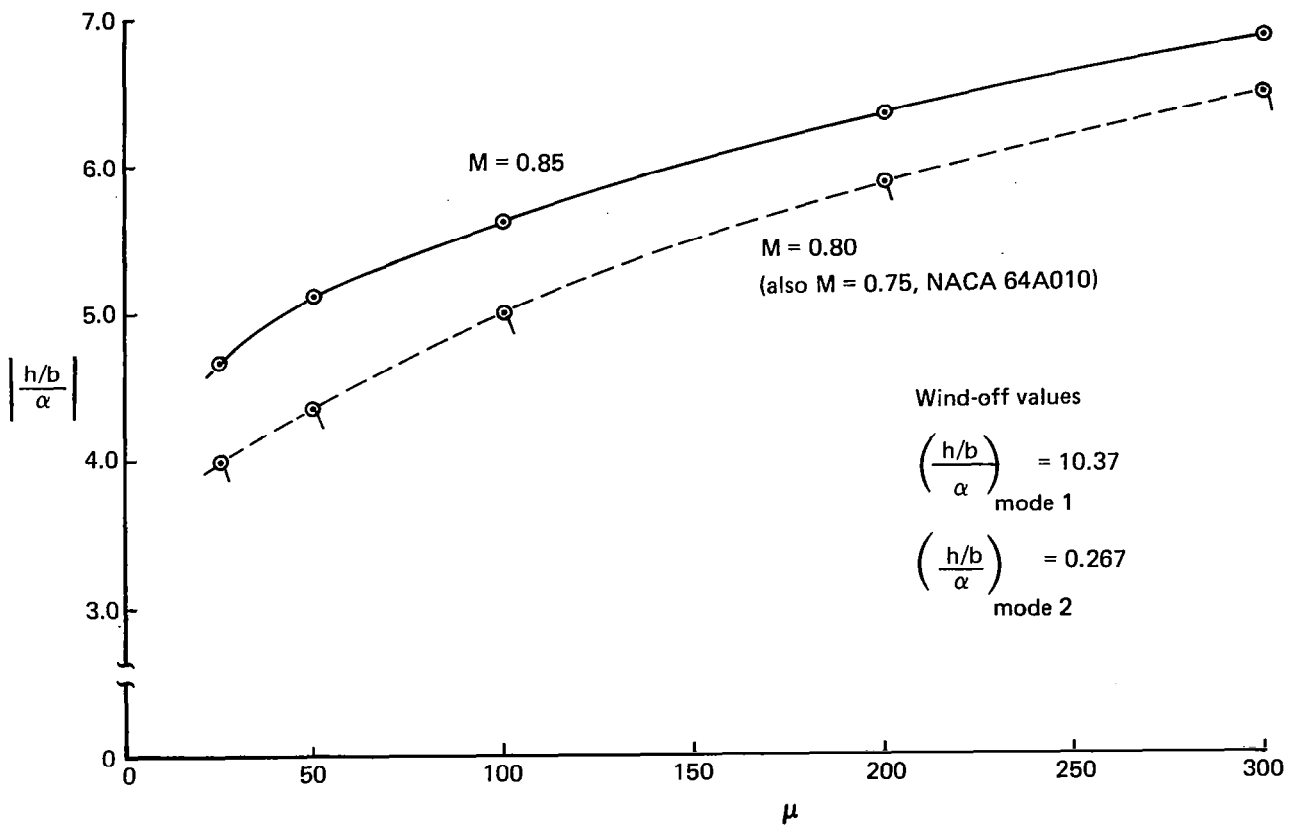


Figure 44.—Flutter Modes (Amplitude Ratio and Phase Difference) Versus Mass Ratio, Flat Plate,  $\omega_h/\omega_\alpha = 0.3$

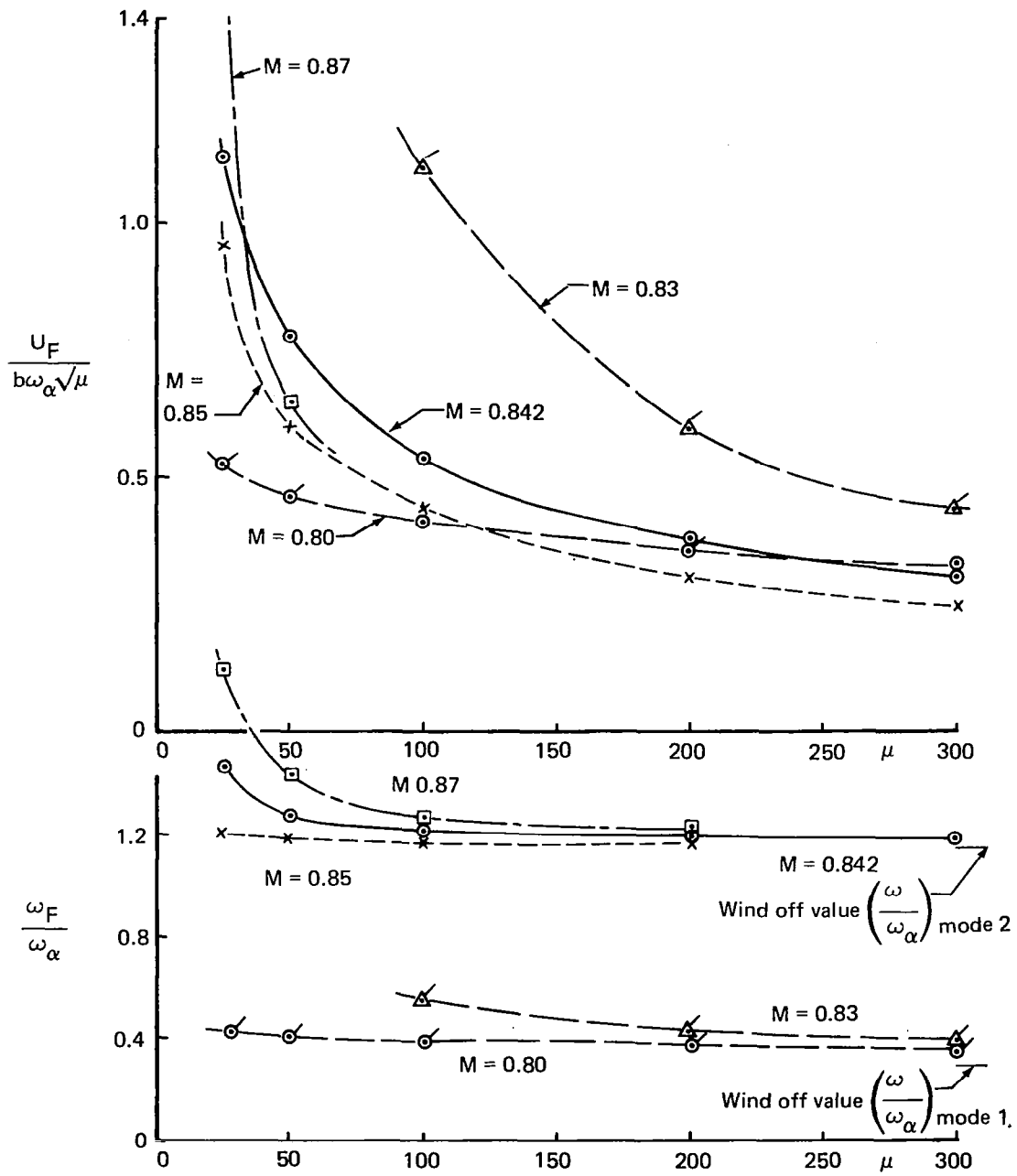


Figure 45.—Flutter Velocity and Frequency Versus Mass Ratio for a NACA 64A010 Airfoil,  $\omega_h/\omega_\alpha=0.3$

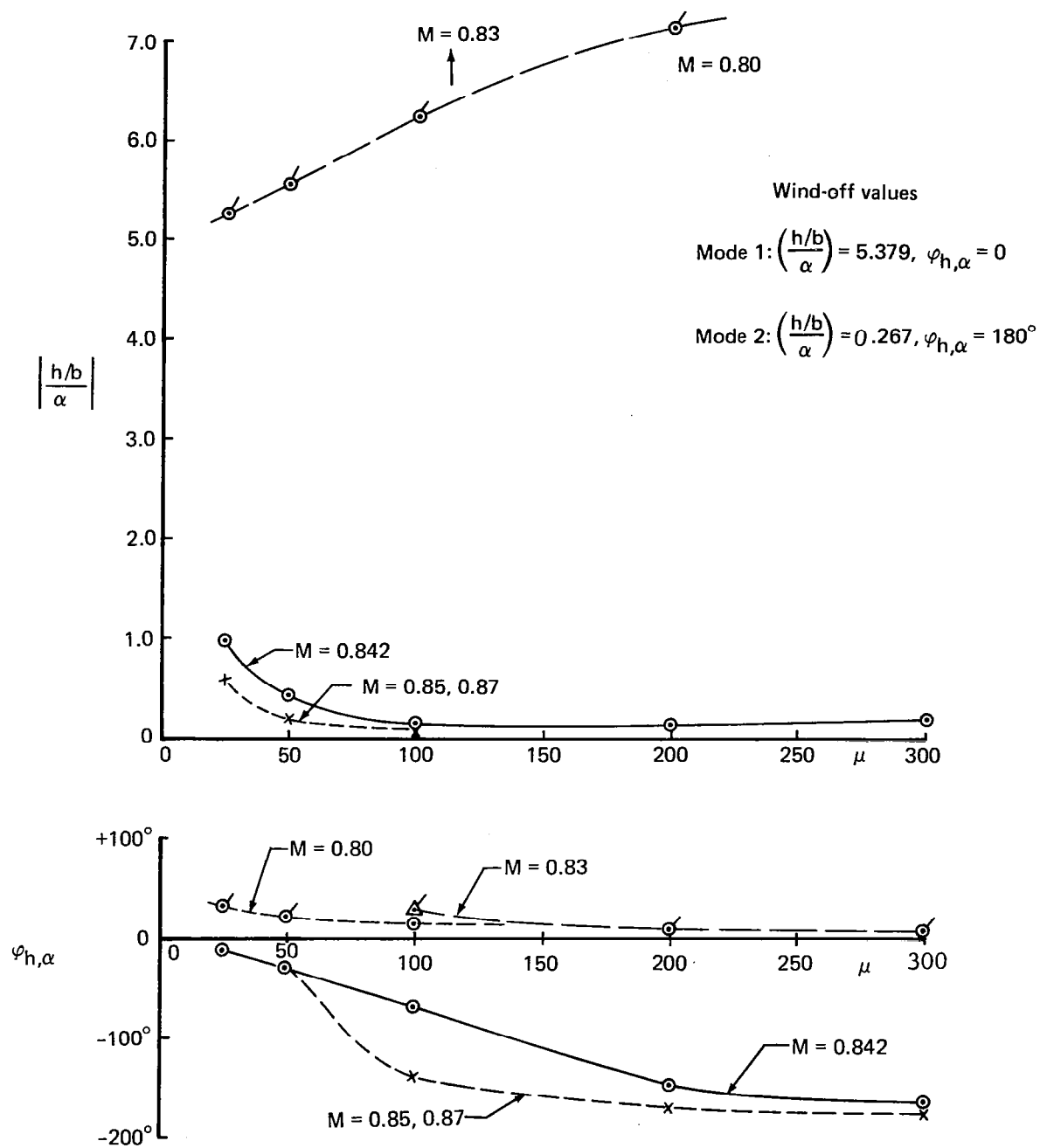


Figure 46.—Flutter Modes (Amplitude Ratio and Phase Difference) Versus Mass Ratio,  $\omega_h/\omega_\alpha = 0.3$

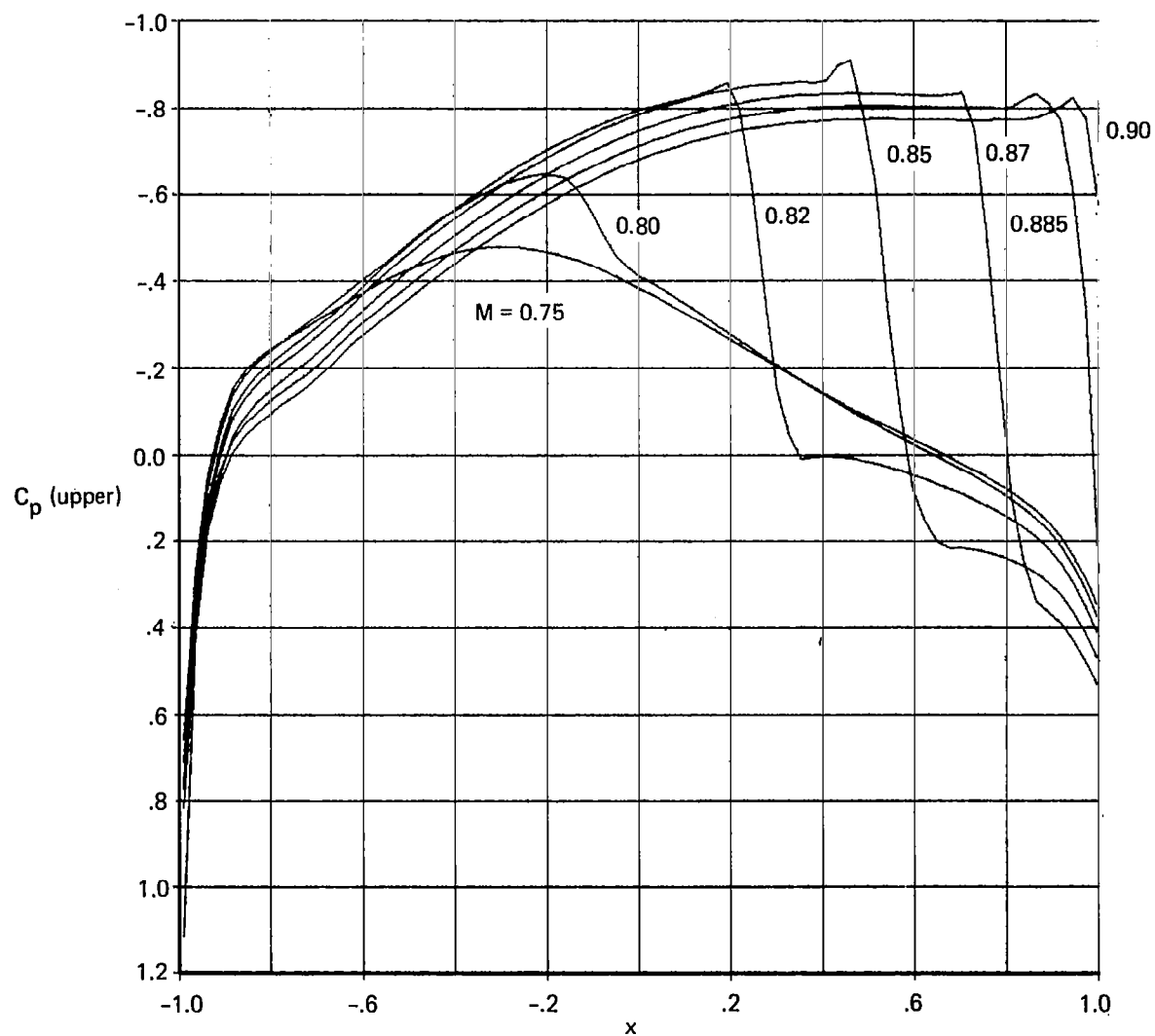


Figure 47.—Effect of Mach Number on the Steady Pressure Distribution on the Upper Surface of a NACA 64A010 Airfoil



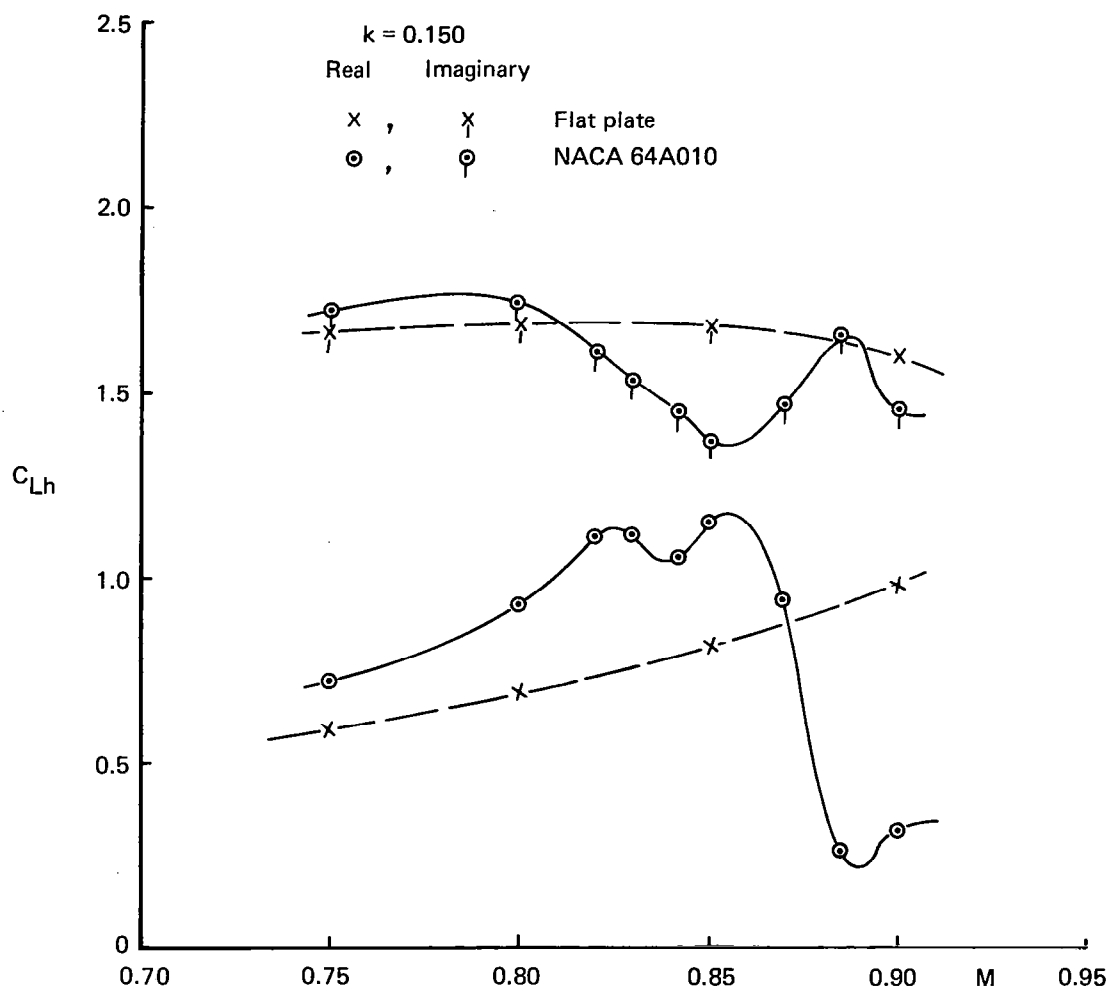


Figure 48.—Lift Coefficient Versus Mach Number for a NACA 64A010 Airfoil Oscillating in Plunge

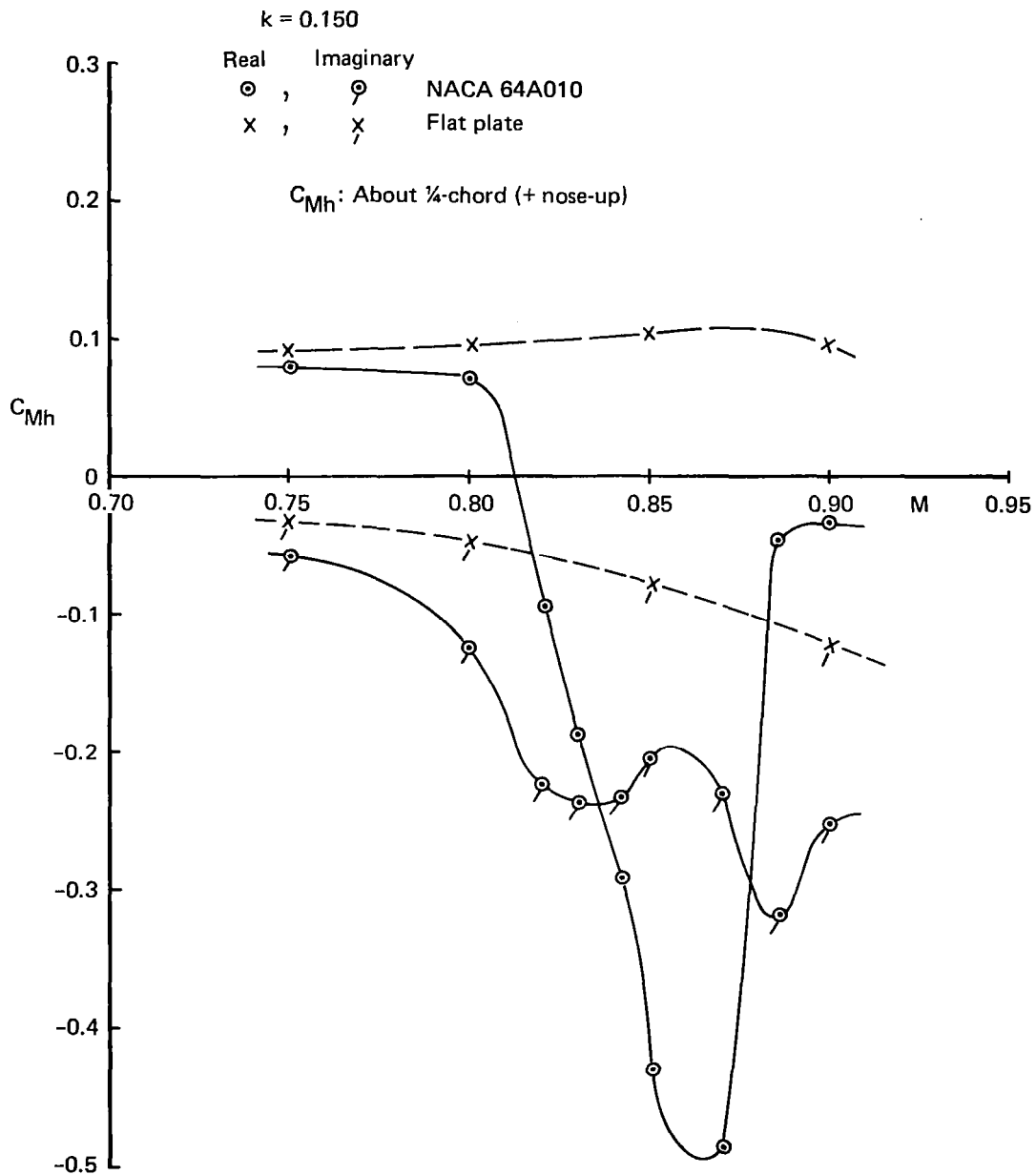


Figure 49.—Moment Coefficient Versus Mach Number for a NACA 64A010 Airfoil Oscillating in Plunge

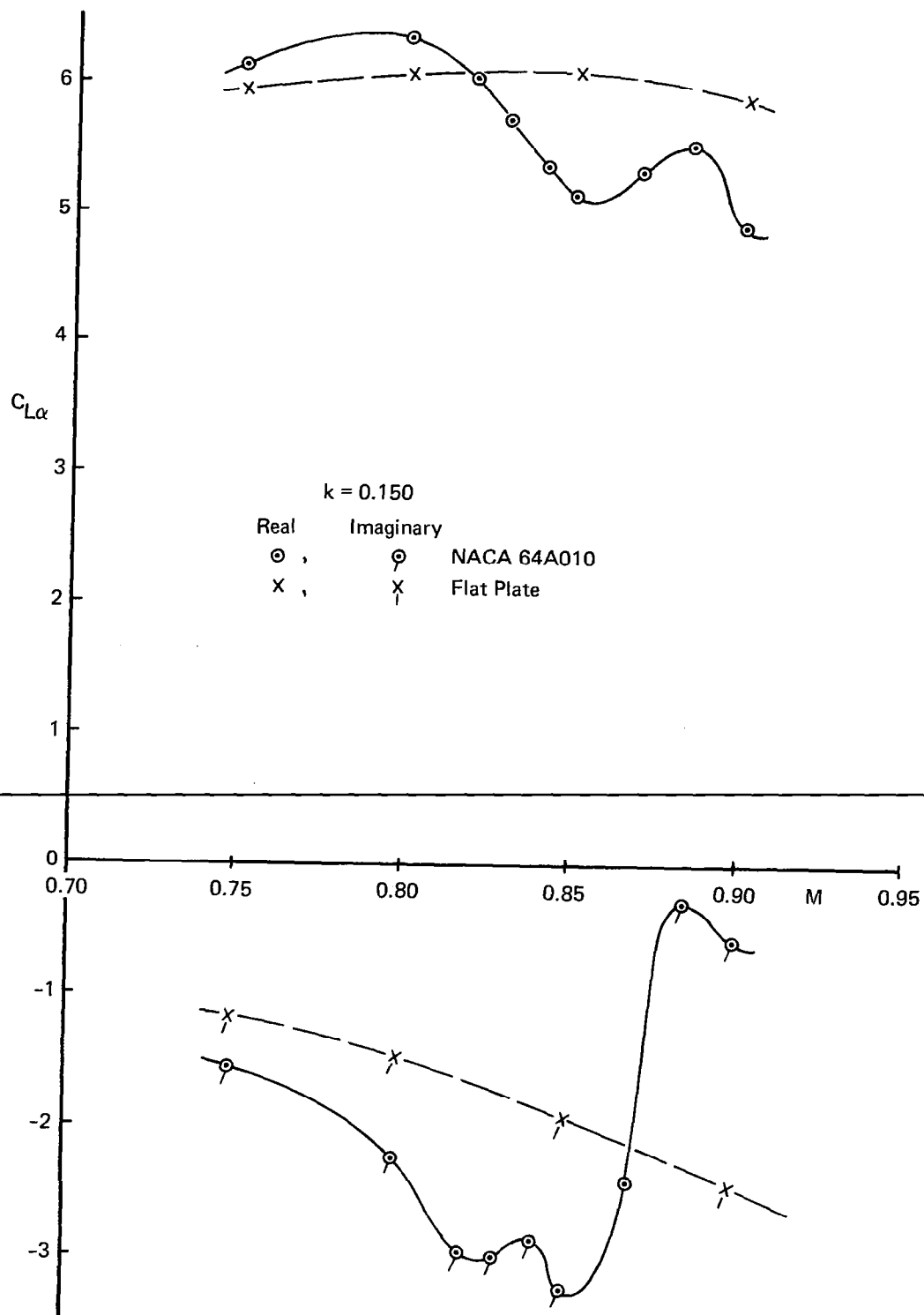


Figure 50.—Lift Coefficient Versus Mach Number for a NACA 64A010 Airfoil Oscillating in Pitch

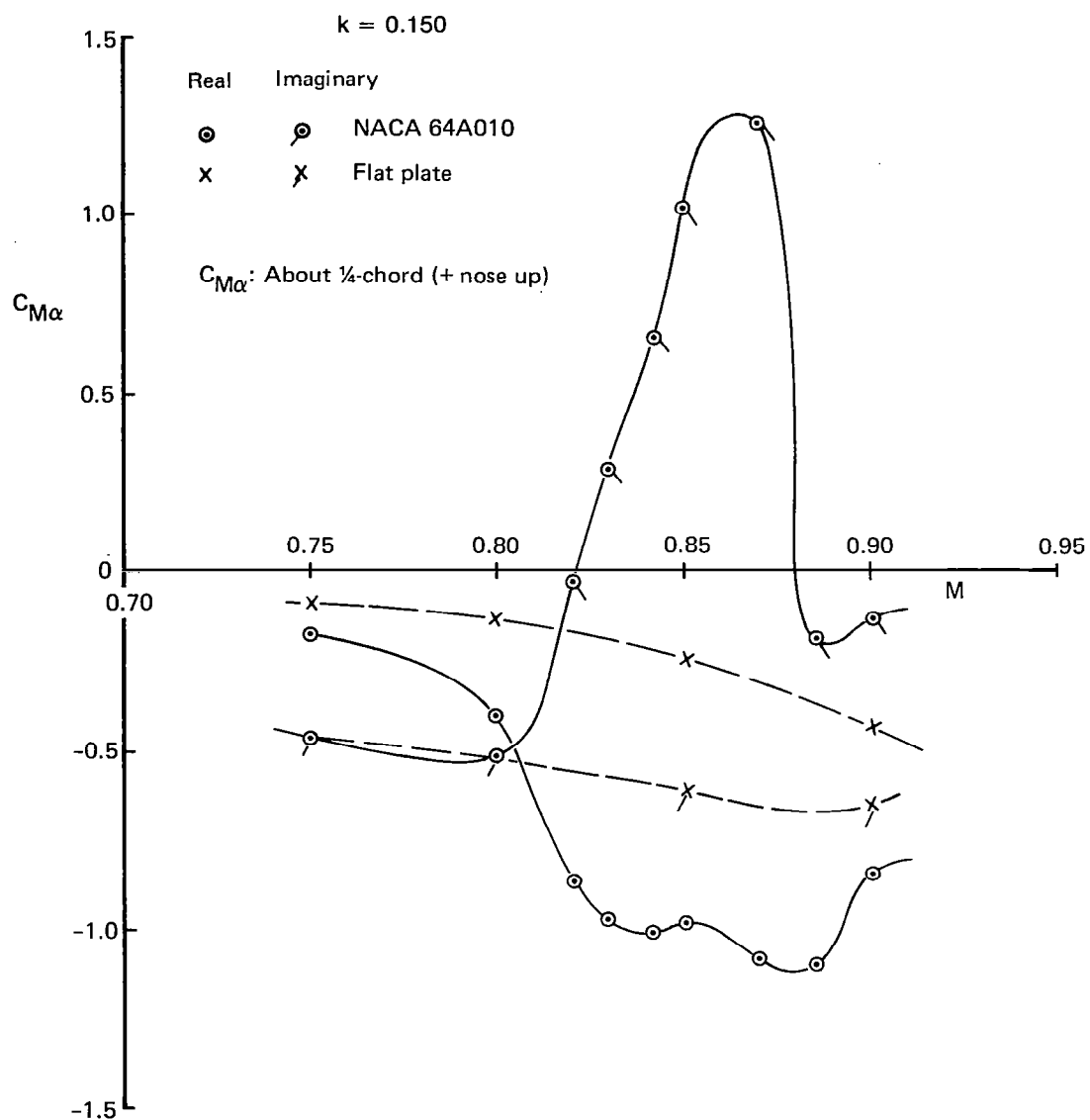


Figure 51.—Moment Coefficient Versus Mach Number for a NACA 64A010 Airfoil Oscillating in Pitch About Quarter-Chord

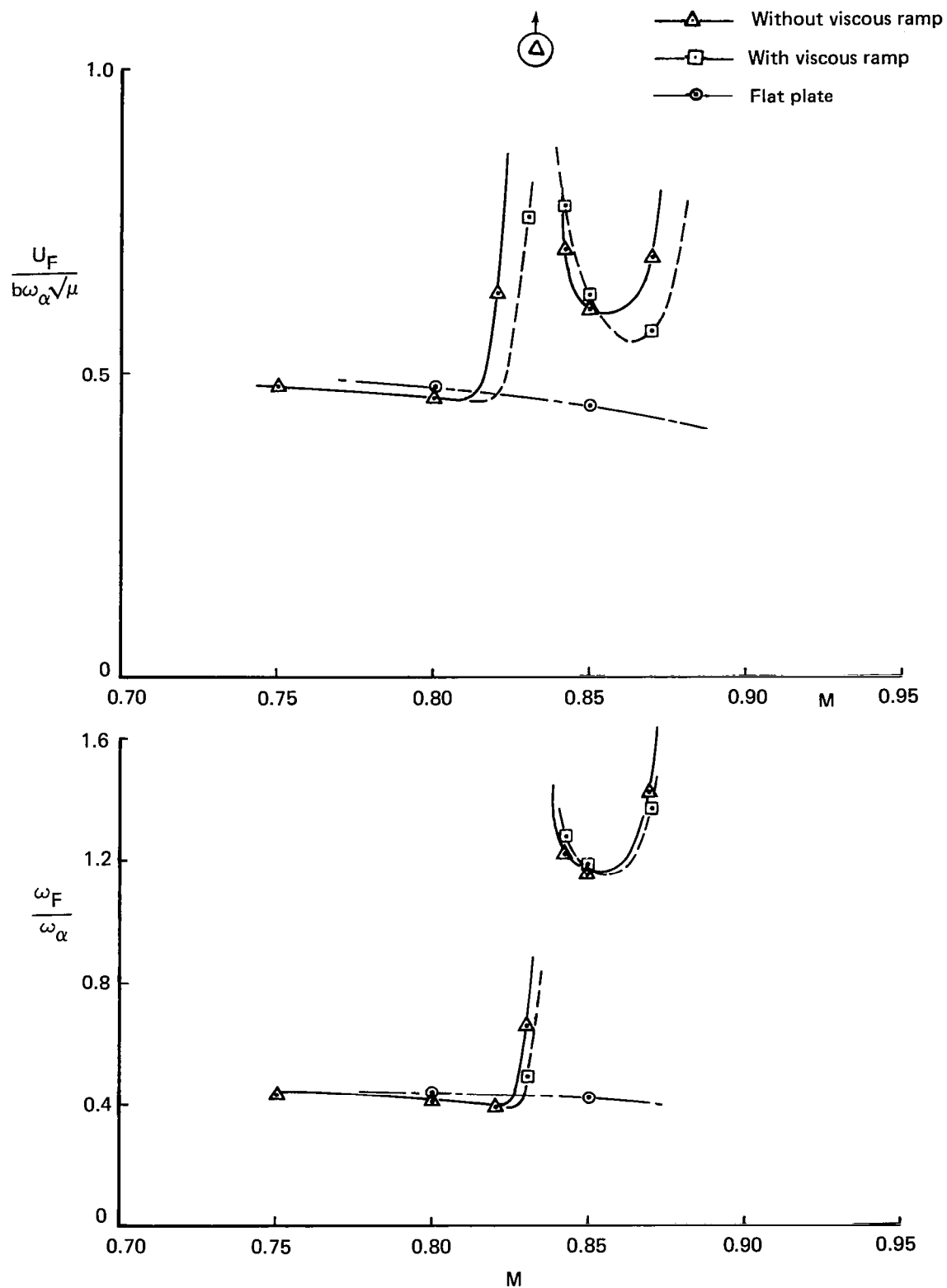


Figure 52.—Flutter Velocity and Frequency Ratio Versus Mach Number for a NACA 64A010,  $\omega_h/\omega_\alpha = 0.3$ ,  $\mu = 50$

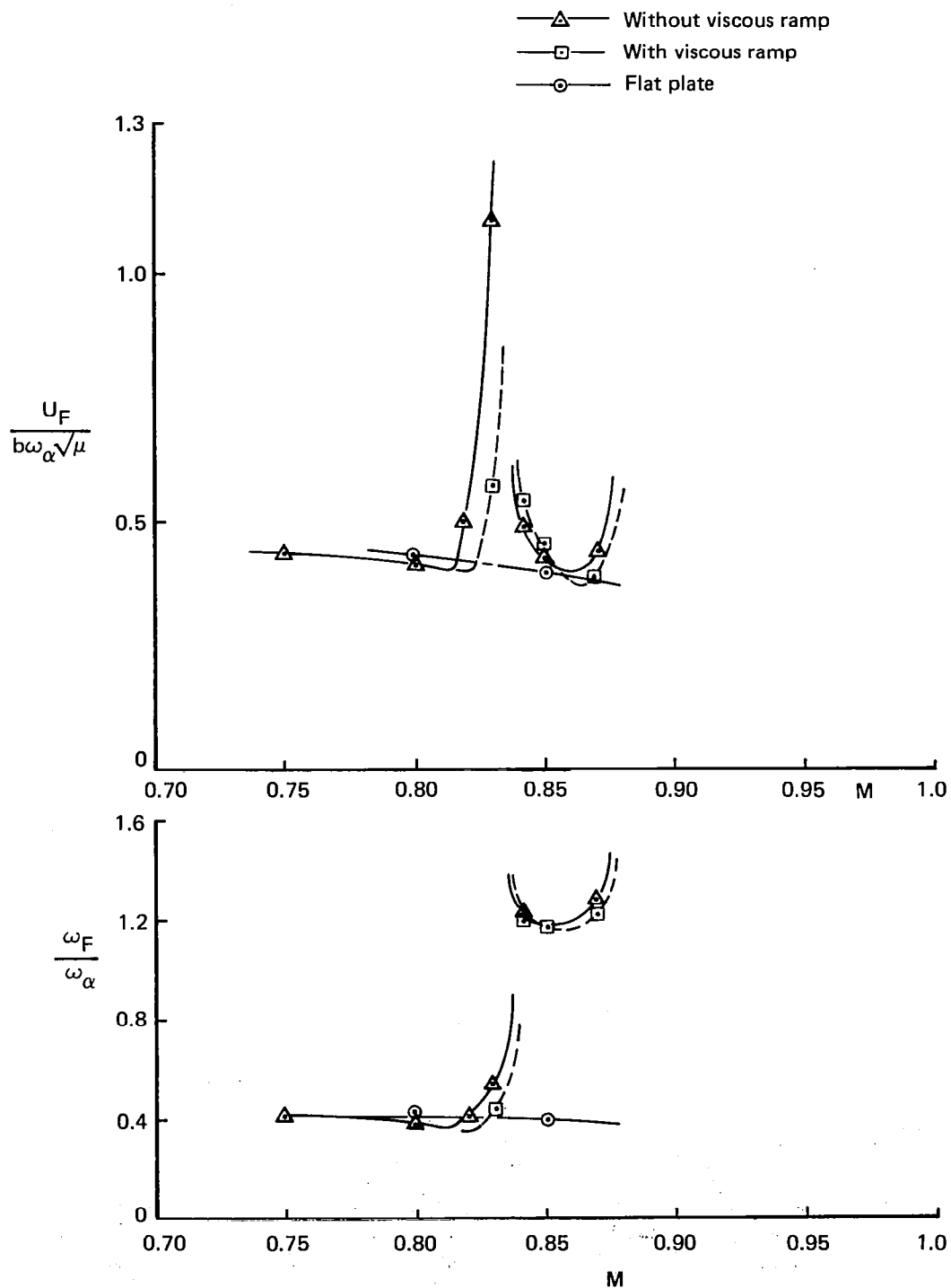


Figure 53.—Flutter Velocity and Frequency Versus Mach Number for a NACA 64A010 Airfoil,  $\omega_h/\omega_\alpha = 0.3$ ,  $\mu = 100$

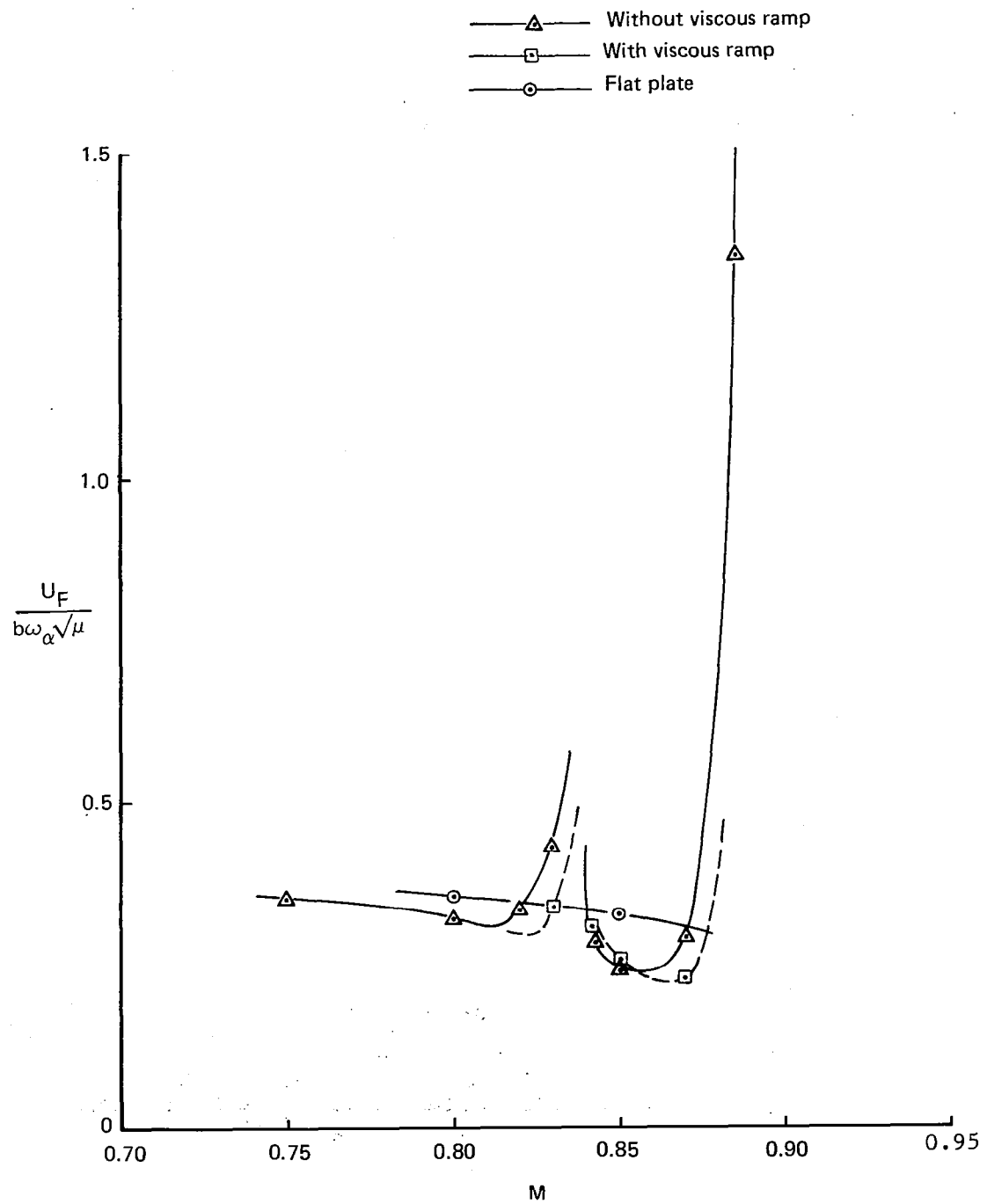


Figure 54.—Flutter Velocity and Frequency Versus Mach Number for a NACA 64A010 Airfoil,  $\omega_h/\omega_\alpha = 0.3$ ,  $\mu = 300$

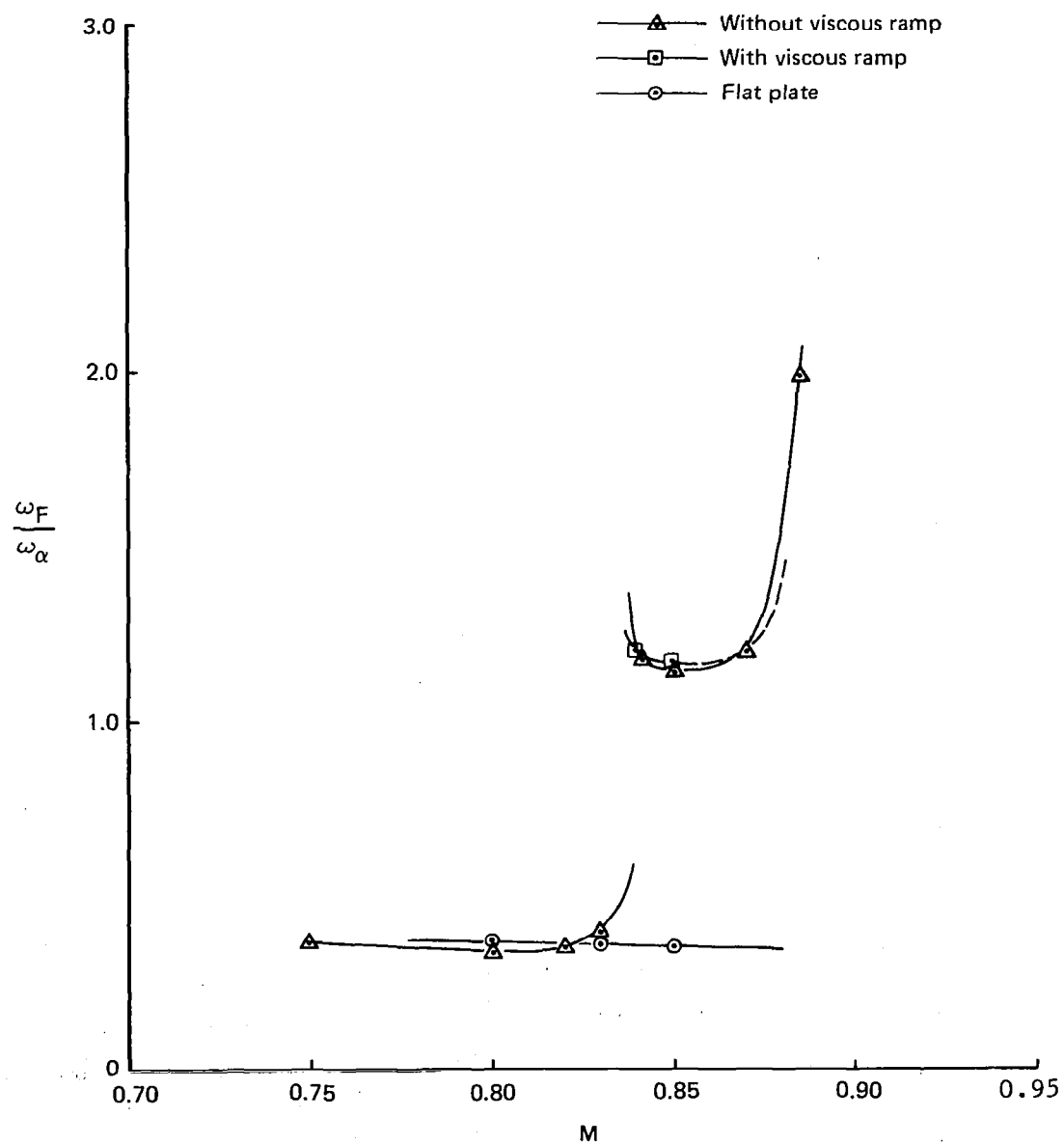


Figure 54.—(Concluded)



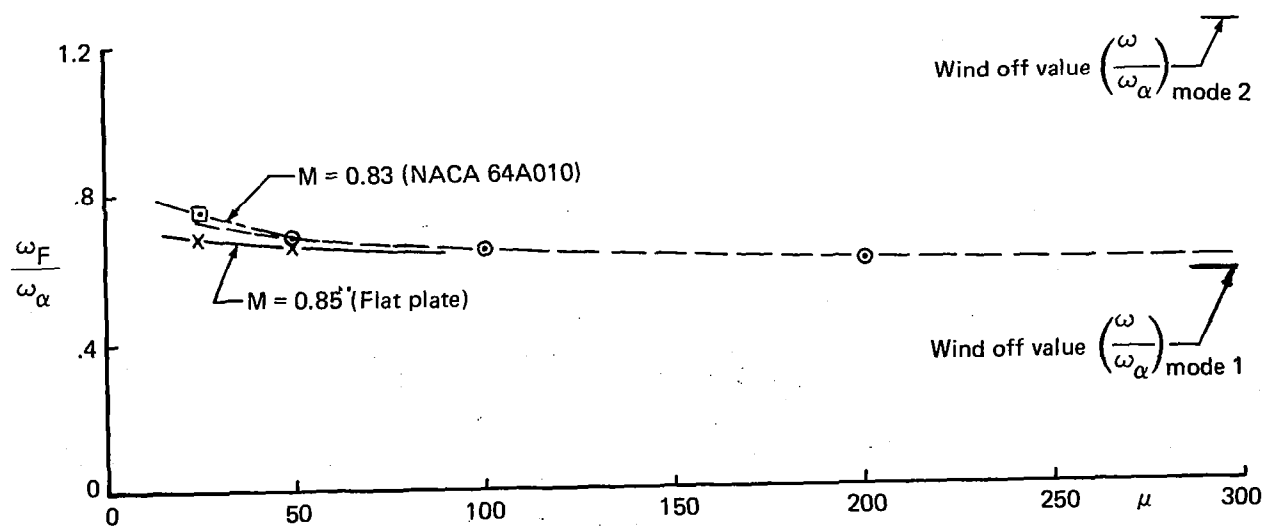
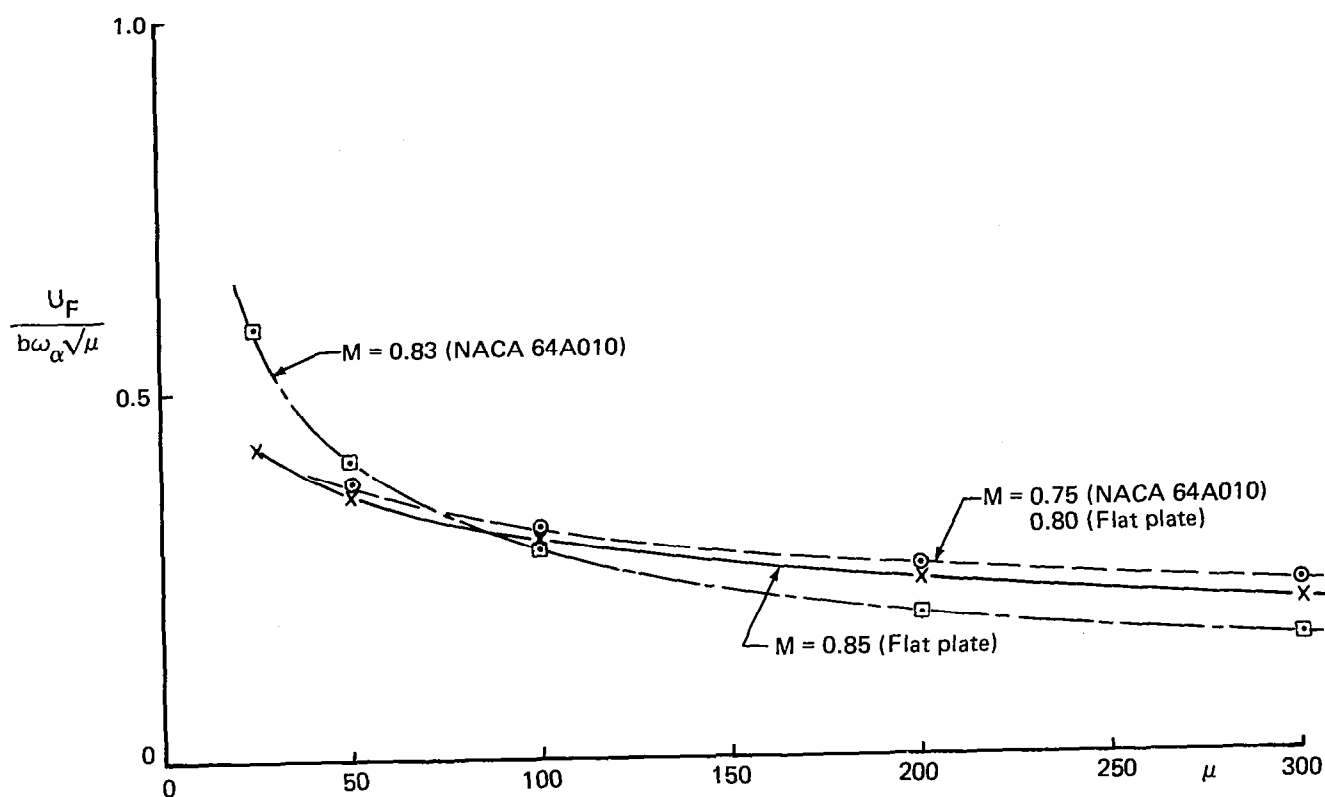


Figure 55.—Flutter Velocity and Frequency Versus Mass Ratio, Subsonic Flow,  $\omega_h/\omega_\alpha = 0.6$

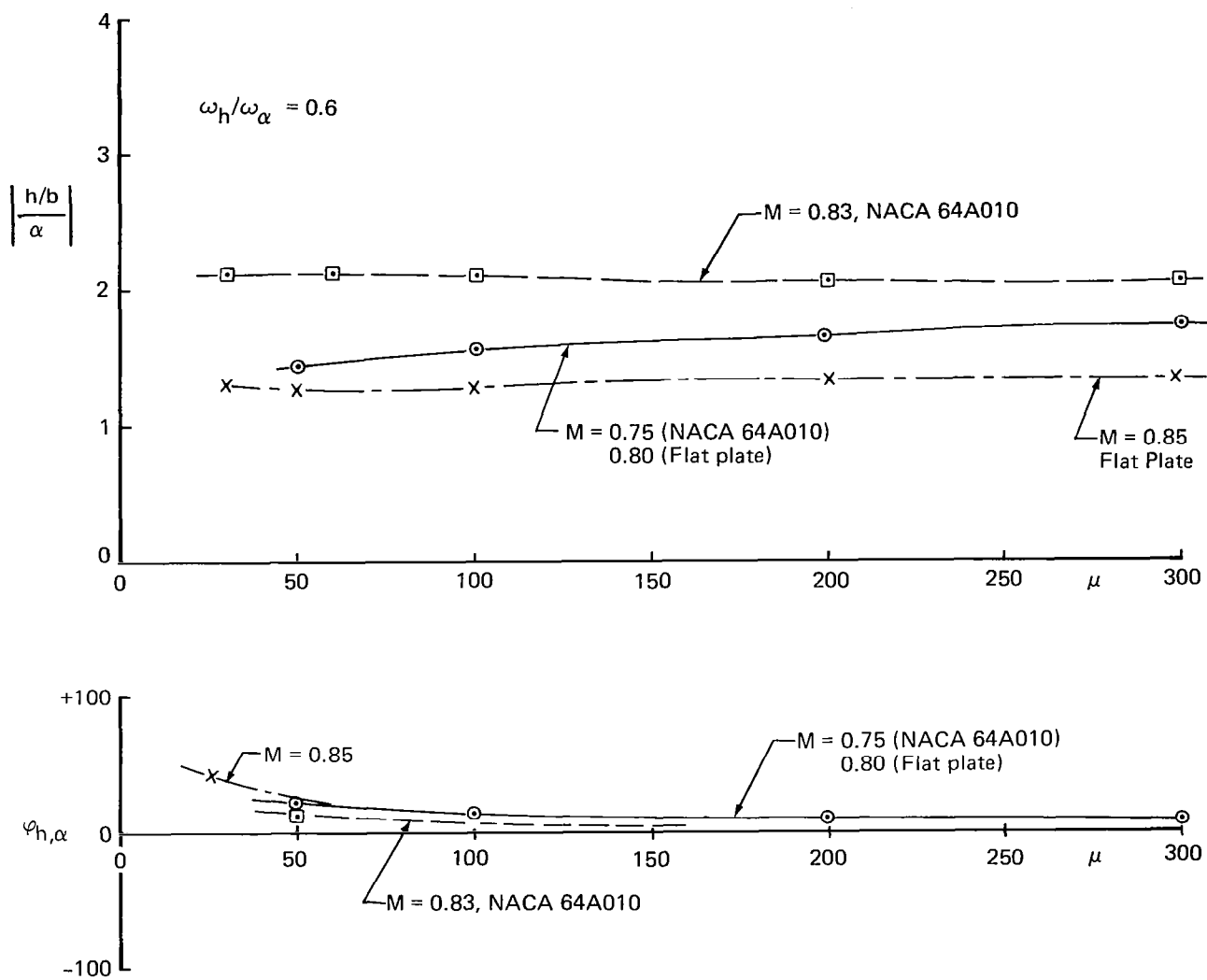


Figure 56. —Flutter Modes (Amplitude Ratio and Phase Difference) Versus Mass Ratio, Subsonic Flow

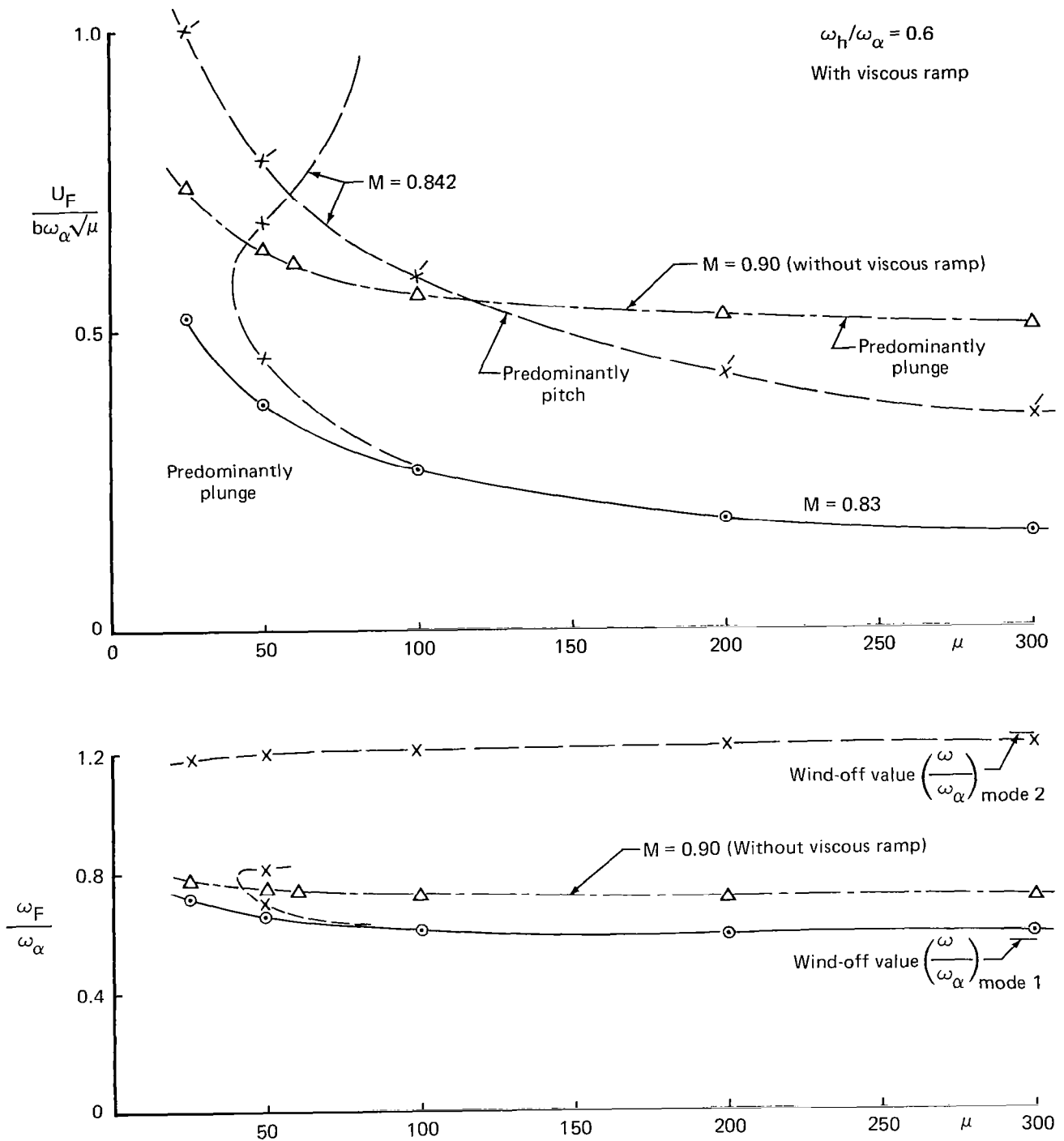


Figure 57.—Flutter Velocity and Frequency Versus Mass Ratio for a NACA 64A010 Airfoil

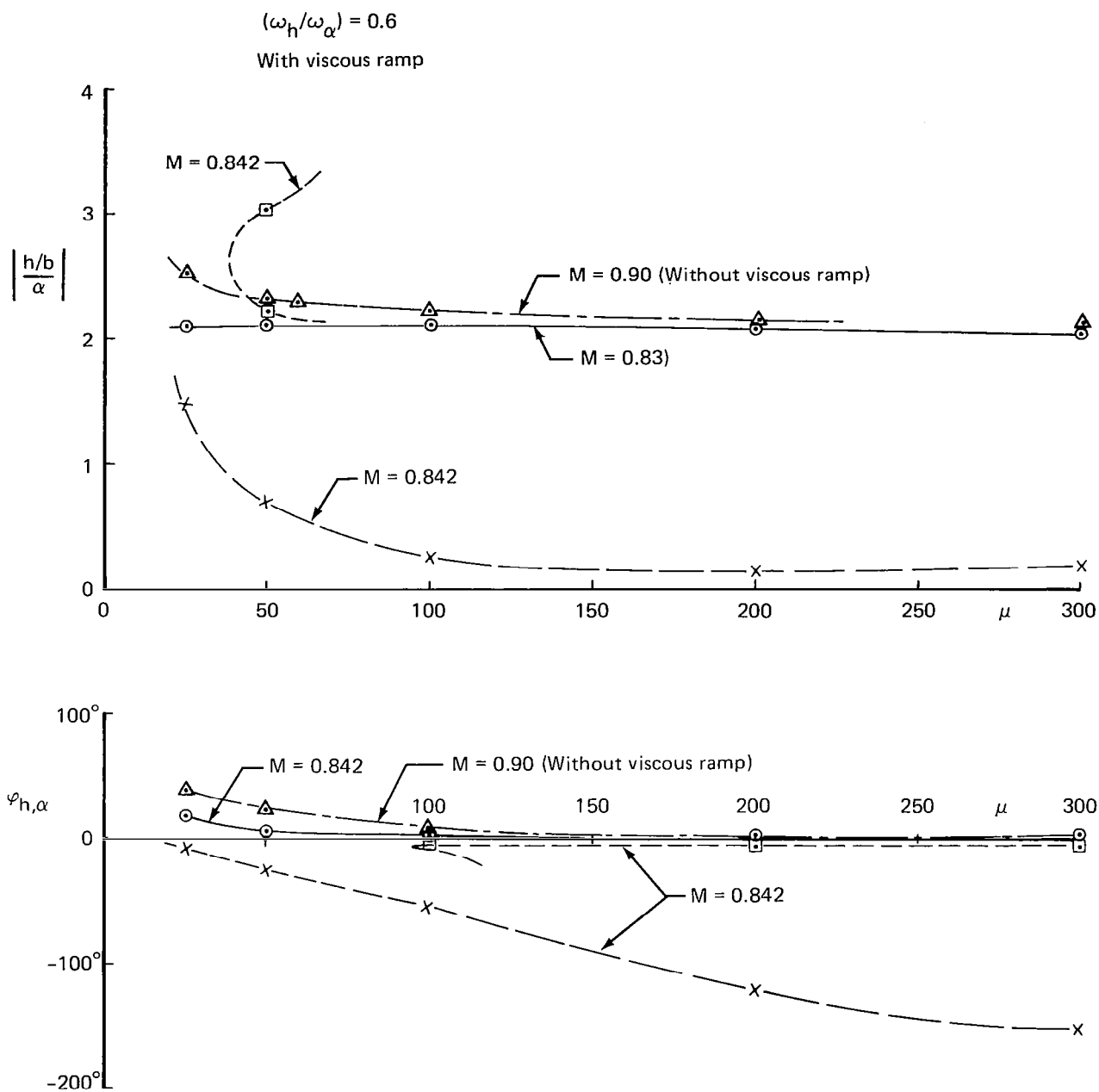


Figure 58.—Flutter Modes (Amplitude Ratio and Phase Difference) Versus Mass Ratio for a NACA 64A010 Airfoil

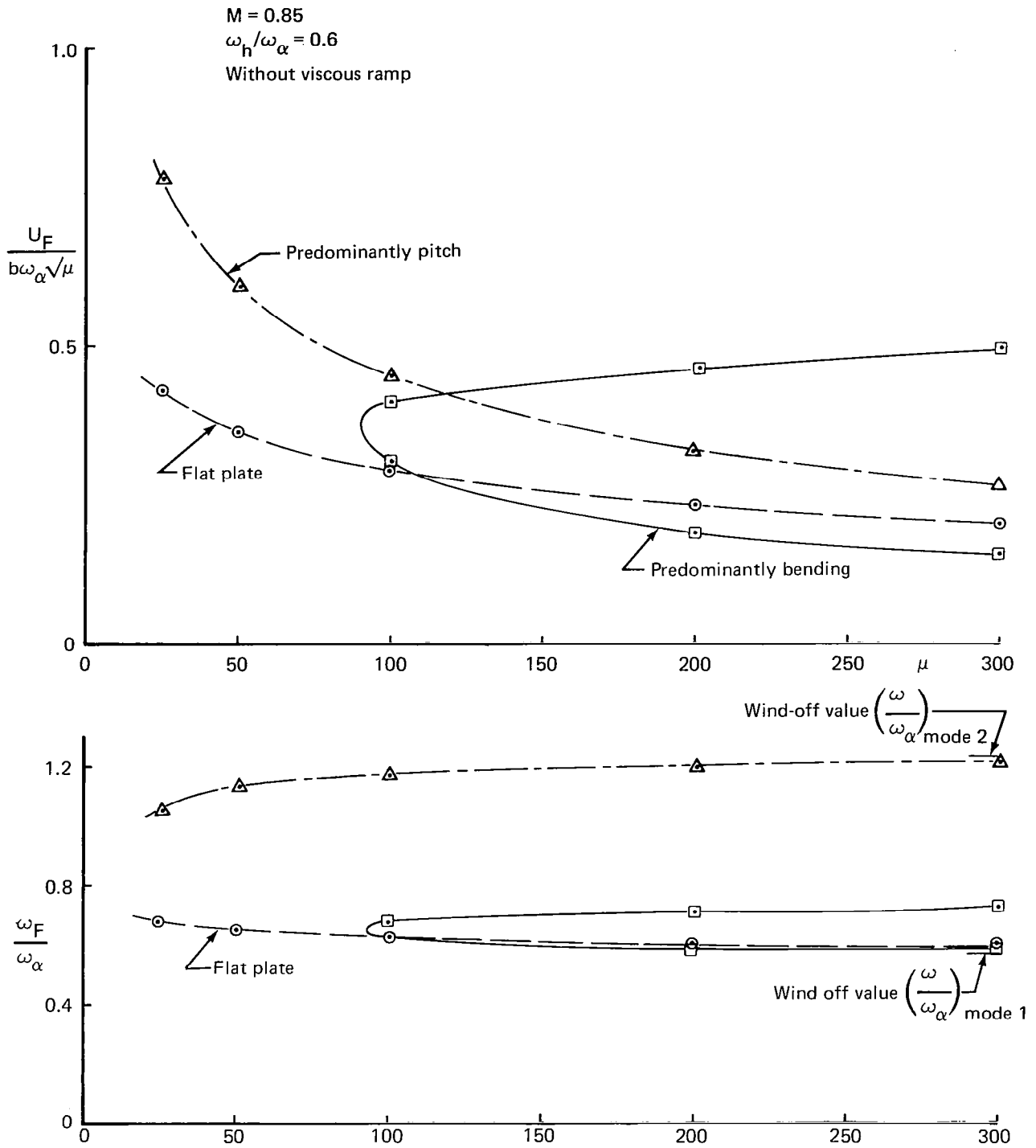


Figure 59.—Flutter Velocity and Frequency Versus Mass Ratio for a NACA 64A010 Airfoil

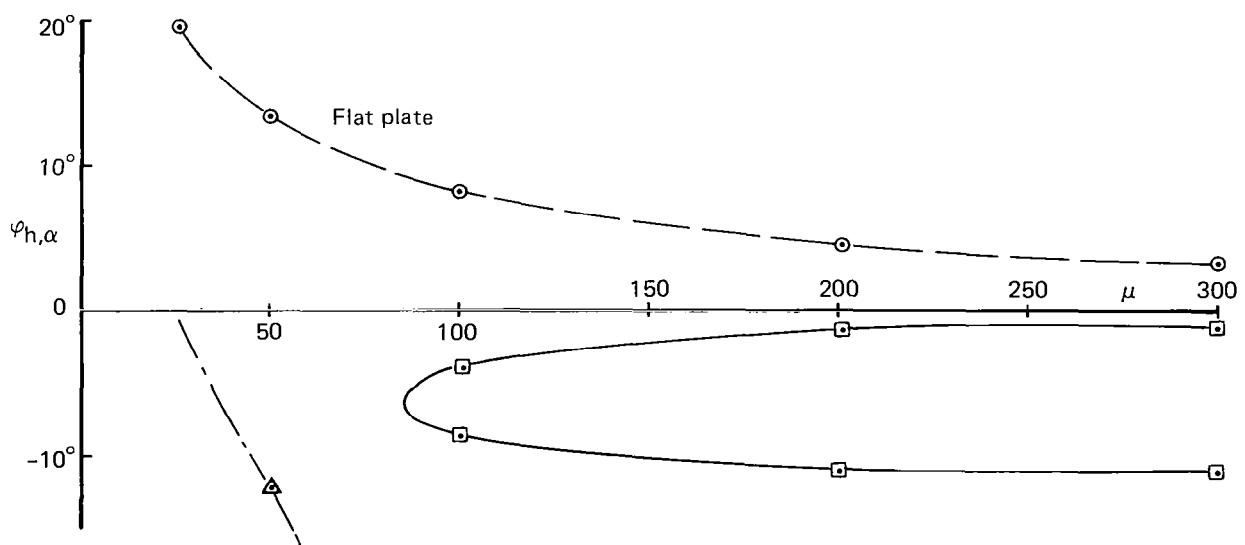
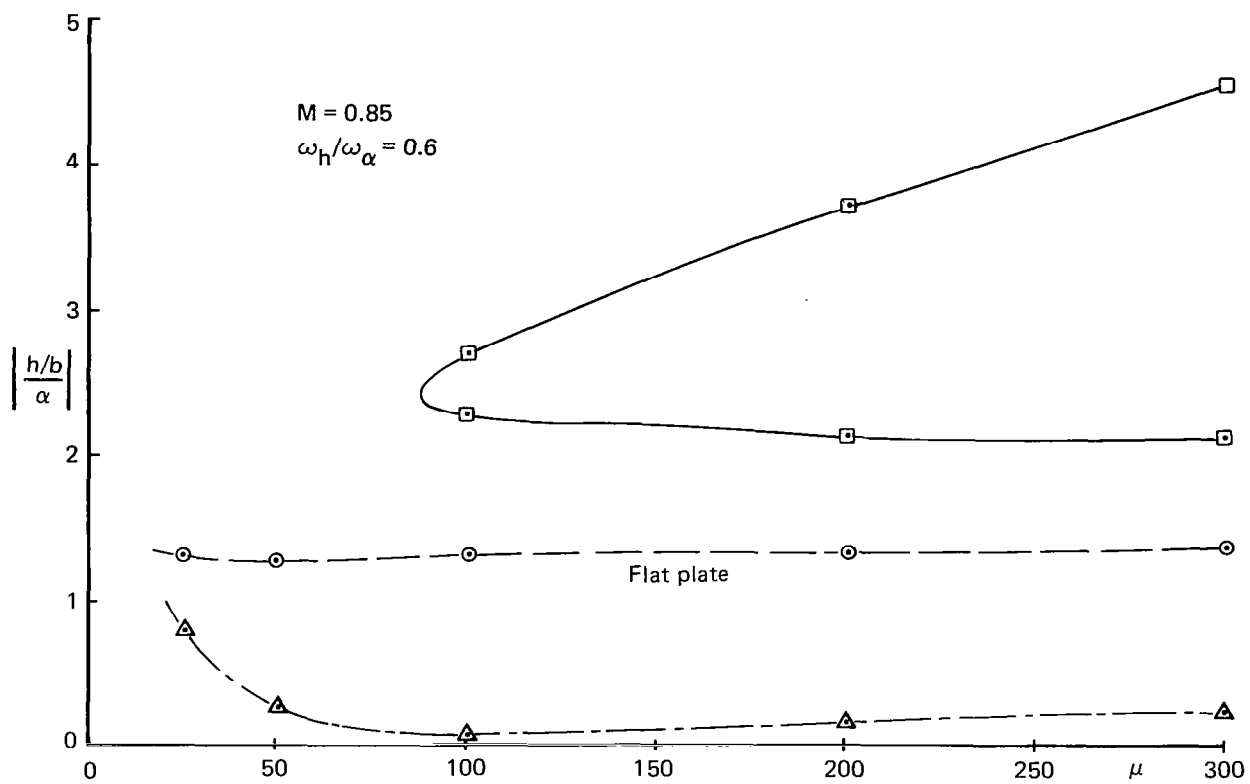


Figure 60.—Flutter Modes (Amplitude Ratio and Phase Difference) Versus Mass Ratio for a NACA 64A010 Airfoil

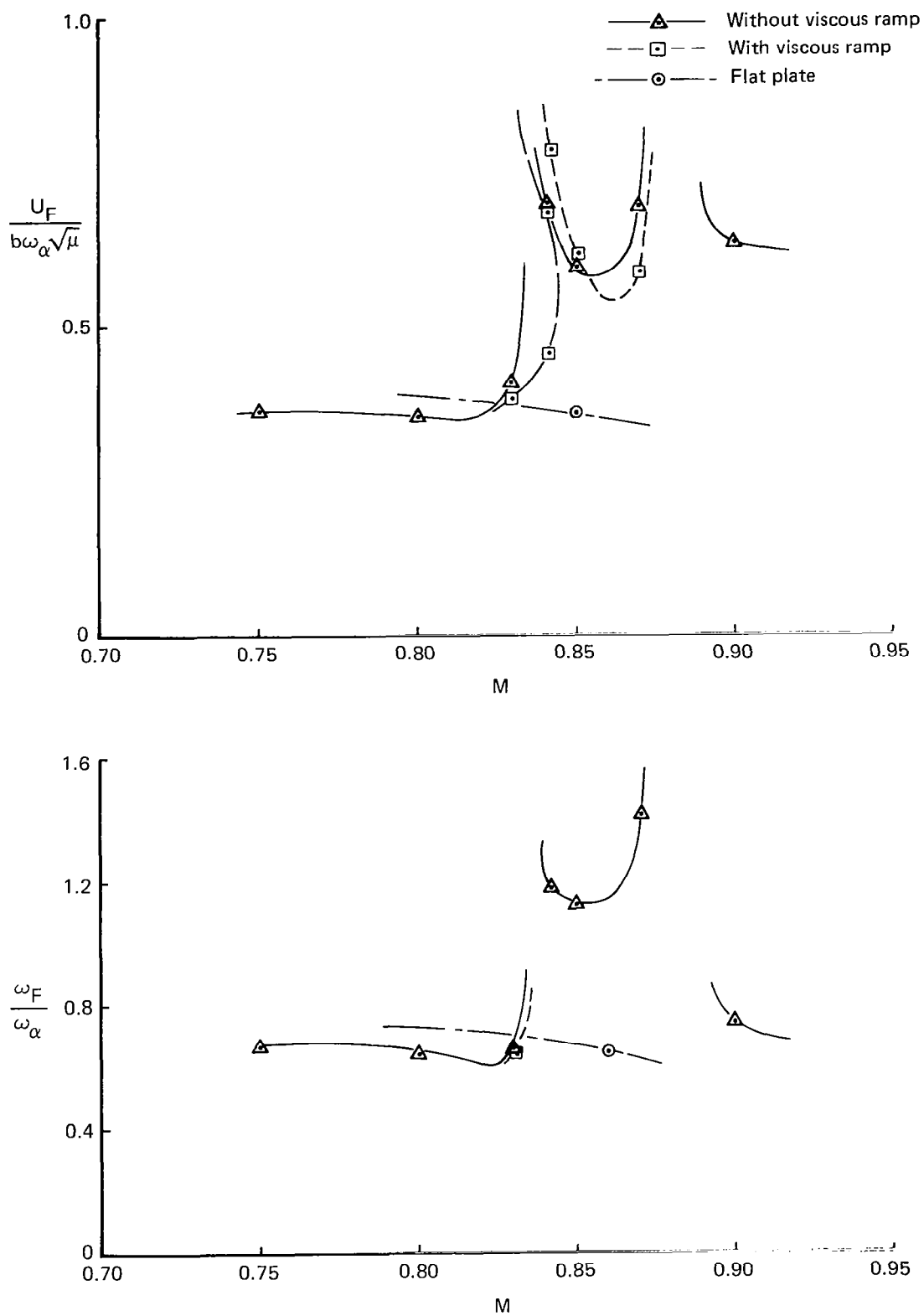


Figure 61.—Flutter Velocity and Frequency Versus Mach Number for a NACA 64A010 Airfoil,  $\omega_h/\omega_\alpha = 0.6$ ,  $\mu = 50$

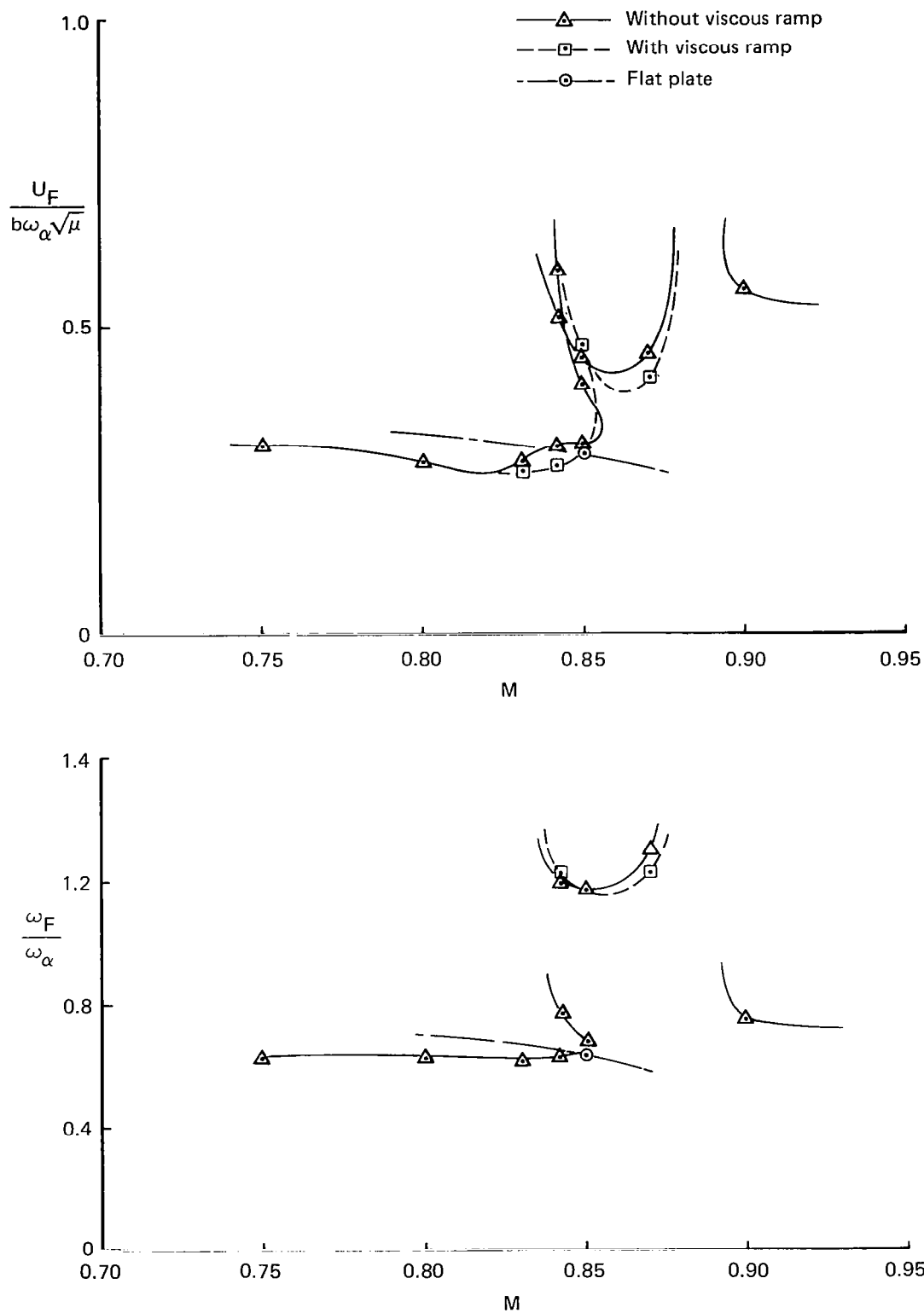


Figure 62.—Flutter Velocity and Frequency Versus Mach Number for a NACA 64A010 Airfoil,  $\omega_h/\omega_\alpha = 0.6$ ,  $\mu = 100$



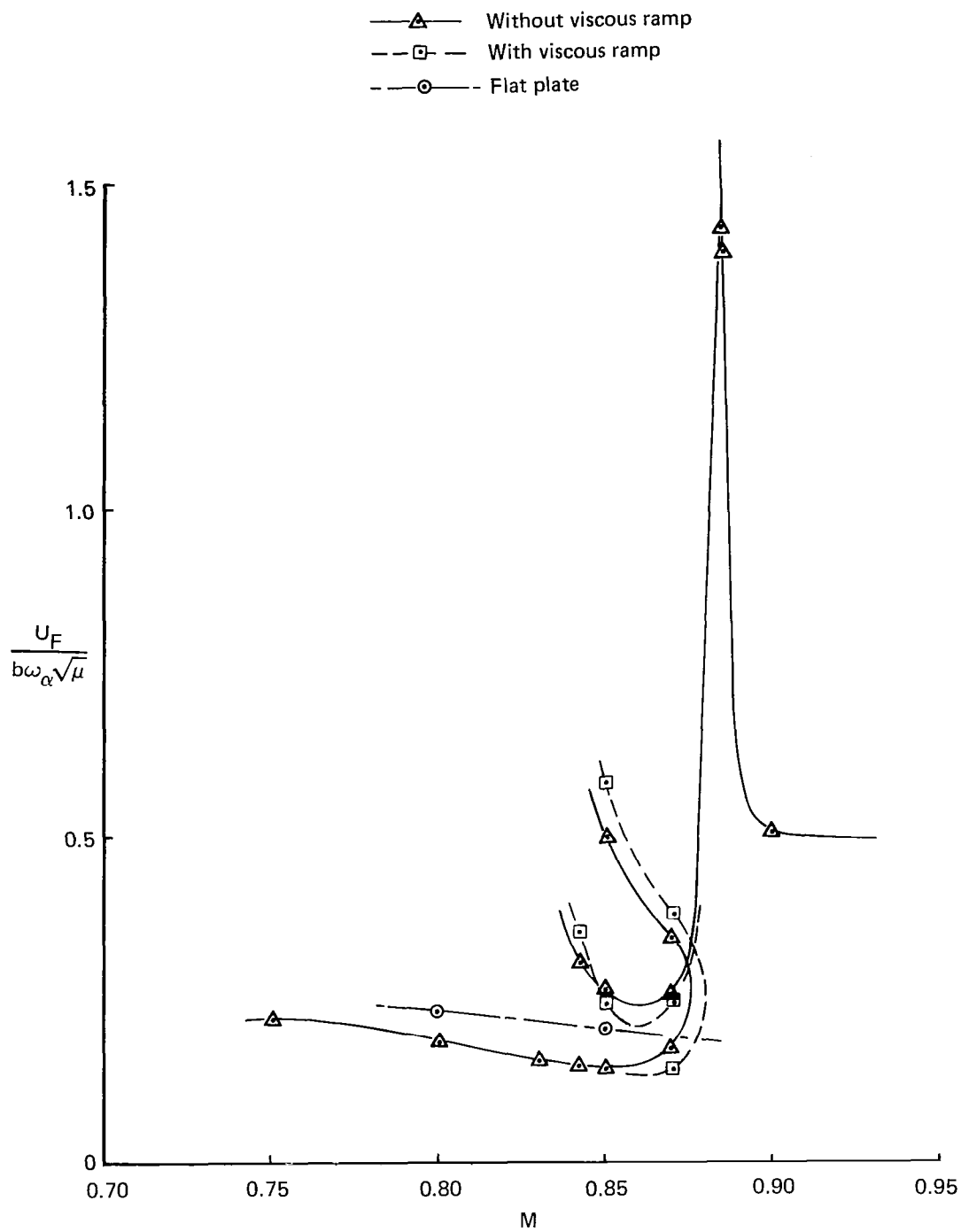


Figure 63.—Flutter Velocity and Frequency Versus Mach Number for a NACA 64A010 Airfoil,  $\omega_h/\omega_\alpha = 0.6$ ,  $\mu = 300$

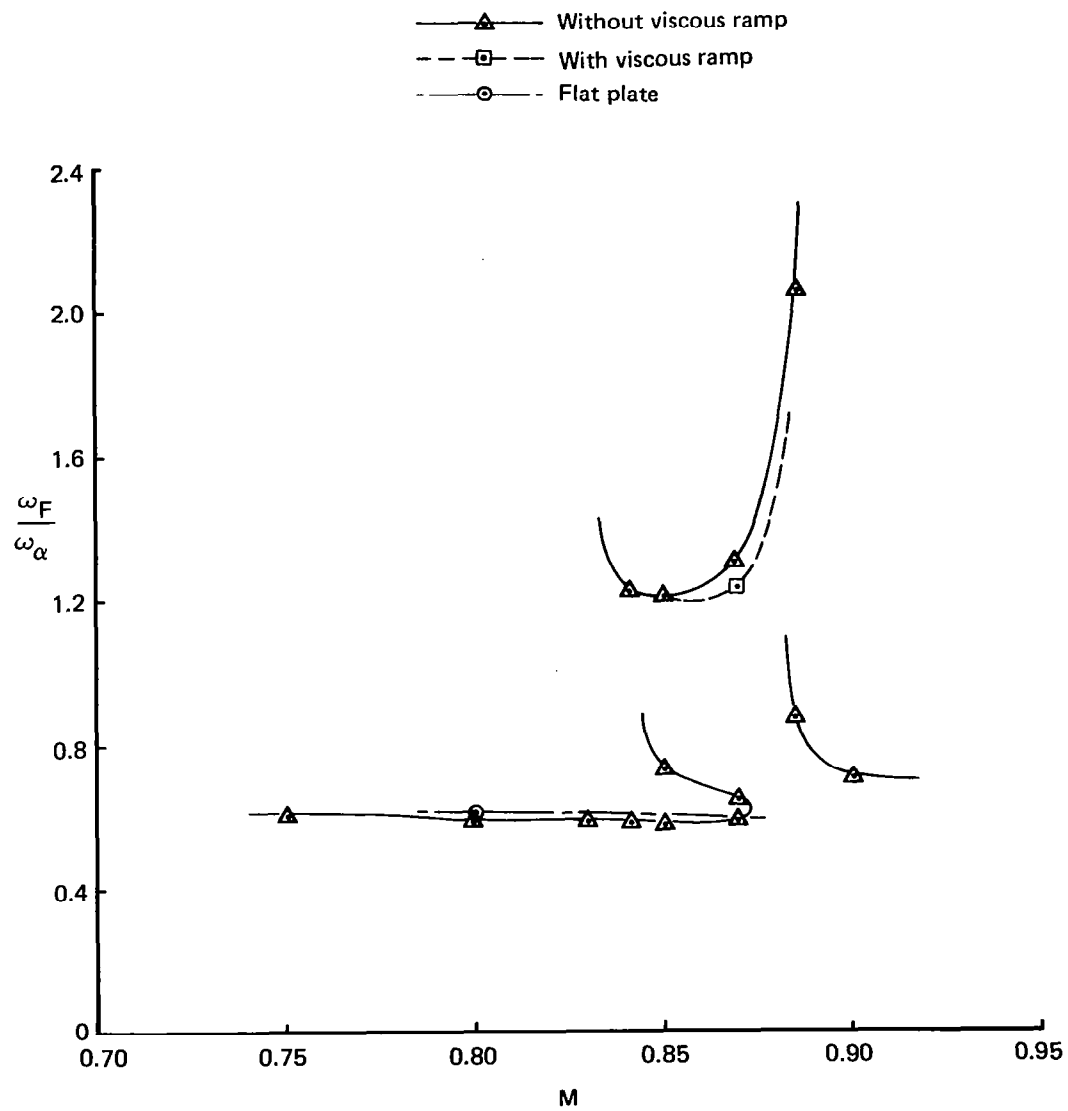


Figure 63.—(Concluded)

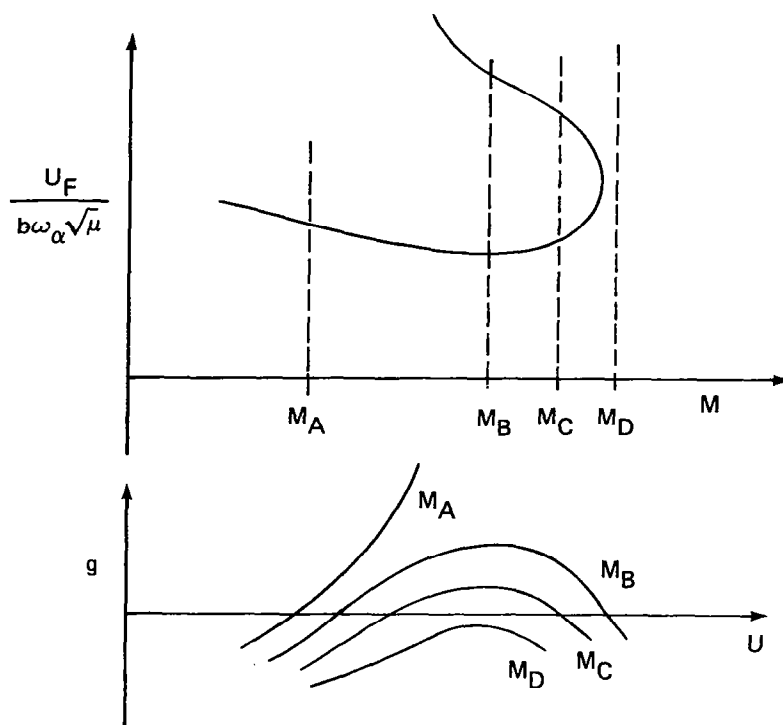


Figure 64.— Behavior of U-g Curves with Variation in Mach Number

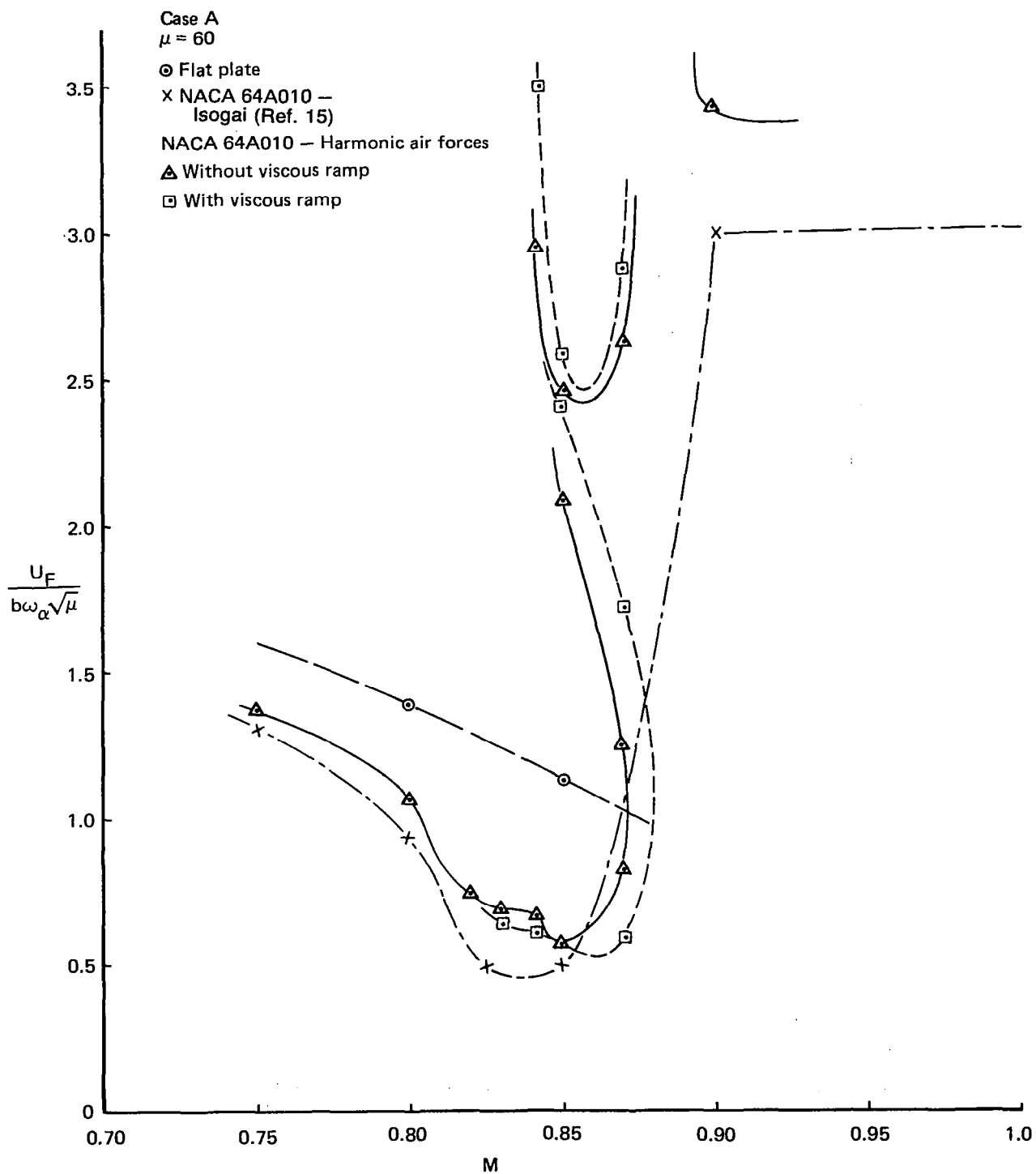


Figure 65.—Flutter Velocity and Frequency Versus Mach Number for a NACA 64A010 Airfoil, "Case A"

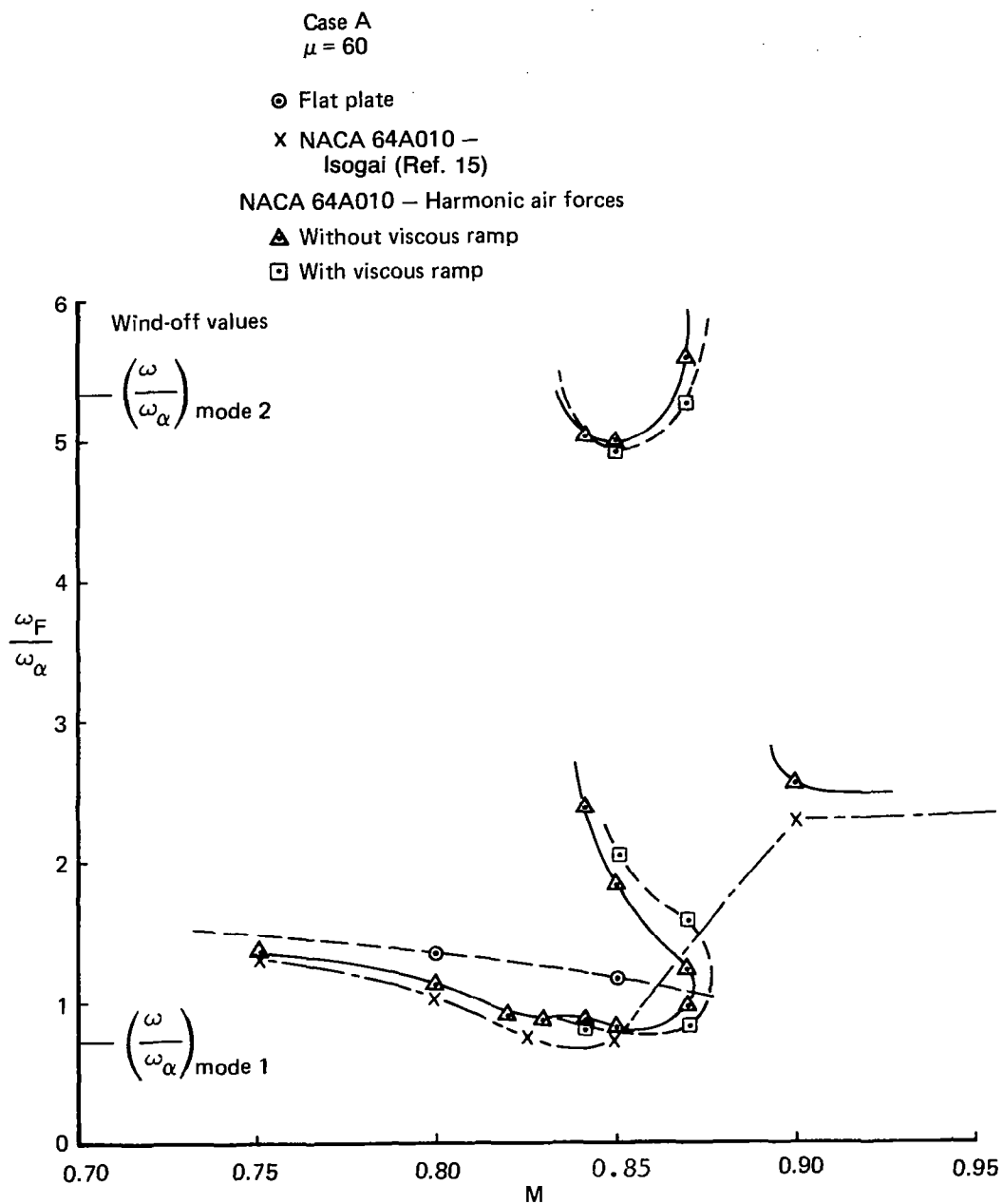


Figure 65.—(Concluded)

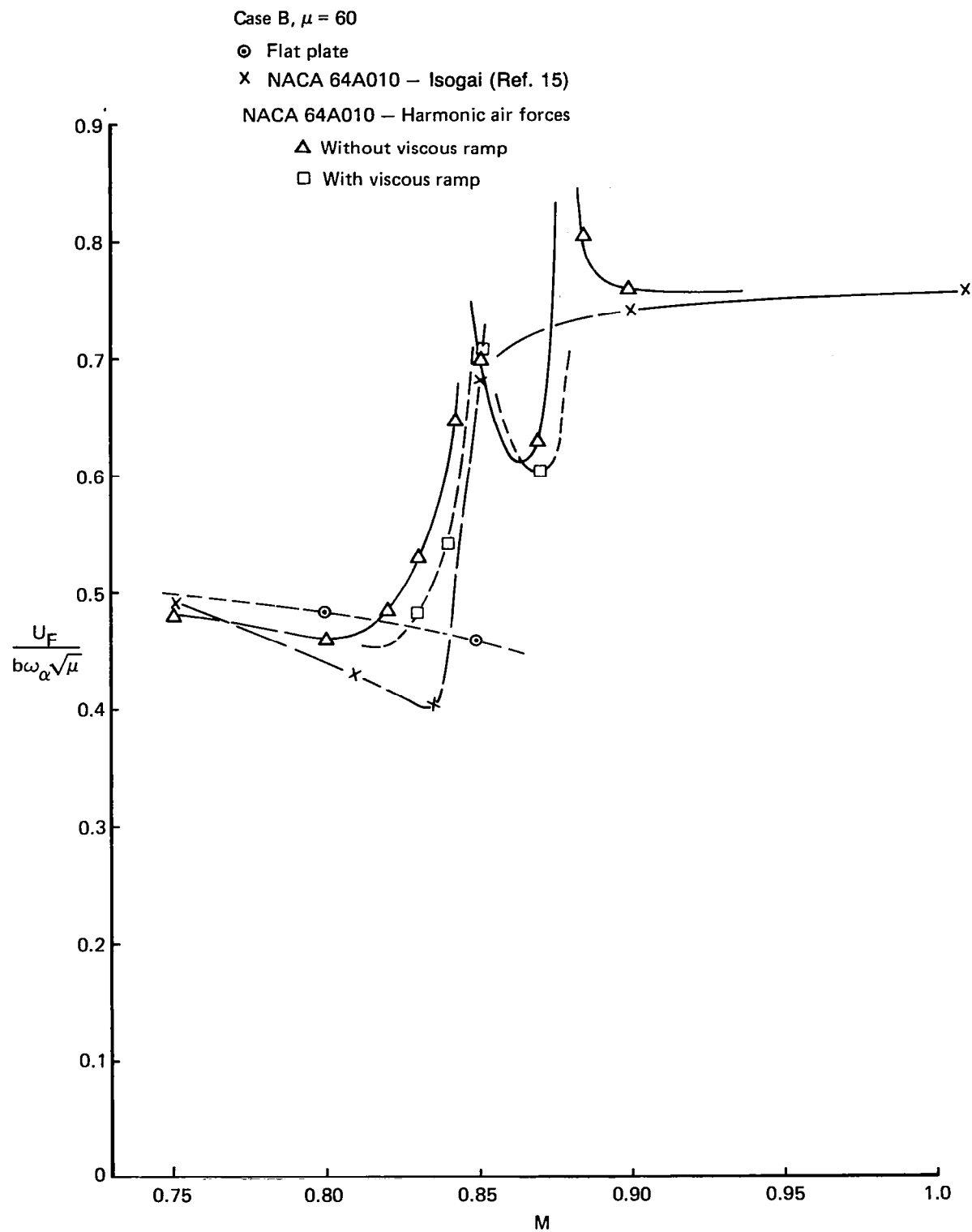


Figure 66.—Flutter Velocity and Frequency Versus Mach Number for a NACA 64A010 Airfoil, "Case B"

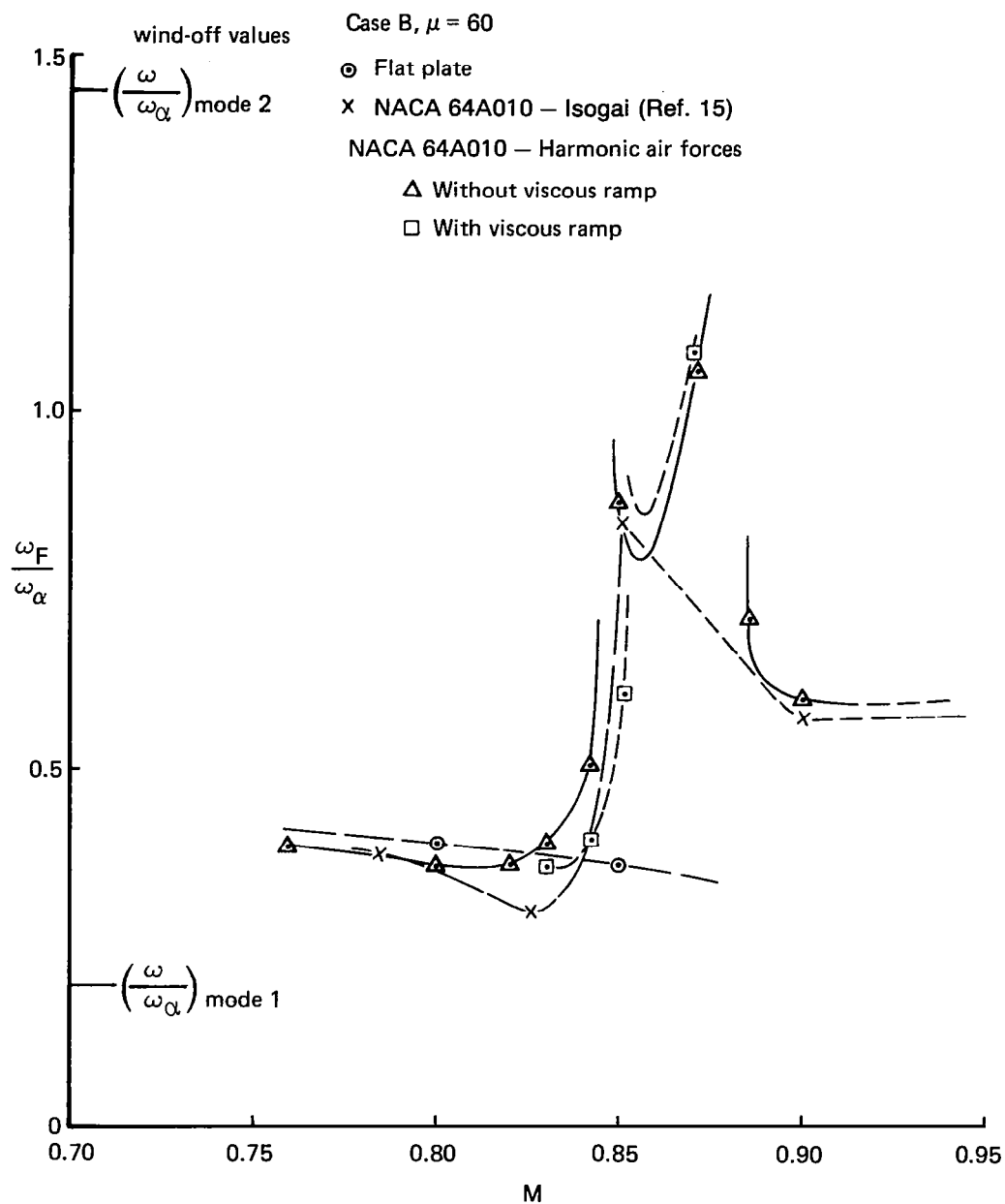


Figure 66.—(Concluded)

NACA 64A010

- " $\phi_2$ " ○ Difference solution  
 " $\phi_1$ " □ Flat plate solution  
 " $\phi_1$ " ◇ Full solution

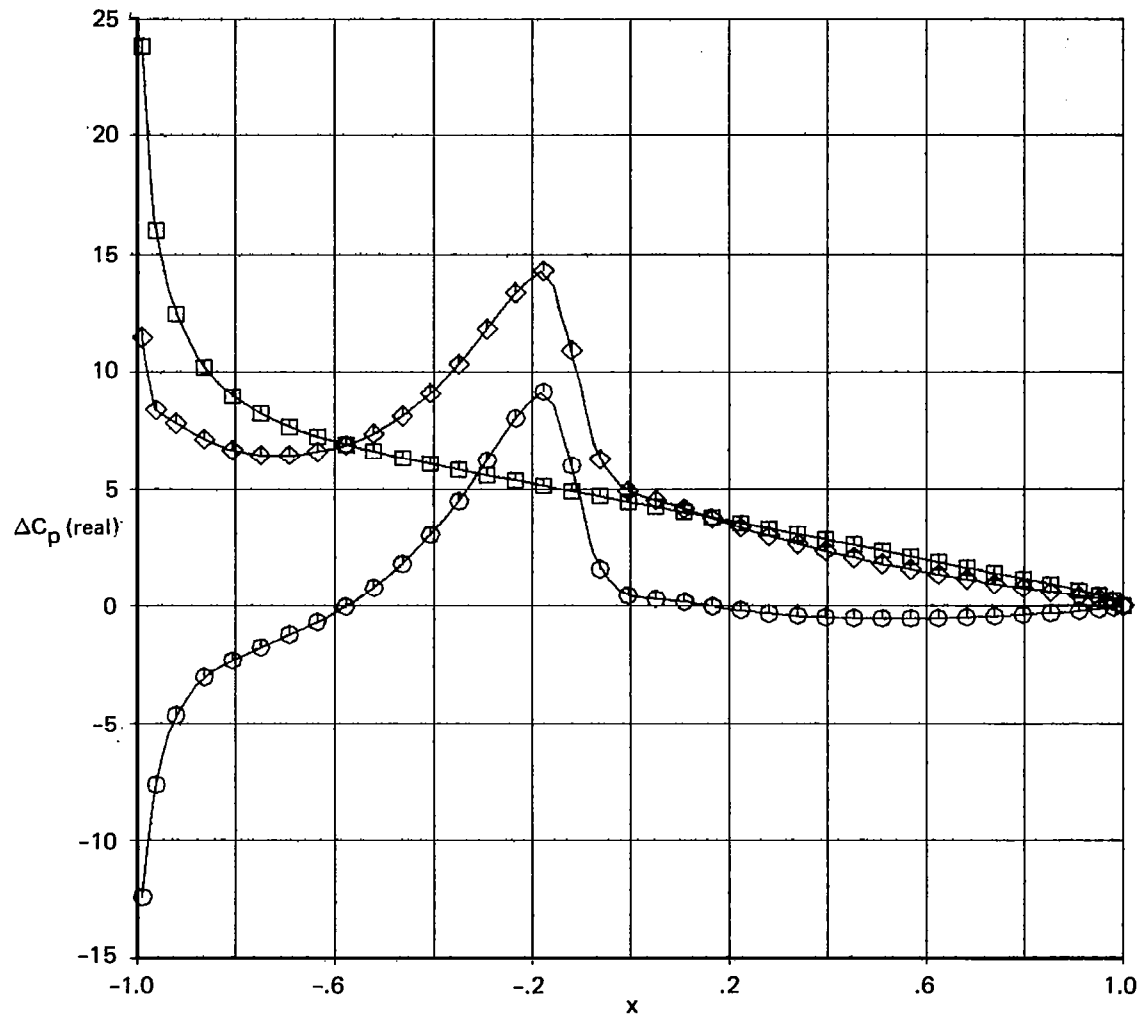


Figure 67.—Real Part of Pressure Coefficient Distributions From One- and Two-Step Solution Procedures for a Fine, Full-Size Mesh,  $M=0.8$ ,  $k=0.3$ ,  $\alpha_m=0^\circ$



NACA 64A010

" $\phi$ "<sub>2</sub> ○ Difference solution  
 " $\phi$ "<sub>1</sub> □ Flat plat solution  
 " $\phi$ "<sub>1</sub> ◇ Full solution

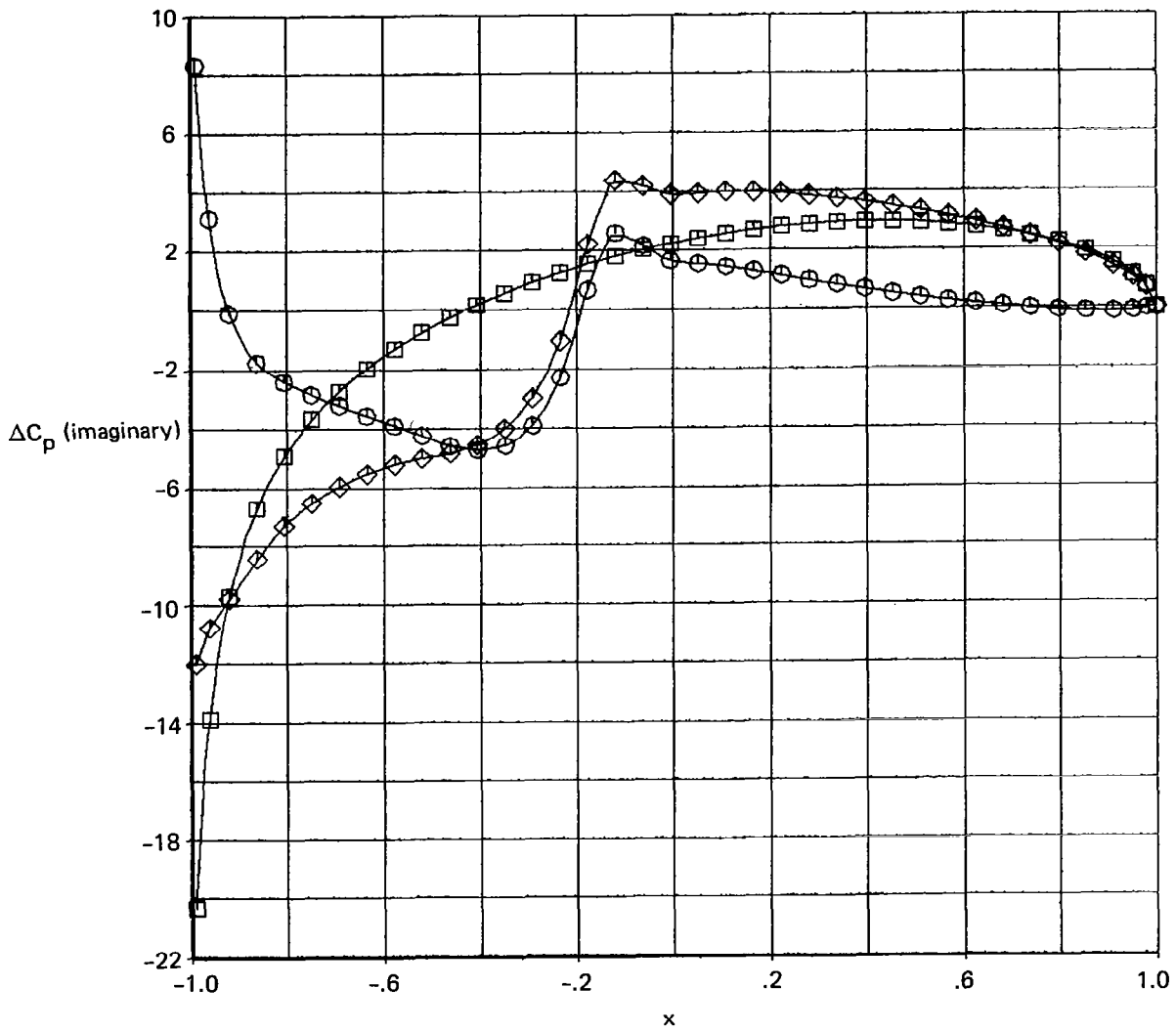


Figure 68.—Imaginary Part of Pressure Coefficient Distributions From One- and Two-Step Solution Procedures for a Fine, Full-Size Mesh,  $M=0.8$ ,  $k=0.3$ ,  $\alpha_m=0^\circ$

NACA 64A010

Reduced  $\circ$   
Full  $\square$

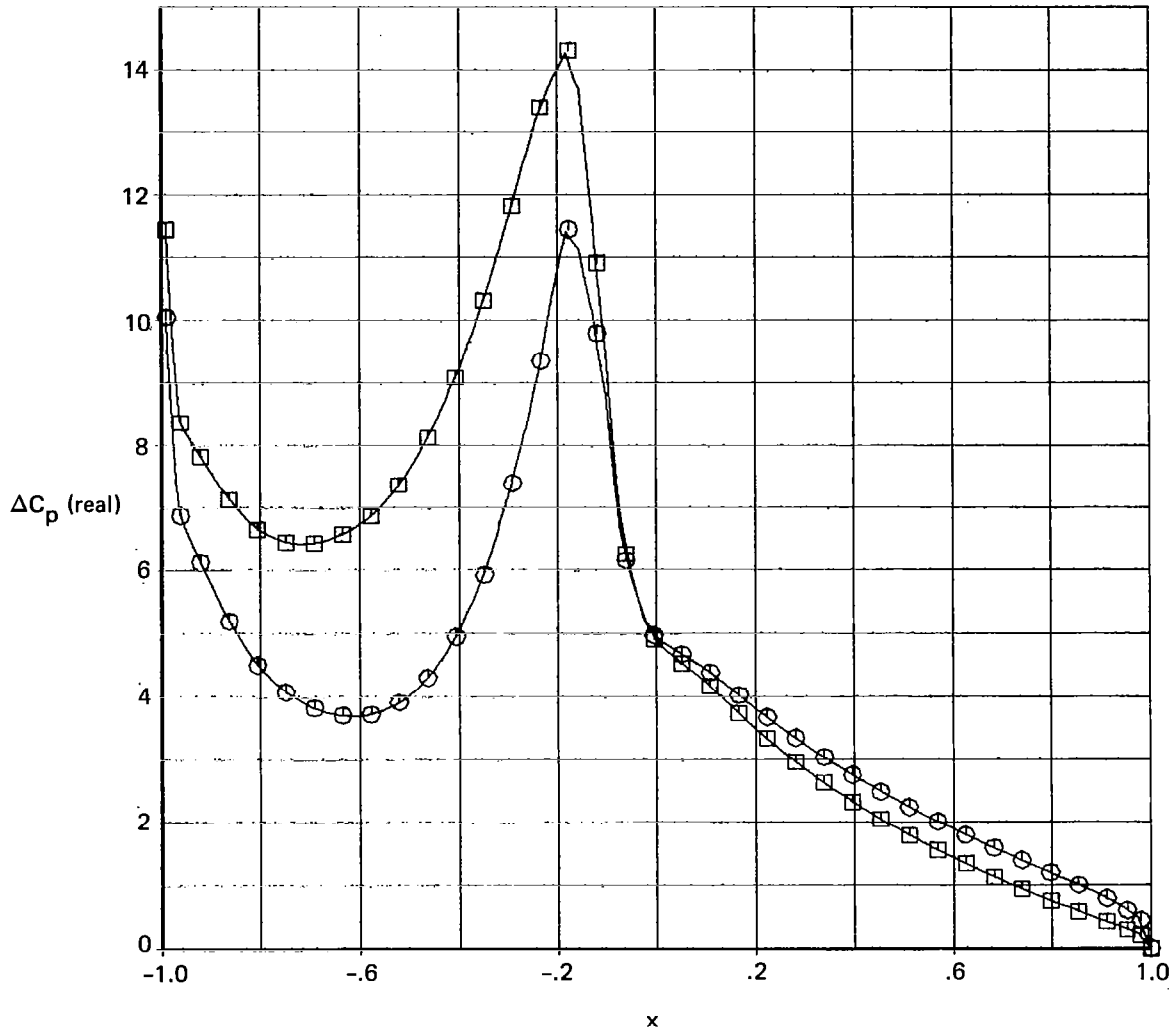


Figure 69.—Comparison of Pressure Coefficient Distribution From a Full-Size Mesh With the Distribution From a Reduced Mesh, One-Step Solution, Real Part,  $M = 0.8$ ,  $k = 0.3$ ,  $\alpha_m = 0^\circ$

NACA 64A010

Reduced  $\circ$

Full  $\square$

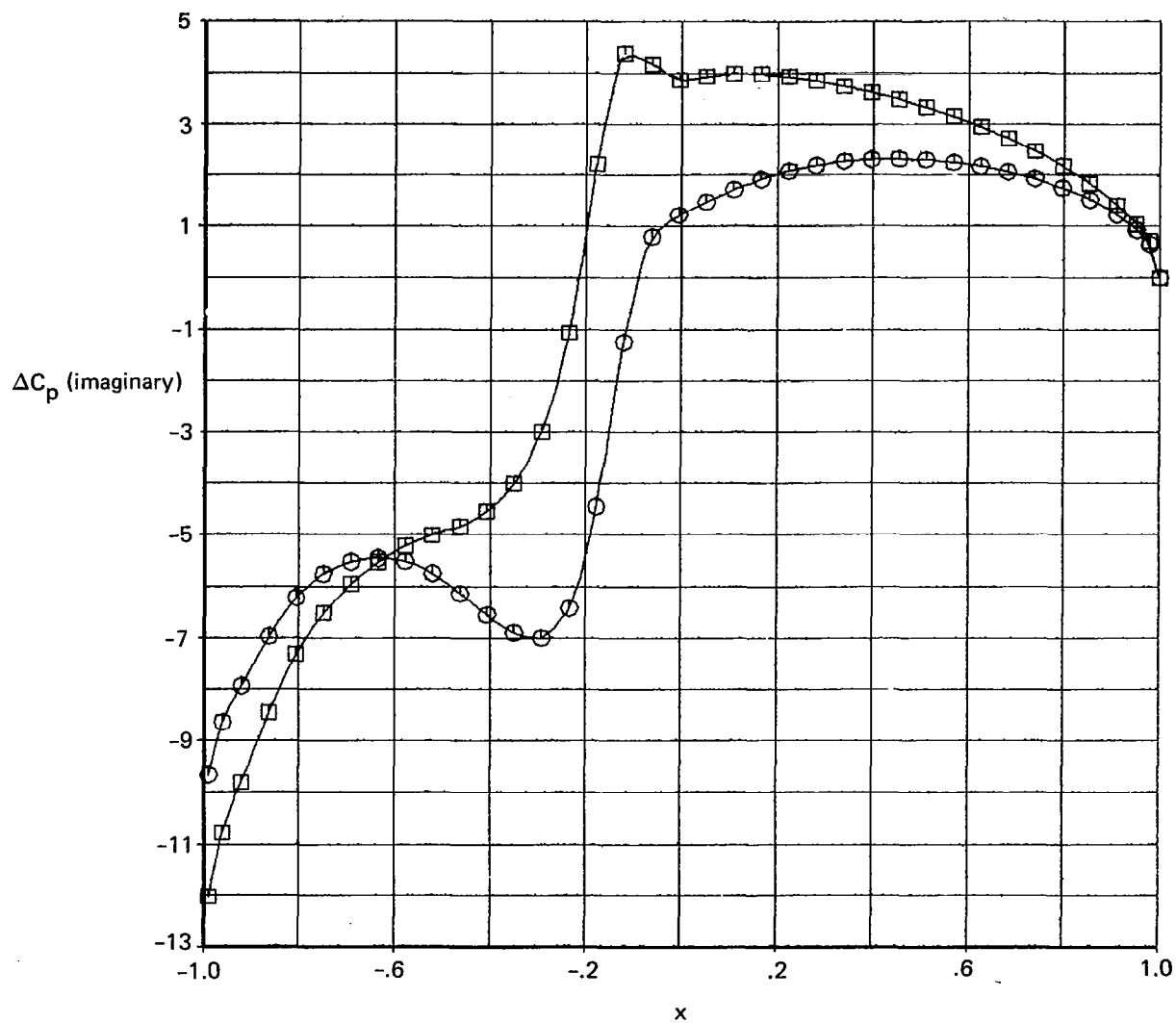


Figure 70.—Comparison of Pressure Coefficient Distribution From a Full-Size Mesh With the Distribution From a Reduced Mesh, One-Step Solution, Imaginary Part,  $M = 0.8$ ,  $k = 0.3$ ,  $\alpha_m = 0^\circ$

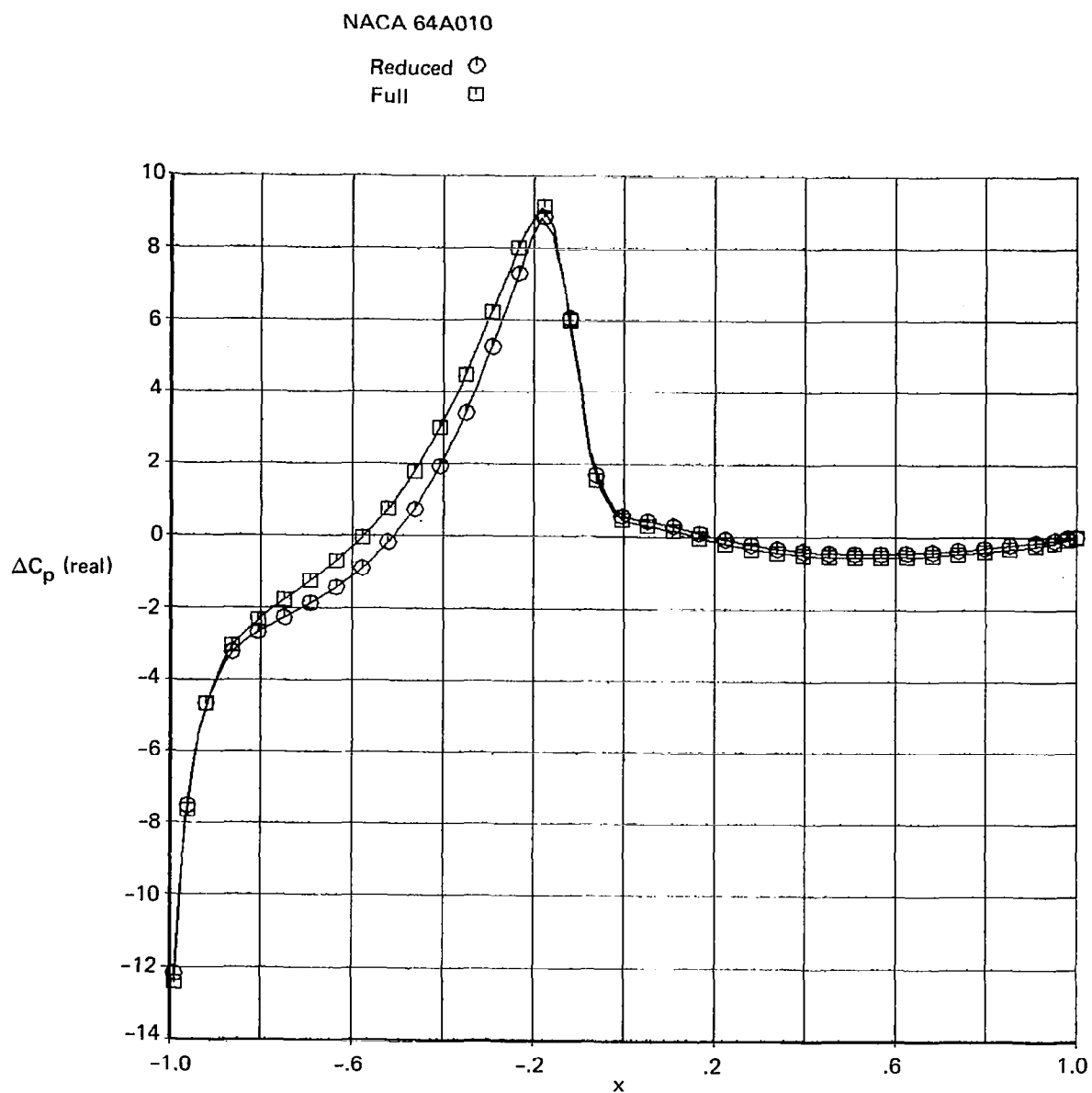


Figure 71.—Comparison of Pressure Coefficient Distribution From a Solution With a Full-Size Mesh With the Distribution From a Two-Step Solution,  $M=0.8$ ,  $k=0.3$ ,  $\alpha_m=0^\circ$ , Real Part

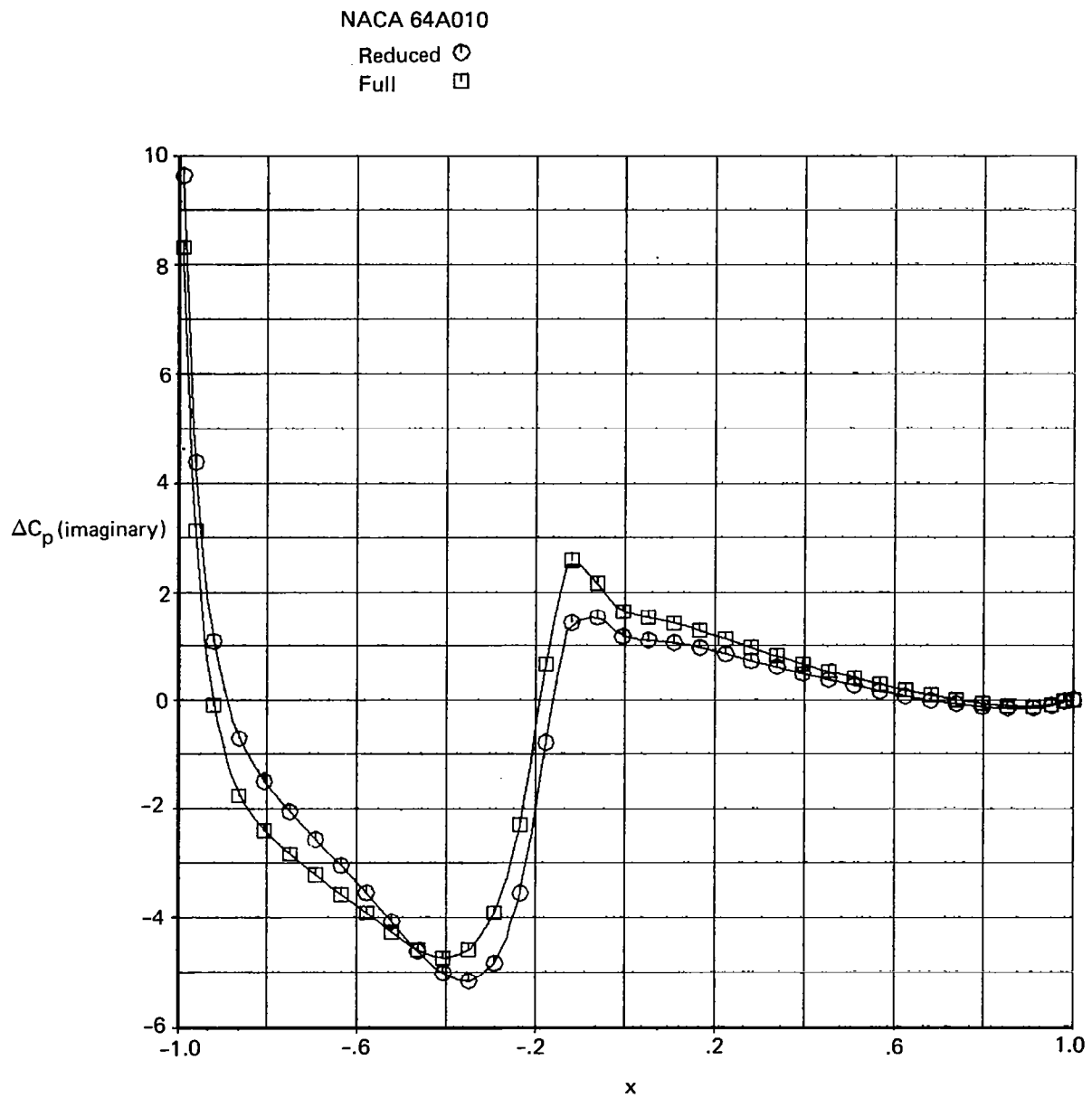


Figure 72.—Comparison of Pressure Coefficient Distribution From a Solution With a Full-Size Mesh With the Distribution From a Two-Step Solution,  $M=0.8$ ,  $k=0.3$ ,  $\alpha_m=0^\circ$ , Imaginary Part

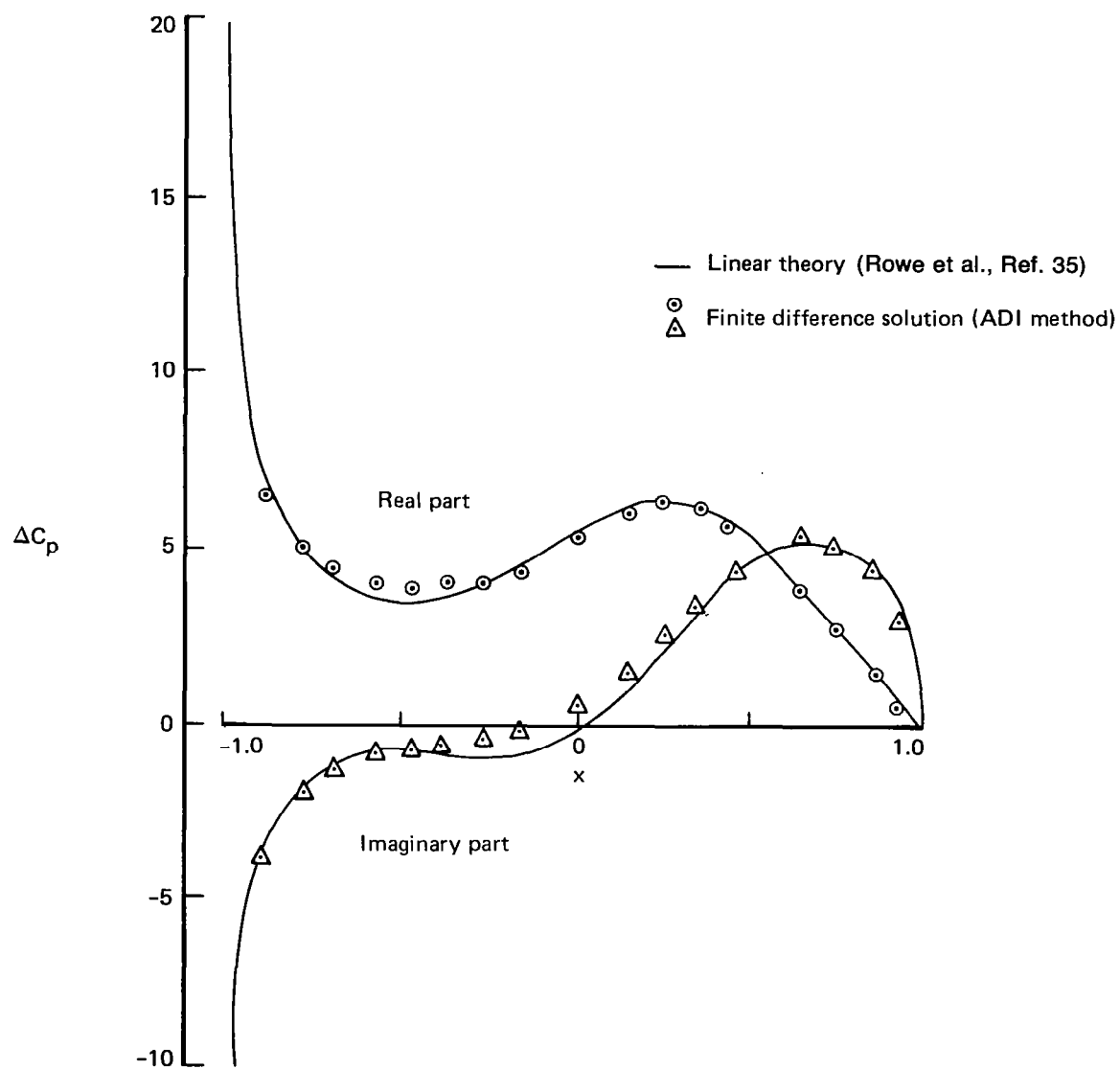


Figure 73.—Comparison of Pressure Coefficient Distribution From an ADI Solution With Linearized Theory for the Flow Over a Flat Plate Oscillating in Pitch About the Leading Edge,  $M = 0.9$ ,  $k = 0.45$

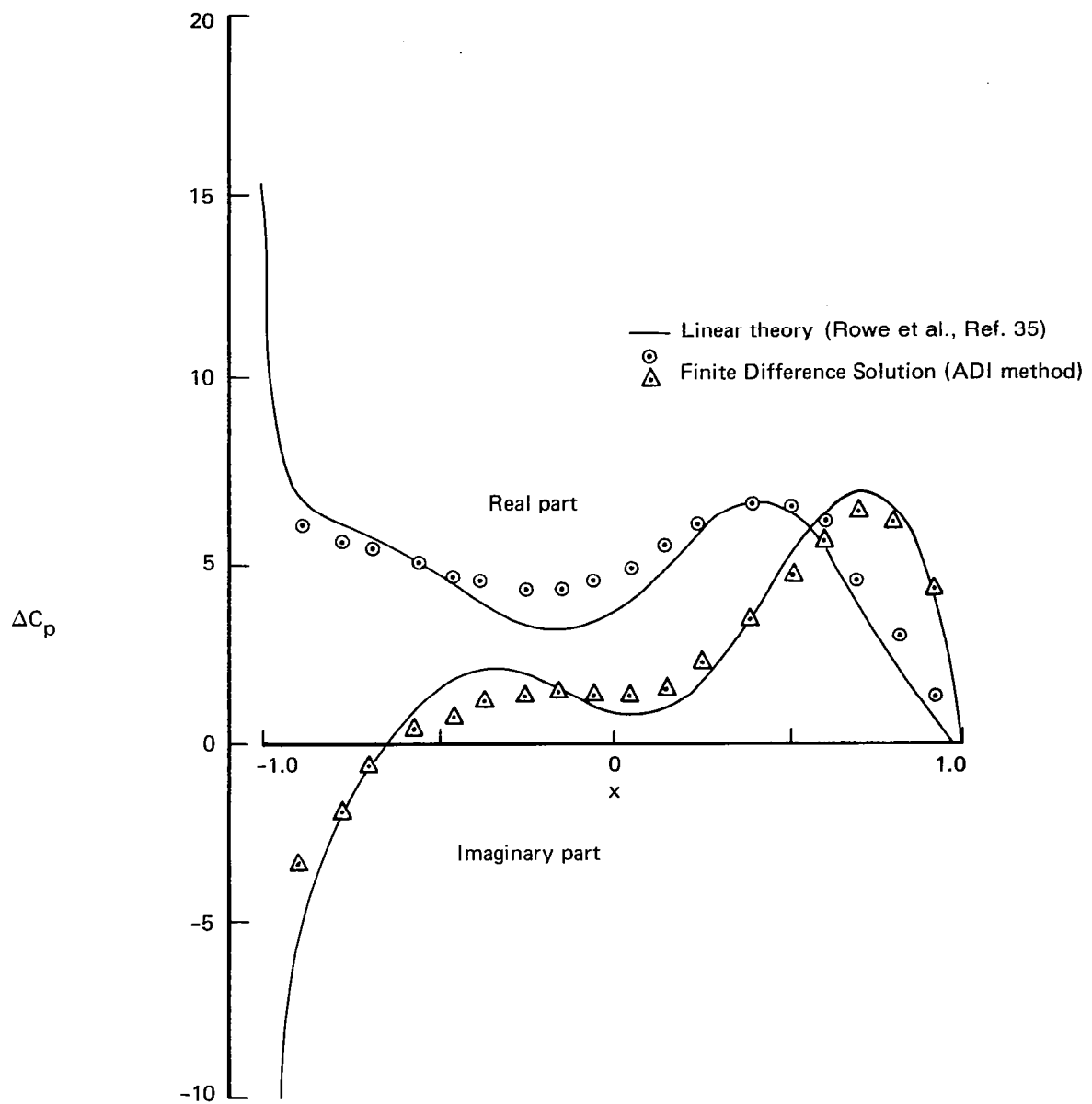


Figure 74.—Comparison of Pressure Coefficient Distribution From an ADI Solution With Linearized Theory for the Flow Over a Flat Plate Oscillating in Pitch About the Leading Edge,  $M = 0.9$ ,  $k = 0.6$

1. Report No. NASA CR-3537	2. Government Accession No.	3. Recipient's Catalog No.	
4. Title and Subtitle A HARMONIC ANALYSIS METHOD FOR UNSTEADY TRANSONIC FLOW AND ITS APPLICATION TO THE FLUTTER OF AIRFOILS		5. Report Date May 1982	
		6. Performing Organization Code	
7. Author(s) F. Edward Ehlers Warren H. Weatherill		8. Performing Organization Report No. D6-49821	
9. Performing Organization Name and Address Boeing Commercial Airplane Company P.O. Box 3707 Seattle, Wa. 98124		10. Work Unit No. .	
		11. Contract or Grant No. NAS1-15957	
12. Sponsoring Agency Name and Address National Aeronautics and Space Administration Washington, D.C. 20546		13. Type of Report and Period Covered Contractor report	
		14. Sponsoring Agency Code	
15. Supplementary Notes Langley Technical Monitor: Robert M. Bennett Final Report			
16. Abstract <p>A finite difference method for solving the unsteady transonic flow about harmonically oscillating wings is investigated. The procedure is based on separating the velocity potential into steady and unsteady parts and linearizing the resulting unsteady differential equation for small disturbances. The differential equation for the unsteady velocity potential is linear with spatially varying coefficients and with the time variable eliminated by assuming harmonic motion.</p> <p>A study is presented of the shock motion associated with an oscillating airfoil and its representation by the harmonic procedure. The effects of the shock motion and the resulting pressure pulse are shown to be included in the harmonic pressure distributions and the corresponding generalized forces.</p> <p>Analytical and experimental pressure distributions for the NACA 64A010 airfoil are compared for Mach numbers of 0.75, 0.80 and 0.842. The results are presented for plunge and pitch modes, and for several reduced frequencies.</p> <p>A typical section, two-degree-of-freedom flutter analysis of a NACA 64A010 airfoil is performed. The results show a sharp transonic bucket in one case and abrupt changes in instability modes.</p> <p>An alternating direction solution method is derived for the harmonic procedure. Also, a two step solution procedure is investigated.</p>			
17. Key Words Unsteady Flow Transonic Flow Oscillating Airfoil Flutter		18. Distribution Statement Unclassified - Unlimited  Subject Category 02	
19. Security Classif. (of this report) Unclassified	20. Security Classif. (of this page) Unclassified	21. No. of Pages 152	22. Price A08